DESIGN AND DEVELOPMENT OF AN ULTRASONIC JET ARRAY (UJA) FOR MICRO PROPULSION

by

Seow Yuen Yee

A dissertation submitted in partial fulfillment
of the requirements for the degree of
Doctor of Philosophy
(Electrical Engineering)
in The University of Michigan
2013

Doctoral Committee:

Professor Khalil Najafi, Chair
Associate Professor Luis P. Bernal
Professor Yogesh Gianchandani
Assistant Research Scientist Rebecca L. Peterson
Emeritus Professor Kensall D. Wise

© Seow Yuen Yee
All rights reserved
2013

To my mother and sisters for their love and support,

and to the memory of my father.

ACKNOWLEDGEMENTS

I would like to take this opportunity to express my sincere appreciation to some important people who supported me throughout my Ph.D. research. First and foremost, I would like to thank my research advisor, Professor Khalil Najafi, for his patience, support, encouragement, guidance and motivation during the course of my graduate education. Without him, I would not have made it this far. Professor Najafi is somewhat of a father figure to me, whose unending support and guidance in both my academic and personal life has helped me through many difficult times.

Next, I would like to express my gratitude towards the members of my thesis committee, who have greatly influenced my Ph.D. career path. I am indebted to Professor Yogesh Gianchandani for introducing me to the exciting field of MEMS and microsystems during my early involvement with the WIMS-ERC undergraduate summer research program back in 2005. It is a great honor to have Professor Kensall Wise as both my academic grandfather and on my thesis committee. Professor Wise has always been an inspiring figure in the MEMS field. I would also like to thank Professor Luis Bernal for his patience, guidance, and support in the modeling effort of this research work since I do not have a background in mechanical or aerospace engineering. I have learned a lot from Professor Bernal in understanding the physics behind this project. Last but not least,

it has been a pleasure to work with Dr. Becky Peterson, who is the most recent addition to the incredible group that has supported my research work. I am grateful for her helpful guidance and support in tackling some of the hardest tasks in this research.

With close to a decade here in Ann Arbor, being so far away from home, the friends that I made here have been like an extended family. They are always there for me through the ups and downs of my roller-coaster life. Without them, I probably would not have survived this far in life. I would like to thank all my friends, both here in Ann Arbor and throughout the world, for their friendship and support. I would especially like to thank Jeffrey Gregory for his help and guidance in my research (and for proof-reading all my written works), for feeding me great food, and for his patience with my never-ending complaints. Xiaoran Tong is like a sister to me and there are no words to express how grateful I am to know her. Finally, I would like to thank Erkan Aktakka for his friendship and support, Karthik Kumar for the many long discussions and guidance on research, Tao Li for his "lunch-time counseling hours", Christine Eun for understanding and supporting the "crazy" me, Tzeno Galchev and Jae Yoong Cho for their mentorship, Niloufar Ghafouri for listening to my endless complaints, Naveen Gupta for his help in understanding the basics of fluid mechanics, Ning Gulari for her friendship and support, Anne Itsuno for being such a great roommate, Emine Cagin for her help in preparing for qualifying examinations, Mark Richardson and Amar Basu for their mentorships during undergraduate researches, Katherine Knisely for her help with the laser vibrometer and calibrated microphone, Kartheek Gangadhara for his help with the hotwire anemometer test, Yutao Qin for his help with the epoxy, the Najafi-students, the Gianchandani-

students, the Wise-students, the Rais-Zadeh-students, the SSEL administration staff, especially Trasa Burkhardt, the LNF staff, my undergraduate friends, my Malaysian friends, and everyone else who has supported me through this critical time in my life.

Last but not least, I would like to thank my family, my mom (Chean Keat Tan) and three sisters (Seow Voon Yee, Seow Yeing Yee, and Xiao Qi Yee), for being there for me unconditionally, and for their boundless love and support. Without them, I would not be who I am today. Dad, I will like to say that I miss you very much and that your spirit and guidance will always stay in my memory.

TABLE OF CONTENTS

Dedication ii

Acknowledgements iii

List of Figures ix

List of Tables xxiii

List of Appendices xxv

Nomenclature xxvi

Abstract xxviii

Chapter 1 Introduction 1

1.1 Background to Micro Propulsion Applications 3

1.1.1 Wing-type Propulsion: Rotary Wings (Helicopters) 4

1.1.2 Wing-Type Propulsion: Flapping Wings (Ornithopters or Entomopters) 4

1.1.3 Jet Propulsion 7

1.1.3.1 Chemical Propulsion 8

1.1.3.2 Electrical Propulsion 9

1.2 Background to Chip Cooling Applications 11

1.3 A Review of Air Micro-jets 14

1.3.1 Non-zero-net-mass Systems 16

1.3.1.1 Pulsed Jets 16

1.3.2 Zero-net-mass Systems 19

1.3.2.1 Synthetic Jets 19

1.3.2.2 Ultrasonic Jets 22

1.4 Research Goals and Objectives 26

1.5 Thesis Overview 29

Chapter 2 design of Ultrasonic jets (U-Jet) using acoustic streaming Theory 30
2.1 Background 30
2.2 Structure and Principles of Operation of the Ultrasonic Jet Array (UJA) 33
2.3 Coupled System Model for a High-Frequency and Large-Deflection U-JET .. 35
2.3.1 Modeling of Non-linear ω_D due to Large Deflection 38
2.3.2 Model Verification 40
2.4 Parameter Optimization Based on Theoretical Results 41
2.4.1 Trapezoidal Voltage Waveform 42
2.4.2 Sinusoidal Voltage Waveform 50
2.4.3 Comparison of Trapezoidal and Sinusoidal Waveform 54
2.5 Design of Perforations on a Rigid Electrode 55
2.6 Design of an UJA for Flow Entrainment Optimization 58
2.7 Dual Cavity Design 59
2.8 Design Variations for Gen. 2 and Gen. 3 60
2.9 Summary 63

Chapter 3 Design and Fabrication of Filleted Electrode using Photoresist Solvent Reflow 65
3.1 Introduction 65
3.1.1 Background 66
3.2 Main Challenges 68
3.3 Filleted Electrode Design 70
3.4 Fabrication Process 71
3.4.1 Materials Selection for High-Frequency and Large-Deflection Diaphragm 72
3.4.2 Fabrication Process Flow 72
3.4.3 Characterization of Photoresist Solvent Reflow Process 83
3.5 Discussions 89
3.6 Summary 92

Chapter 4 Characterization of Diaphragm Actuators with Flat and Filleted Electrodes .. 94
4.1 Custom Drive Circuitry for Diaphragm Actuators 94
4.1.1 Circuit Design using LTSpice Simulation 96
4.1.2 Circuit Implementations 101
4.2 Pull-in Characteristics 103
4.3 Reliability Test 105
4.3.1 Static Pull-in Test 106
4.3.2 Characterization of Dynamic Pull-in 108
4.3.3 Long Term Reliability Test 114
4.4 Summary 119

Chapter 5 Technology Developments and Testing of ultrasonic jets array (UJA) 121
5.1 Development of U-JETs and UJA 122
5.1.1 Design of Contact Pads and Wire Connections 127
5.2 Characterization of the UJA using Calibrated Microphone 131
5.3 Estimation of Air Micro-Jet Velocity 137
5.4 Pendulum Test for Direct Thrust Measurements 138
5.4.1 Thrust measurements for Device A 143
5.4.2 Thrust measurements for Device B 149
5.4.3 Thrust measurements for Device C 152
5.5 Summary 155

Chapter 6 Conclusions and Future Works 157
6.1 Conclusions 157
6.2 Future Work 161

Appendices 163
References 188

LIST OF FIGURES

Figure 1-1: (Left) Illustration of the use of micro flying devices for establishing communication networks between user stations located on the ground for aid in natural disaster rescue [1], (Middle) for visual aid in mining accident rescue [2], and (Left) for chemical monitoring in narrow tunnels or space [3]. 2

Figure 1-2: Examples of the evolution of electronic devices where there is need for smaller and more efficient cooling systems. (Left to right) Mainframe computer [4], workstation [5], laptop [6] and mobile devices [7]. 2

Figure 1-3: Micro rotary wing propulsion (Helicopter) [11] 4

Figure 1-4: Recent technology breakthroughs in micro flapping MAVs [10], [11], [14]–[17]. The comparisons of the performance are included in Table 1-2 5

Figure 1-5: (Left) Prototype and (Right) Controlled flight of the insect-scale robot [17].. 6

Figure 1-6: MAVs flight regime compared to larger scale flight vehicles, adapted and reconstructed from [18]. 7

Figure 1-7: (Top Left) Digital micropropulsion system using lead styphnate as the propellant [20], (Bottom Left) Gun powder-based solid propellant propulsion system [21], (Top Right) Solid propellant rocket array thruster [22] and (Bottom Right) Vaporizing liquid micro thruster [23]. 9

Figure 1-8: (Left) Colloid thruster working principles, (Right) Structure of the micro colloid thruster [24]. 10

Figure 1-9: (Top) Moore's law predicting the increase in the number of transistors per die as technology advances [44], and (Bottom) the power dissipation corresponding to the increase in transistor density [45]. 12

Figure 1-10: Conceptual configurations of chip cooling using the e-jet array [49].......... 14

Figure 1-11: Flow chart showing different categories of air micro-jets and methods of actuation (lowest level). Blue box highlights the focus of this research work. 15

Figure 1-12: (Left) Piezoelectric actuated pulsed actuator [26], and (Right) Magnetically actuated pulsed actuator [27]. An external air supply or piping is needed for this configuration. 17

Figure 1-13: (Left) Plasma pulsed actuators (or known as Dielectric Barrier Discharge Actuators), and (Right) Cross section showing plasma induced flow directions [29]. 18

Figure 1-14: General anatomy of jellyfish and the jet generation sequence [51]. 19

Figure 1-15: Different actuator configurations for creating synthetic jets. Showing from the left to right: Single cavity with a vibrating diaphragm and an exit orifice at the opposite end of the diaphragm [30], single cavity with a vibrating diaphragm and an exit orifice at the side of the diaphragm [31], single cavity with dual vibrating diaphragm [32], and dual cavities with single vibrating diaphragm [32].. 20

Figure 1-16: (Top left) Electrostatic driver [30], (Top right) Piezoelectric driver [35], (Bottom left) Electromagnetic driver [34], and (Bottom right) Ferromagnetic driver [36]. 21

Figure 1-17: (Left) Schematic of the micro-jet actuator and (Right) SEM of the fabricated device [40]. 23

Figure 1-18: (Left) Cross section of the air micro-jet actuator and (Right) SEM of fabricated actuator array [52]. 24

Figure 1-19: (Left) Conceptual illustration of a single resonance micro-thruster and (Right) SEM of micro-fabricated array [42]. 25

Figure 2-1: Some important figures who contributed to the model development of ultrasonic jets generation by acoustic streaming with a Helmholtz resonator. 30

Figure 2-2: Ultrasonic jet array (UJA) with checkerboard arrangements of U-JET and jet holes, with cross section view at A to A'. The important parameters governing the performance of the UJA are labeled on the cross section. 33

Figure 2-3: (Left) Outflow phase where diaphragm moves downwards, pushing the air out from the cavity in one direction, and (Right) Inflow phase where diaphragm moves upwards, where suction of the air into the cavity occurs from all directions. 34

Figure 2-4: Flow chart to obtain equation for ω_D, which is dependent on the second order of the diaphragm's displacement. 38

Figure 2-5: Model verification using the parameters from Chou's work [52]. The frequency response of the thrust shows two clean resonant peaks where the first peak is related to the cavity's resonance and the second peak is related to the diaphragm's resonance. 41

Figure 2-6: Illustrations showing the advantages of utilizing trapezoidal waveform. (1) A sine waveform with small voltage amplitude, A, and (2) A sine waveform with the same rise and fall time as a trapezoidal waveform and notes explaining the advantages of trapezoidal waveform. 43

Figure 2-7: Generated thrust versus varying throat length L_T. 44

Figure 2-8: Flow chart showing design parameter optimization process for trapezoidal drive waveform. 45

Figure 2-9: (Left) The simulated frequency response for the design with h_o = 10 μm at V_o = 380 V, as listed in Table 2-2, and (Right) Transient response of the generated air micro-jet when actuated at the resonant frequency shown on the left plot. 45

Figure 2-10: (Top) Transient diaphragm displacement at 35.1 kHz and (Bottom) Transient diaphragm displacement at 67.1 kHz. 46

Figure 2-11: Parameters optimization with respect to the optimization procedure in Figure 2-8. (a) Generated thrust versus operating voltage, V_o, (b) Thrust-to-weight ratio versus cavity height, h_C, (c) Thrust-to-weight ratio versus throat height, h_T, by keeping area constant, and (d) Thrust-to-weight ratio versus throat width, w_T. 47

Figure 2-12: The influence of L_T on thrust for different h_o values. 48

Figure 2-13: Flow chart showing design parameter optimization process for sinusoidal drive waveform. 50

Figure 2-14: Frequency response curves for three operating voltages: (Top Left) 100 V, (Top Right) 200 V) and (Bottom) 400 V. 51

Figure 2-15: Sweep throat length, L_T at operating voltage of 200 V. 52

Figure 2-16: The three levels of plots correspond to the different throat area, A_T ratios of h_T to w_T; (1) Area0 = 1 to 5, (2) Area1 = 1 to 4, and (3) Area2 = 1 to 2.5 (Left column). The corresponding cavity height sweep for optimum h_T and w_T per each area is attached (Right column). 53

Figure 2-17: (Left) Thrust produced using trapezoidal waveform at 380 V and (Right) Thrust produced using sinusoidal waveform at 380 V. 55

Figure 2-18: (Left) 3 areas of different perforation sizes and the layout of the perforations drawn in Gen. 1 57

Figure 2-19: Layout of different designs of UJA – (Left to Right) Checkerboard pattern, dream catcher pattern and honey comb pattern. Green areas are U-JETs while the black areas are jet holes. 58

Figure 2-20: Dual cavity design. (Top) 3D-illustration of the dual cavity U-JET design, and (Bottom) Layout of dual cavity design where green areas are the U-JETs and the black areas are the jet holes. The U-JETs are connected in a crab-leg manner to reduce damping due to connection sidewalls. 59

Figure 2-21: Layout of the designs listed in Table 2-4 for Gen 2........ 62

Figure 3-1: An example of a fully-clamped diaphragm. For electrostatic actuation, the main components are two parallel plates consisting of a rigid electrode and a suspended fully-clamped diaphragm, separated by an electrostatic gap. 66

Figure 3-2: Cross section of parallel-plate configuration for flat electrode design. Diaphragm pulls in from the center. 67

Figure 3-3: Reliability depends on the deflection angle, deflection distance and the contact area. Illustration based on flat electrode design. 69

Figure 3-4: Cross section of a single actuator with filleted electrode. When there is no voltage, the diaphragm is in a released or suspended position. When voltage is applied, the diaphragm is collapsed onto the perforated filleted electrode, achieving ~ 100 % volume displacement. 71

Figure 3-5: Summary of the fabrication process flow for filleted electrode design. It is a 3-mask process. Fabrication process for flat electrode is similar except photoresist reflow step is skipped. 73

Figure 3-6: (Left two images) Gas bubbles and surface waves occurs when no post baking is performed, and (Right) Smooth surface observed when post baking of the sacrificial photoresist is performed. 74

Figure 3-7: Electroplated nickel on a wafer for Gen. 2 layout. On the wafer, the dark areas are the areas for the jet holes while the light areas are the areas with electroplated nickel. 76

Figure 3-8: (Top left) View from the back side of the detached nickel, (Top right) View of the front side of the silicon frame, and (Bottom left) Side view of the buckled nickel electrode. 78

Figure 3-9: (Left) Successful released diaphragm after backside DRIE step and (Right) Diaphragm cracks after backside DRIE. The diaphragms are made out of silicon oxide-nitride-oxide and are transparent. The surface waves seen here are similar to Figure 3-6. 79

Figure 3-10: Illustration to show electrical shorts happening if crystal bond is removed before sputtering of metal layers. (Left) Crystal bond removed before sputtering of metal layers and (Right) Crystal bond removed after sputtering of metal layers.. 80

Figure 3-11: (Left) A diaphragm actuator with perfect metal coating on backside and (Right) Partial metal lift-off due to incomplete photoresist mask removal. .. 81

Figure 3-12: (Top Left) Microfabricated array of nine diaphragm actuators for Gen. 1 without jet holes etched, (Top Right) SEM of the cross-section and (Bottom) SEM image showing the diaphragm actuators. The tearing of the diaphragm is intentional to show the rigid electrode. 82

Figure 3-13: Photoresist solvent reflow process. The wafer is flipped upside down and exposed to solvent vapor. 84

Figure 3-14: (Top plots) Filleted photoresist profile going from left to right: before reflow, insufficient and optimal reflow. (Bottom images) 0.6 mm square diaphragm with (1) insufficient reflow, (2) optimum reflow, (3) mild over reflow and (4) excessive reflow which changes the base shape into a flattened pancake..... 85

Figure 3-15: (Top images) SEM images of the filleted electrode, and (Bottom) Illustration of the cross section of the actuator with the corresponding SEM image.. 86

Figure 3-16: Photoresist reflow with additional ring to ensure reflow does not go out of bounds. (Top) Photoresist pattern with 2 μm oxide ring defining the base shape and (Bottom) Photoresist reflowed, filling the base shape defined by the ring into a dome-like form. 87

Figure 3-17: Photoresist pattern is larger than the 2 μm oxide ring, showing that photoresist can be reflowed over a step height of 2 μm without going out of bound of the base shape. (Top) Photoresist pattern over a 2 μm oxide ring and (Bottom) Photoresist reflowed into a dome-like form without flowing out of bound of the base shape.. 88

Figure 3-18: The results of the sacrificial photoresist reflow without pre-baking, where the left and right figures correspond to the initial sacrificial photoresist shapes in Figure 3-16 and Figure 3-17 respectively.. 89

Figure 3-19: Flat and filleted electrode profile measured with DEKTAK profilometer. The two sharp peaks at each edge of the flat electrode are due to the non-ideal lithography process. The dips in the profile are due to the perforations on the electrode as the measurement is made on top of the electroplated electrode. 90

Figure 3-20: Electric field concentration simulated in COMSOL. (Left) Flat electrode has a maximum electric field of $6.293e^8$ V/m, which is higher than (Right) filleted electrode of $2.653e^8$ V/m by 2.4 times with an applied voltage of 200

V. The electrode profile is drawn based on the actual measured profile in Figure 3-19 91

Figure 4-1: Schematics showing the drive circuitry for converting DC signal to AC signal for high voltage and high frequency operation. 95

Figure 4-2: Circuit schematic showing the coupling of the driving signal for SW_1 (timing circuit loop) to the main circuit loop using a transformer, as adapted from [73]. 97

Figure 4-3: (Left) Schematic diagram of adding a feedback transistor (HEXFET) to maintain V_{GS} (adapted from [74]) and (Right) STW11NM80 [75] is similar to HEXFET and therefore can be used interchangeably in this design. 98

Figure 4-4: (Left) As suggested by [74], additional SW_4 can be added to increase noise immunity to the circuit, and (Top Right) Clock and V_{GS} signal of SW_1 for design with one feedback transistor and (Bottom Right) with two feedback transistors (Green signal = V_{GS}, Yellow signal = timing clock signal).......... 98

Figure 4-5: (Top) Schematic simulated in LTSpice, and (Bottom) Simulated waveforms for 10 kHz pulse with 20 % duty cycle.. 100

Figure 4-6: (Left) Drive circuitry implemented on a breadboard, (Middle Top) Air core transformer of 1:3 is used for coupling of the clock timing loop of SW_1 to the main circuit loop, (Middle Bottom) Low pass filter, resistive attenuator and series capacitance, and (Left) Transistor STW11NM80 for switches SW_1-SW_4 with heat sink attached for cooling. 101

Figure 4-7: (Left illustrations) Cross section illustration of the pull-in characteristics. (Right microscope images) View from back: Pull-in of diaphragm for flat (left column) and filleted electrode (right column). 104

Figure 4-8: Microscope image of (Left) Diaphragm at rest, (Middle) Diaphragm first pull-in at the center and (Right) Full collapse of the diaphragm, which hugs

the rigid electrode profile. These images are obtained at different actuation voltages. 105

Figure 4-9: Static pull-in (diaphragm actively pulled in towards nickel electrode on the bottom). (Left Column) Only six out of nine diaphragms can be pulled in for flat electrode at one time, and after less than 2 minute all diaphragms stop functioning. (Right Column) All diaphragms can be pulled in for filleted electrode design for 1 hour without any diaphragm breakage.................... 107

Figure 4-10: (Top Left) Laser vibrometer test setup, (Top Right) View from the laser, (Bottom Left) View from top, and (Bottom Right) View from side. 109

Figure 4-11: Comparisons of the diaphragm deflection measured by laser vibrometer for pulse waveforms with varying voltages and duty cycles at 10 kHz. 110

Figure 4-12: (Top) Voltage measured across the DUT, and (Bottom) Diaphragm displacement measured by the laser vibrometer system. The applied voltage is pulse waveform with 20 % duty cycle, at 10 kHz and 360 V peak-to-peak. 110

Figure 4-13: Comparisons of the diaphragm deflection measured by laser vibrometer for pulse waveforms with varying frequencies and duty cycles at 360 V peak-to-peak. 111

Figure 4-14: (Left) Pre-amplifier for powering the calibrated microphone and (Right) The free-field calibrated microphone placed 1.5 cm away from the DUT. 112

Figure 4-15: Comparisons of the sound pressure (measured in voltage) by the free-field calibrated microphone for pulse waveforms with varying voltages and duty cycles at 10 kHz. 113

Figure 4-16: Comparisons of the sound pressure (measured in voltage) by the free-field calibrated microphone for pulse waveforms with varying frequencies and duty cycles at 360 V peak-to-peak.. 114

Figure 4-17: Dynamic pull-in actuation for long-term reliability test: Acoustic pressure. 43 days of continuous actuation. Device can be actuated for an additional of 13 days after a break before the device failure. 117

Figure 4-18: (Left) DUT wired bonded and attached with conductive epoxy on a PCB and (Right) Wire connections made with an edge connector. 118

Figure 4-19: Acoustic pressure versus room humidity. The acoustic pressure is inversely proportional to the humidity in the room. 118

Figure 5-1: Fabrication and assembly process of the U-JET using SU-8 2010 with two curing-steps process. 122

Figure 5-2: The cavity rim of the Helmholtz resonator is attached to the glass slide with SU-8 2010 stamped on the rim. If no curing is performed, overflow of the SU-8 2010 is observed (Left) when the cavity is detached from the glass slide, showing a messy footprint and attachments (Right)................................... 123

Figure 5-3: (Left) Bulging of SU-8 2010 is observed signifying incomplete bonding with glass slide and (Right) No bulging or overflow of SU-8 2010 showing complete bonding... 124

Figure 5-4: UJA arrays with three types of arrangements in Gen. 2 and 3; checkerboard array, honeycomb array and dream catcher array with reference to a US penny... 125

Figure 5-5: (Left) Prototype of a checkerboard UJA showing diaphragm actuator (front and back view) and the assembled UJA, with zoom-in microscope view of a single U-JET. (Right) Prototype of a dream catcher UJA. A diaphragm actuator, a Helmholtz resonator and the assembled UJA with respect to a US penny is displayed.. 125

Figure 5-6: (Left) SEM of the cross section, (Right) Image using laser confocal microscope (top view). The perforations on the electrode can be seen through the throat holes. 126

Figure 5-7: (Top) Illustrations of the cross-section of the contact pad with wire connections, and (Bottom) Photograph of the contact pad showing wire connections. 127

Figure 5-8: (Left) Wire connections made to the contact pad with nickel conductive epoxy and (Right) Connections made with wire bonding and non-conductive epoxy. 128

Figure 5-9: An infrared image obtained using FLIR SC7000 series infrared camera, showing relative temperature difference across the UJA. Significant heating is measured at the conductive epoxy junction. 129

Figure 5-10: Photographs of the final UJA with wire connections, taking from the side view, front view and back view. 130

Figure 5-11: Setup of the calibrated microphone test to obtain a frequency response measurement of the UJA. The UJA is attached to the micro-manipulator fixture and the calibrated microphone is placed ~ 3.5 cm away from the UJA. Different views of the setup are included: (Left) side view, (Top Right) back view and (Bottom Right) front view. 132

Figure 5-12: (Left) Four different waveforms used in test with amplitude A = 200V. (a) Pulse train with 20% duty cycle and 30% DC offset, (b) Sine wave with no offset, (c) Biphasic pulse train with 20% duty cycle, and (d) Biphasic trapezoidal pulse (TRAPZ) (20% duty cycle but with a larger fall time). (Right) Voltage RMS across the device. Frequency is plotted based on the frequency of the diaphragm's motion. 133

Figure 5-13: Calibrated microphone: Acoustic output voltage (peak-to-peak) (right after voltage is turned on). Frequency is plotted based on the frequency of the diaphragm's motion. Corresponding applied voltage RMS is as plotted in Figure 5-12 (Right). 134

Figure 5-14: Calibrated microphone: Acoustic output voltage (peak-to-peak) (after ~30 seconds). Frequency is plotted based on the frequency of the diaphragm's motion. 136

Figure 5-15: Difference in acoustic output voltage from calibrated microphone (discrepancy between Figure 5-13 and Figure 5-14). Frequency is plotted based on the frequency of the diaphragm's motion. 136

Figure 5-16: Jet velocity of 14 m/s peak to peak is calculated (lower trace) from the velocity of the diaphragm measured using a laser vibrometer system (upper trace). 137

Figure 5-17: (Left) Illustrations of the pendulum test setup where a weight (UJA) is suspended on a pivot point with a string or thin wire. (Right) The pendulum test is enclosed with a cardboard enclosure to prevent environment disturbance and a camera is used to record the motion when the device is actuated. 139

Figure 5-18: (Left) Illustration of the pendulum movement where the first swing of the UJA is to the opposite direction as the ejected air micro-jet, and it later reaches maximum left and right swing when modulated at the resonant frequency of the pendulum, (Right) Applied input signal: Amplitude modulation (AM) with sine wave envelope and biphasic waveform with 20% duty cycle and 0 offset at various frequencies from 5kHz to 120 kHz........ 140

Figure 5-19: Comparisons of the thrust performance taken under two types of pendulum tests. The maximum swing and first kick data are collected under the "with AM modulation" test and the static displacement data is collected under the

"without AM modulation" test. As can be seen on the plot, the first kick can be a rough estimate of the static displacement. 143

Figure 5-20: Pendulum test data obtained when actuated at voltage amplitude of 320 V and with AM modulation. The frequency response of the first kick and the maximum swing matches, giving us insights to determine the best signal for maximum thrust performance. Pendulum displacement is to the left of the initial position, as shown in Figure 5-23. 145

Figure 5-21: (Left) Comparisons of the maximum swing and (Right) comparisons of the first kick for varying applied voltages with AM modulation. Pendulum displacement is to the left of the initial position, as shown in Figure 5-23. 146

Figure 5-22: (Left) Static displacements versus varying frequencies for *A* = 320 V, 360 V and 400 V, and (Right) the thrusts calculated from corresponding static displacements. Pendulum displacement is to the left of the initial position, as shown in Figure 5-23. 146

Figure 5-23: Experimental results with device A (snapshots of video clip merged into one): (a) Thruster rest position at time 0 sec, (b) Initial kick-off swing with displacement of ~ 2.55 cm, (c) Maximum swing to the left and (d) Maximum swing to the right when AM modulation is applied. 147

Figure 5-24: The cross-section is drawn to show the operation of a single U-JET. On the left side of the diaphragm, high-speed air micro-jets are expected through the throat holes. On the right side, acoustic streaming effect as explained by Lighthill [56] is observed.. 148

Figure 5-25: (Left) Maximum swing for applied voltage of A = 320 V, 360 V and 400 V with varying frequencies, and (Right) first kick of the pendulum test with AM modulation for device B. 150

Figure 5-26: Data recorded for pendulum test without AM modulation. (Left) Static displacements versus varying frequencies and (Right) the calculated thrusts based on the measured static displacements. For high voltage operation (A = 400 V), the drop in the measured displacement and thrust can be due to one or more diaphragms breaking and eventually at around 80 kHz, the device stops functioning. 151

Figure 5-27: Pendulum test without AM modulation with Device B (snapshots of video clip merged into one): (Left) Static displacement to the right showing that thrust by air micro-jets is greater than thrust by acoustic streaming effect. (Middle) Illustration of the direction of the air micro-jet and the static displacement, and (Right) A total thrust ejected by the air micro-jets is predicted to be ~ 17 μN with the biphasic TRAPZ waveform, with the assumption that the air micro-jets needs to overcome the thrust generated by acoustic streaming effect. 151

Figure 5-28: AM modulation test with Device C (snapshots of video clip merged into one): (a) Thruster rest position at time 0 sec, (b) Initial kick-off swing with displacement of ~ 2.3 cm, (c) Maximum swing to the left and (d) Maximum swing to the right when AM modulation is applied. 153

Figure 5-29: Pendulum test without AM modulation with Device C (snapshots of video clip merged into one): (Left) Static displacement to the right showing a large displacement of ~ 1.3 cm. (Middle) Illustration of the direction of the air micro-jet and the static displacement, and (Right) A total thrust ejected by the air micro-jets is calculated as 46 μN with suppressed acoustic streaming. 154

Figure 7-1: Comparisons of the performance achieved in this work with respect to previous work in the group. An improvement of 4.3 times in the thrust-to-weight ratio is achieved with new fabrication technologies and designs as well as more efficient way to drive the diaphragm actuators. 160

LIST OF TABLES

Table 1-1: Comparisons of the performance of micro rotary wing propulsion [11] 4

Table 1-2: Comparisons of the performance of micro flapping MAVs............................. 6

Table 1-3: Performance of reported chemical jet propulsion systems............................... 9

Table 1-4: Summary of the performance of selected pulse jets actuators. 18

Table 1-5: Summary of the performance of the selected synthetic air micro-jets actuators. 22

Table 1-6: Summary of the performance of ultrasonic jets actuators.............................. 25

Table 2-1: Design parameters of Chou's design [52] used for model verification.......... 41

Table 2-2: Optimized design parameters for best thrust-to-weight ratio performance for h_o=3 μm, 6 μm and 10 μm with 100 kHz – diaphragm................................ 49

Table 2-3: The perforation hole sizes for design A to C in nominal design of Gen. 1..... 57

Table 2-4: Details of the various designs drawn in the layout shown in Figure 2-20 for Gen 2. The blue font highlights the parameter variations from the nominal design of #1.. 60

Table 2-5: Summary of the variation of cavities design in Gen. 3 to observe the influence on the actuator's performance. 63

Table 3-1: Summary of fabricated design parameters for diaphragm actuators.............. 83

Table 4-1: Summary of diaphragm actuation performance. 104

Table 5-1: Properties of the UJA used in this characterization test. 132

Table 5-2: Properties of the three prototypes (A, B, and C) used in the pendulum tests.142

Table 5-3: Summary of this work compared to the state of the art................................ 155

LIST OF APPENDICES

Appendix A 163

Appendix B. 176

NOMENCLATURE

f_o	Helmholtz acoustic resonance frequency
υ	The speed of sound
A_E	Effective throat cross section area
L_E	The equivalent inertia length of the throat
L_T	The physical throat length
V_C	The cavity volume
$u_e(t)$	The maximum velocity at the exit of the throat of the resonator (positive is outflow)
$p(t)$	The relative pressure in the resonator cavity ($p(t) = p_c - p_{amb}$)
η	The air viscosity
$\rho(t)$	The air density in the resonator cavity
h_T	The resonator throat height
L_V	The equivalent viscous length of the throat
ρ_{amb}	The ambient air density
$V(t)$	The rate of change in the cavity volume
A_D	The diaphragm area

L_M The diaphragm width ($A_D = L_M * L_M$)

$h_D(t)$ The diaphragm center displacement

ω_D The diaphragm resonance frequency

K_D The coupling factor of the pressure loading on the diaphragm to the diaphragm inertia

p_e The electrostatic pressure

t_D The diaphragm thickness

ρ_D The density of the diaphragm

U The flow speed outside the resonator

$V_{electric}$ The electric potential difference between the diaphragm and the electrode

V_o The amplitude of the applied electric potential

h_o The distance between the diaphragm and electrode with the diaphragm at rest

w_T The resonator throat width

N_T Number of throat holes

L_C The cavity width

σ The residual stress in the diaphragm

f_V The frequency of operating voltage

ABSTRACT

DESIGN AND DEVELOPMENT OF AN ULTRASONIC JET ARRAY (UJA)

FOR MICRO PROPULSION

by

Seow Yuen Yee

Chair: Khalil Najafi

High-speed air micro-jets can be generated using an array of electrostatically-actuated Helmholtz resonators that form an ultrasonic jet array (UJA) for eventual use in a variety of applications, including micro propulsion and chip cooling. Of these applications, the most challenging is building a flying micro-platform that can generate sufficient thrust to overcome gravity.

This thesis work presents the development and optimization of an UJA which builds on previous work in forming micro-fabricated air micro-jets. The UJA consists of high-frequency and large-deflection actuators that enclose acoustic cavities formed under them. Navier-Stokes equations are used to study the high-frequency and large-gap diaphragm actuator when actuated with a trapezoidal waveform at voltages beyond pull-

in. The high rise and fall time of the trapezoidal waveform and maximum volume displacement when actuated beyond pull-in will provide for additional momentum and larger response of the diaphragm, leading to higher thrust. An optimized design based on these equations was developed, and device and structural parameters were identified.

A new, simple, and versatile fabrication technology was developed to produce high-frequency (> 90 kHz), large-gap (~ 10 μm) electrostatic diaphragm actuators with high yield and reliable actuation (> 229 billion actuation cycles). These actuators utilize a new type of electrode (a filleted electrode), which was fabricated using a photoresist solvent reflow process. The fabricated UJA is compact with a footprint of 0.9 x 0.9 cm^2 and is 5x lighter in weight than previous work.

The thrust generated by the UJA is measured through a pendulum test setup where the UJA was suspended at the end of a 50 cm long wire. A thrust of ~ 46 μN with a thrust-per-weight ratio of 0.043 is measured, which is a 4.3x improvement over previous work. The applied voltage is ± 330 V and the power consumption is < 10 mW per actuator.

The UJA thrust and performance could be further increased by: (1) matching the acoustic resonance of the cavity to the diaphragm's mechanical resonance, (2) reducing damping, (3) measuring and characterizing the air micro-jets in more detail, and (4) improving the analytical and simulation models to match experimental results.

CHAPTER 1

INTRODUCTION

An air micro-jet is a stream of high-speed air ejected through a narrow orifice. High-speed air jets can be used in a variety of applications including micro propulsion, chip cooling, gas pumping and high-performance acoustic transducers. Of these applications, the most challenging application is building a micro flying platform where air micro-jet is generated to create sufficient thrust to overcome gravity. The micro flying platform can be equipped with Global Positioning System (GPS) receivers to support emergency search and rescue operations in times of natural disasters where access on the ground is limited, or in times of accidents such as in mining or construction for access through narrow areas (Figure 1-1). Alternatively, flying platforms equipped with chemical sensors can be sent to harsh environments or into narrow mining areas to detect hazardous gas, reducing the risk to humans.

Another interesting application for high-speed air jets is chip cooling. As the world advances to better lifestyles enhanced by high technology electronics, higher processing power is packed into smaller electronic devices (Figure 1-2), leading to the need for smaller and more efficient cooling systems. Air micro-jets can be designed to impinge air on these electronic devices to enhance air convection for chip cooling.

Figure 1-1: (Left) Illustration of the use of micro flying devices for establishing communication networks between user stations located on the ground for aid in natural disaster rescue [1], (Middle) for visual aid in mining accident rescue [2], and (Left) for chemical monitoring in narrow tunnels or space [3].

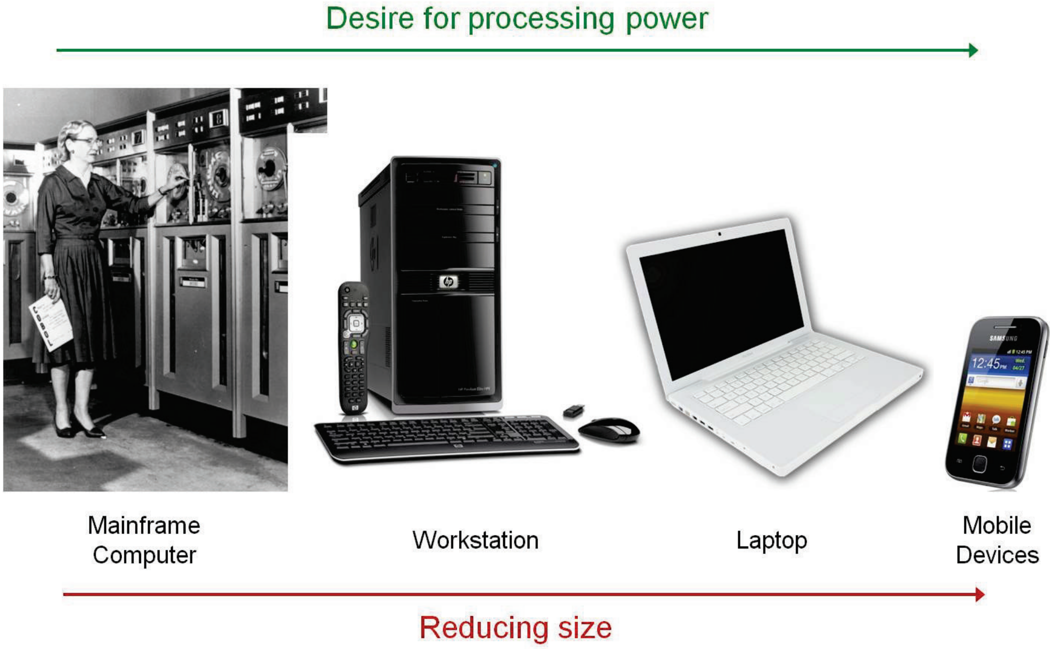

Figure 1-2: Examples of the evolution of electronic devices where there is need for smaller and more efficient cooling systems. (Left to right) Mainframe computer [4], workstation [5], laptop [6] and mobile devices [7].

1.1 Background to Micro Propulsion Applications

A Micro Air Vehicle (MAV) can be loosely defined as an air vehicle less than 15 cm in any dimension because this represents the size at which low Reynolds number effects begin to dominate, creating critical challenges for aviation [8]. The history of MAVs dates back to the 19th century with the development of model airplanes and continued with radio-controlled systems in the 20th century. Propulsion systems have evolved from rubber bands to liquid fuel internal combustion engines and later to battery powered electric motors [9].

Common types of micro air propulsion systems are wing-type propulsion and jet propulsion. Wing-type propulsion includes fixed wing aircraft (aeroplanes), rotary wings (helicopters) and flapping wings (ornithopters or entomopters). Jet propulsion includes chemical propulsion (combustion or liquid, solid, gaseous propellant) or electrical propulsion (electrothermal, electrostatic or electromagnetic). Most of the propulsion systems require a thrust-to-weight ratio greater than one except for fixed-wing propulsion, which uses forward motion and aerodynamics to generate lift. A wingspan of about ten centimeters is the turning point below which it is more efficient to flap wings rather than glide with a fixed wing [10].

The following sub-sections discuss MAVs using micro air propulsion which require thrust-to-weight ratio greater than one. Fixed-wing aircraft will not be discussed here because they utilize different physics for propulsion.

1.1.1 Wing-type Propulsion: Rotary Wings (Helicopters)

Prox Dynamics is recognized as one of the leading companies which made the world's smallest radio-controlled (RC) helicopter in 2005 and the world's lightest RC helicopter in 2006. As Figure 1-3 and Table 1-1 show, their smallest rotor diameter achieved is 6 cm while their lightest helicopter is 0.9 g [11]. Scaling down the rotor diameter is difficult due to the decrease in rotor efficiency with increase in drag force and the low thrust-to-weight ratio at low Reynolds number.

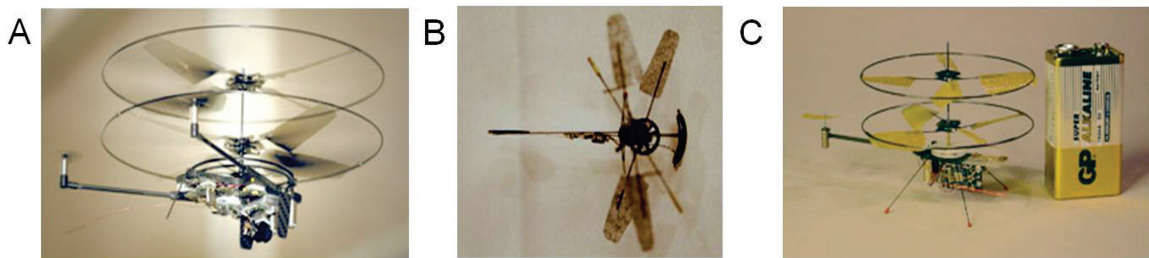

Figure 1-3: Micro rotary wing propulsion (Helicopter) [11]

Table 1-1: Comparisons of the performance of micro rotary wing propulsion [11]

Year	Rotor Diameter	Weight	Flight Time	Camera
(A) 2007	16.0 cm	30.0 g	10 min	Yes
(B) 2006	7.0 cm	0.9 g	< 1 min	No
(C) 2005	6.0 cm	3.0 g	2-3 min	No

1.1.2 Wing-Type Propulsion: Flapping Wings (Ornithopters or Entomopters)

As exemplified by small birds and insects in nature, the flapping-wing mechanism is by far the most efficient when the size decreases compared to fixed or rotary wings. Smaller birds and insects or flapping wing MAVs fly in an unsteady-state regime in which their wingtip speed is faster than their flight speed to overcome their weight and generate lift [12]. Flapping wing MAVs can be divided into two categories: ornithopters

and entomopters. Ornithopters are similar to fixed-wing vehicles because they require forward flight, while entomopters use the flight kinematics of insects and are able to execute vertical takeoff and landing (VTOL) and hovering [13].

Several renowned examples of micro flapping wing MAVs with wingspans ranging from 3 cm to 16.5 cm are listed in Figure 1-4 and Table 1-2. MAVs can be characterized by the following criteria: (1) Is the MAV self-powered?, (2) How long is the flight time?, (3) Does it have stable flight and control?, (4) Can it be autonomously piloted?, (5) Can it perform hovering or indoor and outdoor flight?, and (6) Does the MAV have a payload such as a camera on board?. The ability to fly from indoors to outdoors is probably the most challenging as any gust of air will blow the MAV off balance. Although the hummingbird-like vehicle developed by AeroVironment has the largest wingspan in comparison to others, it is the only MAV to perform indoor and outdoor flight with a camera on board, and it can execute vertical takeoffs and landings (VTOL).

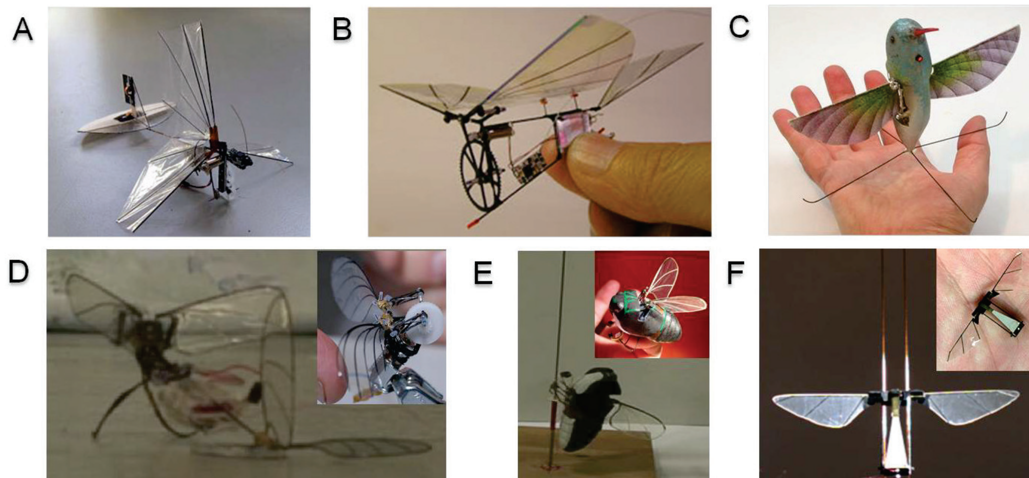

Figure 1-4: Recent technology breakthroughs in micro flapping MAVs [10], [11], [14]–[17]. The comparisons of the performance are included in Table 1-2.

Table 1-2: Comparisons of the performance of micro flapping MAVs.

Reference	Wingspan	Weight	Flight Time	Frequency	Camera
(A) Delfly (2008) [10]	10.0 cm	3.0 g	3 minutes	30 Hz	Yes
(B) Proxdynamics (2007) [11]	10.0 cm	1.1 g	< 1 minutes	N/A	No
(C) AeroVironment (2011) [14]	16.5 cm	19 g	8 minutes	N/A	Yes
(D) A. M. Flynn *et al*. (2007) [15]	7.5 cm	5.5 g	< 3 seconds	N/A	No
(E) A. M. Flynn *et al*. (2008) [15]	7.5 cm	5.8 g	Climbed up rail	N/A	No
(F) R. Wood *et al*. (2007) [16]	3.0 cm	0.06 g	Guided rail	110 Hz	No
(G) R. Wood *et al*. (2013) [17]	3.0 cm	0.08 g	Couple minutes	100 Hz	No

Another outstanding work in micro flapping wing MAVs is the development of an insect-scale micro-robot by Robert Wood's group in Harvard University. Figure 1-5 shows the most recent achievement by Wood's group with the demonstration of controlled flight with the micro-robot [17]. The micro-robot has 3 cm wingspan, weighs 80 mg, and can generate > 1.3 mN of lift force with power consumption of 19 mW.

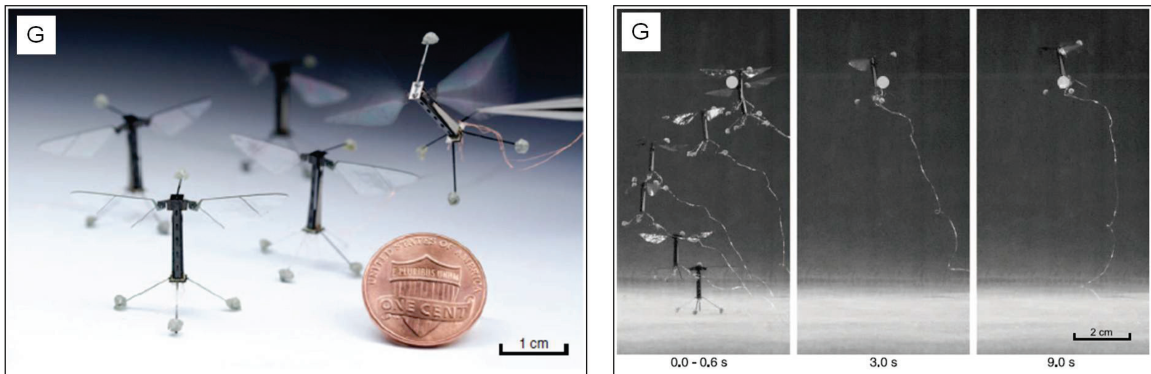

Figure 1-5: (Left) Prototype and (Right) Controlled flight of the insect-scale robot [17].

In summary, exceptional work has been demonstrated for wing-type propulsion; however, for further miniaturization, there exist critical challenges related to poor lift-to-drag ratio and low propeller efficiency [18]. As an alternative, jet propulsion has the potential to load high energy density onto a small package and produce sufficient thrust to generate lift.

1.1.3 Jet Propulsion

By stepping “outside the box” of wing propulsion, jet propulsion as inspired by Hero of Alexandria’s Aeolipile [19] offers interesting potential for micro-propulsion in the bird and insect regime. The Aeolipile utilizes the steam from boiled water to generate thrust by expelling the steam through nozzles. Miniature flying platforms or machines face a mix of physical design constraints such as low Reynolds number aerodynamics, high energy density and extreme miniaturization [8]. The Reynolds number, defined by the ratio of inertial forces to viscous forces, is perhaps the most important figure of merit for characterizing the flight environment. As the size of the device is scaled down into the low Reynolds numbers regime of birds and insects (Figure 1-6), the design faces the critical challenges of poor lift to drag ratio and low propeller efficiency [18]. Due to the low Reynolds number, jets are an attractive means of propulsion.

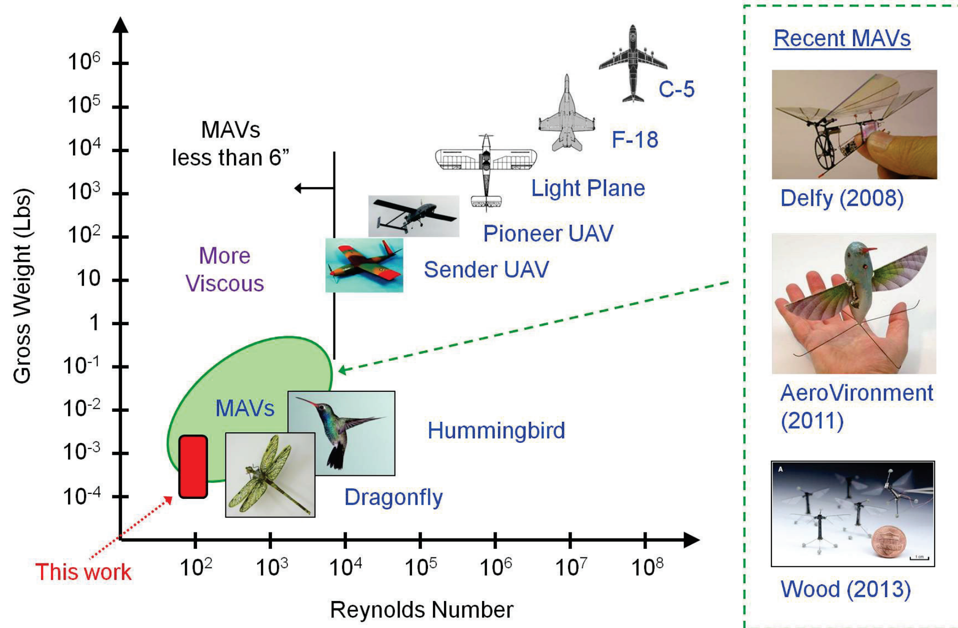

Figure 1-6: MAVs flight regime compared to larger scale flight vehicles, adapted and reconstructed from [18].

Up until now, jet propulsion has been mostly applied to larger systems such as micro spacecraft. Jet propulsion systems are sometimes called micro thrusters as they produce thrust to overcome gravity. In theory, jet propulsion systems can have better performance and are easier to employ than wing-type propulsion when scaled down in size, especially with advancements in micro fabrication technologies. Jet propulsion systems can be divided into two large groups; chemical and electrical. Chemical propulsion systems convert solid, liquid or gas propellants into gas streams through nozzles to generate thrust. Electrical propulsion systems utilize electrical energy to generate jets of air or liquid which can propel the micro thrusters to the opposite direction of the jets.

1.1.3.1 Chemical Propulsion

Chemical propulsion systems, better known as micro combustion thrusters, generally consist of chambers containing the propellants, either solid or liquid or gas, and heaters for igniting the propellants. The ignited propellants generate high impulse combustions that can provide instantaneous thrust for propulsion. Figure 1-7 and Table 1-3 include examples of micro combustion thrusters with solid and fluid propellants. Micro combustion thrusters are advantageous because they produce high thrust and impulse; however, the thrusters have difficulty in establishing self-sustaining combustions since they are normally one-time ignition thrusters. Additionally, the challenges related to producing consistent and efficient combustion include incomplete combustion and heat losses through walls. Solid propellants are easier to handle and

assemble with less leakage problems than liquid propellant systems but many solid propellants contain metal particles and the exhaust is smoky.

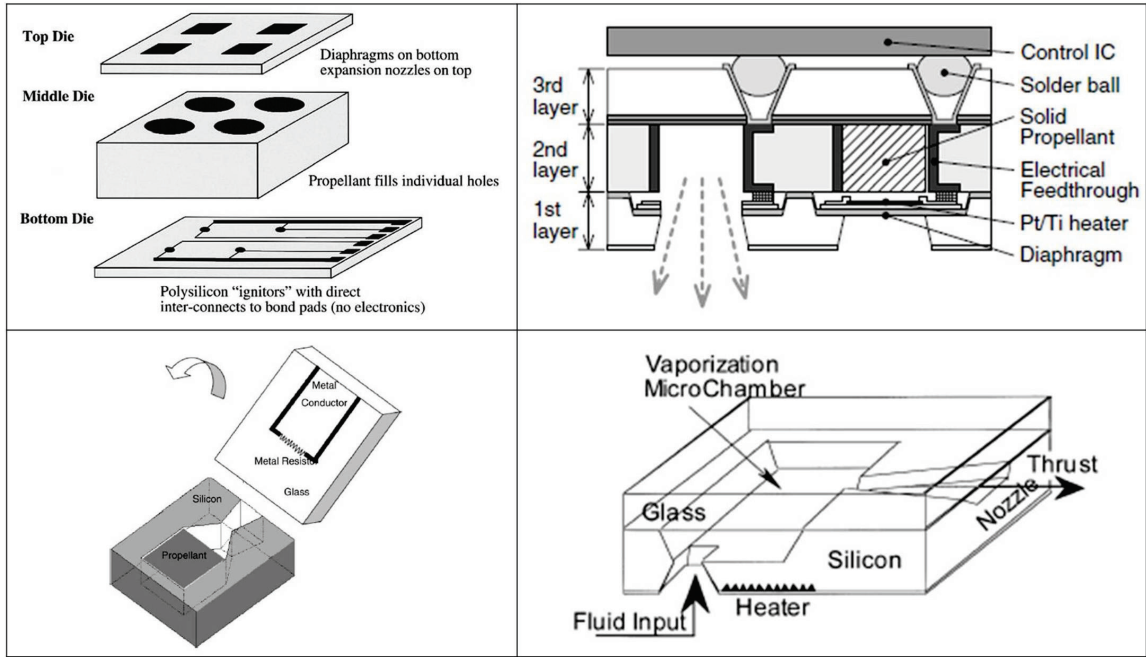

Figure 1-7: (Top Left) Digital micropropulsion system using lead styphnate as the propellant [20], (Bottom Left) Gun powder-based solid propellant propulsion system [21], (Top Right) Solid propellant rocket array thruster [22] and (Bottom Right) Vaporizing liquid micro thruster [23].

Table 1-3: Performance of reported chemical jet propulsion systems.

Chemical Jet Propulsion Systems	Propellant	Thrust (N) or Impulse (Ns)
Digital micropropulsion system [20]	Lead styphnate	10^{-4} Ns
Gun powder-based solid propellant system [21]	Gun powder-based solid propellant	0.05-0.34 N
Solid propellant rocket array thruster [22]	Solid propellant	2×10^{-5} Ns – 3×10^{-4} Ns
Vaporizing liquid micro thruster [23]	Liquid propellant	0.15 mN – 0.46 mN

1.1.3.2 Electrical Propulsion

Electrical propulsion systems utilize electrical energy to generate jets of fluid. The high-speed fluid flow or jets can be produced by three types of micro actuators. The first type is the micro colloid thruster. The basic working principle of a micro colloid thruster

is as illustrated in Figure 1-8 (Left). There are two components, named the source emitter and the extractor. A high electric field is applied between these two components and when a supply of liquid droplets is passed through the source emitter, the high electric field charges and accelerates the liquid droplets. The accelerated liquid droplets are ejected through the extractor in cone-jets and sprays, and generate thrust [24]. Although the micro colloid thruster can produce thrust up to 4.84 μN [25], the device is heavy and weighs 20 g, resulting in a very low thrust-to-weight ratio.

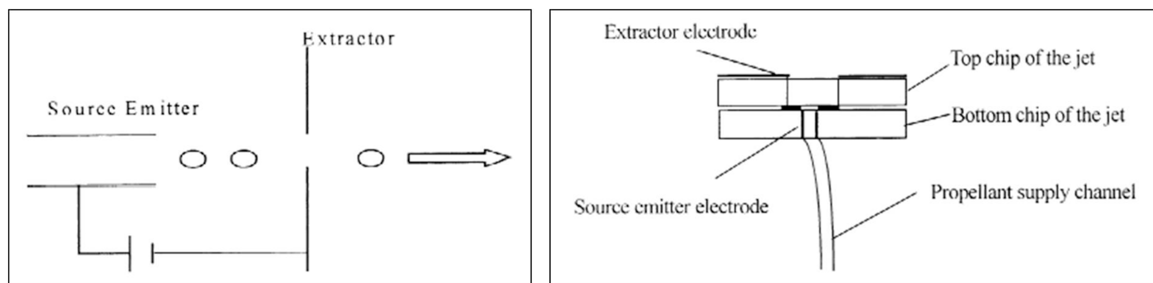

Figure 1-8: (Left) Colloid thruster working principles, (Right) Structure of the micro colloid thruster [24].

The second type is diaphragm-based ejectors and the third type is plasma-pulsed thrusters. For diaphragm-based ejectors, thin diaphragms are actuated electrically to displace volumes of air or fluid through tiny orifices and create micro-jet streams. On the other hand, plasma-pulsed thrusters utilize localized dielectric discharges to create low pressure region compared to the surrounding. The pressure difference allows fluid flow from the surrounding to the low pressure region. Diaphragm-based ejectors scale well at the micro-scale and show great potential to generate high thrust-to-weight ratio when operated at large deflections. While plasma-pulsed thrusters can generate high thrust, the high power consumption makes it less desirable for micro propulsion application.

As relevant to this research work, the following sub-sections will mainly review the generation of air micro-jets using electrical propulsion systems such as diaphragm-based ejectors or the plasma-pulsed thrusters. Although not all air micro-jet thrusters are designed for micro propulsion applications, there were some interesting technologies which can be applied for generating lift with further optimization. In the literature, air micro-jets have been used in flow enhancement and control for boundary layer separation [26]–[39], mixing for combustion control [30], [34], [38], and flow generation for gas pumping or micro-propulsion [31], [32], [39]–[42].

1.2 Background to Chip Cooling Applications

Similar to micro propulsion applications, air micro-jets thrusters can also be used in applications such as chip cooling. Following Moore's law (Figure 1-9 (Top)), the number of transistors per die roughly doubles every 18 months [43] while the corresponding power density increases by roughly two times every 36 months (Figure 1-9 (Bottom)). The steady rise in power density and its negative impact on the performance of electronics has led to rigorous research on electronic cooling systems. In the past, the electronic cooling systems have evolved from liquid cooling to air cooling; however, thermal management issues with micro-chips continue to be a concern to the electronics industry as smaller and higher efficiency cooling systems are required with the shrinkage of electronics sizes.

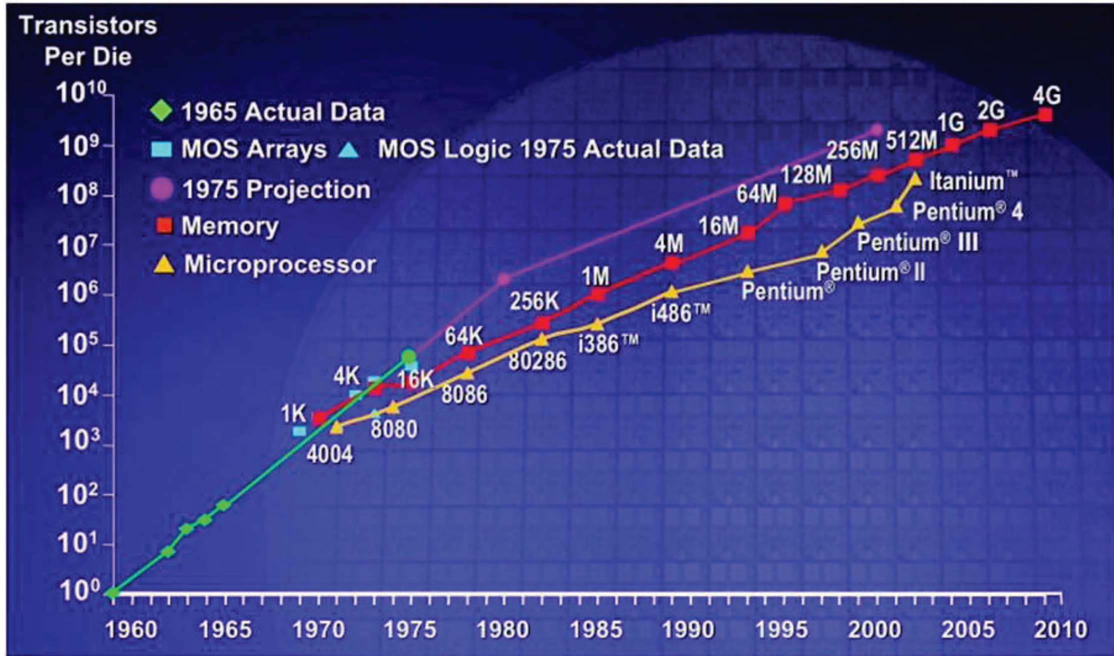

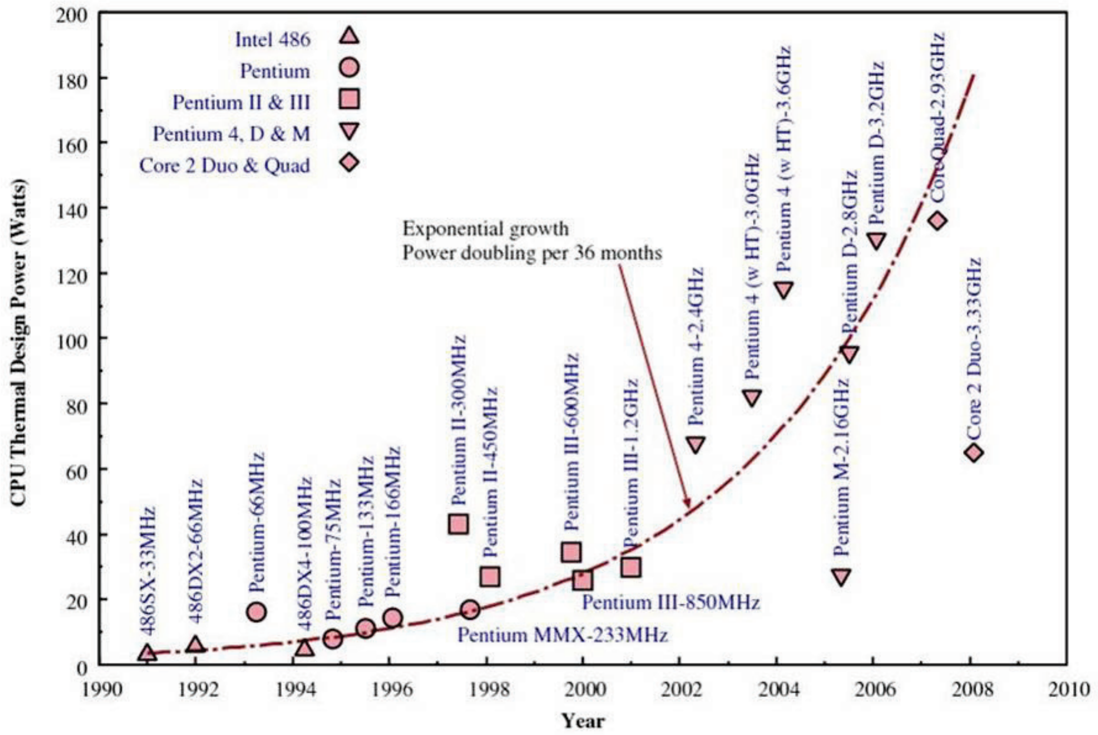

Figure 1-9: (Top) Moore's law predicting the increase in the number of transistors per die as technology advances [44], and (Bottom) the power dissipation corresponding to the increase in transistor density [45].

Air micro-jet thrusters can be used in small and efficient cooling systems. For air cooling systems such as a mechanical fan, the heat dissipation is increased by promoting air movement surrounding the electronic devices to increase air convection; however, as size reduction is required for cooling of smaller devices, the mechanical fan faces challenges in retaining its cooling capability. As aforementioned for micro propulsion application, the efficiency of the air micro-jet thrusters scales well with size. The air micro-jet thrusters can be placed in close proximity to the source of heat dissipation to create additional fluid flow and enhance heat convection for cooling of microelectronics. Numerous works have reported on the possibility of using micro-jet thrusters for impingement for chip cooling to supplement or replace a mechanical computer fan [30]–[32], [34], [39], [46], [47].

In 1995, Coe *et al.* [30] proposed the application of their addressable micromachined jet arrays for Integrated Circuit (IC) thermal management but they did not report any data on their cooling capability. Later, Campbell *et al.* [48] demonstrated that the cooling performance of a microjet was comparable to that provided by a heat sink and Kercher *et al.* [46] showed that air micro-jets can deliver similar cooling effects to conventional jets. However, the device designed in both [48] and [46] are in the centimeter range and the performance reported has to be scaled down to match with the work in this research. For example, Kercher *et al.* [46] use an electromagnetic actuator with 25 mm diameter and 225 µm thick latex diaphragm and exit orifice 2.38 mm in diameter. The actuator with single orifice produces cooling performance of 93.45 $W/m^2 \cdot K$ with driving power of 200 mW.

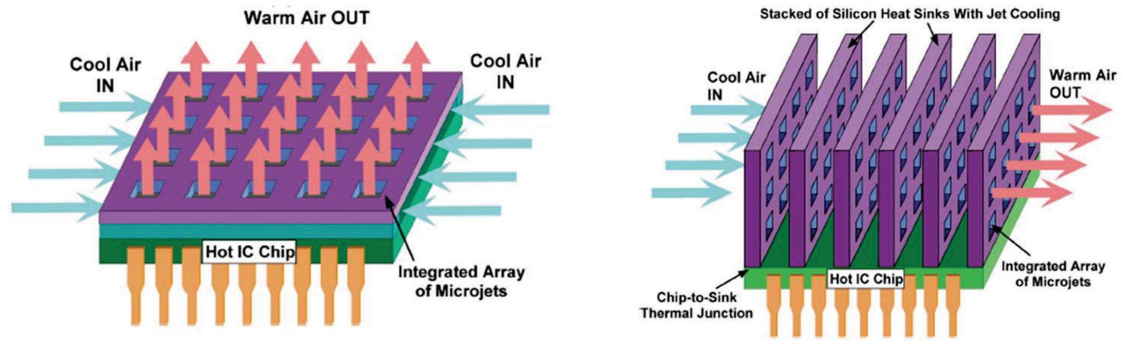

Figure 1-10: Conceptual configurations of chip cooling using the e-jet array [49]

Previous research work by Chou *et al.* [49] and Kim *et al.* [50] showed application of air micro-jets in advanced IC cooling (Figure 1-10). Cooling power of greater than 600 W/m^2 (at ΔT = 100 ^{o}C) was achieved by Chou *et al.* [49] with a flat electrode design placed ~ 1 cm away from the hot surface. Kim *et al.* [50] further improved the design to a curved electrode and showed an improvement in cooling power to 1138 W/m^2 (at ΔT = 100 ^{o}C) when placed 4 mm away from the hot surface. The improved performance of the curved electrode design may be due to the extra volume displacement by the diaphragm or by the reduced distance from the hot surface. Nonetheless, air micro-jets present an attractive means for micro-chip cooling applications.

1.3 A Review of Air Micro-jets

As the air micro-jets offer potential solutions to a wide range of engineering applications, the generation and control of air micro-jets has been widely studied in the micro domain and a review of previous works are presented in this sub-section. Air micro-jets can be categorized into two main categories: (1) non-zero-net-mass where

there is a net air flow into and out of the system (normally a chamber), and (2) zero-net-mass where the air flowing into the system is the same as the air flowing out of the system (generally a cavity), as shown in Figure 1-11. Pulsed jets fall under the non-zero-net-mass category because the generated air jets have an injection-only phase (air is flowing through the exit orifice in only one direction) [26]–[29] and usually need some kind of external air supply or piping sources. On the other hand, synthetic jets fall under the zero-net-mass category where the air jets have injection and suction phases (air flowing into and out of the same exit orifice at alternating phases). Synthetic jets generally involve a cavity with a vibrating diaphragm and an exit orifice [30], [31], [33]–[38], [46], [47]. Air is ejected out of the orifice in one direction but inhaled in from all directions, producing a non-zero-net-momentum in the system. Hybrid jets, as named in [39], have the combined properties of both pulsed and synthetic jets.

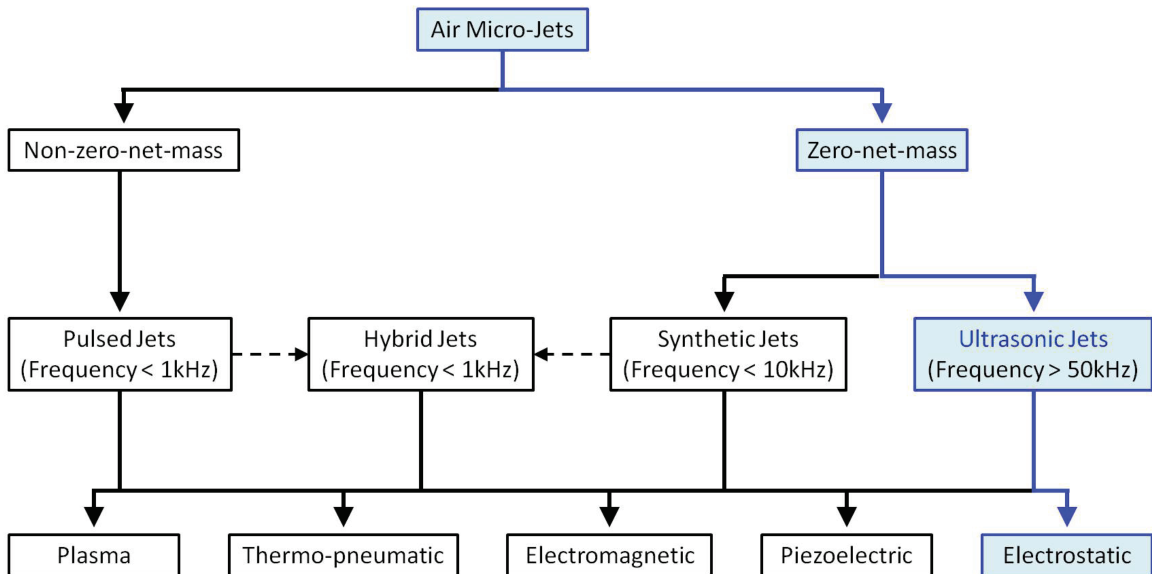

Figure 1-11: Flow chart showing different categories of air micro-jets and methods of actuation (lowest level). Blue box highlights the focus of this research work.

There is a common characteristic between the published examples of pulsed, synthetic and hybrid jets, which is that the operating frequency is low, mostly below 1 kHz except for one synthetic jet actuator which is operated around 10.5 kHz [35]. Since the pumping efficiency is higher with higher operating frequency, it is natural to try to design higher frequency jets. Here, in this research work, a new category is added to the zero-net-mass systems, ultrasonic jets [40]–[42]. Ultrasonic jets are similar to synthetic jets except that the operating frequencies are above the upper limits of human hearing, generally greater than 50 kHz. These ultrasonic jets can be generated with a high-frequency diaphragm coupled with a high-resonance Helmholtz resonator. High-speed air jets are expected at these high frequencies with maximum pumping efficiency.

1.3.1 Non-zero-net-mass Systems

1.3.1.1 Pulsed Jets

Pulsed jets are normally used for active macro flow control. The pulsed air jets are non-zero-net-mass flux formed by inducing continuous or pulsed flow in a single direction. The design and configurations of the pulsed-jet actuators can vary according to the employed actuation methods. Figure 1-12 shows examples of pulsed jets actuators with piezoelectric [26] and electromagnetic actuation [27]. One important feature of the pulsed jets is the need for some kind of external air supply or piping to ensure continuous supply of air flow in a single direction. For the piezoelectric actuator on the left of Figure 1-12, the air supply ensures that flow is always going from the bottom to the top and the piezoelectric actuated cantilever is used to control and pulse the air flow. The produced flow rate can reach as high as 300 m/s [26]. Similarly, for the electromagnetic

actuator on the right of Figure 1-12, a flexible membrane is magnetically modulated to pulse the fluid intake from the top to the bottom. Again, an input pressure is present at the front end of the flow to ensure single direction flow.

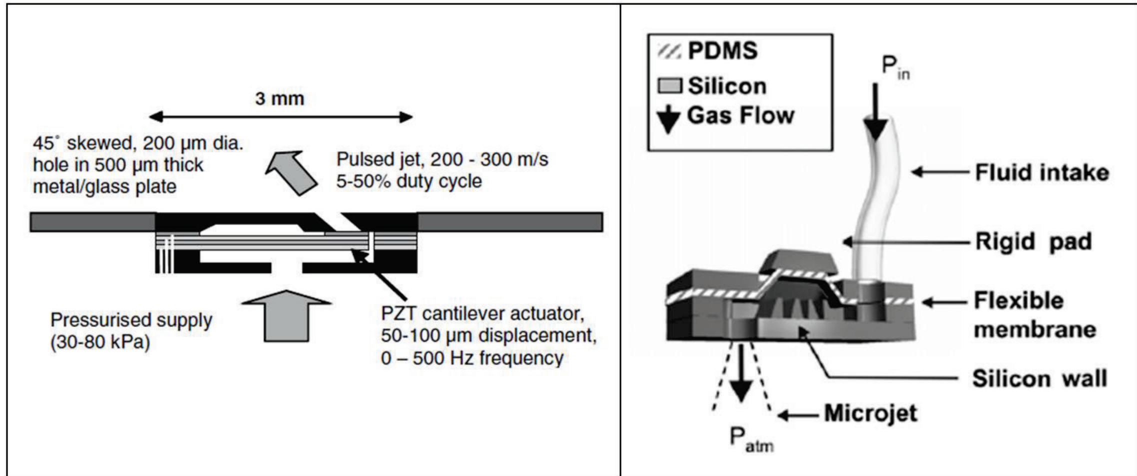

Figure 1-12: (Left) Piezoelectric actuated pulsed actuator [26], and (Right) Magnetically actuated pulsed actuator [27]. An external air supply or piping is needed for this configuration.

The disadvantage of the cantilever-based or diaphragm-based pulsed jets is the need for complex piping or air supply system. One way to eliminate the piping system is using plasma actuation or better known as dielectric barrier discharge (DBD) actuators [28], [29], as shown in Figure 1-13. High plasma power is applied to create localized plasma discharges right above the electrodes. The discharge generates an electrohydrodynamic force which induces a wall of low pressure region right above the dielectric surface and pulls the air from the surroundings to the low pressure region. The disadvantage of the plasma pulsed-jets is the reliability. The reliability is very low due to the high operating voltage which is generally in the kilovolts range.

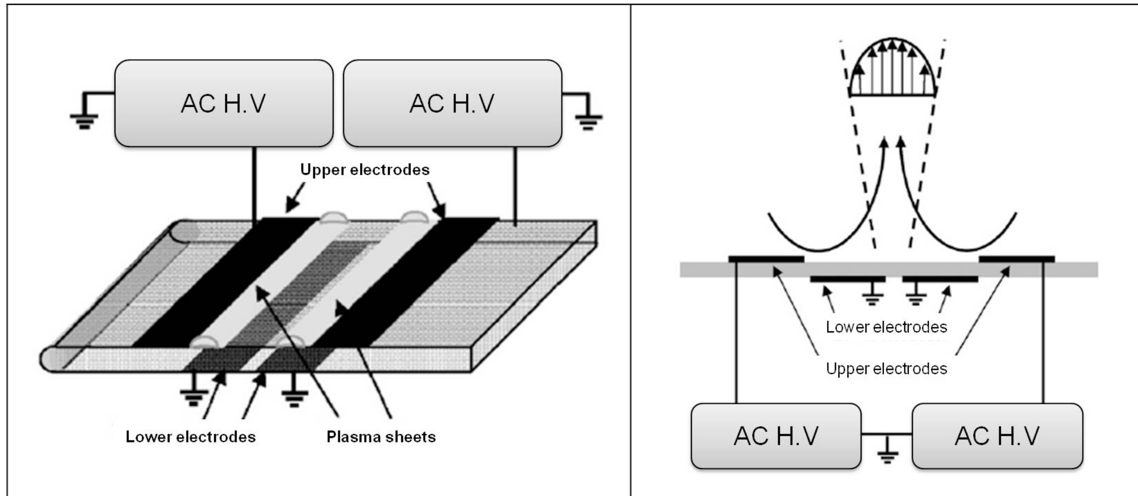

Figure 1-13: (Left) Plasma pulsed actuators (or known as Dielectric Barrier Discharge Actuators), and (Right) Cross section showing plasma induced flow directions [29].

Table 1-4 summarizes the performance of selected pulsed-jet actuators. The pulsed-jet actuators are greater than 3 millimeter in size and operate at frequencies ranging from 400 Hz to 1 kHz. In general, the jet velocities generated by this category range from 2 m/s to greater than 300 m/s but the velocities depend on the pressure and flow of the external air supply. Therefore, the velocities performance cannot be compared directly with the other categories. These actuators also have high power consumption of up to 4 W of power.

Table 1-4: Summary of the performance of selected pulse jets actuators.

[Ref]	Actuation	Frequency (Hz)	Voltage (V) or Current (I)	Power (W)	Size	Performance	Air supply source
[26]	Piezoelectric	1 kHz	90 V	0.05 W	5 x 2 x 1 mm^3	> 300 m/s	Yes
[27]	Electro-magnetic	400 Hz	1 A	-	> 3 x 3 mm^2	150 m/s	Yes
[28]	Plasma	1 kHz	5 kV	15 W/m	10 x 5 x 0.5 mm^3	2 m/s, 2 μN	No
[29]	Plasma	-	20 kV	3-4 W	-	2.2 m/s	No

1.3.2 Zero-net-mass Systems

1.3.2.1 Synthetic Jets

Synthetic air micro-jets are commonly used in flow control, thermal management and flow mixing applications. A synthetic air micro-jet system has zero-net-mass flux formed from an oscillating source such as a diaphragm and a cavity with exit orifice(s). The oscillating diaphragm causes fluid to be sucked into or ejected out from the cavity through the same orifice(s) with alternating phases. The total mass flowing into and out of the cavity is zero but the net momentum is non-zero. During the inflow phase, air is pulled in from all directions, but during the outflow phase, air is ejected in one direction. The non-linearity of the air flow (inflow and outflow) produces a non-zero-net-momentum in the system. An analogy from nature is the locomotion of a jellyfish, as depicted in Figure 1-14 [51].

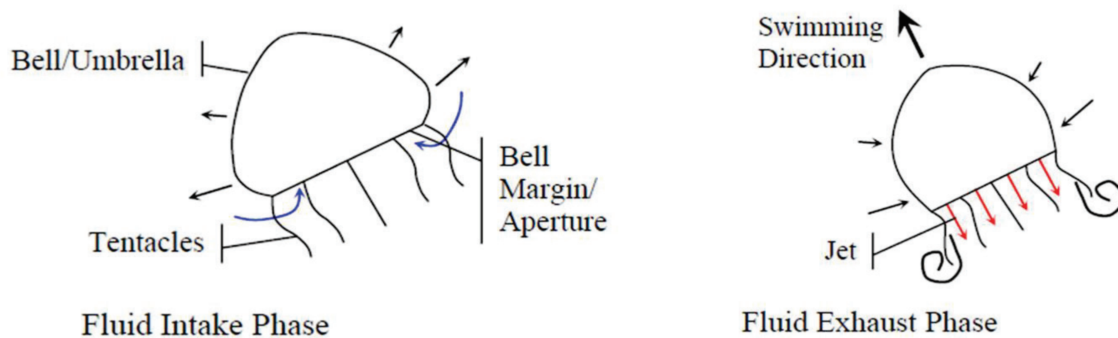

Figure 1-14: General anatomy of jellyfish and the jet generation sequence [51].

Synthetic air micro-jets can be generated in many ways. The basic requirements are a cavity with some moving structure to modulate the air in and out of the cavity and an exit orifice. The reported configurations are summarized in Figure 1-15: (1) single cavity configuration with a vibrating diaphragm and an exit orifice at the opposite end of

the diaphragm [30], (2) similar to the first configuration but the exit orifice is located at the side of the diaphragm [31], (3) single cavity configuration with dual vibrating diaphragms [32], and (4) dual cavity configuration with single vibrating diaphragm [32]. Due to its simplicity and ease in fabrication, the first configuration is the most commonly employed configuration. The other configurations face greater challenges in miniaturization, batch fabrication and assembly.

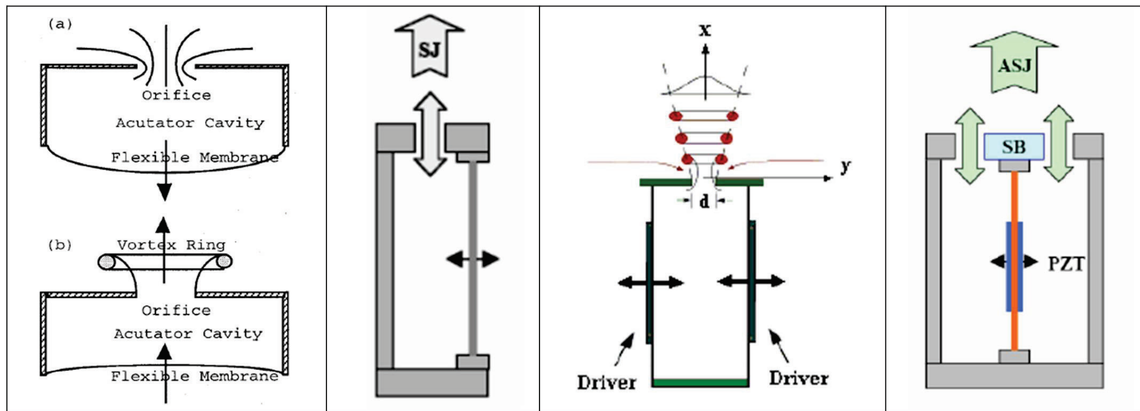

Figure 1-15: Different actuator configurations for creating synthetic jets. Showing from the left to right: Single cavity with a vibrating diaphragm and an exit orifice at the opposite end of the diaphragm [30], single cavity with a vibrating diaphragm and an exit orifice at the side of the diaphragm [31], single cavity with dual vibrating diaphragm [32], and dual cavities with single vibrating diaphragm [32].

There are multiple ways to actuate the oscillating diaphragm. For example, electrostatic [30], piezoelectric [31], [32], [35], [37], [38], [47], electromagnetic [33], [34], [46] or ferromagnetic actuation [36]. Figure 1-16 shows the cross-section of examples of the various actuation methods for synthetic air micro-jets actuators. Electrostatic actuation potentially offers low power consumption, easy integration onto a chip with micro sensors and control electronics, and is compatible with high density

batch fabrication [30]. It requires two parallel plate electrodes where one can be a flexible diaphragm and another can be a rigid electrode. When a voltage difference is applied to the two electrodes, the electrostatic force pulls the flexible diaphragm towards the rigid electrode. The air between the two electrodes is pushed out through an exit orifice, generating a series of vortex rings that induce turbulent air jets as the vortices interact downstream.

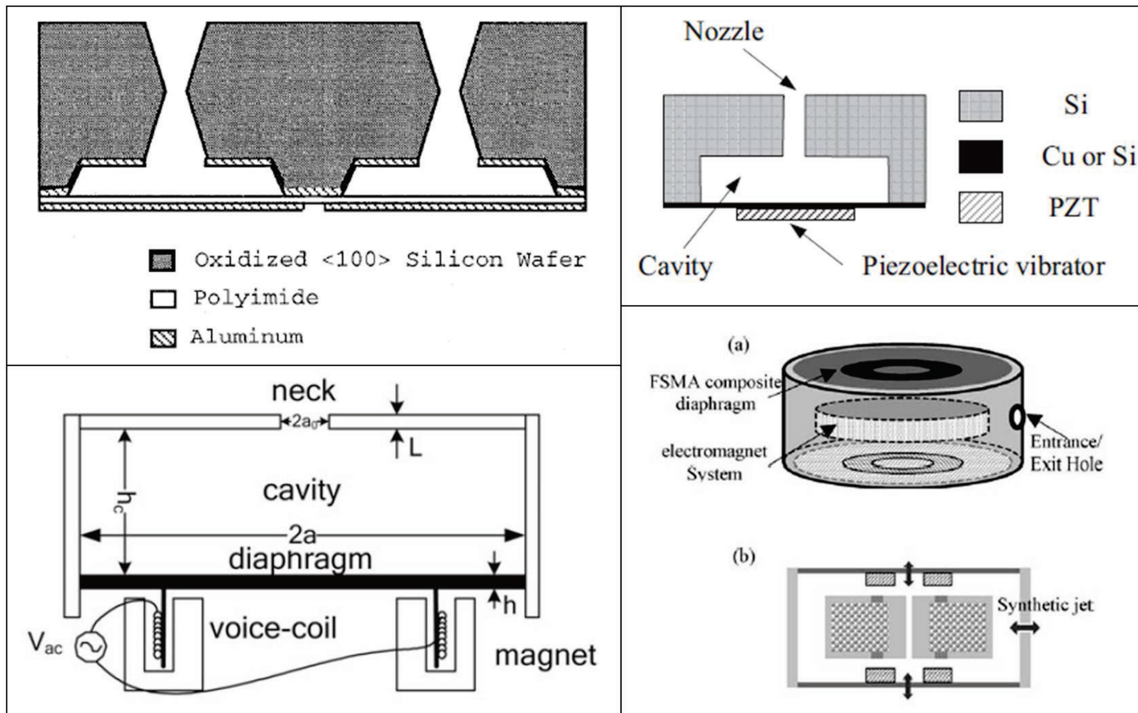

Figure 1-16: (Top left) Electrostatic driver [30], (Top right) Piezoelectric driver [35], (Bottom left) Electromagnetic driver [34], and (Bottom right) Ferromagnetic driver [36].

Piezoelectric actuation is more commonly used because it requires only one flexible diaphragm for actuation. The fabrication becomes simpler without the second electrode in the electrostatic actuation; however, piezoelectric materials are less flexible and difficult to fabricate into more complex systems and shapes. Electromagnetic or

ferromagnetic actuation can produce large pumping force but the magnets and coils needed for the actuator do not scale well into the micro-domain and consume a lot of power.

Table 1-5: Summary of the performance of the selected synthetic air micro-jets actuators.

[Ref]	Actuation	Frequency (Hz)	Voltage (V) or Current (I)	Power (W)	Size	Performance
[30]	Electrostatic	< 1kHz	-	-	1 mm – 4 mm	9 m/s
[35]	Piezoelectric	10.5 kHz	25 V	-	6 mm	8.2 m/s
[37]	Piezoelectric	-	5 V, 2 mA	10 mW	1.25 cm	2 m/s, 10 µN
[38]	Piezoelectric	850 Hz	25 V	-	25 mm diameter	60 m/s
[47]	Piezoelectric	175-182 Hz	25-50 V	0.367 W	40 mm x 40 mm	24 Pa, 28 *l*/min
[33]	Electromagnetic	400 – 700 Hz	400 mA	0.5 W	1 cm^3	25-55 m/s
[46]	Electromagnetic	100 Hz	0.45 V	-	25 mm diameter	-
[36]	Ferromagnetic	220 Hz	25 V	200 W	72 mm x 85.6 mm x 130 mm	190 m/s

Table 1-5 summarizes the performance of the selected synthetic jets actuators. Note that most of the actuators are centimeter range and the operating frequencies are below 1 kHz except [35]. These operating frequencies are in the range of human hearing. Ferromagnetic actuation showed the highest jet velocities for synthetic jets actuators but the size and power consumption of the actuator is also the largest.

1.3.2.2 Ultrasonic Jets

Since larger volume displacement and higher operating frequency is desired for higher gas pumping efficiency, it is natural to design higher frequencies jets. Here, in this research work, a new category is added to the zero-net-mass systems and named the ultrasonic jets. The main feature that differentiates this new category (ultrasonic jets)

from the synthetic jets in the zero-net-mass systems is the high operating frequency, where the operating frequencies are far above the frequency of human hearing. Similar to synthetic jets, the ultrasonic jets utilize the theory of a forced Helmholtz resonator, where the air flow generated by the diaphragm is amplified at resonance by the Helmholtz cavity; however, the ultrasonic jets take advantage of the high Helmholtz resonant frequency for maximum and efficient micro-jets generation.

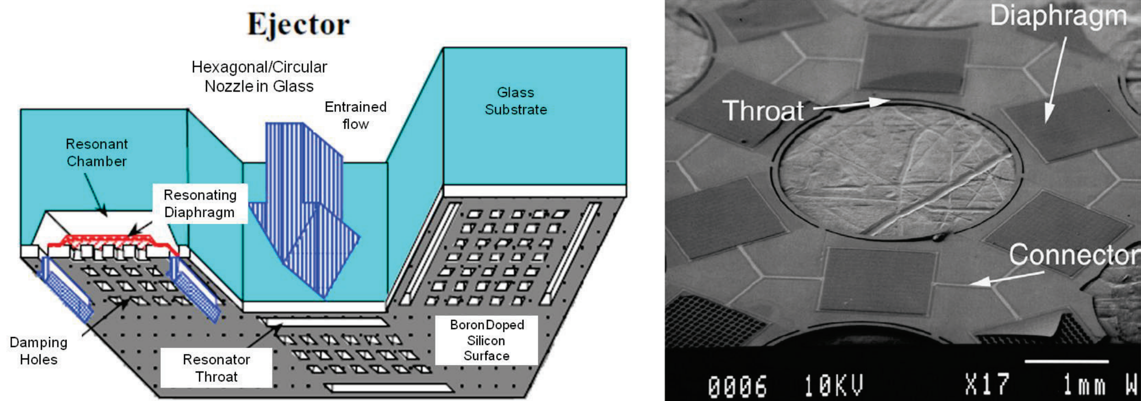

Figure 1-17: (Left) Schematic of the micro-jet actuator and (Right) SEM of the fabricated device [40].

Amirparviz *et al*. [40] was the first to attempt the generation of high-speed air micro-jets using micro-fabricated flat electrode electrostatic actuators (Figure 1-17). An anodic bonding of silicon to glass process was utilized to construct actuators with high-frequency diaphragms (100 kHz) and cavities with Helmholtz resonance of 60 kHz, which has the potential of generating high-speed air micro-jets; however, due to the limitation of the measurement equipment at that time, only low frequency flow velocities were obtained. A measurement of a 1 m/s flow velocity at an operating frequency of 1 kHz was recorded.

Following the work of Amirparviz *et al*., Chou *et al*. [41] demonstrated an all silicon micro-acoustic ejector (MACE) array with a more compact design (Figure 1-18). Due to difficulty in etching glass, a silicon cavity is substituted for the glass cavity of Amirparviz's design and bonding is made with benzocyclobutene (BCB) polymer instead of anodic bonding. Jet holes were added to allow for flow entrainment to further augment flow and thrust performance. This feature was not practical for Amirparviz's design because it was hard to etch through glass wafers. A near-field velocity of ~ 1 m/s and thrust output of 1.35 μN per ejector unit was measured by Chou *et al*. at frequency of 70 kHz [52].

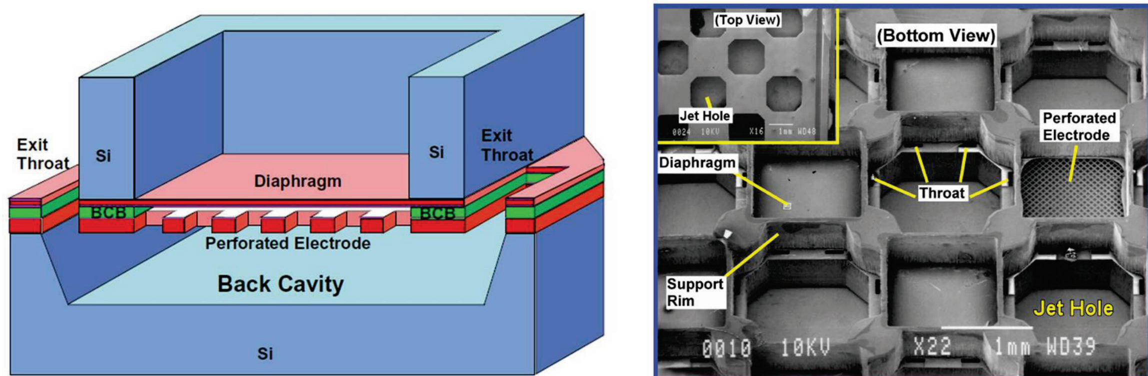

Figure 1-18: (Left) Cross section of the air micro-jet actuator and (Right) SEM of fabricated actuator array [52].

Kim *et al*. [42] modified the flat electrode design in Chou's work [41] to a curved electrode with larger diaphragm displacement by buckling the electrode with the residual stress in the material. From the buckling of the electrode, a larger volume displacement is achieved. An improvement of thrust by a factor of 107% is measured with the curved electrode design without much increase in the operation voltage (Figure 1-19). The

improvements proved that increasing the volume displacement will increase the thrust performance.

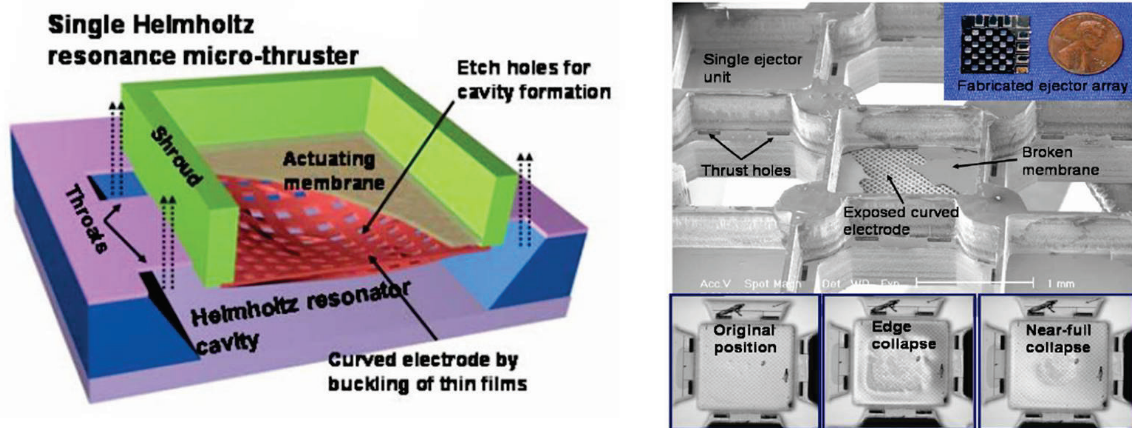

Figure 1-19: (Left) Conceptual illustration of a single resonance micro-thruster and (Right) SEM of micro-fabricated array [42].

Table 1-6: Summary of the performance of ultrasonic jets actuators.

[Ref]	Actuation	Frequency (Hz)	Voltage (V)	Power (W)	Size	Performance
Amirparviz *et al*. [40]	Electrostatic	1 kHz	160 V	4.4 mW	1.73 mm x 1.35 mm x 0.5 mm	1 m/s
Chou *et al*. [41]	Electrostatic	70 kHz	105 V	12 mW	1.35 mm x 1.35 mm x 1 mm	0.8 m/s, 1.35 µN
Kim *et al*. [42]	Electrostatic	70 kHz	200 V	3.1 mW	1.35 mm x 1.35 mm x 1 mm	1.2 m/s, 2.2 µN

Table 1-6 summarizes the different generations of the ultrasonic micro-jet actuators and their improved performances. The main improvement made by Chou *et al.* [41] includes the design of a more compact all-silicon ejector with jet holes for flow entrainment while Kim *et al.* [42] modified the flat electrode design to a curved electrode to increase the total volume displacement.

In summary, the sub-section 1.3 reviewed the related works in the generation of air micro-jets. Pulsed jets are generally used for macro flow control and require complex piping and air supply systems. Plasma pulsed actuators are not reliable and require high operating voltage in the kilovolts range. The synthetic jets have been explored more than the pulsed jets in literature because synthetic jets do not require any piping systems and the operation is simple; however, more work is needed to understand and create a system which is as efficient as the jelly-fish in nature. As the speed and thrust of the generated micro-jets increases with larger volume displacement and higher operating frequency, ultrasonic jets is desirable as it operates at frequencies above the human hearing range. Therefore, as will be shown in the following chapters, this research work is a continuation and improvement of the previous works discussed in ultrasonic jets section.

1.4 Research Goals and Objectives

Based on the motivations mentioned above, this research work focuses on the development and optimization of an electrostatically-actuated ultrasonic jet array (UJA) for potential applications such as micro propulsion and chip cooling. Similar to previous ultrasonic jet ejectors as mentioned in section 1.3.2.2, the UJA has a vibrating diaphragm that can modulate the air in a chamber and eject high-speed air jets out of the chamber through an exit orifice. As diaphragm works best at the micro-scale, it has the potential to achieve high thrust-to-weight ratio due to its light weight. At large deflection compared to its thickness, the diaphragm can move a large fluid volume to generate sufficient thrust to create lift. For maximum performance, the micro propulsion system has to take

advantage of its high frequency and resonance operation, thrust augmentation and flow entrainment.

Multiple challenges were identified in the effort to achieve a higher thrust and speed of air micro-jets compared to the performance presented by Chou *et al*. [41] and Kim *et al*. [42]. Learning from the previous works of Chou *et al*. [41] and Kim *et al*. [42], the high operating frequency of ultrasonic jets and large volume displacement are the main features to achieve high-speed air micro-jets. Chou *et al*. [41] reported the actuation of a high-frequency diaphragm at a 3 μm distance at high speed but the reliability becomes a problem if a larger displacement distance is required for larger volume displacement. Kim *et al*. [42] addressed this issue by modifying the flat electrode design with a 3 μm electrostatic gap to a curved electrode with a ~ 8.8 μm electrostatic gap and the performance is improved by 107 %. Although the curved electrode can have larger volume displacement, the diaphragm fractures before full collapse is achieved. Nonetheless, Kim *et al*. [42] increased the total volume displacement even without achieving full collapse of the diaphragm.

The main challenge to achieve a large-gap and high-frequency diaphragm actuator lies in the design of the diaphragm actuator because the diaphragm has to be able to reliably modulate large volume of air with large force and at high speed. Not only does the diaphragm must be flexible enough to have large deflection, it also must have the force to go against high resistance from built-up pressure in the cavity and force the air through the small exit orifice. If low-frequency or flimsy diaphragm is used, the diaphragm can move at large deflection but the operating frequency will be reduced. On

the other hand, if a high-frequency diaphragm is used, the highly-stretched diaphragm might fracture if displaced at a large distance and reliability of the diaphragm becomes an issue. In addition to the mechanical and structure challenges, a large-gap diaphragm actuator requires high operating voltage and challenges such as charging effects or dielectric breakdowns have to be taken into considerations.

The objective of this dissertation work is to address the primary challenge in designing and fabricating a reliable large-deflection and high-frequency diaphragm actuator to create large perturbations of the surrounding fluid and generate high-speed jets of air.

The goals of this thesis include:

1. Design and development of an ultrasonic jet array (UJA) for potential applications such as micro propulsion and chip cooling.

2. Development of a new fabrication technology to produce high-frequency, large-gap electrostatic diaphragm actuators with high yield and reliable actuation.

3. Analytical modeling and design parameters optimization of forced Helmholtz resonators which form the basis of the micro propulsion system being explored in this research.

4. Characterization and experimental investigation of the performance of the UJA.

1.5 Thesis Overview

Chapter 1 includes the motivation of this research work, a review of air micro-jets, dissertation goals and objectives, and thesis overview. Background to the motivations is discussed. In the review of air micro-jets, a new category, ultrasonic jets, is introduced.

Chapter 2 provides the design and modeling of an ultrasonic jet array (UJA) using acoustic streaming theory of forced Helmoltz resonator. Navier-Stokes equations are utilized and design parameters are optimized for high thrust performance.

Chapter 3 introduces the design and fabrication of a new type of electrode, named the filleted electrode, using a photoresist solvent reflow process. The filleted electrode design greatly improves the reliability of the electrostatic diaphragm actuator.

In Chapter 4, the performance of the filleted electrode design in comparison to flat electrode design is investigated. Various tests are performed to assess the reliability of the diaphragm actuator.

In Chapter 5, the diaphragm actuator is assembled with a Helmholtz cavity and a pendulum test setup is used to conduct direct thrust measurements. The properties of acoustic streaming are analyzed in this chapter.

Chapter 6 summarizes the contribution of this dissertation work to the research field and proposed suggestions for future work.

References and Appendices are included at the ends of the chapters.

CHAPTER 2

DESIGN OF ULTRASONIC JETS (U-JET) USING ACOUSTIC STREAMING THEORY

2.1 Background

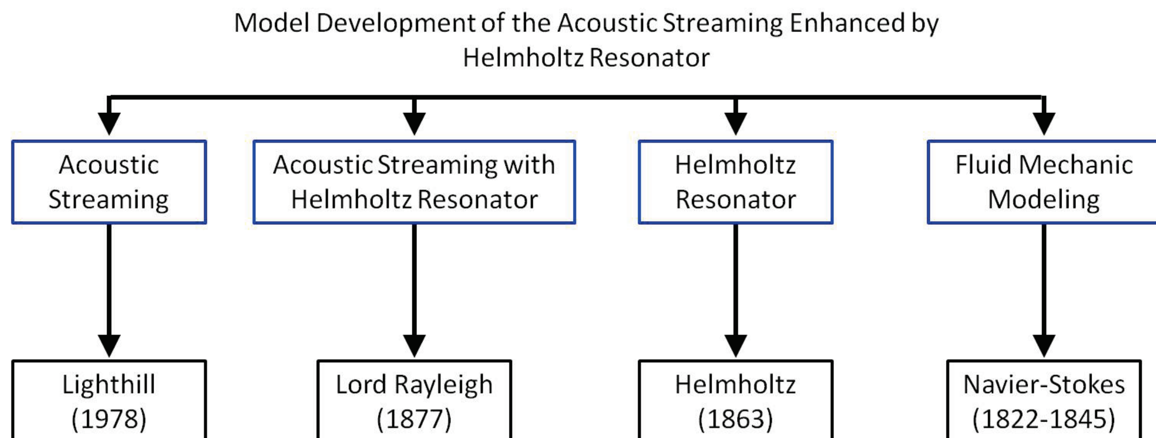

Figure 2-1: Some important figures who contributed to the model development of ultrasonic jets generation by acoustic streaming with a Helmholtz resonator.

Figure 2-1 includes some of the important people who contributed to the background of this work, which is the model development of the acoustic streaming with a Helmholtz resonator. It is commonly known that air jets can produce sound, such as in wind musical instruments. Conversely, sound can produce air jets, known as acoustic streaming. Acoustic streaming, as first noted by Rayleigh [53], Nyborg [54] and

Westervelt [55], and later described in detail by Lighthill [56] in 1978, refers to jet-like winds generated by powerful ultrasonic sources in air. Acoustic streaming occurs when sound energy attenuates non-linearly through a viscous fluid, creating disturbance to the environment. The magnitude of acoustic streaming is influenced by various energy attenuation mechanisms and determined by the power, size and frequency of the ultrasonic source as well as the viscosity and other parameters of the air. Lighthill shows that a powerful ultrasonic source such as a Kerry Vibrason 300 Transducer can produce a 20 kHz beam from a vibrating surface of area of 2 cm^2 and generates jet-like winds; however, the power efficiency at this frequency is very low. At higher frequencies, such as those greater than 1 MHz, the acoustic streaming will be substantial [56] and in a more recent work by Yu *et al*. [57], a jet flow of up to 1.2 m/s can be produced using a high-frequency ultrasonic transducer at the frequency of 10.8 MHz. Here, in this research work, as will be discussed in the Chapter 6, significant thrust can be observed due to acoustic streaming at ultrasonic frequencies near 100 kHz with a diaphragm size of 1.2 mm by 1.2 mm.

In 1877, John William Strutt (Lord Rayleigh) published in "Theory of Sound" [53] that acoustic streaming can be amplified using a Helmholtz resonator. The work of Hermann von Helmholtz in 1863 [58] attracted Lord Rayleigh's attention to the properties of acoustic resonators which leads to his introduction of acoustic conductivity, where the solid walls and orifice can produce changes in acoustic impedance and augmentation to the acoustic streaming. Using acoustic conductivity, Lord Rayleigh came up with a lumped element model, using a simple slug-mass mechanical oscillator analogy

[59]. In his model, the system is decomposed into an equivalent electric circuit that consists of various impedances. These impedances depend on the geometric parameters which are empirically obtained. Although it is straight forward, it is difficult to obtain the empirical end correction parameters accurately since every fabricated device will vary due to the variation in the fabrication process.

Another alternative to lumped element modeling is utilizing the Navier-Stokes equations (developed separately by Claude-Louis Navier and George Gabriel Stokes (1822-1845)). The Navier-Stokes equations are based on the conservation of mass, momentum and energy of the system which avoids the dependence on empirical correlations. These equations can be used to predict the behavior of the Helmholtz resonator more accurately and easily.

Amirparviz *et al*. [60] used the lumped element modeling to design the first ultrasonic jets ejector. Later, Muller *et al*. [61] developed a better mathematical approach using the Navier-Stokes equations to study the ideal as well as coupled systems. Following Muller's work, Chou *et al*. [52] utilized the same analytical model to study the effects of geometric parameters on the performance of the ultrasonic jet ejector. In all these models, it is assumed that the diaphragm's displacement is small and will not induce any non-linearity. In this research work, the previous assumption is no longer valid because large-gap actuator is required to increase the thrust performance. The family of equations used by Chou *et al*. [52] is adapted with slight modifications and will be discussed in the following sub-sections.

2.2 Structure and Principles of Operation of the Ultrasonic Jet Array (UJA)

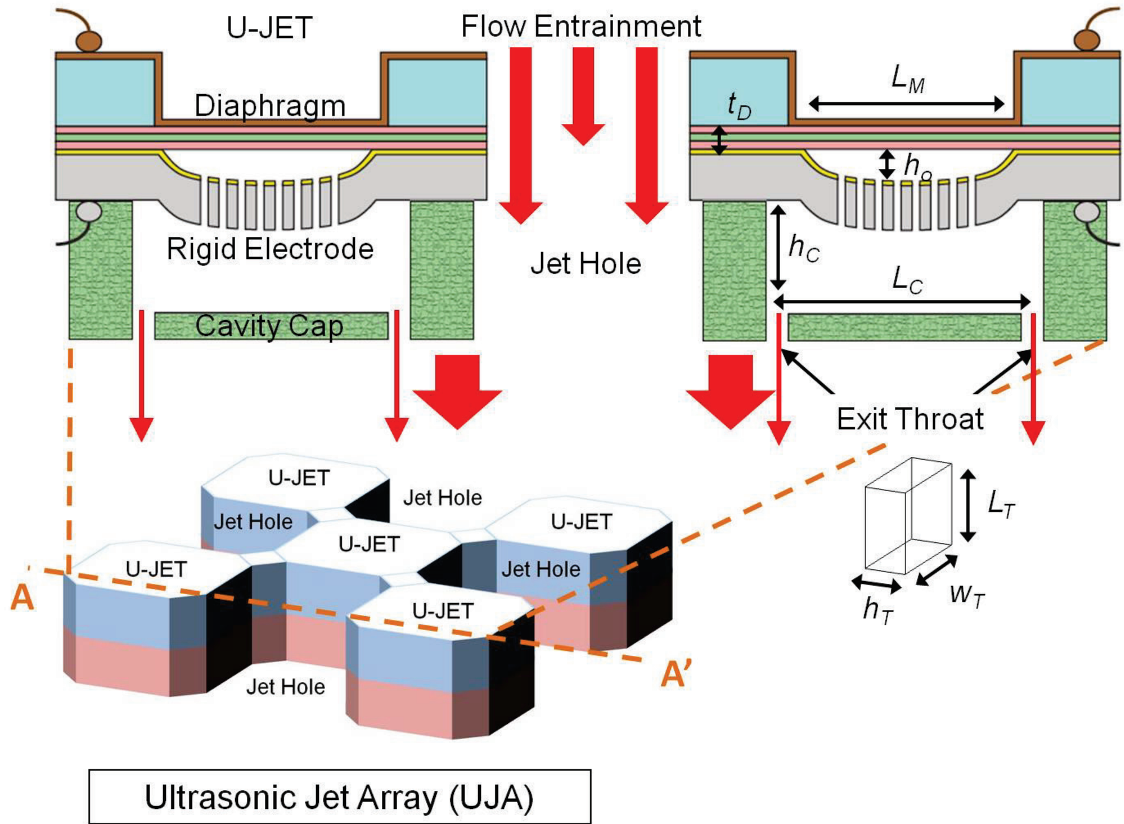

Figure 2-2: Ultrasonic jet array (UJA) with checkerboard arrangements of U-JET and jet holes, with cross section view at A to A'. The important parameters governing the performance of the UJA are labeled on the cross section.

Before the discussion of the modeling work performed for this research work, it is useful to first depict the structure and principles of operation of an ultrasonic jet array (UJA), including the various design parameters that influence the modeling effort. The most basic design for UJA is a checkerboard arrangement of ultrasonic jets (U-JET) and jet holes. Figure 2-2 shows the overall structure and cross section of the UJA with a checkerboard arrangement. It consists of four U-JETs surrounding a jet hole. Each U-JET is formed by attaching an enclosed acoustic cavity (Helmholtz resonator), which consists

of eight exit orifices ("exit throats" as labeled in the figure) with a vibrating diaphragm actuator that can modulate the air volume inside the cavity at high speed. The vibrating diaphragm is actuated electrostatically due to its simple structure and fabrication process, fast response or high operating frequency, large displacement compared to the diaphragm's thickness, and low power consumption. The jet holes allow larger air volume to be entrained by the high-speed air generated through the exit throats, creating more volume flow and thrust.

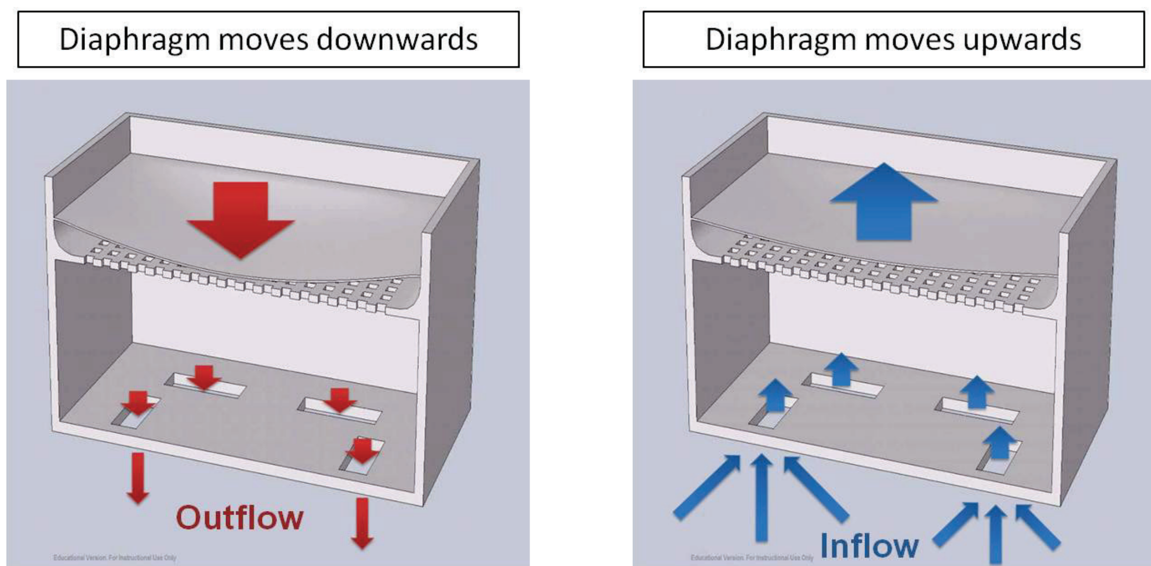

Figure 2-3: (Left) Outflow phase where diaphragm moves downwards, pushing the air out from the cavity in one direction, and (Right) Inflow phase where diaphragm moves upwards, where suction of the air into the cavity occurs from all directions.

The important parameters governing the following modeling effort are labeled on the cross section in Figure 2-2 and listed in nomenclature. The principle of operation of the U-JET is divided into two main phases; outflow and inflow phases (Figure 2-3). The electrostatically-driven vibrating diaphragm causes volume displacement in the cavity.

Air is ejected out from the cavity during the outflow phase and sucked into the cavity during the inflow phase through the same exit throats. When the diaphragm is vibrated at the system's resonant frequency, high-speed air jets are produced through the throats. The system's resonant frequency is influenced by both the diaphragm's natural resonance and the cavity's Helmholtz acoustic resonance. The diaphragm's natural resonant frequency is controlled by the thickness (t_D), mass and residual stress (σ) in the diaphragm. The Helmholtz resonant frequency is controlled by the exit throat and cavity dimensions (h_T, w_T, L_T and V_C).

2.3 Coupled System Model for a High-Frequency and Large-Deflection U-JET

The main goal in the design of the U-JET is to generate high-speed air jets, achieving high volume flow rate and thrust. This work aims to increase the thrust and volume flow rate by increasing the air jet velocity through larger volume displacement or diaphragm deflection at higher operating frequency. In the design of a large-deflection diaphragm actuator, it is important to incorporate the non-linearity due to large displacement into the model.

The modeling work in this chapter is an adaptation of the coupled-system model developed by Muller *et al*. [61] and Chou *et al*. [52], and is utilized to design and analyze the behavior of the air micro-jets. The coupling between electrostatic actuation and Helmholtz acoustic resonance is modeled based on the Navier-Stokes equations and forced Helmholtz resonator theory. In previous works, the diaphragm is assumed to move at small deflections compared to its thickness and therefore flexural rigidity can be neglected in the simulations; however, in our revised model, flexural rigidity is included

because large deflection is desired. On the side where the diaphragm is not mechanically bounded by a rigid electrode, the diaphragm movement is limited by the flexural rigidity and residual stress in the diaphragm as well as the net force from the pressure difference acting on both sides of the diaphragm. Most of the assumptions made by Muller *et al*. [61] are kept in this modeling work: (1) the wavelength of the acoustic field is large compared to the device size (which implies that pressure in the resonator cavity is uniform), and (2) boundary layer separation at the throat exit causes a topological change of the stream lines resulting in high-speed air jets.

The equations used in the coupled system model are listed as below. Helmholtz acoustic resonance is calculated from Equations 2.1. Equations 2.2-2.10 are numerically calculated in MATLAB, using the `ode45` function to simultaneously solve multiple inter-related differential equations. Equations 2.2-2.6 model the acoustic behavior in the cavity while Equations 2.7-2.10 model the electrostatic forcing of the diaphragm. The first two terms in Equations 2.2-2.3 are associated with the inertia of the air mass oscillating in and out of the throat holes while the last term is the damping term. The damping term is related to the damping due to friction and boundary layer separation at the exit of the throats. Although the definition of the throat height, h_T, and throat width, w_T, can be interchangeable in the equations, h_T is assumed to be always smaller than w_T and is used as the limiting factor in the damping term.

The pressure change ($p(t) = p_c - p_{amb}$) in the cavity in Equations 2.4-2.5 is affected by two components. The first term is the compliance term and is related to the pressure change due to the compressibility of the air. The second term is the forcing term

and is related to the pressure change due to the change in volume from the modulation of the vibrating diaphragm. Equation 2.6 calculates the rate of volume change from the diaphragm motion (Equation 2.7), where it depends on two opposite forces acting on it such as the electrostatic force modeled in Equation 2.9-2.10 and the pressure build-up in the cavity. The coupling effect between the two forces, K_D, is estimated by Equation 2.8. Boundary conditions such as limiting the deflection of the diaphragm due to the mechanical stop provided by the fabricated electrode are included in the MATLAB code. The MATLAB code is attached in Appendix A.

$$f_o = \frac{\upsilon}{2\pi}\sqrt{\frac{A_E}{L_E V_C}} \tag{2.1}$$

$$\frac{du_e}{dt} = \frac{1}{L_E}\frac{p}{\rho} - \frac{u_e^{\,2}}{2L_E} - 8\frac{\eta}{\rho}\frac{u_e}{h_T^{\,2}}\frac{L_V}{L_E}, \qquad u_e \geq 0, \tag{2.2}$$

$$\frac{du_e}{dt} = \frac{1}{L_E}\frac{p}{\rho_{amb}} + \frac{u_e^{\,2}}{2L_E} - 8\frac{\eta}{\rho_{amb}}\frac{u_e}{h_T^{\,2}}\frac{L_V}{L_E}, \qquad u_e < 0, \tag{2.3}$$

$$\frac{dp}{dt} = \upsilon^2\frac{d\rho}{dt} = -\rho\upsilon^2\frac{u_e A_E}{V} - \rho\upsilon^2\frac{1}{V}\frac{dV}{dt}, \qquad u_e \geq 0, \tag{2.4}$$

$$\frac{dp}{dt} = \upsilon^2\frac{d\rho}{dt} = -\rho_{amb}\upsilon^2\frac{u_e A_E}{V} - \rho\upsilon^2\frac{1}{V}\frac{dV}{dt}, \qquad u_e < 0, \tag{2.5}$$

$$\frac{dV}{dt} = -\frac{4A_D}{\pi^2}\frac{dh_D}{dt} \tag{2.6}$$

$$\frac{d^2h_D}{dt^2} + \omega_D^{\,2}h_D = -K_D(p - p_e), \text{ where } \omega_D = \pi\sqrt{\frac{2\sigma}{\rho_D A_D}} \tag{2.7}$$

$$K_D = \frac{\pi^2}{4}\frac{1}{\rho_D t_D} \tag{2.8}$$

$$p_e = \frac{\varepsilon_o}{2}\left(\frac{V_{electric}}{h_o}\right)^2 g\left(\frac{h_D}{h_o}\right) \tag{2.9}$$

$$g\left(\frac{h_D}{h_o}\right) = \frac{1}{\left(1-\frac{h_D}{h_o}\right)^{0.846}} \tag{2.10}$$

2.3.1 Modeling of Non-linear ω_D due to Large Deflection

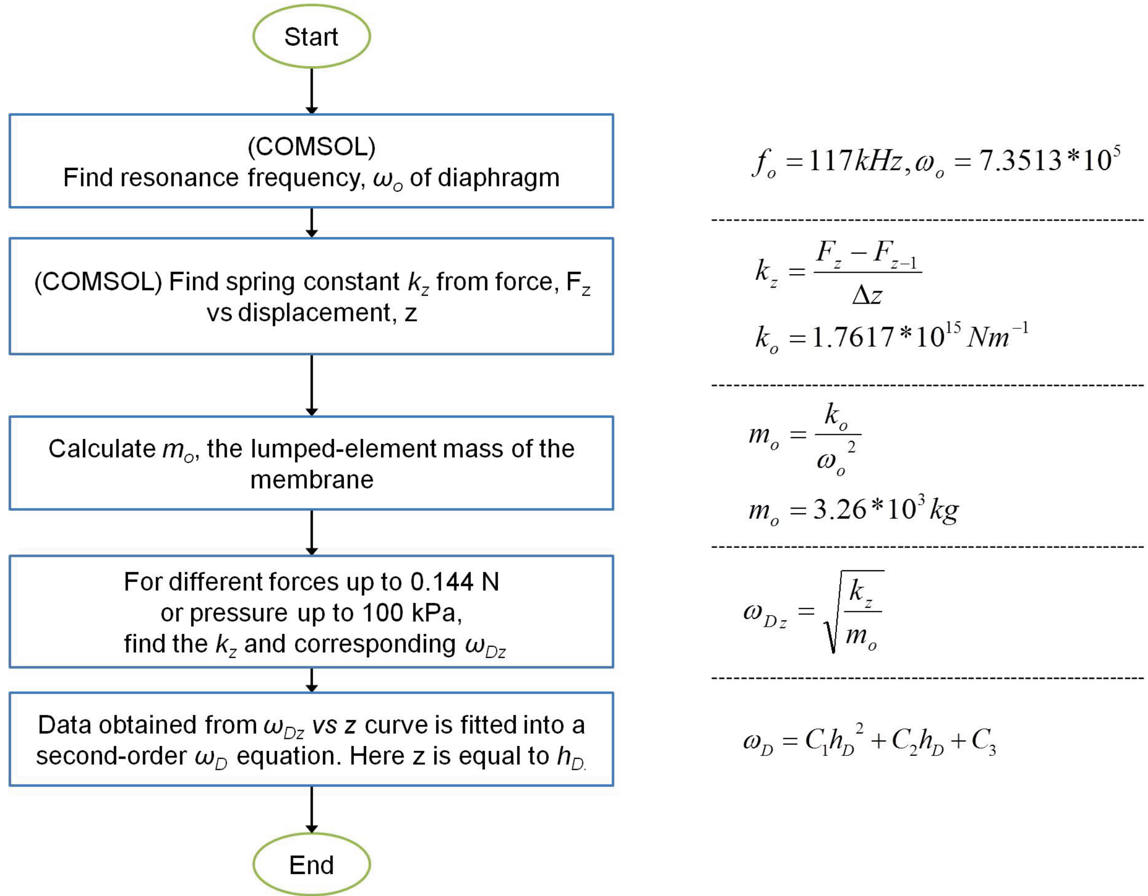

Figure 2-4: Flow chart to obtain equation for ω_D, which is dependent on the second order of the diaphragm's displacement.

On the side where there is no mechanical stop (rigid electrode), the diaphragm maximum deflection is bounded by the resulting force between the pressure in the cavity,

the electrostatic force, and the diaphragm's restoring force. Therefore, accurate estimation of the influence of the diaphragm's restoring force in the modeling equations is important. A Finite Element Analysis (FEA) model in COMSOL is used to incorporate the non-linearity of the diaphragm movement due to its flexural rigidity and residual stress into the modeling equations. From the relationship between applied force and its corresponding deflection, the non-linear stiffness and spring constant dependence on diaphragm displacement are incorporated into the ω_D term in Equation 2.7. Figure 2-4 shows the procedure used to obtain a new ω_D equation (Equation 2.11). Instead of a constant ω_D calculated from the diaphragm's residual stress, the ω_D term is now dependent to the second order of the diaphragm's displacement, where constants C_1, C_2, and C_3 are values fitted from non-linear computational analysis using COMSOL and depend on various characteristics of the diaphragm. The flexural rigidity and residual stress of the diaphragm play a more important part in this simulation work compared to previous work because this is a large-gap actuator with deflection as high as 10 μm towards the electrode side (previous work was 3 μm) and unbounded on the other side, which can deflect up to any value. The "large deflection" option is turned on in the COMSOL simulation to account for the non-linear effects due to large deflection. The obtained values for the constants are: $C_1 = 3\text{x}10^{15}$, $C_2 = 2\text{x}10^{10}$, and $C_3 = 7\text{x}10^{5}$.

$$\omega_D = C_1 h_D^{\ 2} + C_2 h_D + C_3 \qquad (2.11)$$

The L_E and L_V values in Equations 2.1-2.3 are the effective inertia and viscous lengths of the throat. Equations 2.12-2.13 are used for L_E and L_V respectively [52].

$$L_E = L_T + 0.0004\left(\frac{h_T}{h_C}\right) + \frac{L_M}{\pi}\left(\frac{h_T}{h_C}\right) + 2\left(\frac{\sqrt{\pi A_T}}{4}\right) \tag{2.12}$$

$$L_V = L_T + 0.0004\left(\frac{h_T}{h_C}\right)^3 + \frac{L_M}{\pi}\left(\frac{h_T}{h_C}\right)^3 \tag{2.13}$$

The generated thrust by the air micro-jets can be calculated by considering the conservation of momentum for the jet flow outside the exit throats (Equation 2.14). The mean thrust sums the time integral of the momentum flux per cycle, *J*, for the outflow and the drag associated with the inflow, *D*. Based on Muller's assumptions [61], the drag term in Equation 2.14 can be neglected because the flow outside the resonator during the inflow is normal to the jet axis.

$$T_h = J - D = \frac{1}{T}\left(\int_{u_{e>0}} \rho u_e^{\,2} A_E dt + \rho_{amb} U \int_{u_e<0} u_e A_E dt\right) \tag{2.14}$$

2.3.2 Model Verification

Parameters from Chou's design [52], as shown in Table 2-1, is simulated with the modified model and the results are compared to Chou's measured performance. A thrust of 1.2 µN is obtained at 80kHz, which is close to Chou's experimental results of 1.35 µN at 70kHz. The discrepancy can be due to other damping effects that are not taken into account in the model. Two clean frequency peaks are observed in Figure 2-5, where the first peak is related to the cavity's resonance and the second peak is related to the diaphragm's resonance.

Table 2-1: Design parameters of Chou's design [52] used for model verification.

	Chou's Design Values [52]
Diaphragm size (L_M x L_M)	1.2 mm x 1.2 mm
Diaphragm thickness (t_D)	2.16 µm
Diaphragm residual stress (σ)	60 MPa
Electrostatic gap (h_o)	3 µm
Throat dimensions (h_T x w_T)	50 µm x 200 µm
Throat length (L_T)	20 µm
Number of throats (N_T)	8
Cavity height (h_C)	100 µm
Cavity Length (L_C)	1.35 mm x 1.35 mm

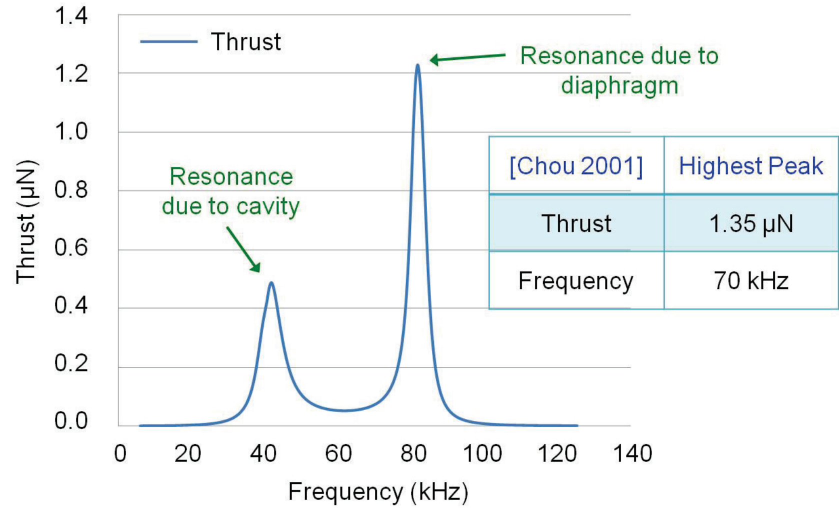

Figure 2-5: Model verification using the parameters from Chou's work [52]. The frequency response of the thrust shows two clean resonant peaks where the first peak is related to the cavity's resonance and the second peak is related to the diaphragm's resonance.

2.4 Parameter Optimization Based on Theoretical Results

As mentioned in the beginning chapter of this dissertation, the ultimate goal of this work is to achieve flight of a silicon wafer. The optimization effort is divided into two sub-sections. The first sub-section describes the procedure to achieve thrust-to-weight ratio greater than one using a trapezoidal voltage waveform. The second sub-section discusses the influence of the design parameters using a sinusoidal voltage

waveform. There are a total of three design generations in this research work, where the first and second generations (Gen. 1 and Gen. 2) are optimized to achieve thrust-to-weight ratio greater than one (optimization work associated with trapezoidal waveform) and the third generation (Gen. 3) is the design to further fine-tune the cavity parameters to achieve higher thrust (optimization work according to sinusoidal waveform).

2.4.1 Trapezoidal Voltage Waveform

This sub-section describes the optimization to achieve thrust-to-weight ratio greater than one with trapezoidal voltage waveform. Although Chou *et al*. [52] uses a sinusoidal drive waveform with low operating voltage in his simulation, further optimization using sinusoidal waveform shows that sinusoidal waveform is inefficient especially when operating at voltages above pull-in, and cannot provide the flow rate and thrust needed.

As shown in Figure 2-6, there are several advantages in utilizing the trapezoidal waveform instead of the sine waveform. It is hypothesized that the higher rise and fall time of the trapezoidal waveform as well as maximum volume displacement when operated at voltages beyond pull-in will provide for additional momentum and larger response of the diaphragm, leading to higher thrust output. If the sine waveform is designed to have the same rise and fall time as the trapezoidal waveform, there will be incident where the voltage applied is greater than needed to pull-in the diaphragm and cause reliability problems such as mechanical and electrical failure. Another advantage of the trapezoidal waveform is the longer rest time (zero voltage) compared to the sine waveform. The rest time is needed to allow the diaphragm to be released from the

perforated electrode. Therefore, for all the following simulations in this sub-section, trapezoidal waveform is utilized in the optimization process to achieve thrust-to-weight ratio greater than one.

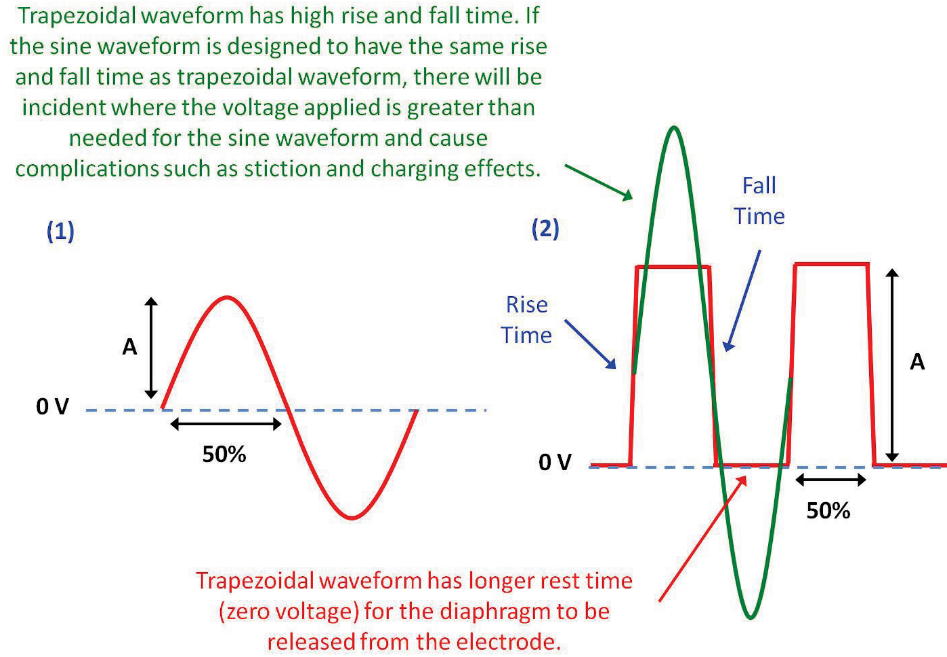

Figure 2-6: Illustrations showing the advantages of utilizing trapezoidal waveform. (1) A sine waveform with small voltage amplitude, A, and (2) A sine waveform with the same rise and fall time as a trapezoidal waveform and notes explaining the advantages of trapezoidal waveform.

As the starting point for the optimization process, the initial nominal values for design parameters are taken from the device with best performance in Chou's work [52], as listed in Table 2-1. The diaphragm resonance is designed to be near 100 kHz with residual stress less than 100 MPa to avoid the diaphragm fracturing due to high residual stress. First, the physical throat length, L_T, is varied while keeping other parameters constant. As shown in Figure 2-7, the optimum L_T is found to be 100 µm for h_o = 3 µm.

The reduction in the generated thrust as L_T increases is due to the higher damping through the exit throat holes introduced by the longer sidewalls.

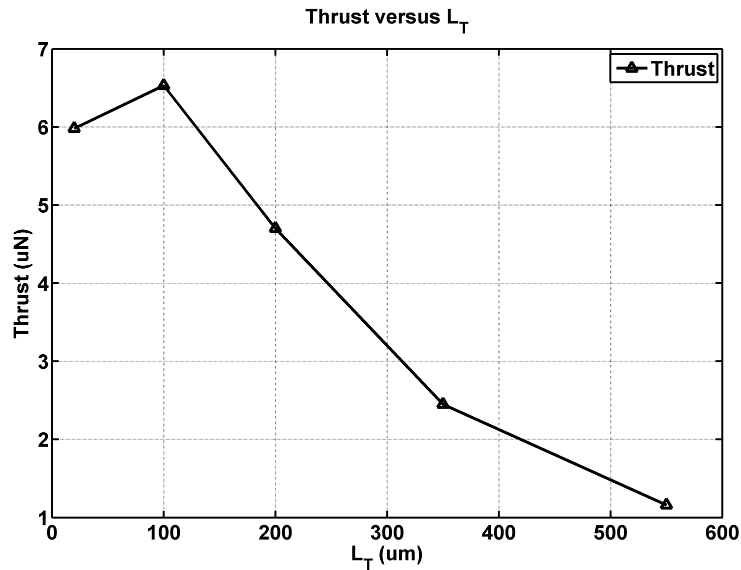

Figure 2-7: Generated thrust versus varying throat length L_T.

With L_T set to be 100 μm, Figure 2-8 shows the flow chart for optimizing other critical design parameters such as operating voltage amplitude (V_o), cavity height (h_C), throat height (h_T), and throat width (w_T) to maximize thrust-to-weight ratio. By sweeping the values of each parameter of interest while keeping the other parameters fixed, the influence of each parameter on the velocity and thrust generation is investigated. Three electrostatic gap height, h_o, is used in this simulation, where h_o = 3 μm, 6 μm and 10 μm. The estimated pull-in voltage for each h_o is 55.0 V, 156.5 V and 341.7 V respectively. First, V_o is varied to find the optimum operating voltage. As the operating voltage is limited by the breakdown of the air, the maximum peak voltage is set to be ± 380 V. If the optimized voltage is found to be greater than ± 380 V, a voltage of ± 380V will be used. Although the breakdown of air can occur at lower voltages, the maximum voltage is

determined to be ± 380 V for modeling purposes. Next, with the new V_o value, the cavity height, h_C, is optimized. Then, with the obtained V_o and h_C values, the exit throat area (h_T x w_T) is optimized. For every design, the frequency of the operating voltage, f_V, is swept from (0.1:0.01:2.1)*f_D Hz to observe the frequency response of the air micro-jet.

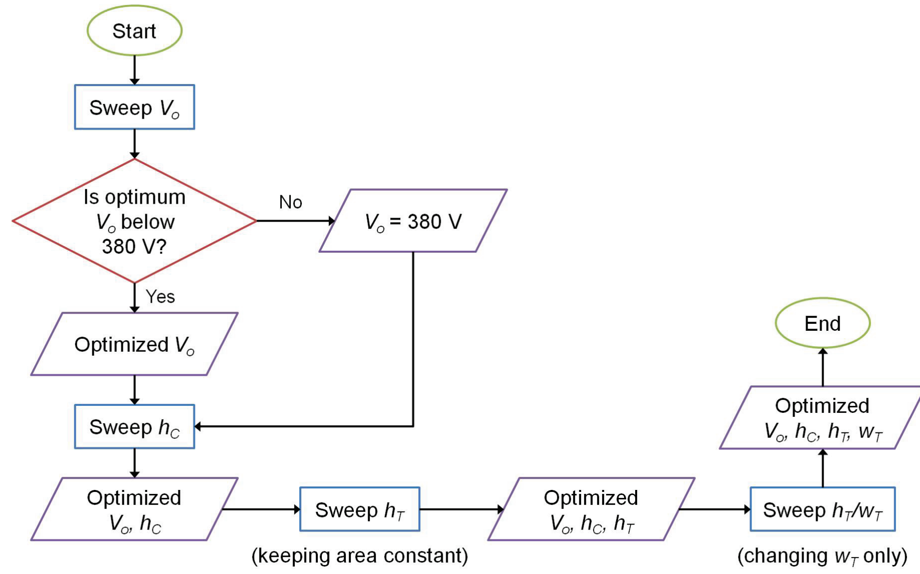

Figure 2-8: Flow chart showing design parameter optimization process for trapezoidal drive waveform.

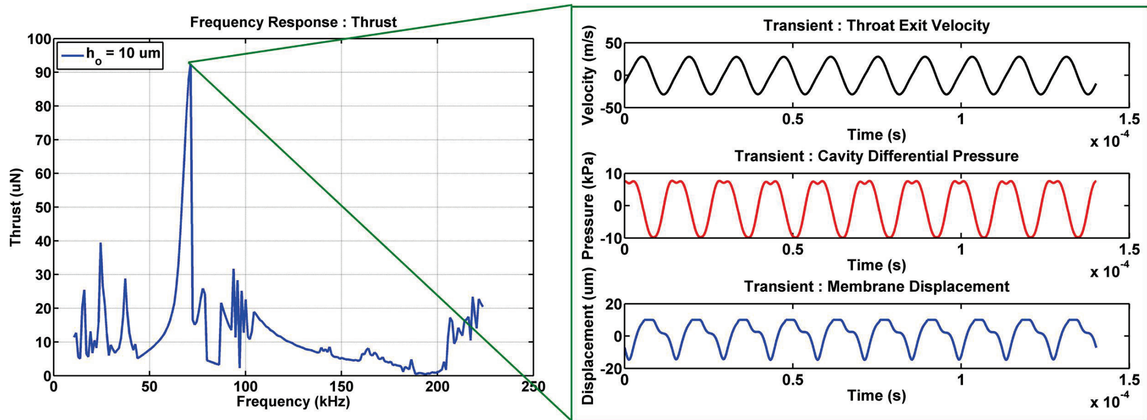

Figure 2-9: (Left) The simulated frequency response for the design with h_o = 10 µm at V_o = 380 V, as listed in Table 2-2, and (Right) Transient response of the generated air micro-jet when actuated at the resonant frequency shown on the left plot.

Figure 2-9 shows the frequency response for the design with h_o = 10 μm at V_o = 380 V, and other parameters as listed in the third row of Table 2-2. Due to operating at voltages above the pull-in voltage, the frequency response curve shows a maximum peak at f_V = 67.1 kHz which is close to the cavity's acoustic resonance (f_o = 76.1 kHz) with a high noise floor. This is very different from Figure 2-5 where there are two clean resonance peaks associated to the Helmholtz resonance and the diaphragm's natural resonance. The high noise floor exists because the duration of time when the diaphragm is collapsed onto the electrode varies for different operating voltages and frequencies. For example, the transient response for two frequency peaks in Figure 2-9 is analyzed and plotted in Figure 2-10. The transient diaphragm displacement for the maximum thrust at 67.1 kHz shows a shorter collapsed time compared to the transient diaphragm displacement at 35.1 kHz.

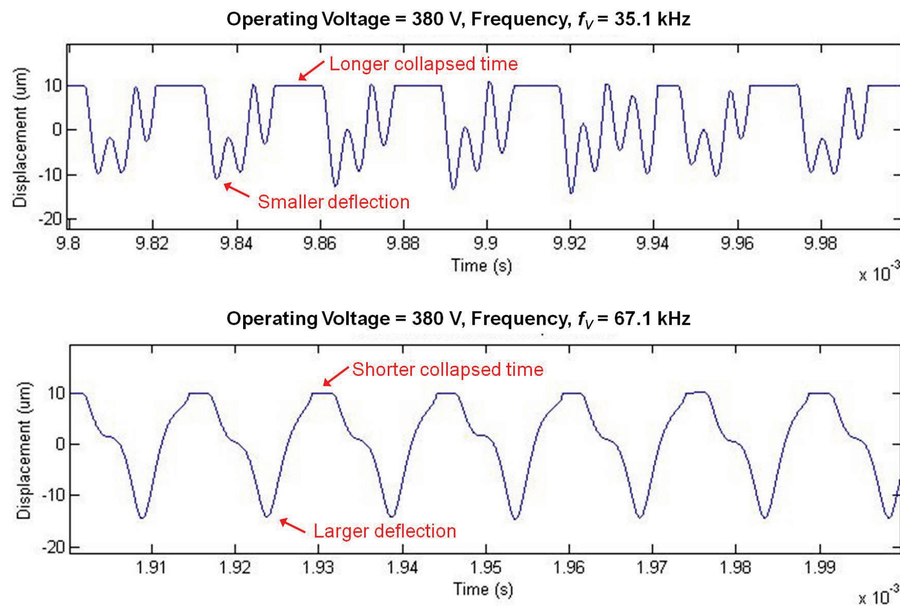

Figure 2-10: (Top) Transient diaphragm displacement at 35.1 kHz and (Bottom) Transient diaphragm displacement at 67.1 kHz.

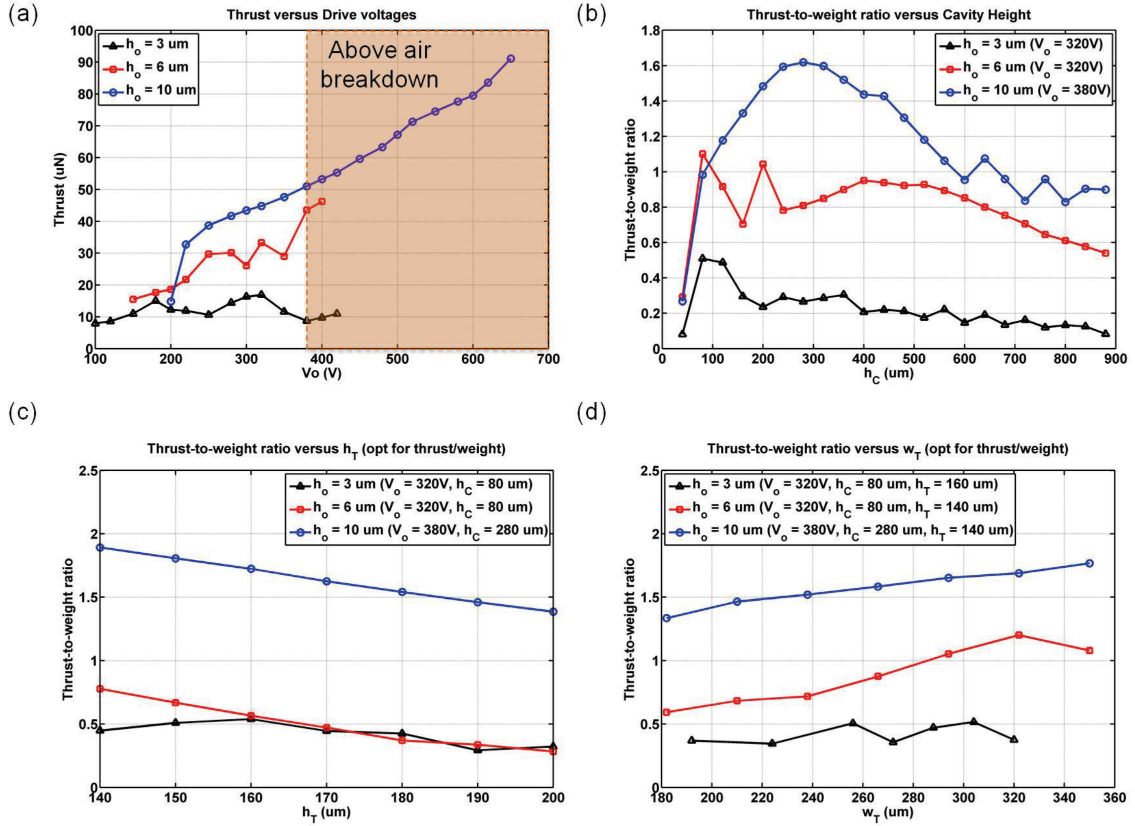

Figure 2-11: Parameters optimization with respect to the optimization procedure in Figure 2-8. (a) Generated thrust versus operating voltage, V_o, (b) Thrust-to-weight ratio versus cavity height, h_C, (c) Thrust-to-weight ratio versus throat height, h_T, by keeping area constant, and (d) Thrust-to-weight ratio versus throat width, w_T.

Following the optimization procedure as shown in Figure 2-8, each design parameter is varied while keeping the remaining parameters the same. For each design, a frequency sweep is performed and the maximum thrust or thrust-to-weight ratio is obtained. These maximum values with the corresponding varying design parameters are plotted Figure 2-11. Figure 2-11(a) shows the thrust performance when V_o is varied. The thrust increases monotonically when V_o is below the pull-in voltage ($V_{pull\text{-}in\ (ho\,=\,3\ \mu m)}$ = 55.0 V, $V_{pull\text{-}in\ (ho\,=\,6\ \mu m)}$ = 156.5 V and $V_{pull\text{-}in\ (ho\,=\,10\ \mu m)}$ = 341.7 V);

however, when V_o is above the pull-in voltage, this behavior is not necessarily maintained because the performance changes depending on the duration of time when the diaphragm is collapsed onto the electrode. The pull-in voltage is estimated using the equations in Chou's work [52]. Looking at Figure 2-11(b), the cavity height, h_C, is optimized for maximum thrust-to-weight ratio. For low cavity heights, the damping in the cavity dominates, as the viscous length is inversely dependent on the cavity heights. At large cavity heights, the thrust decreases as the resonant frequency of the cavity moves further away from the diaphragm's resonant frequency due to less coupling between the two resonant frequencies. For h_o = 10 μm, the optimum cavity height obtained is 280 μm. Although the exit throat area affects the thrust, the effect is much weaker compared to the dependence of thrust on cavity height, as shown in Figure 2-11(c) and (d).

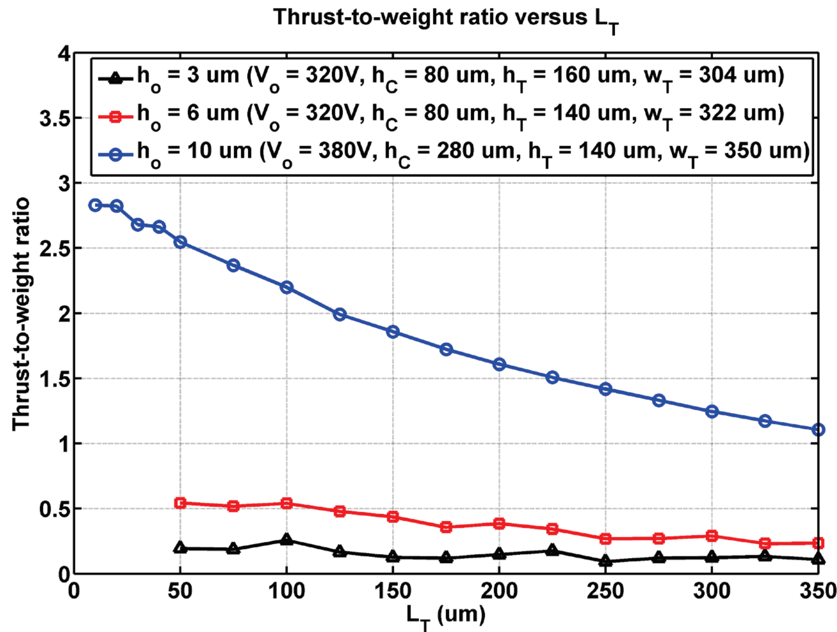

Figure 2-12: The influence of L_T on thrust for different h_o values.

In the previous analysis, all the design parameters were simulated with L_T = 100 µm which was optimized for h_o = 3 um. Further analysis is conducted to study the influence of L_T with the variation of h_o, as shown in Figure 2-12. A maximum thrust-to-weight ratio of 2.8 can be theoretically achieved with L_T = 20 µm and h_o = 10 µm. A significant difference in the thrust-to-weight ratio between h_o = 6 µm and h_o = 10 µm is observed due to the difference in the cavity height. Using Equation 2.13, L_V is governed by the cavity height, h_C, and the throat length, L_T. Since L_V is inversely proportional to the cube of h_C, it will be dominated by L_T if the cavity height is large. Therefore, the influence of L_T is more significant for h_o = 10 µm which has a cavity height of 280 µm compared to h_o = 6 µm which has a cavity height of 80 µm.

Table 2-2 summarizes the optimized parameters for maximum thrust-to-weight ratio for air gap of h_o = 3 µm, 6 µm and 10 µm. As seen in the table, h_o = 10 µm produces the highest thrust-to-weight ratio of 2.8 and shows the potential for flight.

Table 2-2: Optimized design parameters for best thrust-to-weight ratio performance for h_o=3 µm, 6 µm and 10 µm with 100 kHz – diaphragm.

	Design Parameter	Thrust	Thrust/Weight	Flowrate (sccm)
h_o = 3 µm	f_D ~ 100 kHz, f_o ~ 86 kHz	Optimized for Max Thrust/Weight		
	V_o = 320 V, f_V = 38.3 kHz	13.63 µN	0.2569	50.00
	h_C = 80 µm			
	h_T x w_T = 160x304 µm			
	L_T = 100 µm			
h_o = 6 µm	f_D ~ 100 kHz, f_o ~ 86 kHz	Optimized for Max Thrust / Weight		
	V_o = 320 V, f_V = 70.3 kHz	24.42 µN	0.5423	92.36
	h_C = 80 µm			
	h_T x w_T = 140x322 µm			
	L_T = 50 µm			
h_o = 10 µm	f_D ~ 100kHz, f_o ~ 76 kHz	Optimized for Max Thrust / Weight		
	V_o = 380 V, f_V = 67.1 kHz	92.48 µN	2.822	208.23
	h_C = 280 µm			
	h_T x w_T = 140x350 µm			
	L_T = 20 µm			

2.4.2 Sinusoidal Voltage Waveform

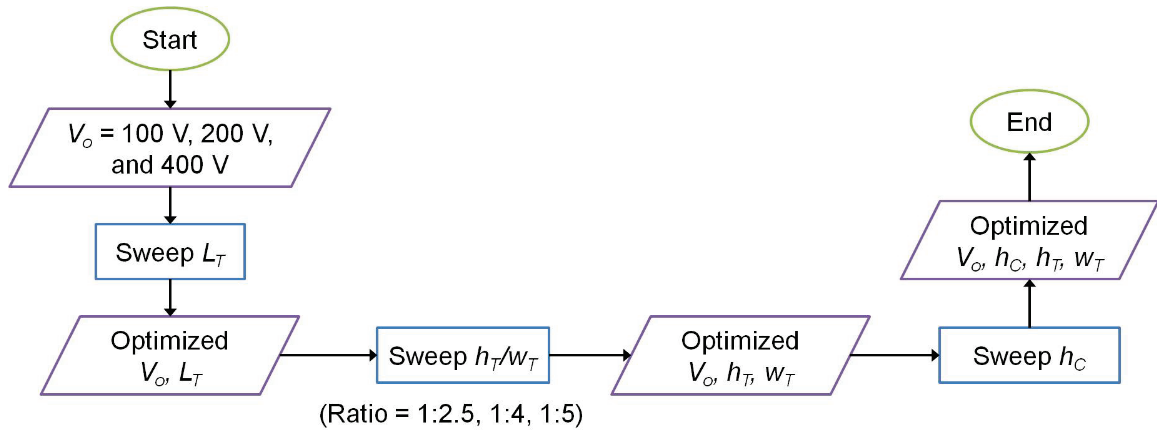

Figure 2-13: Flow chart showing design parameter optimization process for sinusoidal drive waveform.

The performance of the U-JET is presented in the previous sub-section where trapezoidal drive waveform and voltages beyond the pull-in voltage is applied. The usage of the trapezoidal waveform and high voltage produces noisy frequency response with single peak. This makes it hard to obtain an intuitive sense for the design work. Therefore, use of a sinusoidal drive waveform is investigated in this sub-section, and with three different levels of voltages: (1) 100 V (representing voltages well below the pull-in voltage), (2) 200 V (representing voltages close to the pull-in voltage), and (3) 400 V (representing voltages well above the pull-in voltage). Figure 2-13 summarizes the optimization process based on sinusoidal drive waveform.

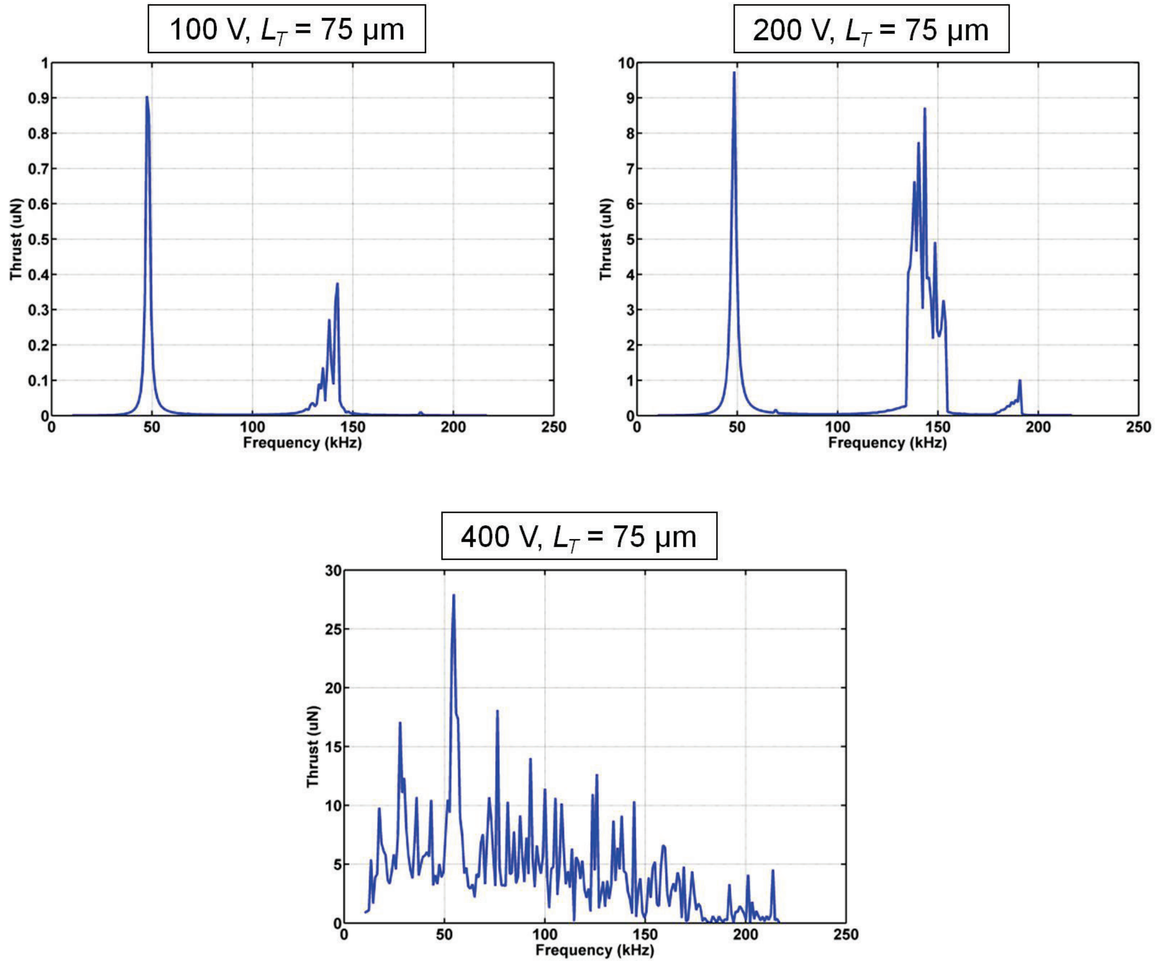

Figure 2-14: Frequency response curves for three operating voltages: (Top Left) 100 V, (Top Right) 200 V) and (Bottom) 400 V.

Dissimilar frequency response is obtained for the three levels of operating voltages (Figure 2-14). The two resonance peaks related to the cavity and diaphragm resonance can be clearly seen only in plots of 100 V and 200 V. The first resonant peak is due to the acoustic resonance of the cavity while the second peak is due to the coupling between the diaphragm's resonance (100 kHz) and the cavity's resonance, where the cavity enhances the diaphragm's resonance to higher frequency. Therefore, by having the

resonance of the cavity closer to the resonance of the diaphragm, the first peak can be moved to higher frequency for more efficient pumping. It is also observed that the performance at actuation voltage of 100 V is substantially lower than when actuated at higher voltages. In the plot of 400 V, the frequency response is noisier than that of 100 V or 200 V, which is as expected from the previous simulations shown in trapezoidal drive waveform. This is because when the diaphragm is operated above the pull-in voltages, the diaphragm will collapse onto the electrode for a long time and produce low thrust. Therefore, for further analysis, only actuation with 200 V is explored.

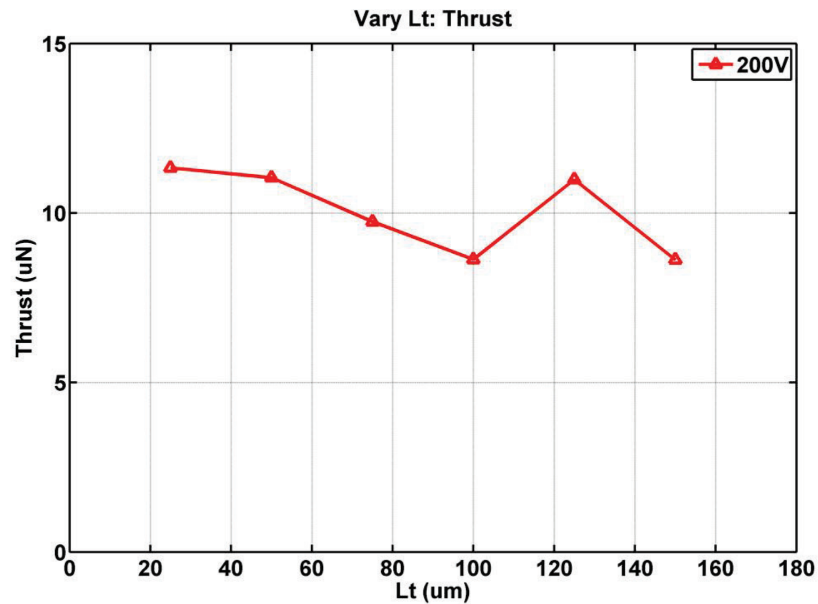

Figure 2-15: Sweep throat length, L_T at operating voltage of 200 V.

In Figure 2-15, the L_T values do not significantly influence the thrust performance when actuated at 200 V. Therefore, for all subsequent simulations, an average value of 75 µm is chosen for L_T.

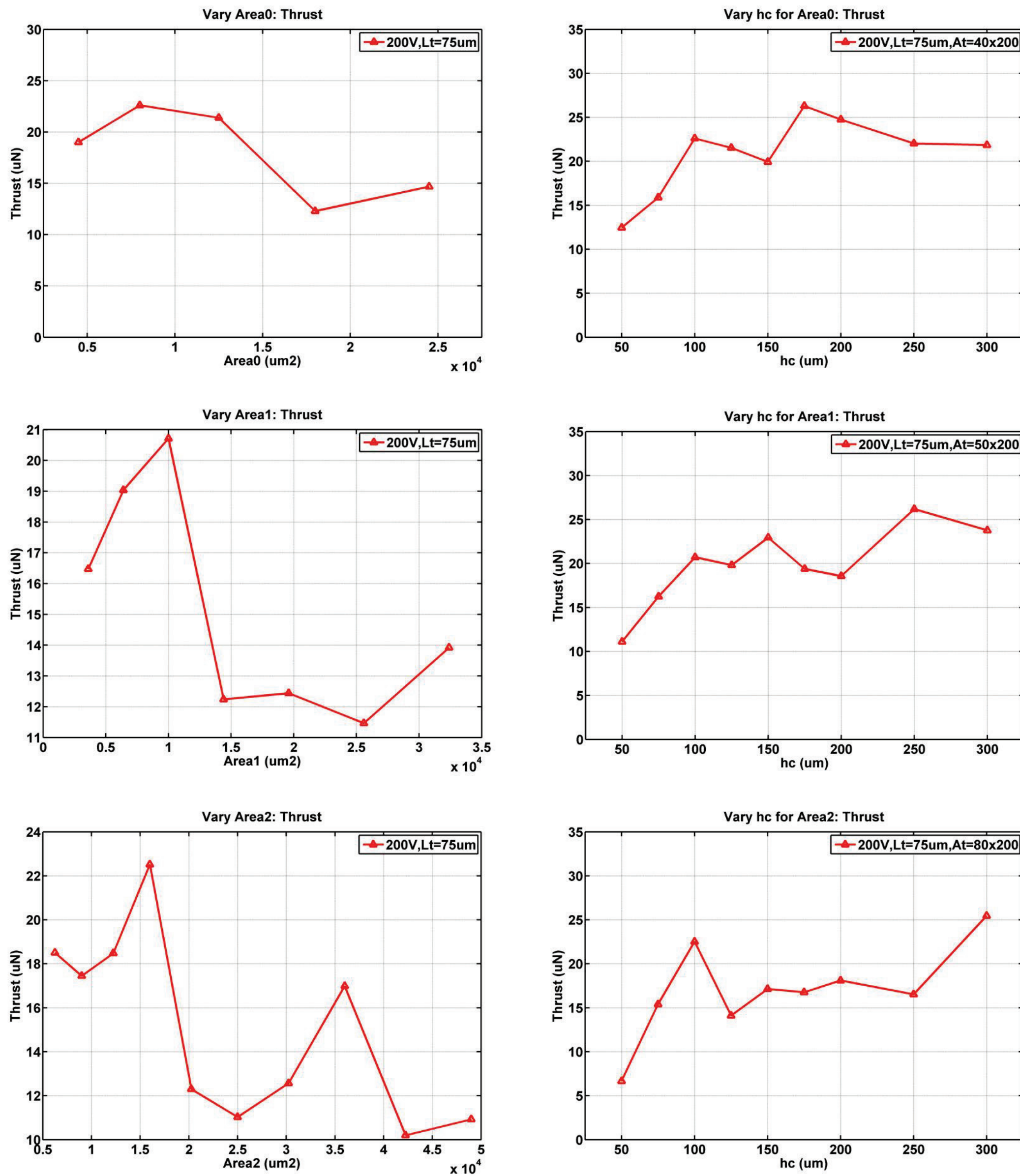

Figure 2-16: The three levels of plots correspond to the different throat area, A_T ratios of h_T to w_T; (1) Area0 = 1 to 5, (2) Area1 = 1 to 4, and (3) Area2 = 1 to 2.5 (Left column). The corresponding cavity height sweep for optimum h_T and w_T per each area is attached (Right column).

Using the geometric parameters chosen by Chou [52] as the starting point, the throat cross section area, A_T, is optimized for different ratios of h_T to w_T = 1 to 2.5, 1 to 4 and 1 to 5. The 1 to 4 ratio was based on the parameters chosen by Chou [52] while the others were chosen to perform a sensitivity analysis. As shown in the left column of Figure 2-16, the optimized A_T values (h_T x w_T) for ratios of h_T to w_T = 1 to 2.5, 1 to 4 and 1 to 5, are 80 μm x 200 μm, 50 μm x 200 μm and 40 μm x 200 μm respectively. Using these A_T values, the cavity height, h_C, is optimized, as shown in the right column of Figure 2-16. It is found that the maximum thrust obtained for all designs varies marginally but has different cavity heights. Since the maximum variation in thrust is marginal, the 1 to 4 ratio is chosen as the basis for experimental investigations in subsequent chapters.

2.4.3 Comparison of Trapezoidal and Sinusoidal Waveform

The optimization procedures using the trapezoidal waveform and sinusoidal waveform were outline previously in Figure 2-8 and Figure 2-13 respectively. For the trapezoidal waveform, the important design parameters of h_T and w_T were varied individually, while for the sinusoidal waveform, h_T and w_T were varied according to a fixed ratio of h_T to w_T. The obtained parameters using the procedure for the sinusoidal waveform resulted in more realistic h_T and w_T values in comparison to the method used for the trapezoidal waveform. This suggested that the optimization procedure needs to be modified to incorporate this ratio.

While the optimization procedure influences the design parameters, the most efficient actuation waveform needs to be chosen. As shown in Figure 2-17, a trapezoidal

or square waveform is found to be more efficient in driving the diaphragm than a sinusoidal waveform by producing a thrust nearly 3x higher. This is due to the increased momentum and energy obtained from the higher rise and fall times of the trapezoidal waveform. Additionally, the longer rest time in the trapezoidal waveform allows for the release of the diaphragm from the electrode which produces larger deflection as seen in Figure 2-10.

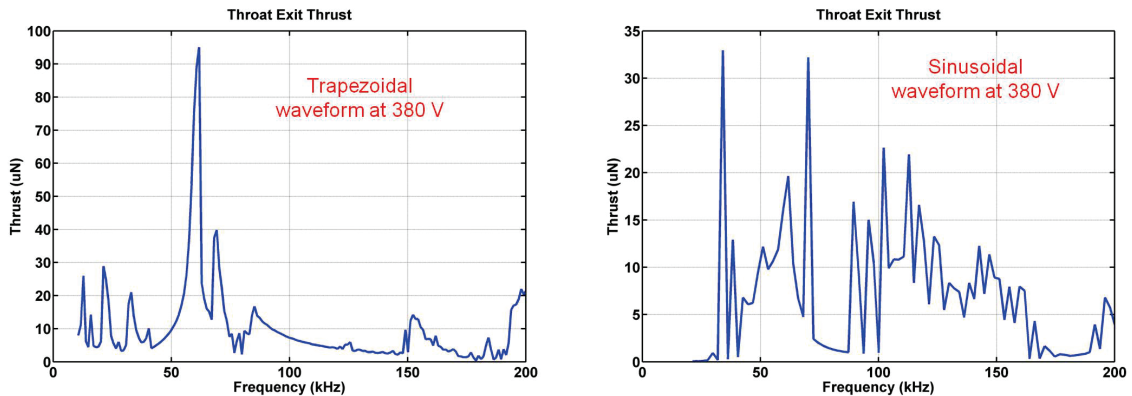

Figure 2-17: (Left) Thrust produced using trapezoidal waveform at 380 V and (Right) Thrust produced using sinusoidal waveform at 380 V.

2.5 Design of Perforations on a Rigid Electrode

For electrostatic actuation, the diaphragm is actuated by applying a voltage difference between the diaphragm and a rigid electrode. The rigid electrode is perforated such that the squeeze-film damping (damping associated with the gap reduction of two parallel plates) is low and will minimally affect the performance of the U-JET. To design for low fluidic resistance, the perforation width should be larger than the thickness of the rigid electrode.

The thickness of the rigid electrode has to be determined before designing the size and number of perforations on the rigid electrode. COMSOL simulation is used and the assumptions in estimating the thickness of the rigid electrode are: (1) the rigid electrode acts like a membrane, and (2) the maximum back-pressure on the membrane is 20 kPa. The simulation results show that a solid membrane (without perforations) of 19 μm and made out of nickel (material chosen for the rigid electrode) will deflect 0.2 μm with applied pressure of 20 kPa. Considering a perforation of 40% on the rigid electrode, the nickel membrane of 30 μm thick will have almost no deflection and can be considered as a rigid electrode; however, due to the fabrication challenges with the residual stress in thick electroplated nickel, the final design for the rigid electrode is ~ 20 μm.

The design for the size of the perforations is based on the analysis done by Amirparviz [62] in Chapter 4.4 of his thesis work. For Gen. 1 of this research work, the perforations on the rigid electrode are designed such that the electrode holes are larger at the center and smaller at the edges. The hypothesis behind this design is such that at the center of the electrode where maximum diaphragm displacement is achieved, lowest damping should be present (largest perforation holes) while at the edges where highest diaphragm stress is present, highest electrostatic force is needed (smallest perforation holes). The perforation holes are divided into 3 designs: (design A) blue area, (design B) green area and (design C) red area. As shown in Figure 2-17, the total area for design A is 20 %, design B is 40 % and design C is 40 % of the electrode area. The perforation holes sizes for design A to C for nominal design of Gen. 1 are listed in Table 2-3.

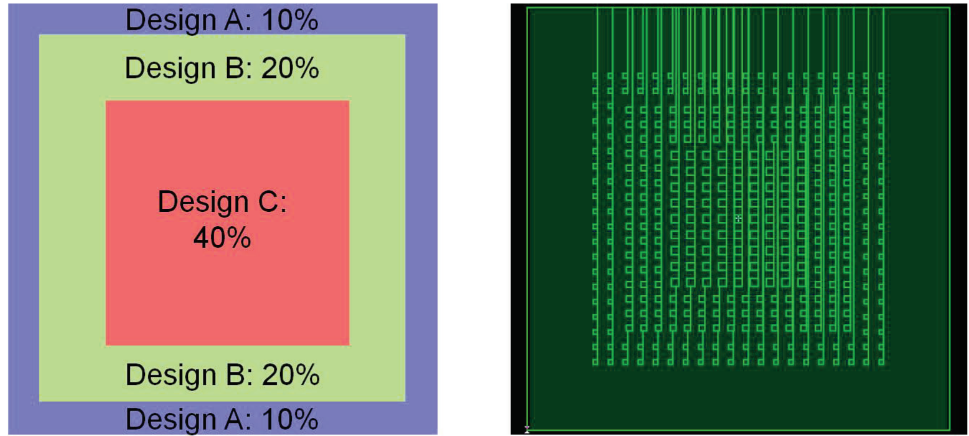

Figure 2-18: (Left) 3 areas of different perforation sizes and the layout of the perforations drawn in Gen. 1.

Table 2-3: The perforation hole sizes for design A to C in nominal design of Gen. 1.

Electrode solid | Electrode hole | Electrode solid | Electrode thickness = 20 µm

Design	Electrode hole	Electrode solid
A	17 µm	40 µm
B	22 µm	33 µm
C	29 µm	29 µm

From the yield in fabrication of Gen. 1, the perforations in Gen. 2 and Gen. 3 are changed to be a constant size with design C instead of gradual variation as in Gen. 1. This is because the small holes can trap particles easily and make it harder to achieve a clean release of the diaphragm during fabrication. In addition, the small holes create more damping to the system. In general, larger holes are better as long as the electrostatic force is not reduced significantly.

2.6 Design of an UJA for Flow Entrainment Optimization

Until now, the modeling effort mainly comprises of analyzing the performance of a square U-JET. Alternating with jet holes, these U-JETs can be connected in parallel having different arrangements to form a UJA. These different arrangements produce various levels of flow augmentation which is controlled by the density of U-JETs in a UJA as well as the size of the U-JET versus the size of the jet holes. Therefore, three different arrangements are proposed as shown in Figure 2-18. The first is the checkerboard arrangement which has the best symmetry and uniform behavior for a square U-JET. The second is a dream catcher arrangements of similar square U-JETs with varying jet hole sizes to study the effect of flow entrainment. Finally, the third design is a modification of the first by incorporating hexagonal U-JETs arranged in a honey comb manner to study the effect of different U-JETs shape and number of U-JETs surrounding a single jet hole.

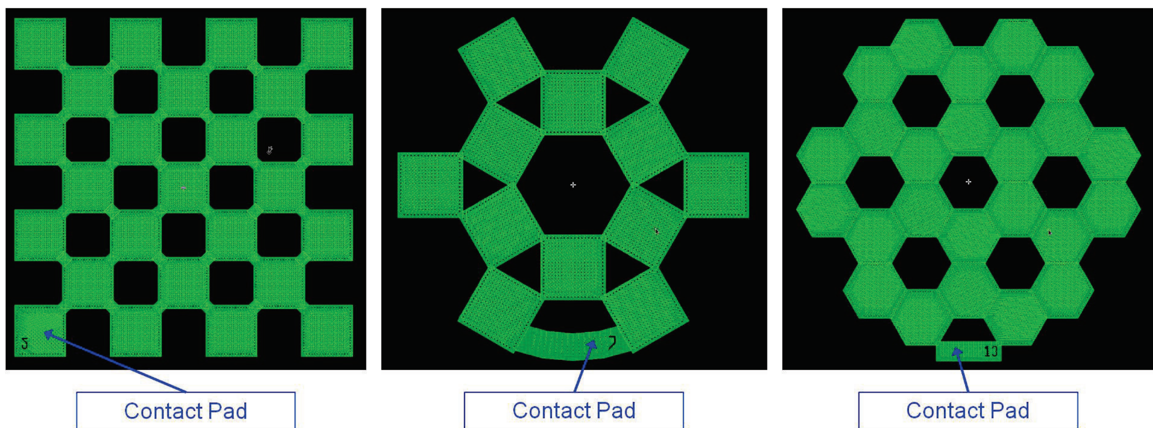

Figure 2-19: Layout of different designs of UJA – (Left to Right) Checkerboard pattern, dream catcher pattern and honey comb pattern. Green areas are U-JETs while the black areas are jet holes.

2.7 Dual Cavity Design

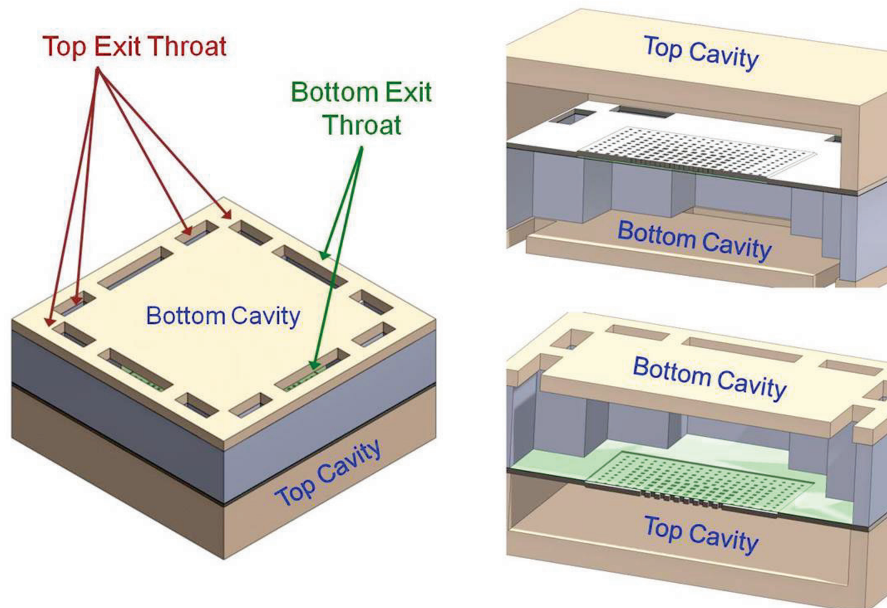

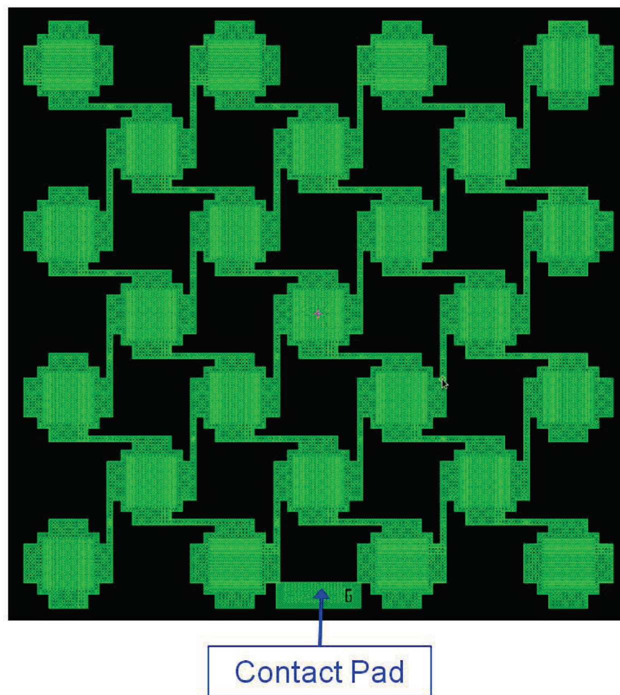

Figure 2-20: Dual cavity design. (Top) 3D-illustration of the dual cavity U-JET design, and (Bottom) Layout of dual cavity design where green areas are the U-JETs and the black areas are the jet holes. The U-JETs are connected in a crab-leg manner to reduce damping due to connection sidewalls.

Besides the various arrangements of the UJA, another design was included in the fabrication. A dual cavity U-JET design is proposed where the diaphragm is coupled with Helmholtz cavity on both sides, with the exit throats routed to the same direction, as shown in Figure 2-19(Top). The U-JETs are connected in a crab-leg manner such that the top and bottom air micro-jets experience the same damping effects. This design is expected to produce twice the thrust of a single cavity U-JET design as both sides of the diaphragm are utilized.

2.8 Design Variations for Gen. 2 and Gen. 3

From the optimized parameters listed in Table 2-2, a variation of the designs is drawn on the layout (as shown in Figure 2-20) and fabricated to experimentally investigate the influence of each parameter (Table 2-4). With the simulation results from the optimization with sinusoidal waveform, designs with varying cavity parameters (Table 2-5) are included in the new layout for Gen. 3. This new layout only includes masks to fabricate new cavities and is used to fine-tune the cavity parameters to achieve higher jet velocities and thrust. The detailed experimental analyses of these designs are discussed in Chapter 5.

Table 2-4: Details of the various designs drawn in the layout shown in Figure 2-20 for Gen 2. The blue font highlights the parameter variations from the nominal design of #1.

#	Design	Diaphragm Size	Electrode Hole Size	Cavity	Throat Holes	Diaphragm shape	Actuator arrange shape
1	Nominal_45	1.2 mm	Hole: 30 um Spacing: 45 um	Single	140um x 350um (8) 2.5 ratio	Square	Checker board

#	Design	Diaphragm Size	Electrode Hole Size	Cavity	Throat Holes	Diaphragm shape	Actuator arrange shape
2	Nominal_sq_30	1.2 mm	Hole: 30 um Spacing: 30 um	Single	140um x 350um (8)	Square	Checker board
3	Nominal_45_th4	1.2 mm	Hole: 30 um Spacing: 45 um	Single	140um x 700um (4)	Square	Checker board
4	Nominal_45_thFat	1.2 mm	Hole: 30 um Spacing: 45 um	Single	180um x 272um (8) 1.5 ratio	Square	Checker board
5	Nominal_45_thThin	1.2 mm	Hole: 30 um Spacing: 45 um	Single	100um x 350um (8) 3.5 ratio	Square	Checker board
6	Double_45	1.2 mm	Hole: 30 um Spacing: 45 um	Double	140um x 350um (8)	Square	Checker board
7	Nominal	1.2 mm	Hole: 30 um Spacing: 45 um	Single	140um x 350um (8)	Square	Dream catcher (6)
8	Nominal_oct	1.2 mm	Hole: 30 um Spacing: 45 um	Single	140um x 350um (8)	Square	Dream catcher (8)
9	Nominal_12	1.2 mm	Hole: 30 um Spacing: 45 um	Single	140um x 350um (8)	Square	Dream catcher (12)
10	2mm_Nominal_sq	2.4 mm	Hole: 30 um Spacing: 45 um	Single	140um x 350um (8)	Square	Checker board
11	2mm_Nominal	2.4 mm	Hole: 30 um Spacing: 45 um	Single	140um x 350um (8)	Square	Dream catcher (6)
12	2mm_Nominal_oct	2.4 mm	Hole: 30 um Spacing: 45 um	Single	140um x 350um (8)	Square	Dream catcher (8)
13	Nominal_45hex	1.2 mm	Hole: 30 um Spacing: 45 um	Single	140um x 700um (3)	Hexagon	Honey comb (6) 2 layer

#	Design	Diaphragm Size	Electrode Hole Size	Cavity	Throat Holes	Diaphragm shape	Actuator arrange shape
14	Nominal_ 45hex2x	1.2 mm	Hole: 30 um Spacing: 45 um	Single	140um x 700um (3)	Hexagon	Honey comb (6) 3 layer
15	2mm_ hex	2.4 mm	Hole: 30 um Spacing: 45 um	Single	140um x 700um (4)	Hexagon	Ring (6)

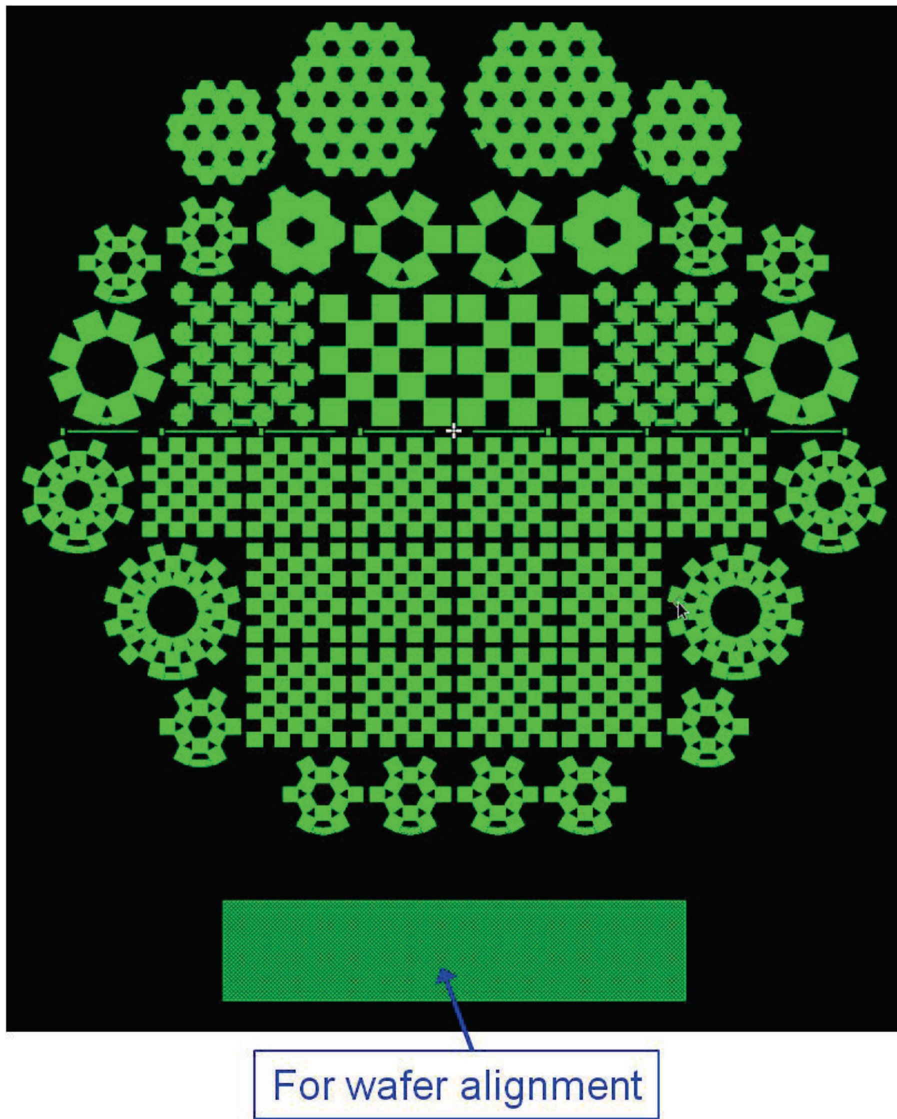

Figure 2-21: Layout of the designs listed in Table 2-4 for Gen 2.

Table 2-5: Summary of the variation of cavities design in Gen. 3 to observe the influence on the actuator's performance.

Design #	Top Cavity	h_T to w_T ratio	h_T x w_T
Design 1	Vary area A_T	1 to 4 ratio	50 x 200 um^2
Design 2			70 x 280 um^2
Design 3			40 x 160 um^2
Design 4	Vary ratio of h_T to w_T	1 to 3 ratio	60 x 180 um^2
Design 5		1 to 5 ratio	45 x 225 um^2
Design 6	Dream catcher		50 x 200 um^2
Design 7	2 mm diaphragm		50 x 200 um^2
Design 8	Dual cavity design		140 x 350 um^2

2.9 Summary

The U-JET is designed using acoustic streaming theory of a forced Helmholtz resonator. A non-linear structural model, obtained computationally and incorporated with the Navier-Stokes equations, were used to study the response of a high-frequency and large-gap diaphragm actuator. With the detailed design optimization procedures developed for the trapezoidal and sinusoidal waveform, it is found that more realistic parameters were produced where h_T and w_T were varied at the same time while keeping a constant ratio of h_T to w_T. Additionally, the higher rise and fall times of the trapezoidal waveform as well as maximum volume displacement when actuated beyond pull-in will provide for additional momentum and larger response of the diaphragm, leading to higher thrust output. The frequency response obtained using the trapezoidal waveform at voltages beyond pull-in shows a single distinct peak with high thrust which is related to the resonance of the Helmholtz cavity. The peak thrust obtained for the trapezoidal waveform is much higher than the peak thrust obtained with a sinusoidal waveform.

Although the theoretical results showed the possibility of achieving high thrust performance, the expected thrust produced by the fabricated device might be much lower because other damping and non-ideal effects were not incorporated in the modeling effort. Additional thoughts and designs are included in the design of the U-JET to optimize the components that were not included in the coupled system modeling such as the perforations on the rigid electrode and the arrangements of the U-JETs in the UJA which allows for flow entrainments. The perforations on the rigid electrode are designed such that the air damping in the electrostatic gap is low while maintaining reasonable electrostatic force. Various U-JET arrangements in the UJA are proposed to investigate the properties of flow augmentation.

With the optimized design parameters, a nominal design is chosen as the most promising design that will produce high thrust performance. Other design variations are included in the layout to investigate the influence of each design parameters on the thrust performance. Now, with the designs for high-thrust UJA, the next step will be developing fabrication technologies that can manufacture the desired parameters for the UJA.

CHAPTER 3

DESIGN AND FABRICATION OF FILLETED ELECTRODE USING PHOTORESIST SOLVENT REFLOW

3.1 Introduction

As presented in Chapter 2, the ultrasonic jets (U-JET) consist of an enclosed acoustic cavity and a diaphragm actuator that can modulate the air volume inside the cavity at high speed. The diaphragm is electrostatically actuated with a parallel-plate configuration and is fully clamped on all four edges of the square diaphragm (a fully-clamped diaphragm). From theoretical calculations, the high performance U-JET requires high frequency and large deflection of the diaphragm which means large electrostatic gap, but this leads to multiple challenges in the fabrication process. In this chapter, the fabrication challenges related to the yield and reliability of the diaphragm actuator (main component of U-JET) are addressed with the design of a filleted electrode using a photoresist solvent reflow process. The design of filleted electrode is introduced here and more details will be discussed in the following.

3.1.1 Background

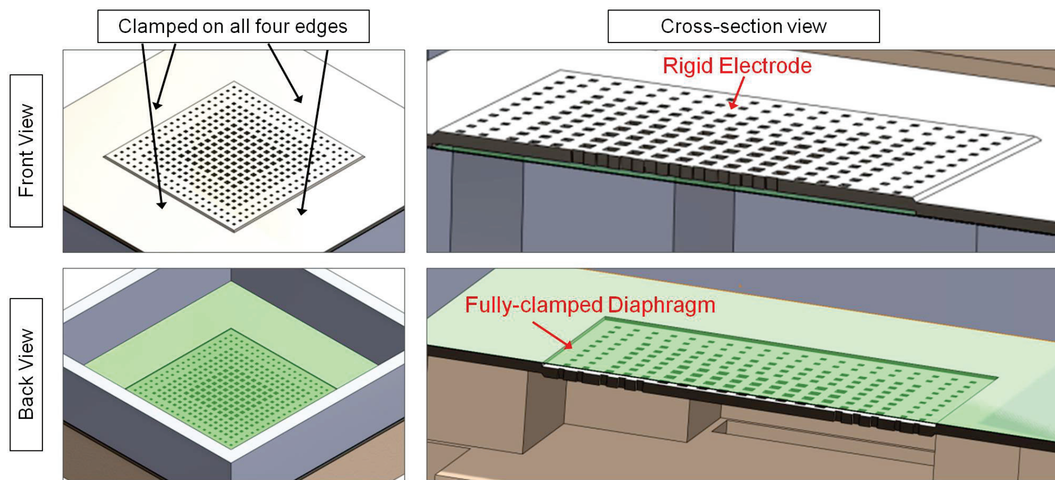

Figure 3-1: An example of a fully-clamped diaphragm. For electrostatic actuation, the main components are two parallel plates consisting of a rigid electrode and a suspended fully-clamped diaphragm, separated by an electrostatic gap.

Fully-clamped diaphragms (Figure 3-1) are used in various applications such as micro-fluidics, gas micro-pumps, micro-valves, and micro cooling. The fully-clamped diaphragms have large pumping force and great sealing capabilities. Fully-clamped diaphragm actuators ensure that all fluid is transferred in the same direction as the diaphragm movement and provide segregation between chambers of fluids. In most applications, a large volume displacement (~ 10 µm) at high frequency (~ 100 kHz) is a desired characteristic for generating a high volume flow rate and high thrust or pressure.

There are multiple ways to actuate a fully-clamped diaphragm. Examples include electrostatic actuation using a parallel-plate or zipper configuration [30], [41], [42], electromagnetic [34], piezoelectric [37], and thermo-pneumatic [63] actuation. Electrostatic actuation offers multiple advantages over the other actuation methods such as easy miniaturization for small size and weight, low power consumption, and large

deflection relative to diaphragm thickness. For electrostatic actuation, the main components are two parallel plates consisting of a rigid perforated electrode and a suspended diaphragm, separated by an electrostatic gap. The electrostatically actuated fully-clamped diaphragms are divided into two main configurations: parallel plate (flat or filleted electrode) and zipper (curved electrode) configuration. For a parallel plate configuration (Figure 3-2), the diaphragm is pulled in from the center because this is where the mechanical restoring force is lowest. For the zipper configuration, the diaphragm is zipped or collapsed from the edges towards the center because the electrostatic force is close to infinity due to the near-zero gap at the edges of the zipper electrode.

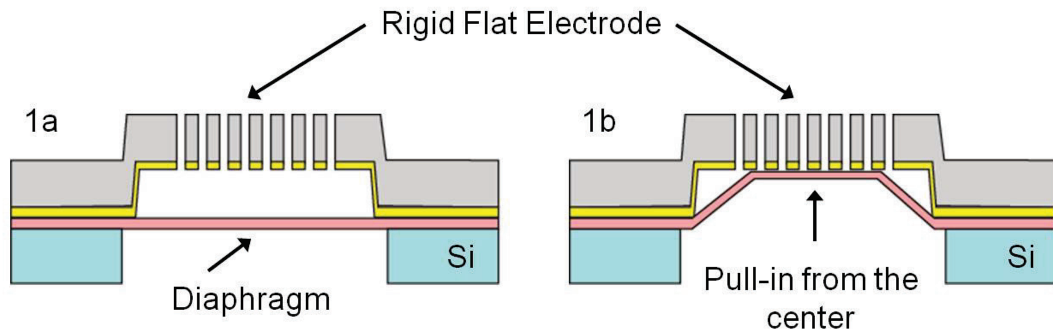

Figure 3-2: Cross section of parallel-plate configuration for flat electrode design. Diaphragm pulls in from the center.

Electromagnetic actuation can generate large actuation force but at the cost of size and power. Miniaturizing electromagnetic actuators is a challenge as the electromagnetic force reduces with 1/radius^2. Piezoelectric actuation can be a great alternative to electrostatic actuation because the perforated rigid electrode can be omitted in the design and simplifies the structure of the actuator; however, integration of high quality

piezoelectric materials with other MEMS structures can be challenging [64]. Thermo-pneumatic actuation could generate large force but is limited to low frequency operation which is not suitable for this application.

3.2 Main Challenges

There are two main challenges to the reliable actuation of a high-frequency and large-deflection diaphragm: the mechanical fracture of the diaphragm due to the increase in the flexural rigidity at large deflection, and charging issues or electrical breakdown of air and dielectric layers due to high-voltage application across a large electrostatic gap. In the design of a reliable diaphragm, the maximum residual stress of the diaphragm is chosen conservatively to be less than 100 MPa. The residual stress and the flexural rigidity due to large deflection have to be at least one or two orders of magnitude lower than the yield strength of the diaphragm material to ensure good reliability.

There are two scenarios where the diaphragm can fracture during or after pull-in occurs. In the first scenario, the tightly stressed diaphragm breaks before complete collapse onto the rigid electrode due to the increase in the flexural rigidity during large displacement and bending. If the diaphragm can sustain the stress from the large bending and can fully collapse at the center onto the rigid electrode, the second scenario of fracture may occur. When higher than pull-in voltage is applied, the area of full collapse expands and the deflection angle, θ, increases (as shown in Figure 3-3), causing breakage at the sharp edges. When there are arrays of diaphragm actuators actuated in parallel, the second scenario becomes particularly relevant because the application of higher than

pull-in voltage is inevitable with the manufacturing non-ideality and the slight variation of the electrostatic gap heights.

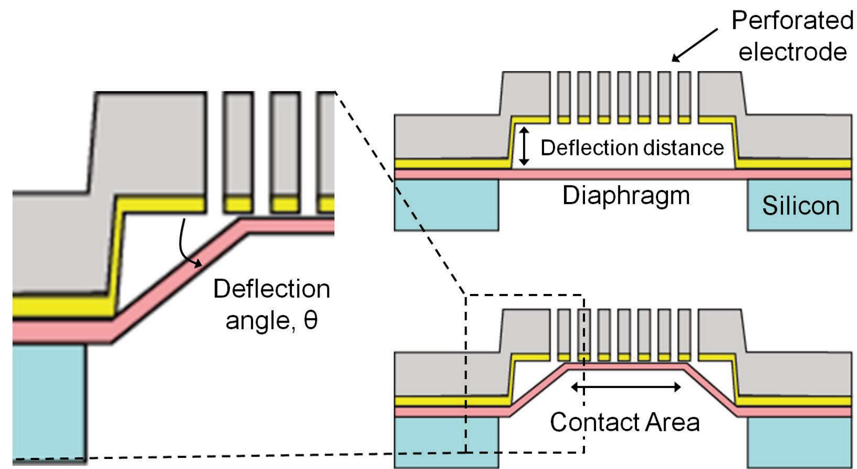

Figure 3-3: Reliability depends on the deflection angle, deflection distance and the contact area. Illustration based on flat electrode design.

The second reliability issue is associated with the charging effect and the electrical breakdown of the dielectric layers. Charge buildup in the dielectric layer occurs when the discharging time constant is longer than the time when the voltage is turned off. This can be observed as a direct current (DC) drift in the applied voltage, and after some time, the amplitude of the oscillations decreases as the charging effect increases. The discharging time increases when high voltage is applied and when the charges have to discharge through thick layers of dielectrics. When sufficient charge accumulates, the diaphragm is held onto the electrode without any voltage applied (stiction) and zero output is observed. If voltage is applied after stiction occurs, the dielectric layers are constantly under high electrical stress and eventually the dielectric breaks down, causing electrical shorts and permanent actuator damage.

Most previous works show the possibility of deflecting diaphragms at large distances (> 100 µm) under pneumatic loads but only a couple of works show large deflections of up to 18 µm with applied voltage. There are multiple interesting methods used to lower the spring constant of the diaphragm to achieve large deflection actuation or reduce the required pull-in voltage such as corrugated diaphragms [65], stacked multi-electrodes [66], zipper electrodes [67], [68], and curved electrodes [42]. Literature shows diaphragm deflections as high as 18 µm [68] but at static or DC actuation. Diaphragm deflection of ~ 9 µm at 70 kHz was achieved with a curved electrode by Kim *et al*. [42]; however, long term reliability remains an issue. The diaphragm with curved electrodes will start zipping from the edges towards the center with increasing applied voltage. As the zipping proceeds towards the center, the clamped boundary of the diaphragm is reduced. The reduced boundary increases the strain in the diaphragm. If this strain is greater than the yield strength of the material, the diaphragm fractures, as mentioned in [42].

Here, we propose the design of a filleted electrode that can achieve large deflection and be operated reliably at high frequency without diaphragm breakage, addressing both mechanical and electrical reliability issues.

3.3 Filleted Electrode Design

Chamfering is a well-known way to reduce mechanical stress when two surfaces contact. In MEMS, smoothed or rounded corners on electrodes produce actuators with enhanced reliability. For example, cantilever beam electrodes with rounded corners, which alleviate stress concentration in magnetic actuators, are fabricated using reflow of

phosphosilicate glass in [69], and metal bridges for capacitive radio frequency MEMS switches are made with reflow of sacrificial photoresist to reduce mechanical fracture of the bridges in [70]. In this work, a filleted electrode design is introduced for the first time. For electrostatic actuators, creating curvature or filleting of an electrode can decrease the susceptibility to mechanical fracture as well as reduce the pull-in voltage compared to a flat electrode, reducing the total power consumption.

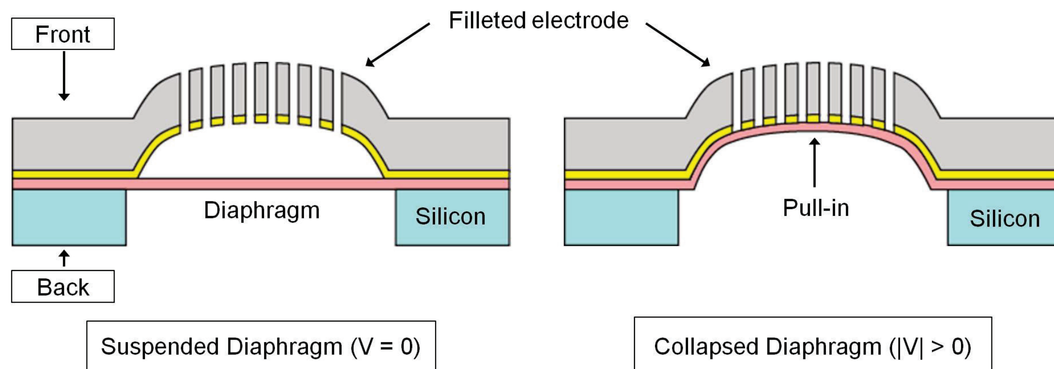

Figure 3-4: Cross section of a single actuator with filleted electrode. When there is no voltage, the diaphragm is in a released or suspended position. When voltage is applied, the diaphragm is collapsed onto the perforated filleted electrode, achieving ~ 100 % volume displacement.

Figure 3-4 shows the cross section of the filleted electrode where the corners of the flat electrode are rounded. Filleted electrodes were designed to maximize volume displacement and improve the reliability of the large-gap electrostatic actuator by reducing the large electric field and mechanical stress at the edges of the diaphragm.

3.4 Fabrication Process

This sub-section includes the fabrication process to manufacture a high-frequency and large-deflection diaphragm with filleted electrode. First, the materials selection for

the diaphragm is discussed. Next, the fabrication process flow as well as the characterization of photoresist solvent reflow process is described.

3.4.1 Materials Selection for High-Frequency and Large-Deflection Diaphragm

Selection of the appropriate materials for the fully-clamped diaphragm is important because the material properties affect the mechanical and electrical performance. The diaphragm can be a composite of polymers, silicon dielectrics and/or metals, each having different residual stresses and electrical breakdown properties. As shown in Equation 2.7, the residual stress controls the mechanical restoring force and the resonant frequency in the diaphragm. A higher residual stress increases the resonant frequency of the diaphragm, resulting in a higher actuation voltage needed to overcome the mechanical restoring force. Therefore, in order to design a diaphragm with a resonant frequency of > 90 kHz, silicon oxide-nitride-oxide having a residual stress of < 100 MPa are chosen due to the ease in fabrication and high electrical breakdown properties.

3.4.2 Fabrication Process Flow

The fabrication process to create the high-frequency diaphragm and flat or filleted electrode is a simple, robust, and high yield process. Figure 3-5 summarizes the fabrication process flow for the filleted electrode design for Gen. 1. The fabrication process for a flat electrode differs from that of the filleted electrode in that the photoresist reflow step is not included when fabricating the flat electrode. First, an oxide-nitride-oxide diaphragm of total thickness ~ 1.75 μm with residual intrinsic stress of 74 MPa is LPCVD-deposited on a double-side polished silicon wafer.

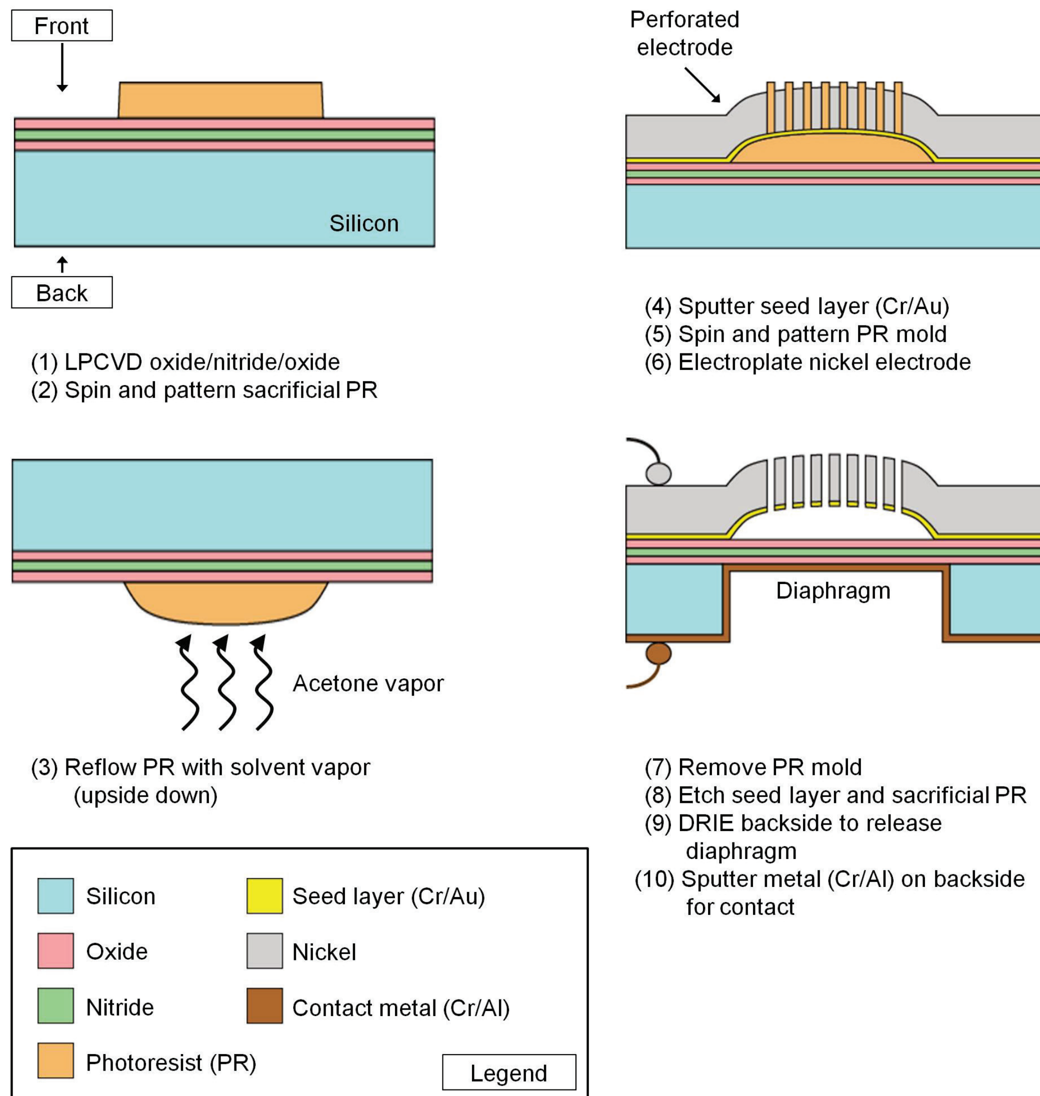

Figure 3-5: Summary of the fabrication process flow for filleted electrode design. It is a 3-mask process. Fabrication process for flat electrode is similar except photoresist reflow step is skipped.

Next, a layer of sacrificial photoresist (AZ 9260) is spun and patterned. For the filleted electrode design, the sacrificial photoresist is reflowed in acetone vapor. More details of the reflow process will be discussed in next sub-section. The initial thickness of the sacrificial photoresist is different for flat and filleted electrode design although the target final electrostatic gap is the same. For the flat electrode design, the initial

photoresist thickness should be ~ 2 μm greater than the target final gap. This is because there will be a second lithography step to create the electroplating mold and the baking step during lithography shrinks the thickness of the sacrificial photoresist. For the filleted electrode design, the initial photoresist thickness should be ~ 2 μm less than the target final gap. The discrepancy of this thickness with the flat electrode exists because of the additional reflow process. Although the filleted electrode goes through similar baking steps in the second lithography (shrinking by ~ 2 μm), the reflow process increases the height of the photoresist by ~ 4 μm as the photoresist from the edges reflows towards the center into a dome-like shape, increasing the center thickness.

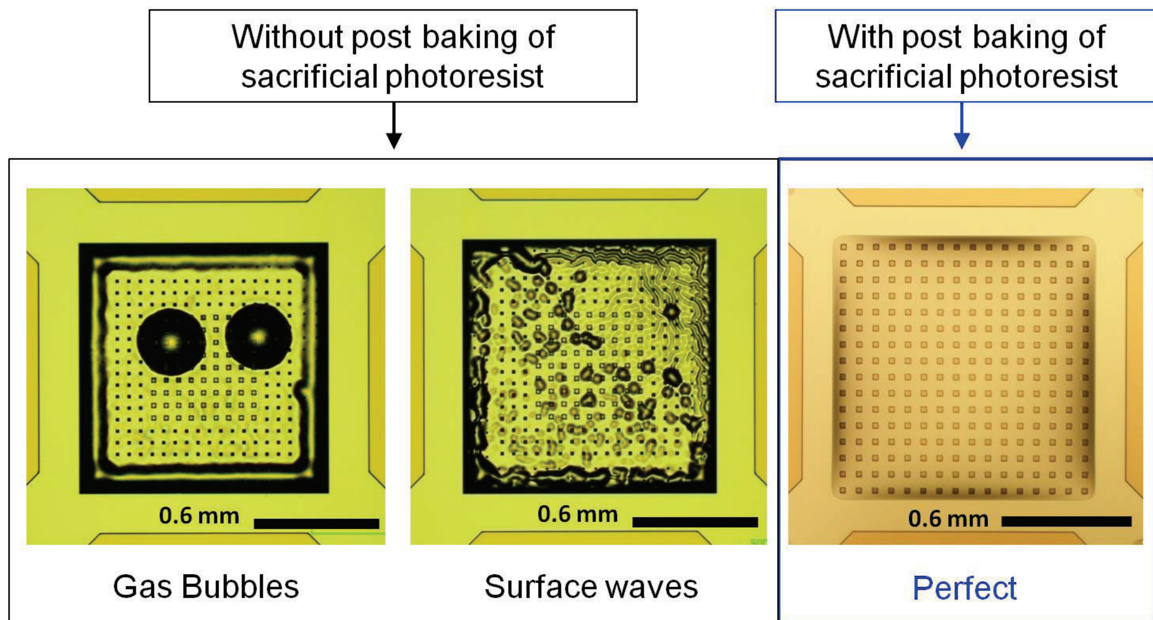

Figure 3-6: (Left two images) Gas bubbles and surface waves occurs when no post baking is performed, and (Right) Smooth surface observed when post baking of the sacrificial photoresist is performed.

After the reflow process, the photoresist is hard baked in an oven at 135°C for 30 minutes to ensure thermal stability of the photoresist. Without the post-hard bake step,

thermal instabilities such as gas bubbles or surface waves can appear on the seed layer during the following second lithography step, compromising the smooth surface achieved by the reflow. With a post-baking step, the profile of the sacrificial photoresist with plating mold is very smooth, making it suitable for the subsequent electroplating step (Figure 3-6).

Next, a thin metal seed layer of chrome/gold is sputtered over the sacrificial photoresist and a second lithography layer (> 25 µm thick AZ 9260) for the electroplating mold is patterned on top of the reflowed structure. Normally, AZ 9260 spun at 2 krpm with spreading step of 4 seconds and spinning step of 30 seconds will create a ~ 10 µm thick photoresist. To create a > 25 µm thick photoresist, two layers of AZ 9260 are needed, requiring two baking steps. In order to minimize the amount of baking, spinning one layer of thick AZ9260 is desired but if the spin speed is reduced to lower rates for higher thickness, there are many bubbles in the photoresist after spinning. It is recommended by [71] that instead of reducing the spin-rates, it is better to reduce the spinning time such that there are no bubbles. The AZ 9260 is spun at the same speed of 2 krpm but with no spreading step and 3 seconds of spinning step. A ~ 23 µm to 25 µm thick photoresist is obtained. With these settings, the AZ 9260 has no bubbles after spinning but the downside is that the thickness uniformity might be compromised. Since the photoresist is a plating mold, as long as the thickness is greater than the desired plating thickness, the uniformity of the photoresist will not affect the process.

Subsequently, plating of nickel with low current density of 10 mA/cm^2 is performed to form low stress nickel electrodes that take the form of the reflowed

photoresist underneath, molded by the photoresist of the second lithography. Although the plating rate is very slow for the low current density (0.12 μm/min), the electroplated nickel of ~ 18 μm has low residual stress of < 5 MPa, which is desired. Nickel is chosen as the material for the rigid electrode because it has low residual stress after plating but there is a trade-off. Electroplated thick nickel electrode, with the suspended structures designed in this work, is very sensitive to elevated temperature (> 100 ^{o}C for longer than 1 hour). Any successive steps after the plating which involves high temperatures will make the nickel electrode buckle as it shrinks.

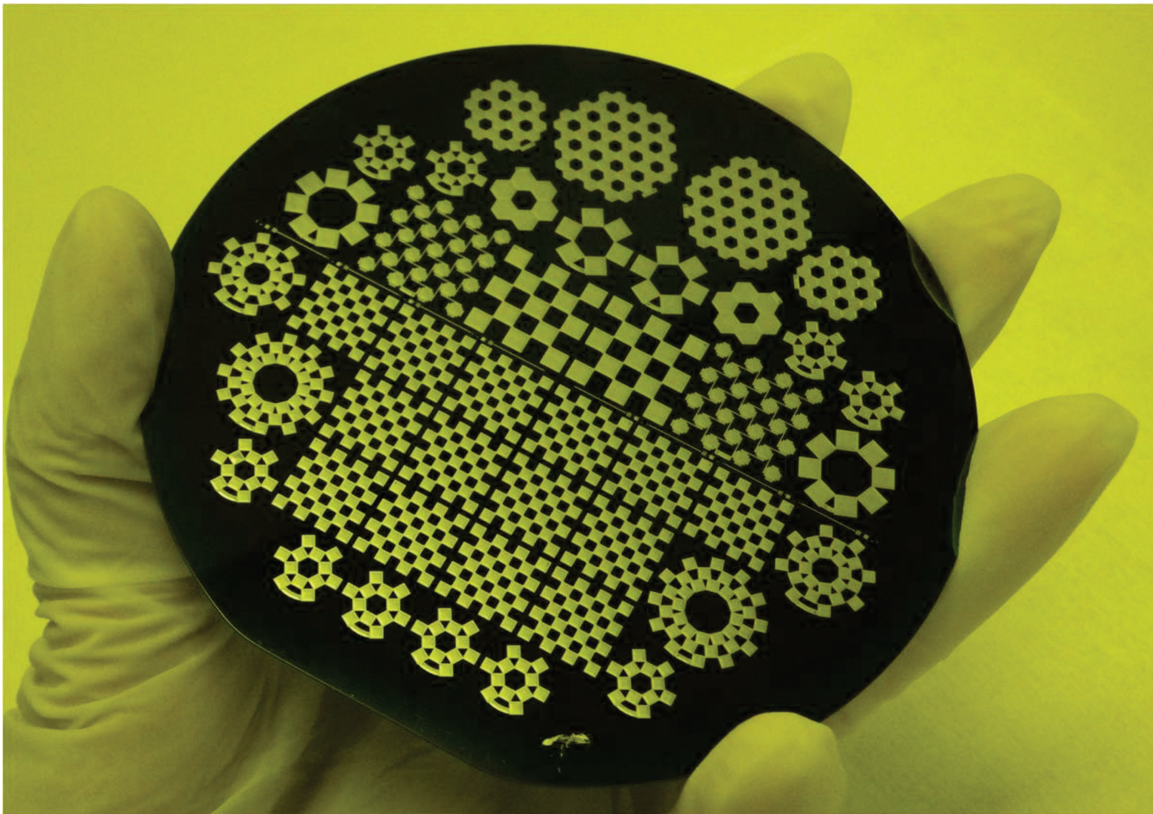

Figure 3-7: Electroplated nickel on a wafer for Gen. 2 layout. On the wafer, the dark areas are the areas for the jet holes while the light areas are the areas with electroplated nickel.

Figure 3-7 shows the electroplated nickel on a wafer for Gen. 2 design. On the wafer, the dark areas are the areas for the jet holes while the light areas are the areas with electroplated nickel. After electroplating, the photoresist mold is removed with acetone and rinsed with isopropyl alcohol and deionized (DI) water. The wafer is left in the DI water and transferred directly without drying to the gold etchant to remove the seed layer. The gold etchant, GE 8148 (Transene Company, Inc., Danvers, MA), is used to etch gold instead of the common TFA solution (Transene Company, Inc., Danvers, MA) because it does not attack nickel, and chromium etchant, CR-14 (Cyantek Corporation, Fremont, CA), is used to etch the chromium. At this point, the sacrificial photoresist is still there, covering the diaphragm material beneath the electroplated nickel, and the only exposed area is that of the jet holes (dark areas on wafer in Figure 3-7). Reactive ion etching (RIE) of oxide-nitride-oxide is performed to remove the dielectric layers in the jet holes area, with the nickel electrode and the sacrificial photoresist acting as a mask to protect the diaphragm area. Then, the sacrificial layer is removed by soaking in PRS 2000, acetone, and isopropyl alcohol for greater than one day. The rinsing step is important to ensure no particles remain in the electrostatic gap.

The diaphragm is then released through a backside deep reactive ion etch (DRIE). The DRIE step is the determining step for the yield of this process because many diaphragms fracture during this step. For support, the wafer is mounted to a carrier wafer with the suspended nickel electrode facing the carrier wafer. The mounting material used is low-temperature crystal bond (Crystalbond™ 555, Electron Microscopy Sciences, USA-Hatfield, PA) because it has better thermal conduction properties compared to

photoresist and it dissolves in water. The etching recipe and the mounting method is the key to a successful DRIE etch. As mentioned before, the electroplated nickel electrode is very sensitive to temperature. If the wafer does not have good thermal conduction to the cooling system of the DRIE tool or if high-power plasma etch recipe is used, the wafer's temperature will increase and the nickel electrode will buckle, as shown in Figure 3-8.

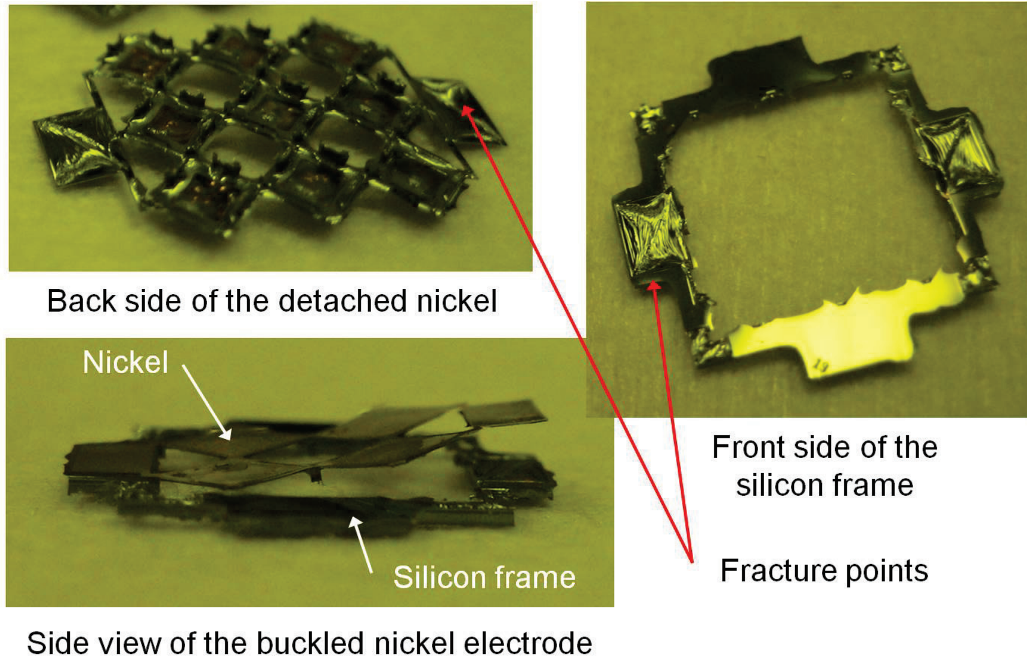

Figure 3-8: (Top left) View from the back side of the detached nickel, (Top right) View of the front side of the silicon frame, and (Bottom left) Side view of the buckled nickel electrode.

The crystal bond has to fill the entire gap between the suspended perforated nickel electrode and the diaphragm without any trapped gas pockets to ensure good thermal conduction. The gas pockets create localized thermal insulation and when the thin diaphragm is released by DRIE, it will crack when the trapped gas pockets expand due to the localized temperature rise from the ion bombardment, as shown in Figure 3-9. Hot plate heating alternated with vacuum environment treatment is used to reduce or

eliminate the gas pockets in the gap. First, with the wafer on a hot plate, the crystal bond is melted and flowed into the air gaps through the nickel perforations. Then, the wafer is put under vacuum for 10 minutes to remove gas pockets. Bubbles can be observed surfacing through the thick crystal bond. The process of melting more crystal bond and placing the device under the vacuum jar to remove the gas pockets can be done multiple times until no more bubbles are observed.

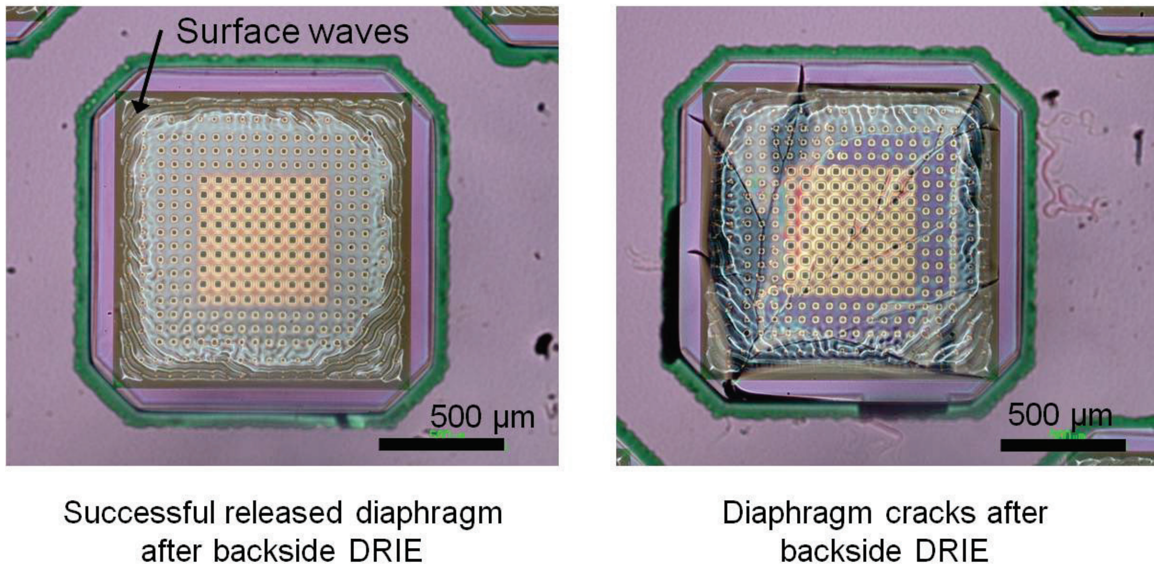

Figure 3-9: (Left) Successful released diaphragm after backside DRIE step and (Right) Diaphragm cracks after backside DRIE. The diaphragms are made out of silicon oxide-nitride-oxide and are transparent. The surface waves seen here are similar to Figure 3-6.

The trade-off of the lower power silicon etch recipe used is that it is not be optimized for producing vertical sidewalls. Greater under-cut and non-uniformity is observed in the DRIE etch. Devices on the outer ring of the wafer etch faster than those at the center. It is also observed that if the DRIE etch continues after the diaphragm is completely released with the transparent film exposed to the bombardment of the ions,

the diaphragm has the tendency to fracture as not all gas pockets can be eliminated. This can be avoided if Kapton® tape is used to manually mask the parts where the diaphragms are released by slowly closing in on the area from the outer ring towards center. The yield of the process can be increased from 10 % to greater than 64 % and the under-cut can be reduced in the device with this manual masking method.

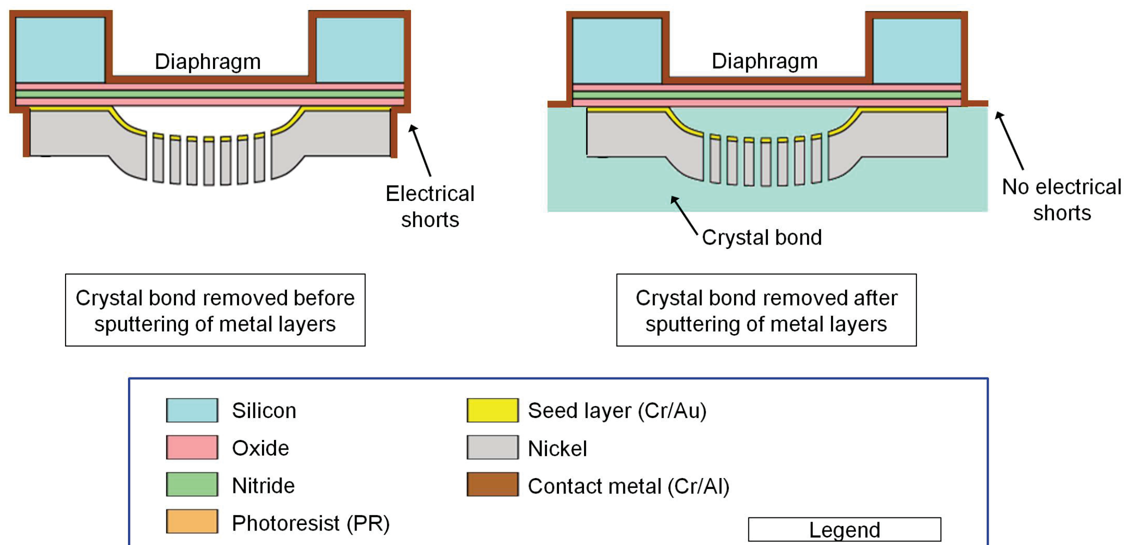

Figure 3-10: Illustration to show electrical shorts happening if crystal bond is removed before sputtering of metal layers. (Left) Crystal bond removed before sputtering of metal layers and (Right) Crystal bond removed after sputtering of metal layers.

Finally, a chromium/aluminum layer is sputtered on the diaphragm from the backside for electrical connections. For Gen. 1, the devices are released from the carrier wafer into individual pieces by removing the crystal bond. The devices are dried with critical point drying before the chromium/aluminum layer is sputtered. The benefit of doing this is that the photoresist mask for DRIE can be cleanly removed with solvents but the disadvantage is that electrical shorts between the nickel electrode and the diaphragm

might occur during the sputtering of the metal layers, as shown in Figure 3-10(Left). Therefore, for Gen. 2 and Gen. 3, the photoresist mask for the DRIE is removed using a RIE oxygen plasma etch and metal is sputtered before individual devices are released in DI water and dried. This method can reduce or eliminate the electrical shorts in the devices due to sputtering, as shown in Figure 3-10(Right); however, if the RIE step does not remove the photoresist mask completely, some remains of the mask residue might lift-off the sputtered metal. This creates an electrical open-circuit among the diaphragm actuators, as shown in Figure 3-11.

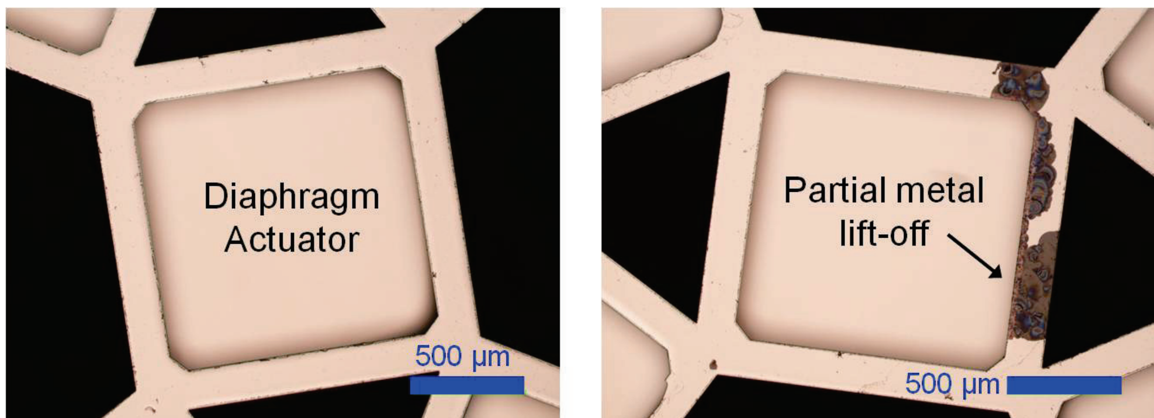

Figure 3-11: (Left) A diaphragm actuator with perfect metal coating on backside and (Right) Partial metal lift-off due to incomplete photoresist mask removal.

The high residual stress diaphragms allow the diaphragm actuators with 1.2 mm by 1.2 mm diaphragm size to be dried on a hotplate while larger diaphragms have to be dried with the critical point dryer to avoid stiction. Detailed recipe for the fabrication process is attached in Appendix B.

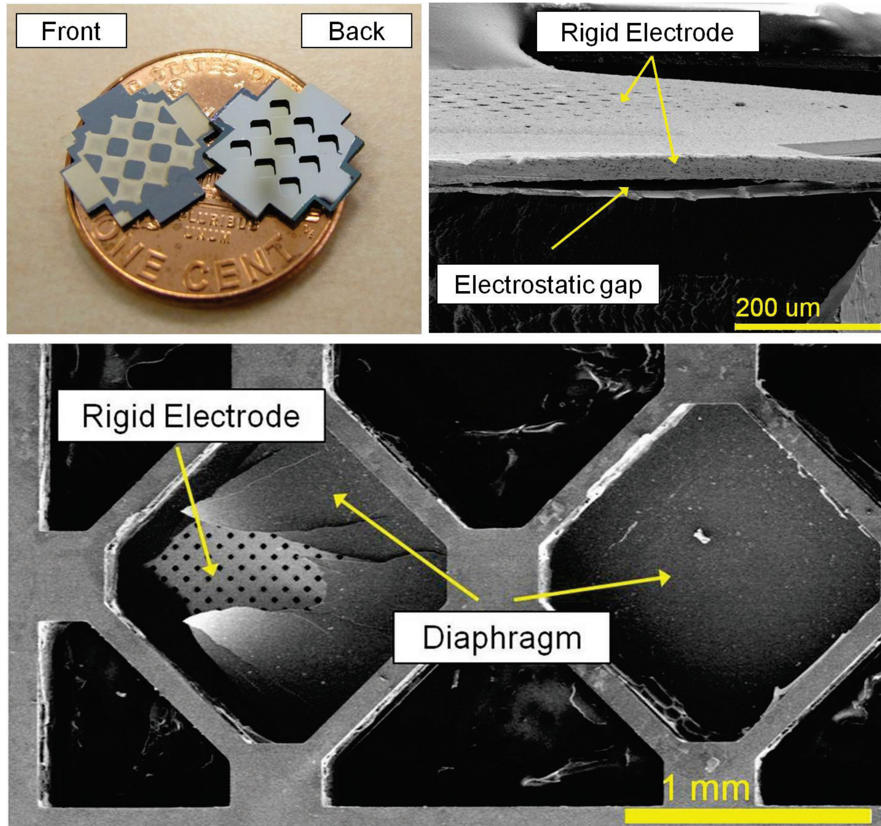

Figure 3-12: (Top Left) Microfabricated array of nine diaphragm actuators for Gen. 1 without jet holes etched, (Top Right) SEM of the cross-section and (Bottom) SEM image showing the diaphragm actuators. The tearing of the diaphragm is intentional to show the rigid electrode.

Figure 3-12 shows the prototype of 9 diaphragm actuators in Gen. 1 and the scanning electron microscope (SEM) images of the cross section and backside view of the diaphragm actuators. The fabricated design parameters are listed in Table 3-1 for both flat and filleted electrode.

Table 3-1: Summary of fabricated design parameters for diaphragm actuators.

Design Parameters	Flat Electrode	Filleted Electrode
Diaphragm resonance frequency	97 kHz	
Diaphragm residual stress	74 MPa	
Diaphragm are (L_M x L_M)	1.2 x 1.2 mm^2	1.3 x 1.3 mm^2
Diaphragm thickness, t_D	1.74 μm	
Sacrificial photoresist height without reflow	8.33 μm	6.2 μm
Average gap at center, h_O		8.14 μm
Applied signal for diaphragm pull-in	(DC) 337 V (AC) N/A	(1 kHz) ± 240 V (10kHz) ± 279 V
Air gap volume (calculated)	11.52 x 10^{-12} m^3	9.7 x 10^{-12} m^3
Volume displaced (calculated)	8.65 x 10^{-12} m^3	9.7 x 10^{-12} m^3

3.4.3 Characterization of Photoresist Solvent Reflow Process

Reflow of photoresist is a straightforward process and can be done thermally by heating at an increased temperature or with solvent vapor, but careful control is needed to achieve the desired shape. Several parameters influence the reflow process such as temperature, surface tension and viscosity of the photoresist, gravity, and substrate surface hydrophobicity. Thermal reflow uses heat to soften the photoresist and surface tension rearranges the photoresist shape to be closer to a hemisphere, in order to minimize the surface energy. Thermal reflow is normally used to change the small surface area and volume of photoresist into small hemispherical bumps (dome-like shape); however, due to the viscosity of the photoresist, a photoresist region with a large surface area (> 1 mm lateral dimension) will have difficulty reflowing thermally.

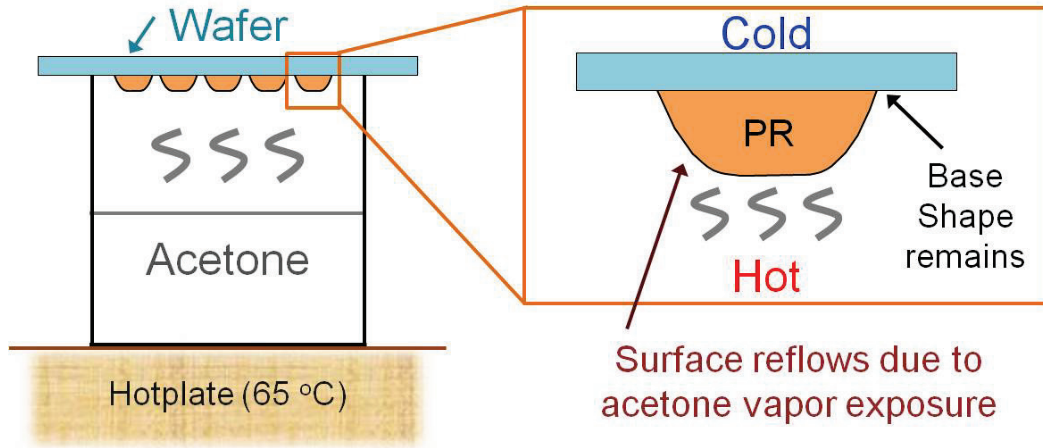

Figure 3-13: Photoresist solvent reflow process. The wafer is flipped upside down and exposed to solvent vapor.

Here, solvent vapor is utilized to reduce the viscosity of the photoresist and enable easier reflow over a large distance. The initial photoresist profile is defined by the lithography pattern and it can be any shape (square, rectangular, hexagonal or circular). With surface tension and gravity both acting on the photoresist (by flipping the wafer upside down during reflow (Figure 3-13)), the initial photoresist shape re-forms itself to be as close to spherical as possible. In this case, the hydrophobicity of the substrate surface can affect the reflow outcome. Surfaces with high hydrophobicity help to create a large angle between the photoresist edges and the substrate surface. Hydrophilic substrate surfaces such as silicon oxide will tend to reflow into a flattened pancake-like shape as shown on the bottom right image (number 4) of Figure 3-14.

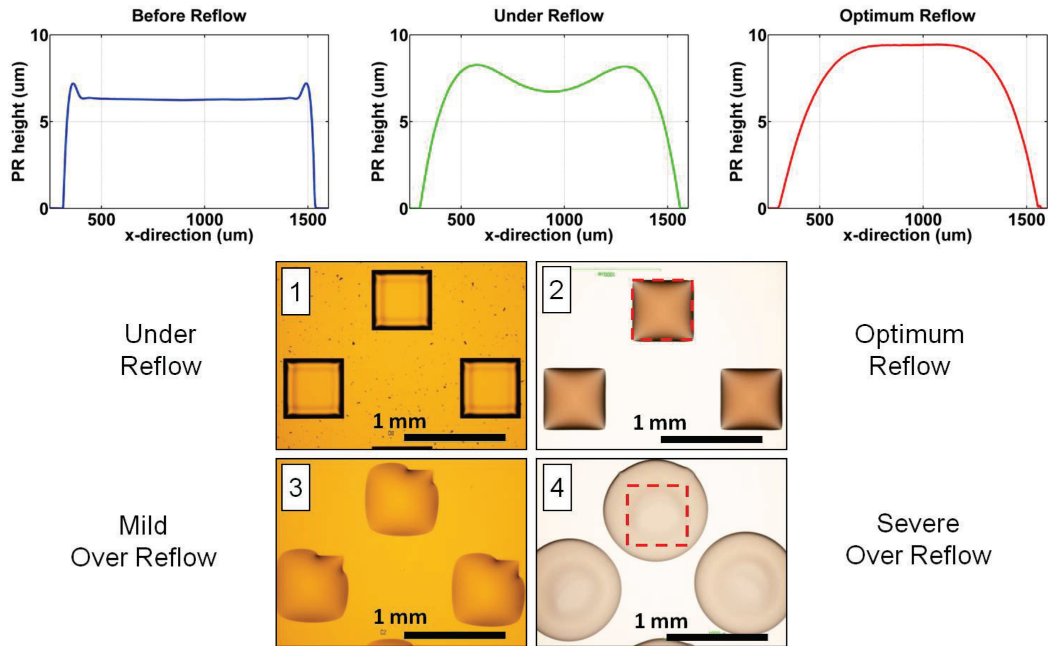

Figure 3-14: (Top plots) Filleted photoresist profile going from left to right: before reflow, insufficient and optimal reflow. (Bottom images) 0.6 mm square diaphragm with (1) insufficient reflow, (2) optimum reflow, (3) mild over reflow and (4) excessive reflow which changes the base shape into a flattened pancake.

One way to avoid this is by pre-baking the photoresist on a hotplate at 150 ºC for two minutes before performing the solvent reflow process. By preheating the substrate, the base of the photoresist absorbs the solvent vapor less than the exposed surface of the photoresist. By controlling the time and temperature as well as the distance between the vaporizing solvent surface and the wafer, an optimal photoresist shape can be realized to create a filleted electrode. The photoresist reflow process can have good uniformity if the size of the photoresist is the same across the whole wafer. In addition, rotating the wafer every couple minutes increases the uniformity of the reflow process. In the future, a

better control of the photoresist solvent reflow process can be conducted in a temperature-controlled oven with solvent environment.

Figure 3-15 presents the SEM images and cross-sections of the fabricated filleted electrodes. Due to the reflow process, the electroplated nickel has low surface roughness (S_a < 0.25 μm), as measured by a confocal laser microscope. In the SEM image showing the cross-section of the actuator, the electrostatic gap is slightly larger because the electroplated nickel detached during dicing. Nonetheless, the nickel electrode, the diaphragm and the silicon cross-sections are clearly observed in the SEM image.

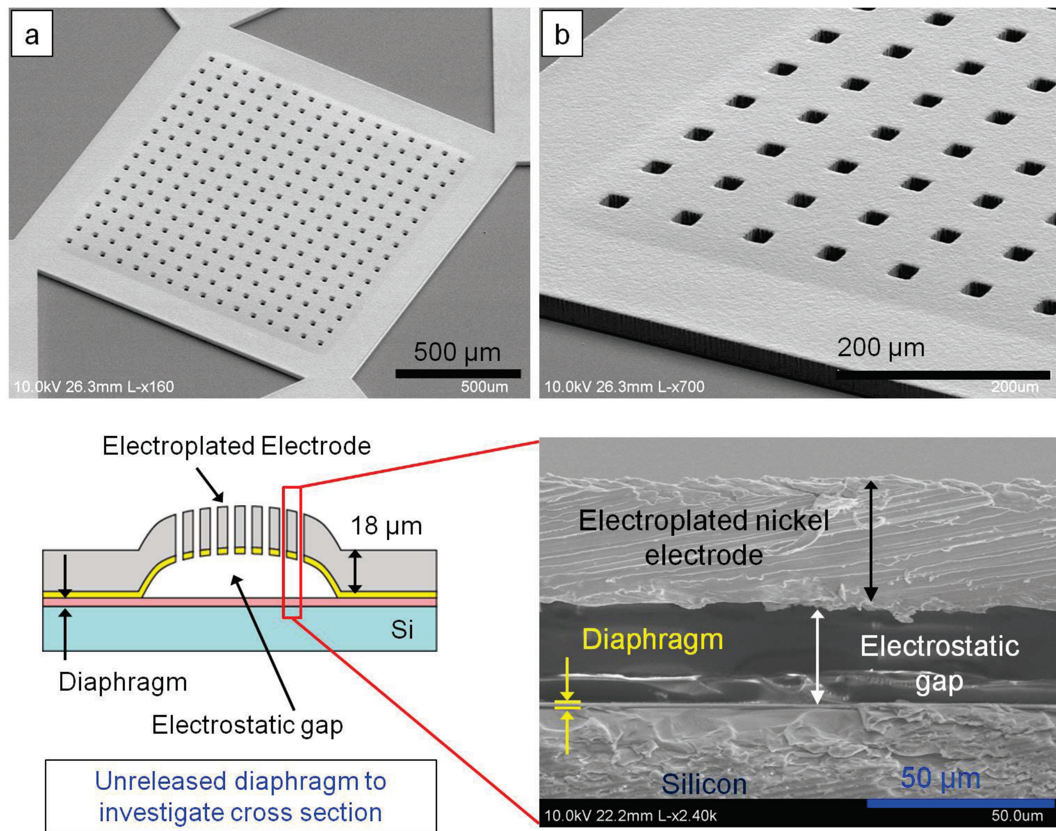

Figure 3-15: (Top images) SEM images of the filleted electrode, and (Bottom) Illustration of the cross section of the actuator with the corresponding SEM image.

Up until now, all literature and previous works only showed a photoresist reflow process on a flat surface; however, the photoresist can also be reflowed on an uneven surface or over a step height. As previously mentioned, a pre-bake of two minutes is recommended to ensure that the photoresist will not reflow out of bound of the base shape. Additional design can be added to ensure this, such as having a ring (an oxide ring in this example) with a step height of 2 μm surrounding the photoresist pattern (photoresist area smaller than the oxide ring), as presented in Figure 3-16. The photoresist reflowed, filling the area and shape defined by the ring.

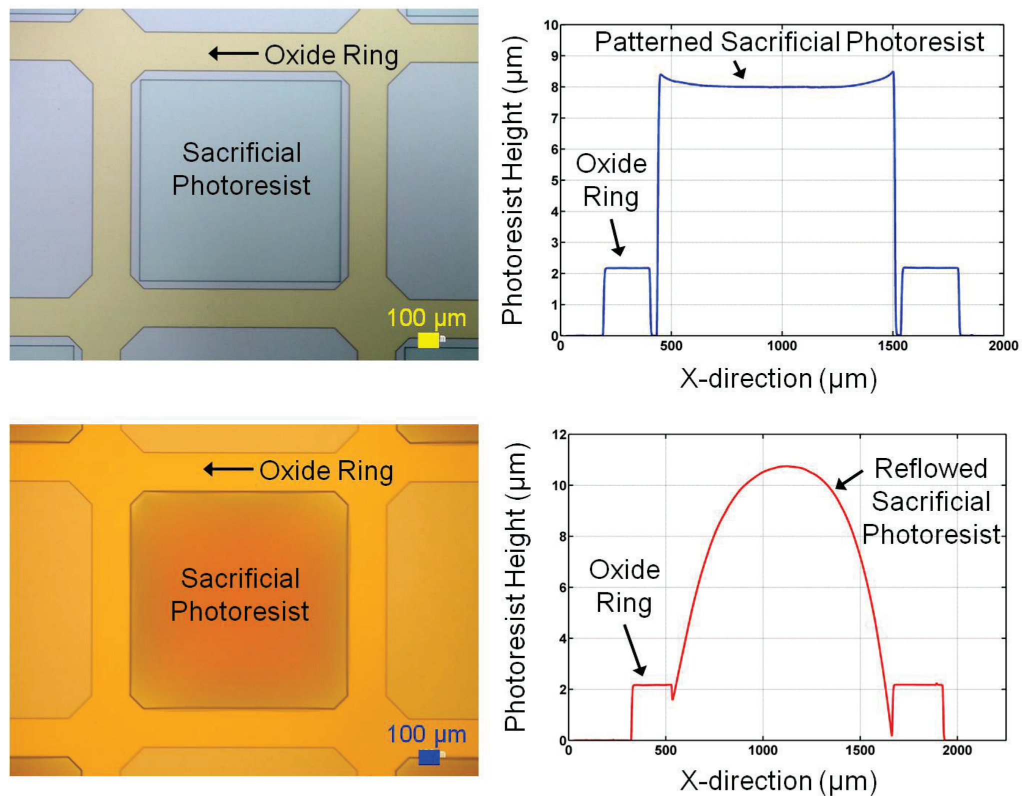

Figure 3-16: Photoresist reflow with additional ring to ensure reflow does not go out of bounds. (Top) Photoresist pattern with 2 μm oxide ring defining the base shape and (Bottom) Photoresist reflowed, filling the base shape defined by the ring into a dome-like form.

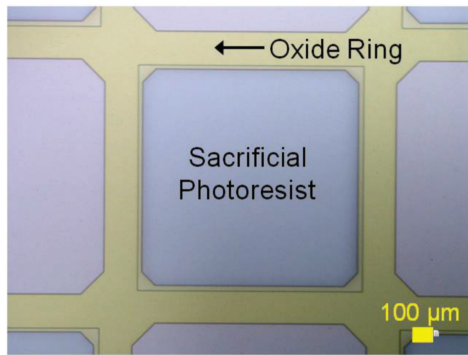

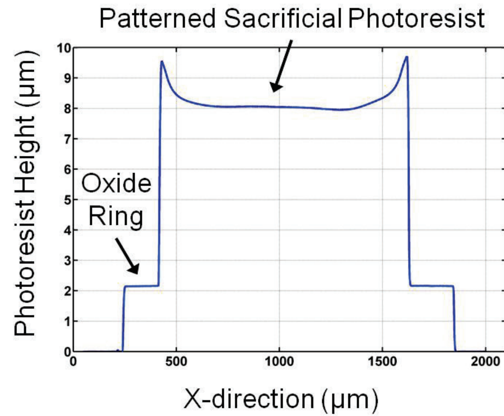

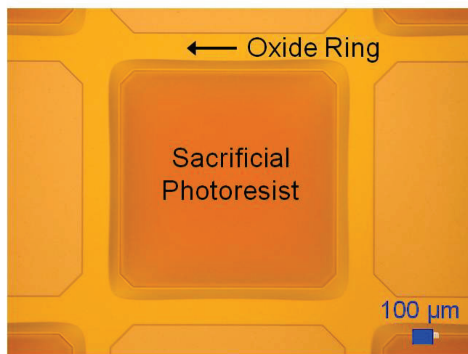

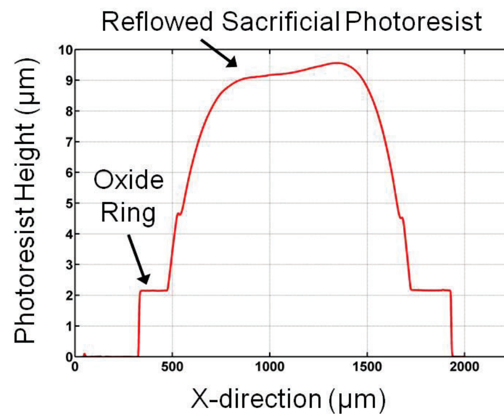

Figure 3-17: Photoresist pattern is larger than the 2 μm oxide ring, showing that photoresist can be reflowed over a step height of 2 μm without going out of bound of the base shape. (Top) Photoresist pattern over a 2 μm oxide ring and (Bottom) Photoresist reflowed into a dome-like form without flowing out of bound of the base shape.

On the other hand, the oxide ring can be used for a different purpose. The oxide ring can be used to enhance the electrical insulation between the diaphragm and the nickel electrode without changing the properties of the diaphragm. A slight overlap between the oxide ring and the edge of the diaphragm is desired to ensure good insulation. Therefore, the pattern of the photoresist is designed to be slightly greater than the area defined by the oxide ring, as shown in Figure 3-17 (Top). Figure 3-17 (Bottom) shows

that it is possible to reflow over a step height of 2 μm and still maintain the base shape of the photoresist. Although the shape is not a perfect dome-like shape as seen in Figure 3-16, further optimization of the process such as increasing the reflow time can be conducted to realize the desired shape.

It is important to note that although the oxide ring as shown in Figure 3-16 can help define the base shape of the photoresist, the oxide ring is not to be used as an alternative to the 2 minutes pre-bake step. Figure 3-18 shows the results of the reflow without the 2 minutes pre-bake step.

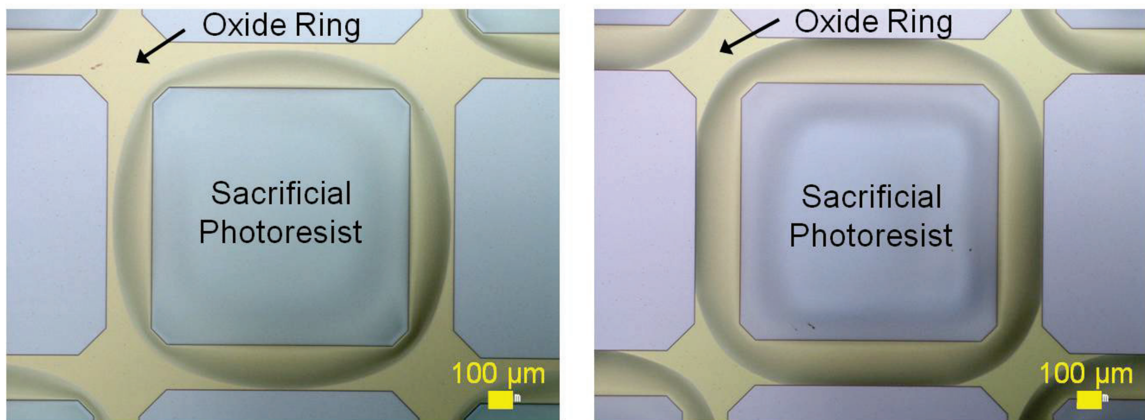

Figure 3-18: The results of the sacrificial photoresist reflow without pre-baking, where the left and right figures correspond to the initial sacrificial photoresist shapes in Figure 3-16 and Figure 3-17 respectively.

3.5 Discussions

With the developed fabrication process for a high-frequency diaphragm with filleted electrode, the performance of the diaphragm actuators are assessed. The reliability of the diaphragm actuator is increased through the manipulation of shape and structure of the actuator and more details will be discussed in the next chapter. Smooth

surfaces and rounded corners are key features of a highly reliable electrostatic actuator. The smooth surfaces and rounded corners can reduce high mechanical stress points at the sharp edges of the diaphragm to reduce fractures. Additionally, the rounded corners can reduce the pull-in voltage and decrease the susceptibility to over-voltage. At the nano-scale, rough surfaces have sharp peaks where the electric field is concentrated, causing dielectric breakdown or sparks in the air (air breakdown).

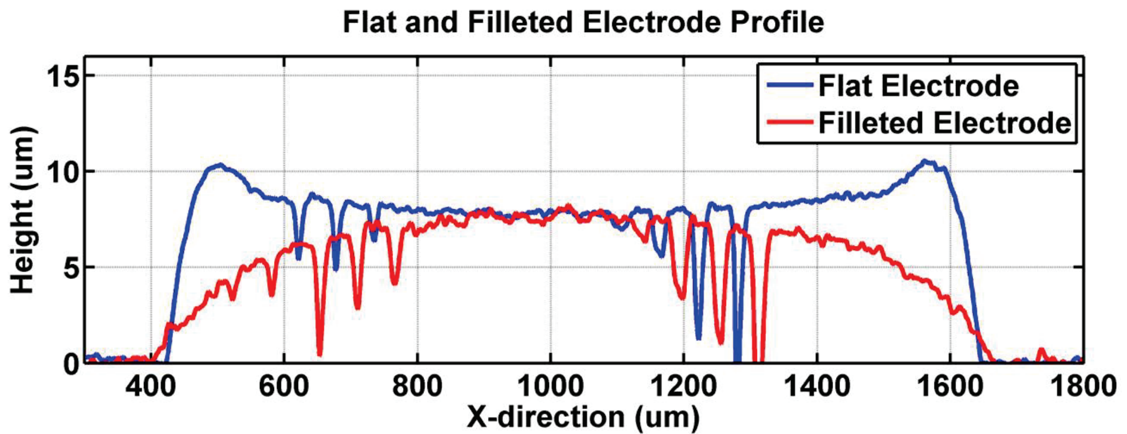

Figure 3-19: Flat and filleted electrode profile measured with DEKTAK profilometer. The two sharp peaks at each edge of the flat electrode are due to the non-ideal lithography process. The dips in the profile are due to the perforations on the electrode as the measurement is made on top of the electroplated electrode.

The profile of the flat and filleted electrode is measured using a DEKTAK profilometer, as shown in Figure 3-19. The surface roughness seen in the figure is due to the oxidation of nickel but this will not affect the performance of the diaphragm actuators because the inner side of the electrode has a seed layer that conforms to the reflowed photoresist and has low surface roughness. The profile is then drawn in COMSOL and the electric field is simulated.

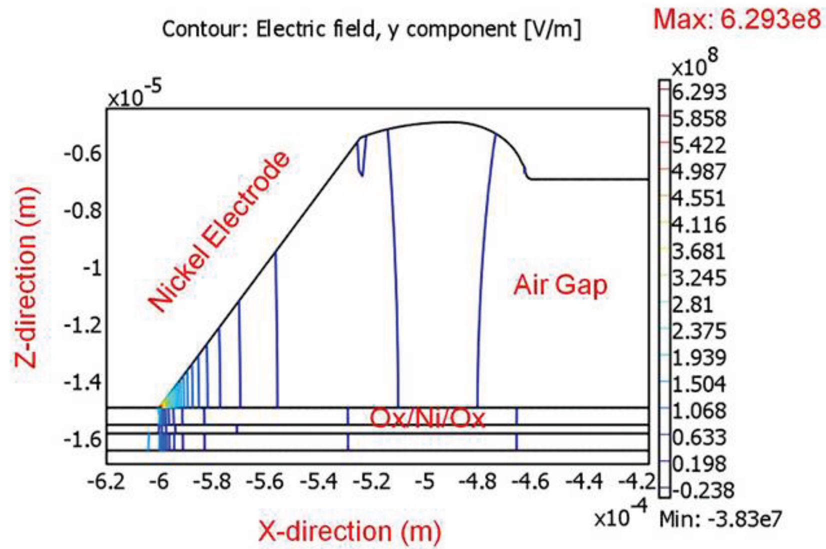

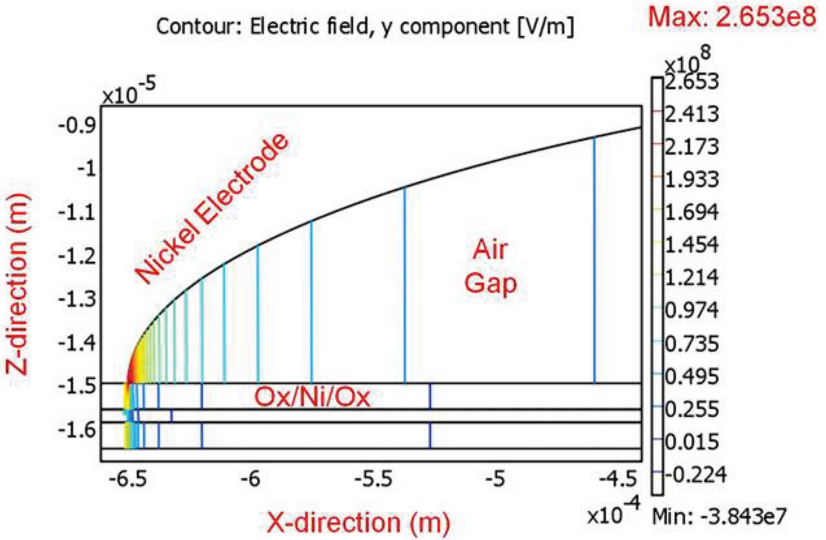

Figure 3-20: Electric field concentration simulated in COMSOL. (Left) Flat electrode has a maximum electric field of $6.293e^8$ V/m, which is higher than (Right) filleted electrode of $2.653e^8$ V/m by 2.4 times with an applied voltage of 200 V. The electrode profile is drawn based on the actual measured profile in Figure 3-19.

From the simulation results in Figure 3-20, the rounded corners of the filleted electrode helped to spread out the electric field concentration at the corners between the diaphragm and the electrode. The maximum electric field for the flat electrode is found to be concentrated near the sharp edges and is around 2.4 times greater than the filleted electrode with an applied voltage of 200 V. As will be shown in Table 4-1 experimentally, the pull-in voltage for the filleted electrode is lower than that of the flat electrode.

3.6 Summary

This chapter addressed the challenges in fabricating a high-frequency and large-gap electrostatic diaphragm actuator. The mechanical and electrical reliability of the large-gap diaphragm actuator is increased through the design of the filleted electrode. Extensive characterization procedure has been conducted to overcome the difficulties mainly in the development of the solvent reflow process, the wafer mounting process for DRIE etch and metal deposition on the diaphragm. Good control of the reflow process allows us to create the desired three-dimensional photoresist shape and a short pre- and post-baking of the reflowed photoresist ensures a smooth surface for subsequent nickel plating. The removal of air pockets in the crystal bond used for wafer mounting is found to be the key for a successful diaphragm release step using DRIE backside etch. The conformal properties of the sputtered metal allows good electrical connection for contacts on the diaphragm but the same conformal properties create unwanted problems such as electrical shorts between the nickel electrode and the diaphragm. One way to avoid the electrical shorts is to keep the device attached to the carrier wafer for both the DRIE etch

and the sputtering step. The crystal bond used to mount the device can be utilized to avoid direct connections between the diaphragm and the nickel electrode.

An additional feature to enhance the electrical insulation between the diaphragm and the nickel electrode is the oxide ring surrounding the sacrificial photoresist. The robustness of the photoresist solvent reflow process enables us to reflow over a step height of ~ 2 μm without much difficulty. To the best of the author's knowledge, the reflow of the photoresist over uneven surface is the first to be demonstrated in this work.

In summary, a new, simple, and robust fabrication process is developed to realize a high-frequency and large-gap diaphragm actuator with high reliability. In the future, better control of the photoresist solvent reflow process can be conducted in a temperature-controlled oven with solvent environment to obtain better uniformity throughout the wafer.

CHAPTER 4

CHARACTERIZATION OF DIAPHRAGM ACTUATORS WITH FLAT AND FILLETED ELECTRODES

Following the previous chapter, the microfabricated diaphragm actuators are experimentally tested and characterized for maximum performance. Drive circuitry is designed for actuating the diaphragms at high AC (alternating current) voltage. The performance of the diaphragm actuators can be assessed by first observing under an optical microscope to quickly determine whether the diaphragm can be pulled in and collapsed onto the rigid nickel electrode, followed by characterization of individual diaphragm deflection using a Polytec laser vibrometer, and finally, characterization of an array of diaphragm actuators using a calibrated microphone. The reliability depends on the applied voltage waveforms and charging effects associated with the high voltage application as well as the different electrode types (flat versus filleted electrode).

4.1 Custom Drive Circuitry for Diaphragm Actuators

The desired drive signals for actuating high-frequency, large-deflection diaphragms are voltages up to ± 400 V and frequencies of at least 100 kHz. For the Gen. 1 design, the estimated combined capacitance of an array of 9 diaphragm actuators at rest

is 609 pF where each actuator's capacitance is 1 pF and the parasitic capacitance is 600 pF. After pull-in, the capacitance for each actuator will change to 50 pF, resulting in a total of 1.05 nF. A capacitor, C_s, is added in series with the diaphragm actuators, providing negative capacitive feedback to the system [72]. This is especially helpful because lower voltage is needed after pull-in occurs and stress from applying over-voltage can be reduced. The series capacitor acts like a voltage divider and reduces the impact of any additional voltage after pull-in occurs with the diaphragm actuators. With the capacitor C_s value of 1.36 nF, the voltage changes from roughly 2/3 of the input voltage to 1/2 of the input voltage after pull-in occurs. The resulting load seen by the drive circuit at the maximum is around 593 pF. With such high capacitive loads, there are multiple challenges in driving the diaphragm actuators. Most amplifiers are capable of driving high voltages at high frequencies but with low capacitive loads, high voltages at low frequencies, or low voltages at high frequencies. The large bandwidth (0-100 kHz) needed for testing further restricts the choice of an amplifier. Therefore, a drive circuit is custom built for driving the diaphragm actuators or device under test (DUT).

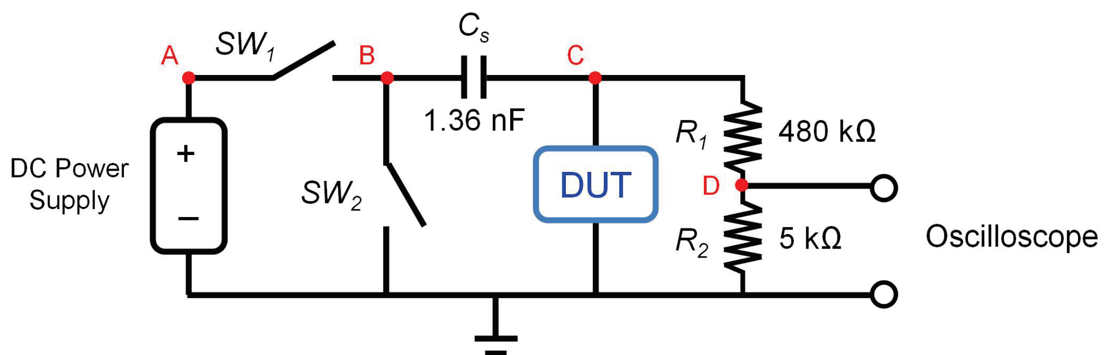

Figure 4-1: Schematics showing the drive circuitry for converting DC signal to AC signal for high voltage and high frequency operation.

Figure 4-1 shows the schematic for a simple drive circuit designed to convert a DC voltage of 600 V into AC voltage with pulse train waveforms. The circuit consists of a DC power supply, Sorensen XFR600-2, and two switches, SW_1 and SW_2, for the charging and discharging cycle respectively. N-channel MOSFET transistors, STW11NM80 are used for SW_1 and SW_2. Resistors R_1 and R_2 are used as a resistor divider to attenuate the signal by a factor of 1/97 for monitoring with the oscilloscope.

4.1.1 Circuit Design using LTSpice Simulation

Although the circuit looks simple, there are multiple challenges associated with implementing the circuit. LTSpice simulation is used to design the circuit. The design of the circuit is pretty straightforward and standard except two main parts: (1) switch SW_1 and (2) the resistive divider or attenuator.

The implementation for switch SW_1 is very tricky. Transistor STW11NM80 is used as SW_1 because the operating drain-to-source voltage (V_{DS}) is 800 V. The maximum rating for the gate-to-source voltage (V_{GS}) for this transistor is ± 30 V. The V_{DS} of SW_1 ideally starts with a voltage difference of 600 V and as the DUT charges up, the voltage difference becomes 0 V. During the discharge cycle, V_{DS} eventually becomes 600 V again. Node B which is the source of SW_1, and as shown in Figure 4-1, is a floating point. Therefore, the clock signal driving SW_1 (timing circuit loop) has to be coupled to the main circuit loop using a transformer for electrical isolation, as illustrated in Figure 4-2. The transformer maintains V_{GS} voltage of SW_1 based on the current supplied by the clock to the other winding of the transformer.

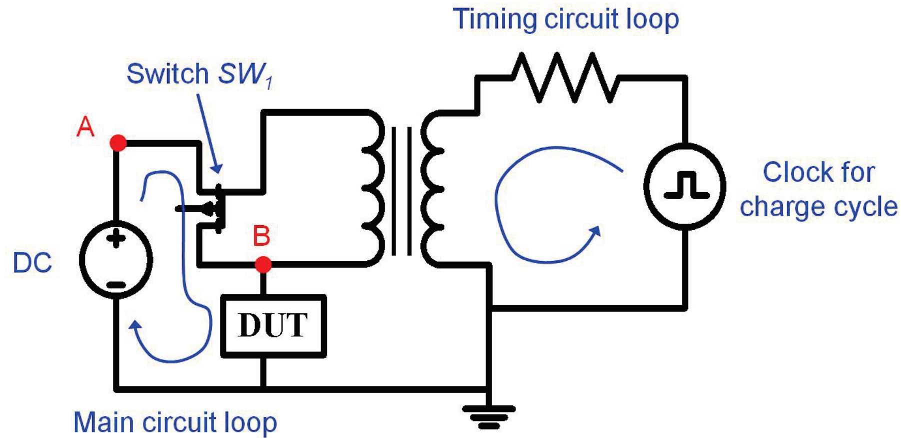

Figure 4-2: Circuit schematic showing the coupling of the driving signal for SW_1 (timing circuit loop) to the main circuit loop using a transformer, as adapted from [73].

There is a disadvantage of using a transformer to couple the two main loops, especially to create a pulse AC voltage as desired for this research work. As a current flux in the transformer is needed to maintain the V_{GS} voltage in SW_1, when the current flux dissipates quickly during the flat parts of the clock signal for a pulse train waveform, the voltage V_{GS} also reduces to zero voltage quickly. To overcome this issue, an additional feedback transistor, SW_3, is added across the V_{GS} of SW_1 to help to keep the voltage on for a longer time, as shown in Figure 4-3 [74]. The schematic for STW11NM80 [75] is similar to HEXFET and therefore can be used interchangeably in this design.

The functionality of the transistor SW_3 can be explained as follows. The V_{GS} of SW_1 is initially zero. When the clock creates a voltage difference across the transformer, current flows through the diode of SW_3. The current flow will charge up the gate of SW_1 and turn on the switch. When there is no current flux and the voltage across the transformer drops, the diode of SW_3 turns off. This prevents the charge on the gate of SW_1

from dissipating, keeping SW_1 on. The turn-on time for SW_1 is limited by the leakage current. As the clock transitions to the opposite direction, a negative voltage forms on the transformer. SW_3 turns on and drains the charges at the gate of SW_1, turning SW_1 off. This cycle repeats itself and the desired signal for V_{GS} of SW_1 and control of the charging switch, SW_1, is realized.

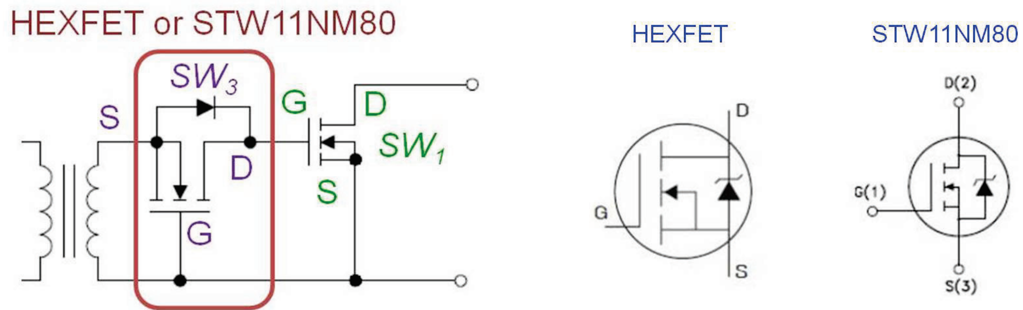

Figure 4-3: (Left) Schematic diagram of adding a feedback transistor (HEXFET) to maintain V_{GS} (adapted from [74]) and (Right) STW11NM80 [75] is similar to HEXFET and therefore can be used interchangeably in this design.

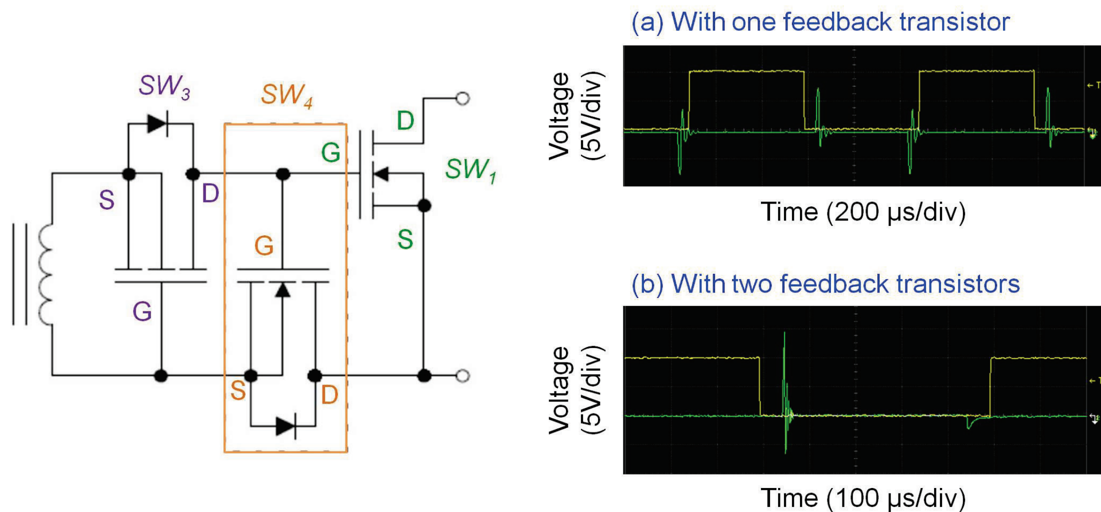

Figure 4-4: (Left) As suggested by [74], additional SW_4 can be added to increase noise immunity to the circuit, and (Top Right) Clock and V_{GS} signal of SW_1 for design with one feedback transistor and (Bottom Right) with two feedback transistors (Green signal = V_{GS}, Yellow signal = timing clock signal).

Figure 4-4 (Top Right) shows the clock signal (yellow line) and V_{GS} of SW_1 (green line) for one feedback transistor, as shown in Figure 4-3. It is observed that as the clock transitions from high to low, the current flux creates a positive V_{GS}. When the clock transitions from low to high, a negative V_{GS} is created; however, the ringing in the circuit creates positive voltage peaks that can turn on transistor SW_1. Since the charging and discharging phases have to be non-overlapping and exclusive of each other, the ringing causes SW_1 to turn on during the discharging phase and create a short between the power supply and ground. To avoid this, another feedback transistor SW_4 is added, as shown in Figure 4-4 (Left) (as adapted from [74]). The transistor SW_4 is used to maintain a negative V_{GS} for SW_1 and avoid turning on transistor SW_1 during the discharge phase, as observed in Figure 4-4 (Bottom Right).

The discharge transistor, SW_2, is used to discharge the DUT with the clock signal that is non-overlapping with switch SW_1. A low-pass filter can be added after the discharging transistor and before the series capacitor, C_s, to avoid voltage overshoot during the rise time of the pulse as a precaution, and is shown in Figure 4-5. The low-pass filter is designed to not affect the operation of the circuit with a cut-off frequency of 55.55 MHz (R_{LP} = 383 Ω and C_{LP} = 47 pF).

Due to the high voltage applications, a resistive divider or attenuator is required for monitoring the voltage across the DUT on the oscilloscope. For a ~ 100 kHz resonant frequency diaphragm, the response time of the diaphragm is experimentally determined to be ~ 2 μs. Therefore, the time constant of the resistive divider combined with the capacitance of C_s and the DUT is designed such that it is at least two orders of magnitude

greater than the pull-in time of the DUT. The time constant is 291 μs for the overall resistance of 485 kΩ and capacitance of 600 pF. The schematic for the final circuit design is shown in Figure 4-5.

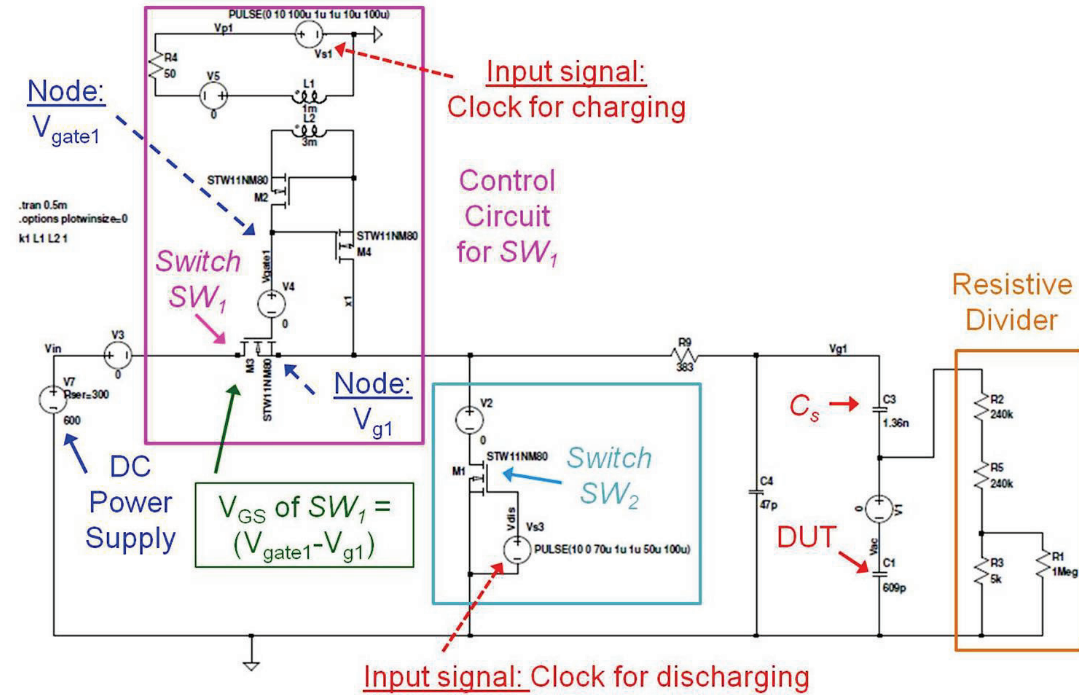

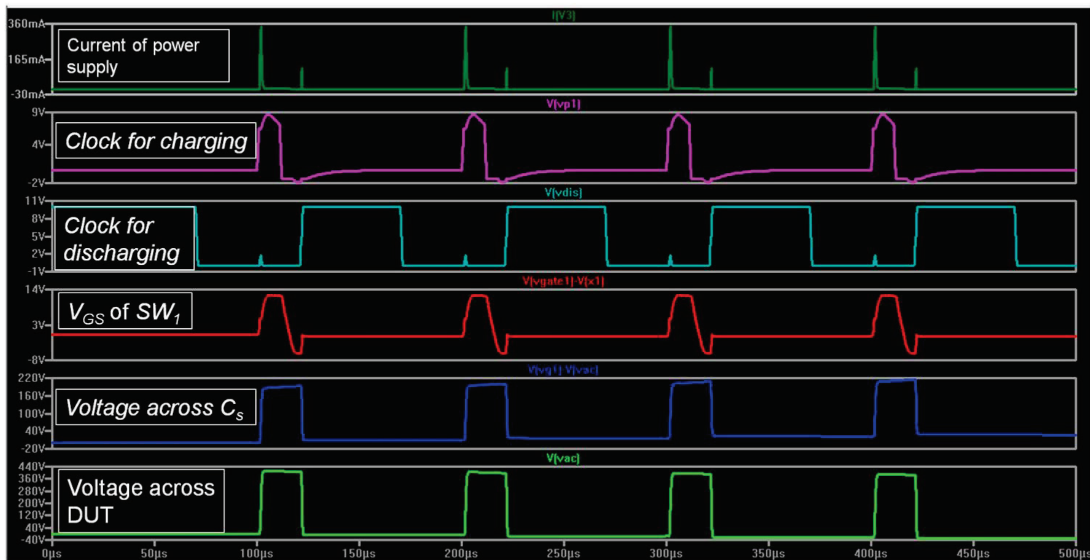

Figure 4-5: (Top) Schematic simulated in LTSpice, and (Bottom) Simulated waveforms for 10 kHz pulse with 20 % duty cycle.

The expected voltage across the DUT is a pulse waveform going from 0 V to 400 V, but due to the nature of the series capacitance the voltage is shifted to range from – 40 V to 360 V (Figure 4-5 (Bottom)). This can be advantageous for driving the DUT because the now bipolar signal can help to reduce charging effects. The low but longer duration of the negative voltage can help to cancel out the charge build-up in the diaphragm during the positive cycle.

4.1.2 Circuit Implementations

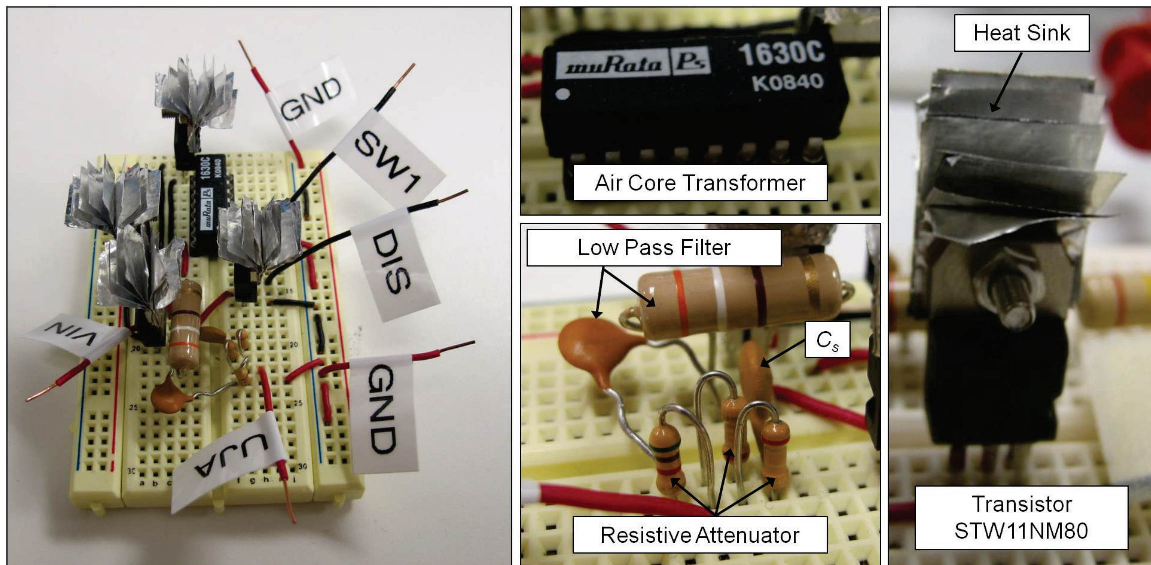

Figure 4-6: (Left) Drive circuitry implemented on a breadboard, (Middle Top) Air core transformer of 1:3 is used for coupling of the clock timing loop of SW_1 to the main circuit loop, (Middle Bottom) Low pass filter, resistive attenuator and series capacitance, and (Left) Transistor STW11NM80 for switches SW_1-SW_4 with heat sink attached for cooling.

The circuit is implemented and tested on a breadboard (Figure 4-6 (Left)). An air core isolation transformer, MuRata 1630C, with a turns-ratio of 1:3 is used to couple the clock timing loop of SW_1 to the main circuit loop. Due to the high current flowing

through the STW11NM80 transistors, heat sinks custom made out of aluminum foil are attached to increase the lifetime of the transistors (Figure 4-6 (Right)). The main challenge in this circuit design is for high frequency operation. Both the charging and discharging switches cannot have overlapping time where both transistors are on. If this happens, the power supply will be shorted to ground with high current flowing through the switches. The transistors will not withstand the high current and will break the electrical connections. The ringing in the transformer limits the minimum on-time charging switch.

Reliable operation of this circuit is at frequency of 10 kHz with peak-to-peak voltage of 400 V. Although the frequency is far from the desired drive signal, nonetheless, the DUT can be tested at high AC voltage and preliminary testing can be conducted to evaluate the reliability of the DUT. Higher frequency can be achieved with lower voltage with this circuit but then it will be no different than using a commercial power amplifier such as Krohn-hite 7602M which has a large bandwidth of 1 MHz and voltage up to less than ± 200 V. In the future, further optimization of the circuit can increase the operating frequency. For the rest of this chapter, testing is performed with either a sinusoidal waveform amplified by Krohn-hite 7602M or a pulse waveform driven by the custom built drive circuitry.

A LABVIEW program is used to control the function generators and DC power supply with a general purpose interface bus (GPIB) and a data acquisition (DAQ) card. The clock signals for the switches are generated by two synchronized function generators and the signals cannot be replaced by the digital outputs on the DAQ card because it is

current-limited. In addition, an oscilloscope is used instead of the DAQ card in order to obtain the highest resolution of monitoring the input and output signal. The oscilloscope has larger sampling rates than the available DAQ card.

4.2 Pull-in Characteristics

The pull-in characteristics of the flat and filleted electrode diaphragm actuators are investigated in this sub-section. There are two diaphragm designs for the flat electrode: higher frequency (97 kHz) diaphragm and lower frequency (64 kHz) diaphragm. The higher frequency diaphragm is harder to deflect because it has higher residual stress (high stiffness) while the lower frequency diaphragm is easier to deflect and requires lower operating voltage. The flat electrode with the 97 kHz diaphragm has a gap of ~ 8.33 μm and pulls in at ~ 337 V DC (direct current). Due to the limitation of the drive circuitry, the full collapse of the 97 kHz diaphragm was not observed at AC (alternating current). For the flat electrode with the 64 kHz diaphragm with an electrostatic gap of 7.4 μm to 8.22 μm, the diaphragm pulls in at pulse waveforms of ± 210 V at 10 kHz (Table 4-1); however, both diaphragm designs for the flat electrode easily fracture due to the large electric field and mechanical stress at the edges. For the flat electrode design, the diaphragm displaces ~ 75 % of the total gap volume. The incomplete collapse at the corners creates high stress and vulnerable points on the diaphragm. Any additional voltage applied will pull the diaphragm sideways towards the corners and eventually fractures will occur.

Table 4-1: Summary of diaphragm actuation performance.

Design Parameters	Flat Electrode		Filleted Electrode
Diaphragm resonance frequency	64 kHz	97 kHz	97 kHz
Diaphragm residual stress	32 MPa	74 MPa	74 MPa
Average gap at center, h_O	7.9 µm	8.33 µm	8.14 µm
Applied signal for diaphragm pull-in	(10kHz) ±210 V	(DC) 337 V	(1 kHz) ±240 V (10kHz) ±279 V
Reliable actuation (Static pull-in)	< 2 minutes	< 2 seconds	1 hour
Reliable actuation (Dynamic pull-in)	-	-	> 43 days

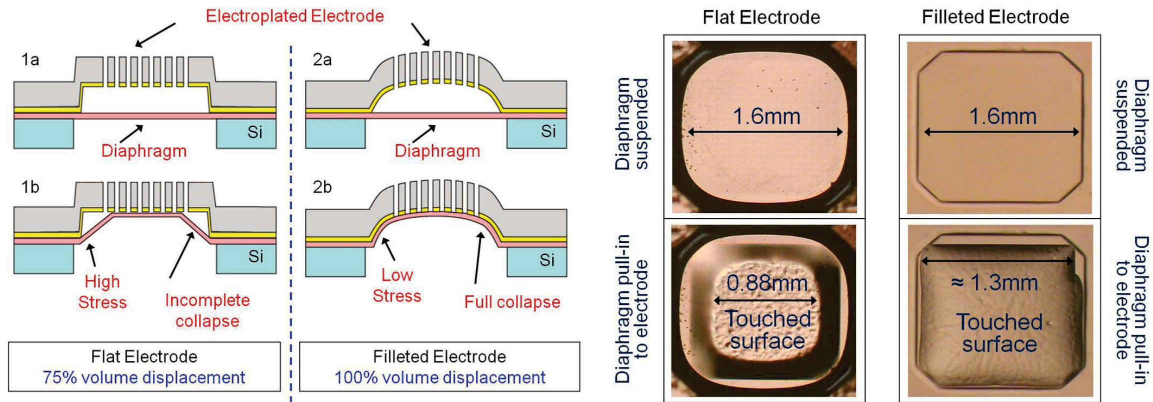

Figure 4-7: (Left illustrations) Cross section illustration of the pull-in characteristics. (Right microscope images) View from back: Pull-in of diaphragm for flat (left column) and filleted electrode (right column).

On the other hand, the filleted electrode has only one design, high-frequency diaphragm (97 kHz) with an electrostatic gap ranging from 7.7 µm to 9.58 µm. The diaphragm pulls in at a pulse waveform of ± 240 V at 10 kHz (Table 4-1). The rounded corners of the filleted electrode help create a more gradual collapse of the diaphragm when pulled in and ~ 100 % volume displacement is observed, where the diaphragm hugs the profile of the rigid filleted electrode. The rounded corners of the filleted electrode prevent the diaphragm from being pulled sideways, eliminating the occurrence of fracture when voltage above pull-in voltage (over-voltage) is applied. Figure 4-7 compares the

pull-in characteristics of the flat versus filleted electrode, and shows optical microscope images viewed from the backside of the actuator.

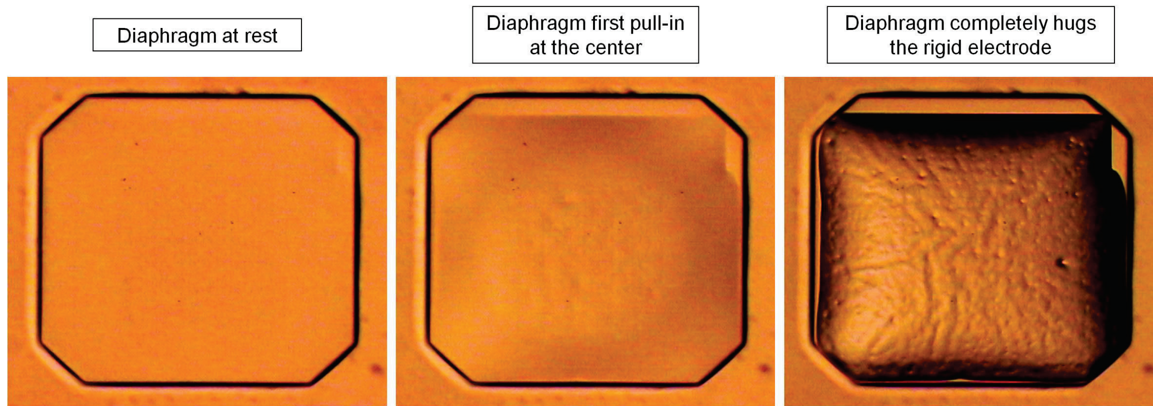

Figure 4-8: Microscope image of (Left) Diaphragm at rest, (Middle) Diaphragm first pull-in at the center and (Right) Full collapse of the diaphragm, which hugs the rigid electrode profile. These images are obtained at different actuation voltages.

In Figure 4-8, the microscope images prove that the filleted electrode is indeed a parallel-plate configuration design and not a zipper configuration because the diaphragm pulls-in from the center and expands toward the edges.

4.3 Reliability Test

Reliability tests with different degrees of mechanical and electrical stress were performed to investigate the device limits on the filleted electrode. Due to diaphragm fracture, the diaphragm for the flat electrode design did not survive long enough for further reliability testing and therefore the following reliability tests are conducted mostly with filleted electrode designs.

4.3.1 Static Pull-in Test

For the worst-case scenario, the diaphragm is collapsed and held to the rigid filleted electrode for an amount of time. This test is named the static pull-in test and has maximum charge effects. Charges are injected into the dielectric layer from both the rigid electrode (when in contact) and metal layer on diaphragm, similar to the tests in [76], [77]. The charges injected by the rigid electrode have the worst charging effects on the diaphragm. This is because when voltage beyond pull-in is applied, the diaphragm is collapsed onto the rigid electrode. During this time, charges are injected to the surface of the diaphragm that is in contact with the rigid electrode. When voltage is removed, the diaphragm releases back to its rest position and no longer in contact with the rigid electrode. The charges injected by the rigid electrode have no other path for dissipation except through the thickness of the diaphragm, towards the metal layer on the diaphragm. The diffusion through the thickness of the diaphragm is very slow, causing charge build-up in the diaphragm. On the other hand, charges injected by the metal layer on the diaphragm also contribute to the charging effect but with lower impact. The charges accumulate at the interface between the metal layer and the dielectrics of the diaphragm and when the voltage is removed, the charges at the interface can easily dissipate through the metal layer.

In addition to maximum charging effects, the diaphragm is maximally deflected in this static test, inducing maximum mechanical stress on the diaphragm edges. A pulse waveform of 10 kHz, ± 279 V and 50 % duty cycle is applied across the device for this test. The large duty cycle (50 %) and large actuation voltage cause the diaphragm to be

held to the electrode continually. Looking through the microscope, the most obvious failure is when the diaphragm fractures. It is hard to determine whether the diaphragm is under stiction due to the applied voltage or the charging effect. Therefore, the static test is conducted such that voltage is applied for 20 minutes and then removed to check if the diaphragm releases back to its rest position. If the diaphragm releases back to normal, then voltage is applied for 40 minutes and then removed to check again. This routine is repeated until stiction is observed even when voltage is removed.

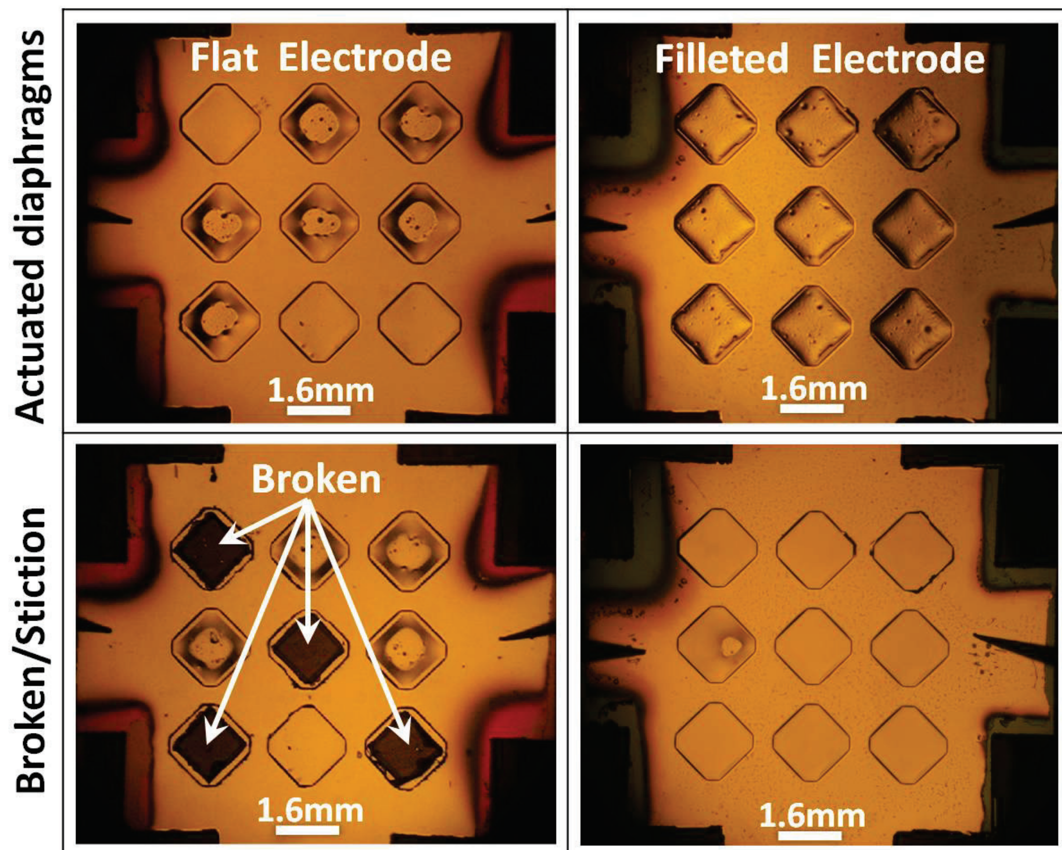

Figure 4-9: Static pull-in (diaphragm actively pulled in towards nickel electrode on the bottom). (Left Column) Only six out of nine diaphragms can be pulled in for flat electrode at one time, and after less than 2 minute all diaphragms stop functioning. (Right Column) All diaphragms can be pulled in for filleted electrode design for 1 hour without any diaphragm breakage.

The results for the static pull-in test are summarized in Figure 4-9. Several diaphragms for the flat electrode design broke after ~ 2 seconds of actuation and all of them stop functioning after ~ 2 minutes of actuation. On the other hand, only one diaphragm for filleted electrode exhibits stiction after applying 1 hour of continuous voltage. All diaphragms are still intact. After leaving the device for 2 weeks, the diaphragm which has stiction returns to its initial rest suspended position and the device can be actuated again normally. In fact, the same device is utilized in sub-sections 4.3.2 and 4.3.3 for dynamic test and long-term reliability test.

4.3.2 Characterization of Dynamic Pull-in

Although a static pull-in test is essential for investigating the maximum charging effects, continuous actuation of the diaphragm with alternating voltage (dynamic pull-in) is more important for gas pumping applications. The dynamic pull-in can be evaluated using two non-contact measurement systems: (1) a Polytec laser vibrometer system or (2) a calibrated microphone. With the two testing systems, the best electrical voltage waveform for driving the diaphragm actuators for maximum performance is determined.

A Polytec laser vibrometer system (PSV-400) from Professor Karl Grosh's laboratory is used for the characterization process (Figure 4-10). The laser beam from the vibrometer is focused by a mirror onto the center of one diaphragm actuator. The vibrometer estimates the velocity of the vibrating DUT by measuring the frequency difference between the laser beam as reflected back by the DUT and an internal reference beam. As shown in Figure 4-10, the laser beam is smaller than the diaphragm's size and can produce reliable data on the velocity measurements. Positive voltage is applied

through the two probes that are holding the DUT in place while the grounded bottom copper plate is connected to the rigid nickel electrode on the backside of the DUT.

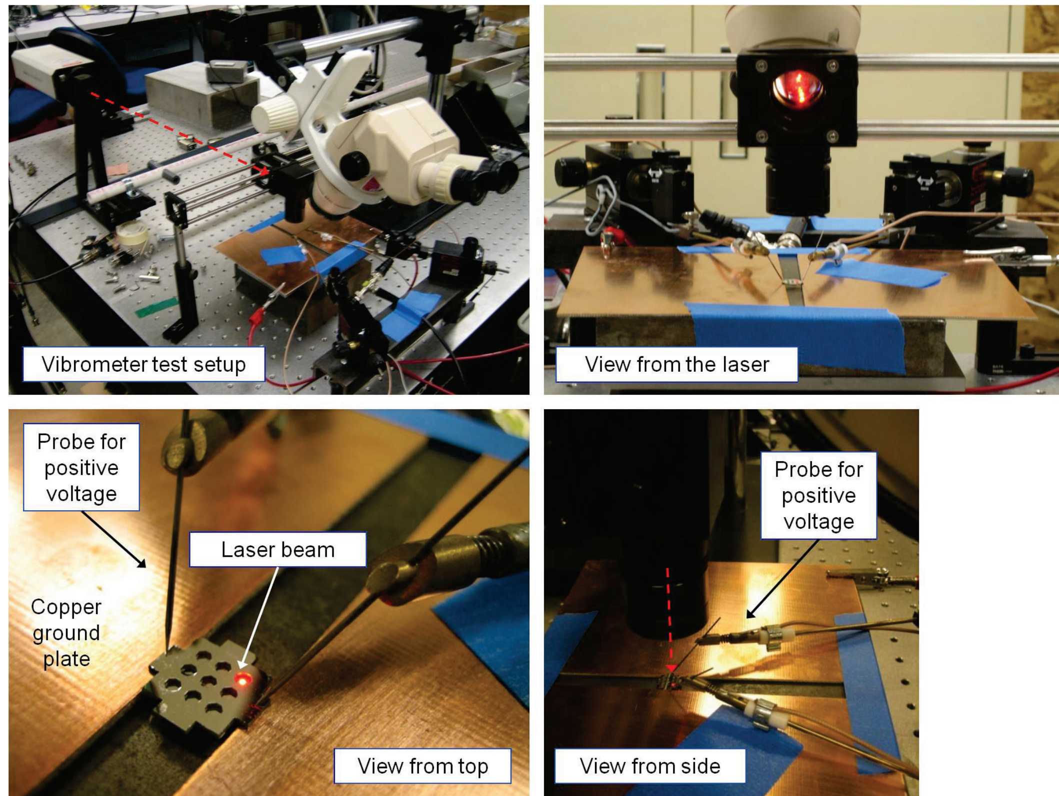

Figure 4-10: (Top Left) Laser vibrometer test setup, (Top Right) View from the laser, (Bottom Left) View from top, and (Bottom Right) View from side.

With the custom built circuit, pulse waveforms with varying voltages (peak-to-peak voltage of 60 V to 540 V with intervals of 60 V) and duty cycles (20 %, 30%, 40 %, and 45 %) at 10 kHz are applied to the DUT. The time-varying displacement of the diaphragm is detected by the laser vibrometer system and is recorded using an oscilloscope. The peak-to-peak displacement for all the varying parameters are obtained and plotted in Figure 4-11. From the plot, maximum displacement is achieved with a 20 % duty cycle and at 360 V peak-to-peak. As observed in the left corners of the plot,

near zero displacement is observed because the diaphragm is pulled-in and stuck to the rigid electrode at voltages above the maximum displacement.

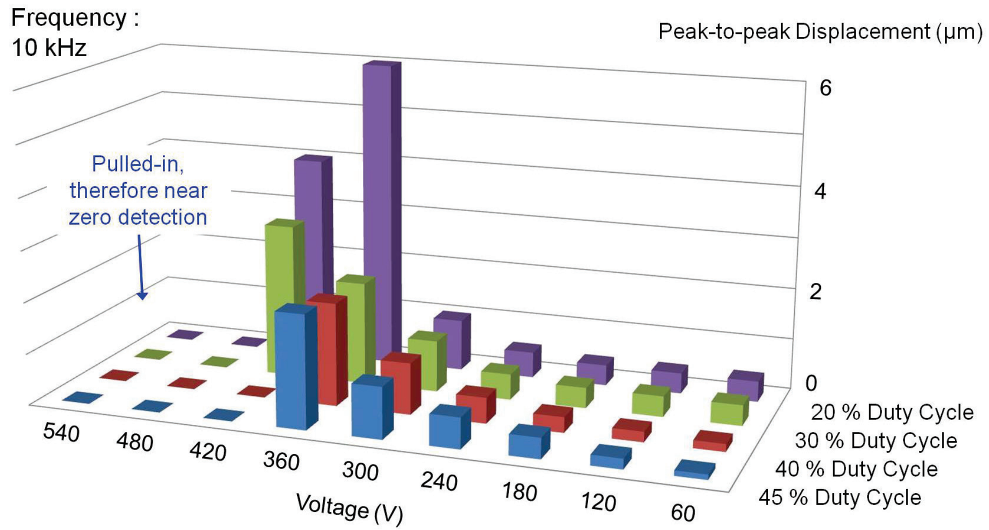

Figure 4-11: Comparisons of the diaphragm deflection measured by laser vibrometer for pulse waveforms with varying voltages and duty cycles at 10 kHz.

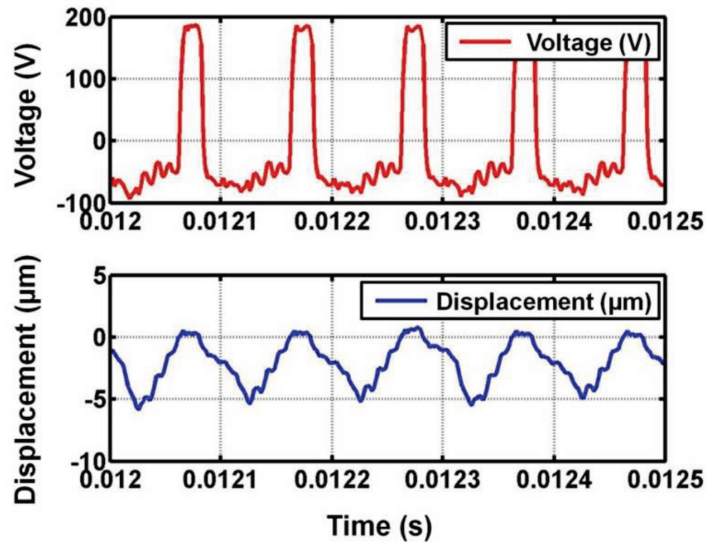

Figure 4-12: (Top) Voltage measured across the DUT, and (Bottom) Diaphragm displacement measured by the laser vibrometer system. The applied voltage is pulse waveform with 20 % duty cycle, at 10 kHz and 360 V peak-to-peak.

Figure 4-12 shows the time varying applied voltage with the corresponding detected diaphragm displacement. Note that the voltage plotted in Figure 4-11 and Figure 4-13 are the applied voltage on the power supply while the voltage plotted in Figure 4-12 are across the DUT. The voltage across DUT is lower than the applied voltage because a portion of the voltage is dropped across the series capacitance C_s.

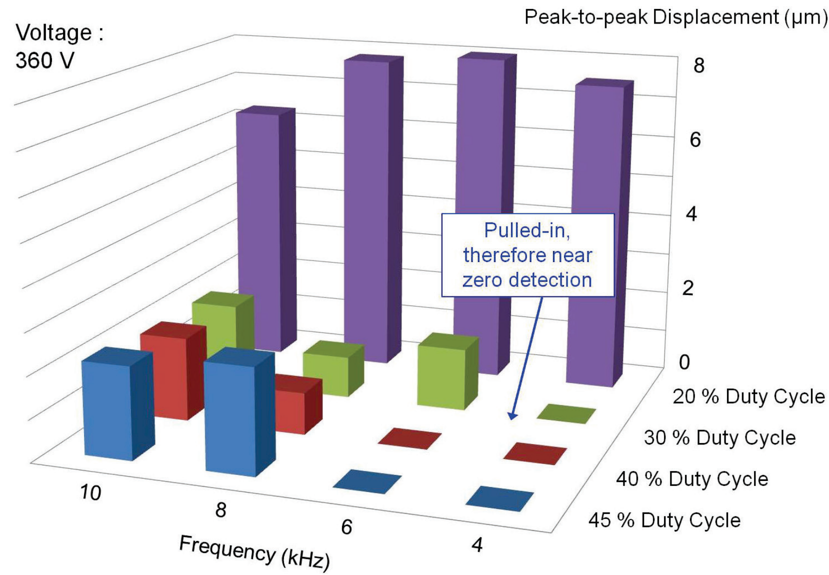

Figure 4-13: Comparisons of the diaphragm deflection measured by laser vibrometer for pulse waveforms with varying frequencies and duty cycles at 360 V peak-to-peak.

As the maximum voltage is determined to be 360 V peak-to-peak, another set of tests are conducted with varying frequencies (4 kHz, 6 kHz, 8 kHz and 10 kHz) and varying duty cycles (20 %, 30 %, 40 % and 45 %), as shown in Figure 4-13. This time, the bottom right corner of the plot shows near zero-displacement because at larger duty-cycle and lower frequency, the duration of applied voltage is larger than the time needed to collapse the diaphragm. The additional duration after the full collapse occurs will induce high charge injection into the diaphragm and even after the voltage's polarity is

switched, the diaphragm continues to be collapsed onto the rigid electrode. Actuation with 20 % duty cycle continues as the best waveform for driving the diaphragm and will be used in all future tests.

The laser vibrometer is a good tool for measuring the corresponding response of the diaphragm with the applied voltage but measuring multiple diaphragms in parallel takes a long time and cannot be performed simultaneously. Therefore, a free-field calibrated microphone (Larson-Davis 1/4" Microphone – Model 2520) powered by a pre-amplifier with a gain of 40 is used to obtain a measurement of the sound pressure produced by the actuator arrays (shown in Figure 4-14). The output of the calibrated microphone is measured in voltage and it is monitored and recorded with an oscilloscope. The output voltage can be converted to acoustic pressure with the calibration data provided by the manufacturer of the microphone.

Figure 4-14: (Left) Pre-amplifier for powering the calibrated microphone and (Right) The free-field calibrated microphone placed 1.5 cm away from the DUT.

Similar sets of tests to the laser vibrometer are performed with the calibrated microphone for characterizing the diaphragm. It is important to note that the responses recorded by the calibrated microphone are the combined output generated by all the

diaphragm actuators in the array while the output recorded by the laser vibrometer is generated by only one diaphragm actuator. The peak-to-peak voltage output as detected by the calibrated microphone is plotted and compared in (Figure 4-15 and Figure 4-16). Again, the actuators have highest performance when driven with pulse waveform of 20 % duty cycle. The best applied peak-to-peak voltage is 420 V instead of 360 V. This can be because there are slightly larger gap diaphragm actuators in the array and higher voltage is needed to pull-in all diaphragms, resulting in higher combined output. It is observed that beyond 420 V peak-to-peak, the output starts to drop due to one or more diaphragms in the array showing characteristics of stiction, as shown in the laser vibrometer test. To summarize, the best pulse waveform is determined to be a peak-to-peak voltage of 420 V at 10 kHz, with ~ 30 V peak-to-peak voltage output detected by the calibrated microphone.

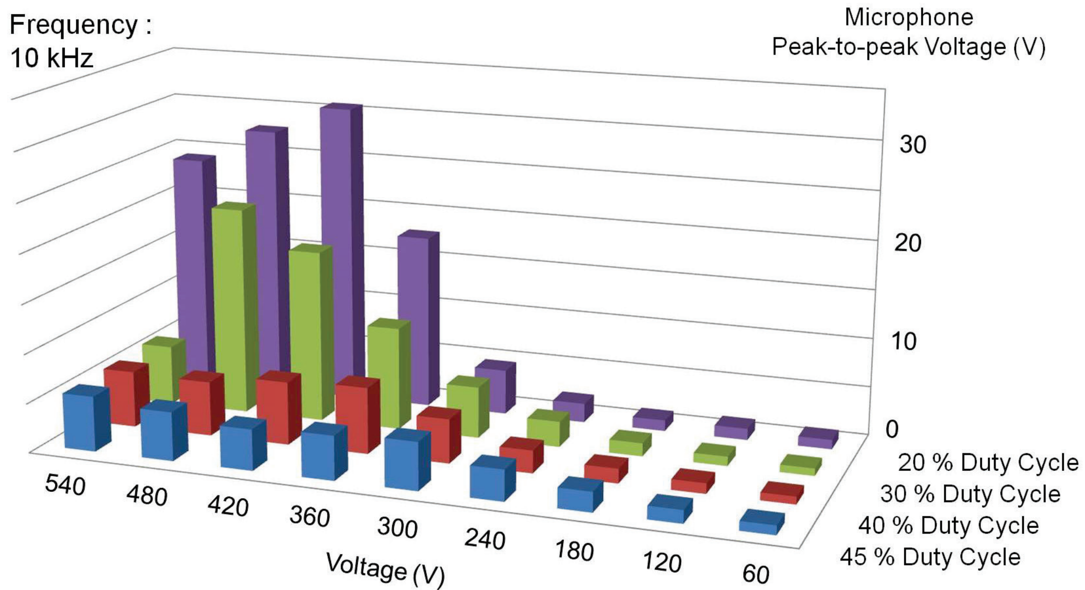

Figure 4-15: Comparisons of the sound pressure (measured in voltage) by the free-field calibrated microphone for pulse waveforms with varying voltages and duty cycles at 10 kHz.

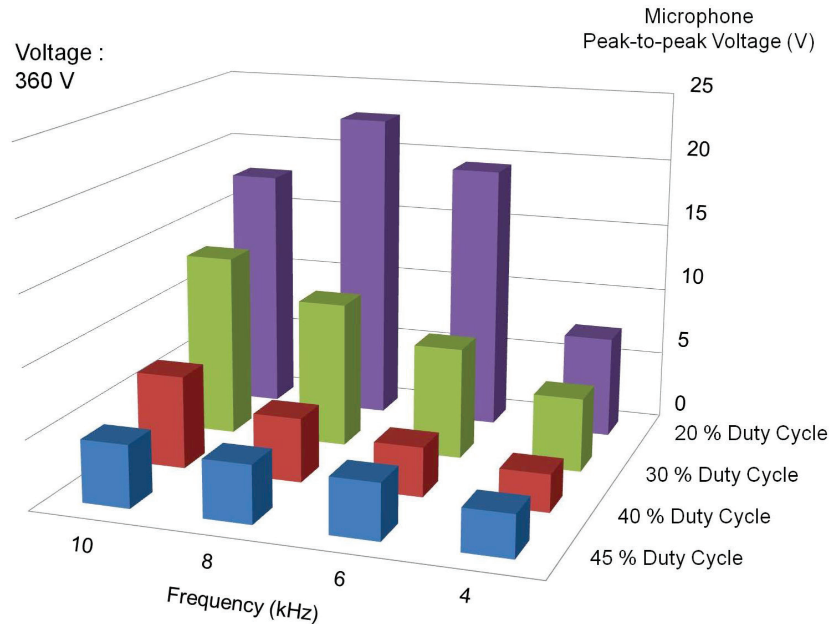

Figure 4-16: Comparisons of the sound pressure (measured in voltage) by the free-field calibrated microphone for pulse waveforms with varying frequencies and duty cycles at 360 V peak-to-peak.

4.3.3 Long Term Reliability Test

A long-term reliability test is conducted with the best pulse waveform (420 V peak-to-peak at 10 kHz) as determined by the calibrated microphone in the dynamic pull-in test. In this test, the reliable dynamic actuation of the diaphragm at large deflection when actuated beyond pull-in is investigated. Although higher frequency actuation is desired, the operating frequency is limited by the capability of the custom built circuit. For comparisons, reliability test with a sine waveform of 300 V peak-to-peak voltage at 40 kHz is conducted and compared with the pulse waveform. With the sine wave test, the performance of the diaphragm vibrating at high frequency (80 kHz because the diaphragm vibrates at twice the frequency of the applied voltage) but at low amplitude (before pull-in) is explored. The frequency for the sine wave is chosen because the

calibrated microphone is calibrated up to 80 kHz. The low applied voltage ensures that the diaphragm will not stick to the rigid electrode and has minimal charging effects with no charge injected from the rigid electrode.

With the calibrated microphone positioned ~ 1.5 cm away from the actuator array, the sound pressure was recorded with the calibrated microphone. If one or more of the diaphragms stop functioning, either due to mechanical failure or stiction, the sound pressure is expected to decrease by a certain fraction. The long-term reliability performance of the diaphragm actuator is summarized and plotted in Figure 4-17.

The dynamic pull-in actuation with a low amplitude sine wave shows stable output for more than 30 days with almost no charging effects. This verifies the theory that there is minimum charging when the diaphragm is not fully collapsed onto the rigid electrode. Sine waveform can be a good choice if the diaphragm is actuated at low deflection; but, at large deflection where the diaphragm collapses onto the rigid electrode, a different waveform will be needed. Sine waveform alternates from positive to negative voltage with only a short period of time where the voltage is zero. This zero voltage zone or rest time (as shown in Figure 2-6) is reduced especially when high voltage and high frequency is applied. Due to the nature of electrostatic actuation where the diaphragm is pulled in with both polarity of the voltage, a long rest time is required for the diaphragm to respond and release from the rigid electrode. Therefore, sine waveform is not suitable for actuation beyond pull-in voltage.

Since the output shows no significant deterioration with low voltage sine waveform, the electrical drive waveform is changed to a high voltage pulse waveform. With the pulse waveform of 20 % duty cycle and 30 % DC offset, low negative voltage is applied for 80% of the period while high positive voltage is applied for the other 20 % of the time. The diaphragm is expected to be released from the rigid electrode at these low negative voltages due to the high restoring force of the diaphragm. In addition, the negative polarity is used to compensate for the charging effects due to the positive applied voltage. The actual voltage across the DUT is a peak-to-peak voltage of 334 V (+ 273 V to – 61 V) at 10 kHz. It is observed that although the sound pressure starts at a higher level compared to when actuated with the sine waveform, it decays with time at a high rate, showing higher charging effects than with the sine waveform. The charging effect starts to plateau after some time and this perhaps can be due to saturation of charge injections into the surface of the diaphragm.

A break is introduced to allow the charges to dissipate and discharge from the dielectric through the metal layer on the diaphragm. It is interesting to note that after a break of 13 days, the high acoustic output is resumed. Shorter decay time is observed and the acoustic output plateaus at a higher acoustic level. Assuming that after the break, the charges dissipate and device returns to its initial condition before testing, the higher plateau level perhaps can be attributed to the absence of the 30 days of sine waveform actuation.

It is important to note that due to the different actuation frequencies, the acoustic output level for both sine and pulse waveforms cannot be compared directly. Only the

relative changes of the acoustic output level for each waveform are used to access the reliability of the actuation. Nonetheless, the total reliable actuation was greater than 30 days for sine actuation and 26 days for pulse actuation, with a total of greater than 56 days. Greater than 229 billion actuation cycles are accounted with the diaphragm moving at twice the applied frequency for sine waveform and the same frequency as the pulse waveform.

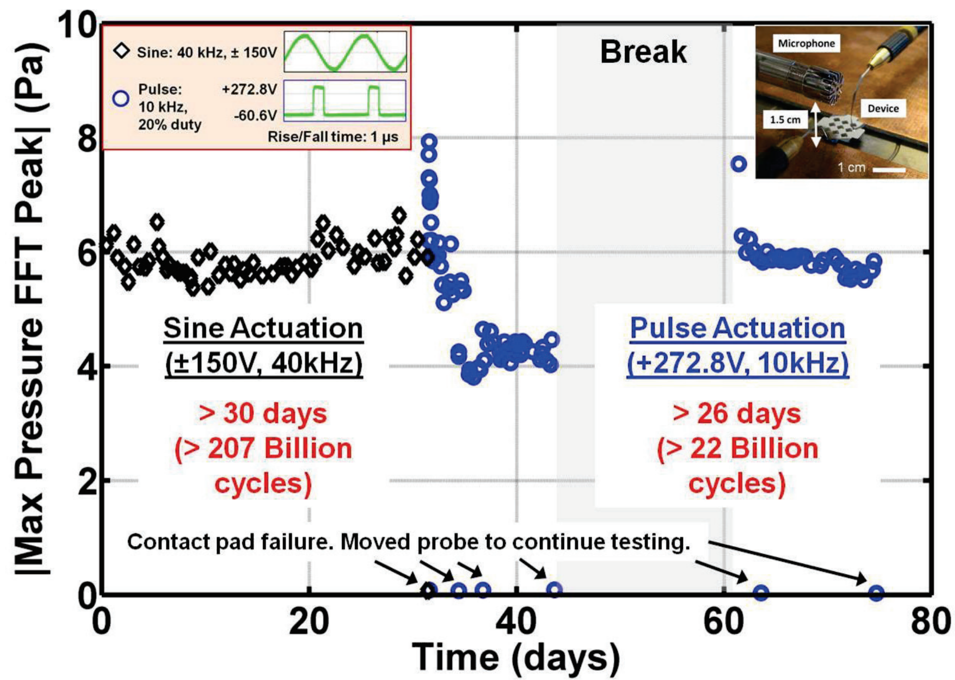

Figure 4-17: Dynamic pull-in actuation for long-term reliability test: Acoustic pressure. 43 days of continuous actuation. Device can be actuated for an additional of 13 days after a break before the device failure.

There were occasional losses of electrical connection due to contact pad failure. The electrical connection was regained by moving the probe to another location on the contact pad. Better electrical connection can be made by wire bonding to a printed circuit board (PCB) and connected with an edge connector, as shown in Figure 4-18.

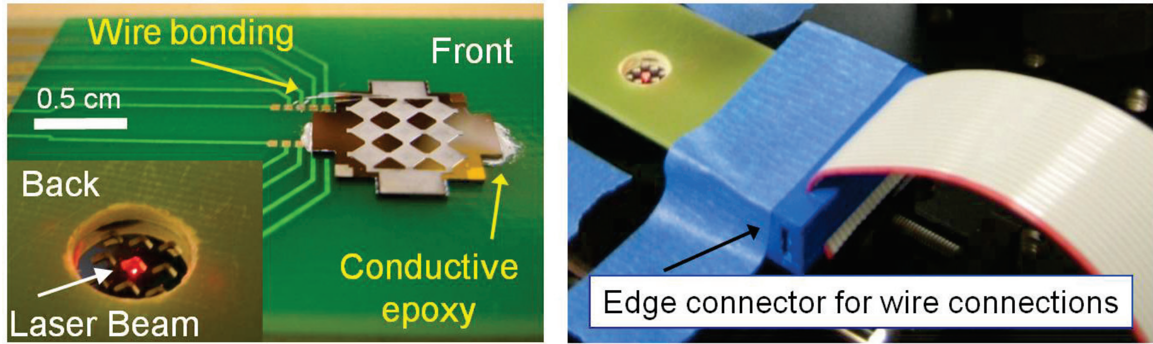

Figure 4-18: (Left) DUT wired bonded and attached with conductive epoxy on a PCB and (Right) Wire connections made with an edge connector.

In addition, environment humidity fluctuations can also influence the actuator performance where the acoustic pressure is inversely proportional to the humidity in the room, as shown on Figure 4-19. The influence of the humidity can be compensated electrically.

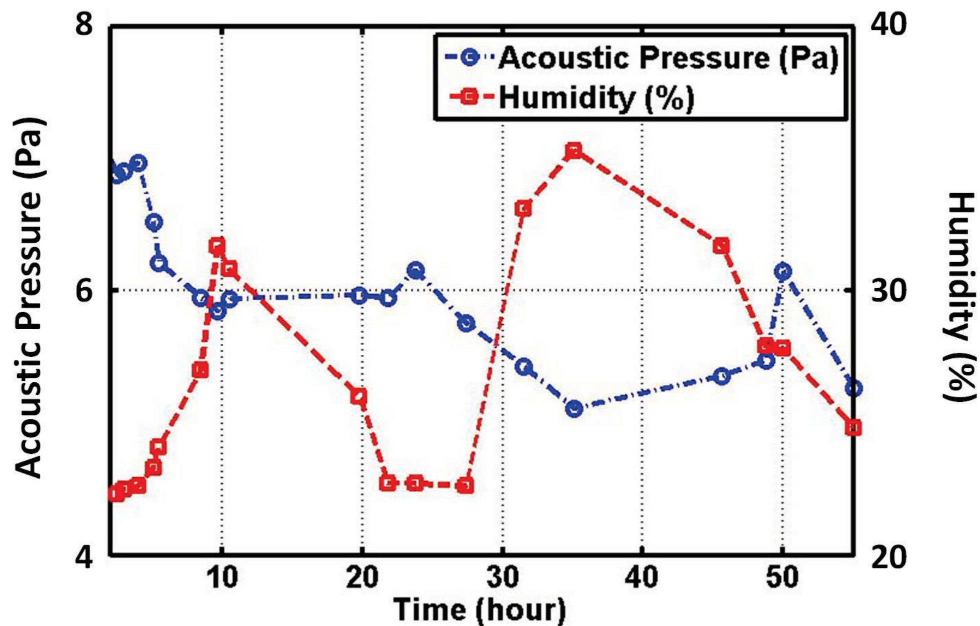

Figure 4-19: Acoustic pressure versus room humidity. The acoustic pressure is inversely proportional to the humidity in the room.

4.4 Summary

Extensive characterizations with the optical microscope, laser vibrometer, and calibrated microphone were performed to explore the best way to actuate the diaphragm actuators reliably and efficiently for maximum output performance. Under observation with an optical microscope, the filleted electrode can be actuated reliably and achieve near 100 % volume displacement. The rounded corners of the filleted electrode allowed complete collapse of the diaphragm without exerting large mechanical stress on the diaphragm, and significantly increased the reliability of the actuator.

Efficient waveforms are needed to ensure maximum displacement with minimal charging effects. A sine wave is the best waveform to use if the diaphragm is actuated at low voltages and when the diaphragm does not collapse completely onto the rigid electrode. No significant charging effects are seen and stable actuation can be achieved for a long period of time when the diaphragm is not in contact with the rigid electrode during actuation but the volume displacement will be small and pumping performance may be low. A pulse train waveform with 20 % duty cycle can drive the diaphragm more efficiently than the sine waveform for touch-mode actuation where the diaphragm is completely pulled in onto the rigid electrode. As a high voltage is required to pull-in the diaphragm, a custom drive circuit is designed for high voltage and high capacitive loads applications.

Interesting charging effects can be observed from the long term reliability data obtained with the calibrated microphone. Actuation with low voltage sine waveform showed minimum charging effects while actuation with high voltage pulse waveform

showed high charging effects but the charging saturates to a plateau region after some time. This effect perhaps can be related to the saturation of charges at the surface of the dielectric layer. After a break from the continuous actuation during which the charges dissipate from the dielectric, resumed actuation with pulse waveform showed shorter output decay time and the output saturates to a higher plateau region. This perhaps can be attributed to the absence of the long sine wave actuation.

CHAPTER 5

TECHNOLOGY DEVELOPMENTS AND TESTING OF ULTRASONIC JETS ARRAY (UJA)

The previous chapter discussed the development and characterization of the high-frequency, large-deflection diaphragm actuators with a filleted electrode design for maximum volume displacement and high reliability. In this chapter, Ultrasonic Jets Arrays (UJA) are developed and tested for potential micro propulsion applications. The UJA consists of an array of Ultrasonic Jets (U-JET) connected in parallel interspersed with jet holes. For checkerboard array arrangements, there are four U-JETs surrounding a jet hole. Each U-JET is formed by creating an enclosed acoustic cavity (Helmholtz resonator), consisting of eight throats for air to exit, and a diaphragm actuator (as developed in the previous chapter) that can modulate the air volume inside the cavity at high speed. High-speed air jets are produced through the throats. Additional air is entrained through each jet hole, producing high thrust.

In the following discussions, a pendulum test is set up for direct thrust measurements, which is the standard test used in aerospace engineering. Optimization and better understanding of the design parameters for UJA is achieved using the pendulum test setup.

5.1 Development of U-JETs and UJA

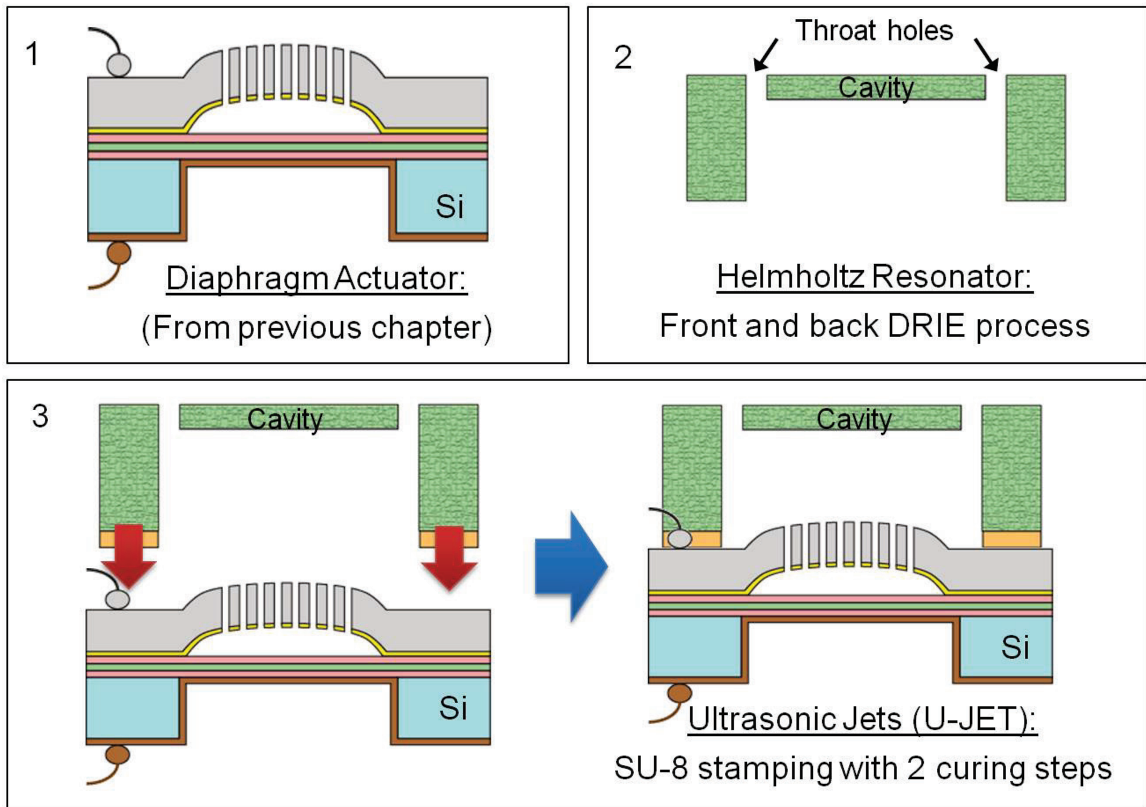

Figure 5-1: Fabrication and assembly process of the U-JET using SU-8 2010 with two curing-steps process.

The U-JET is formed by assembling the diaphragm actuators with a Helmholtz resonator (a cavity with throat hole(s)). Figure 5-1 shows the fabrication and assembly process for the U-JET. First, the Helmholtz resonator is fabricated using a front and back DRIE process on a double-sided polished silicon wafer. The diaphragm actuator, as fabricated and developed in the previous chapter, is then bonded to the Helmholtz resonator using SU-8 2010 in a two curing-steps process. In the first curing step, a thin layer of SU-8 2010 is transferred onto the Helmholtz resonator array using a stamping process and is semi-cured for 1 minute on a 95 ºC hotplate such that clean alignment and

attachment can later be performed. Next, the Helmholtz resonator is aligned with the diaphragm actuator under a microscope and held in place with flat-tip alligator clips (RadioShack® Micro 1-1/8" Smooth Clips) or some $1 handy clips from the hardware store. In the second curing step, the assembled parts that are held in place by clips are cured on a 150 ºC hotplate for 10 minutes. Finally, the clips are removed and the part is allowed to cure for an additional minute.

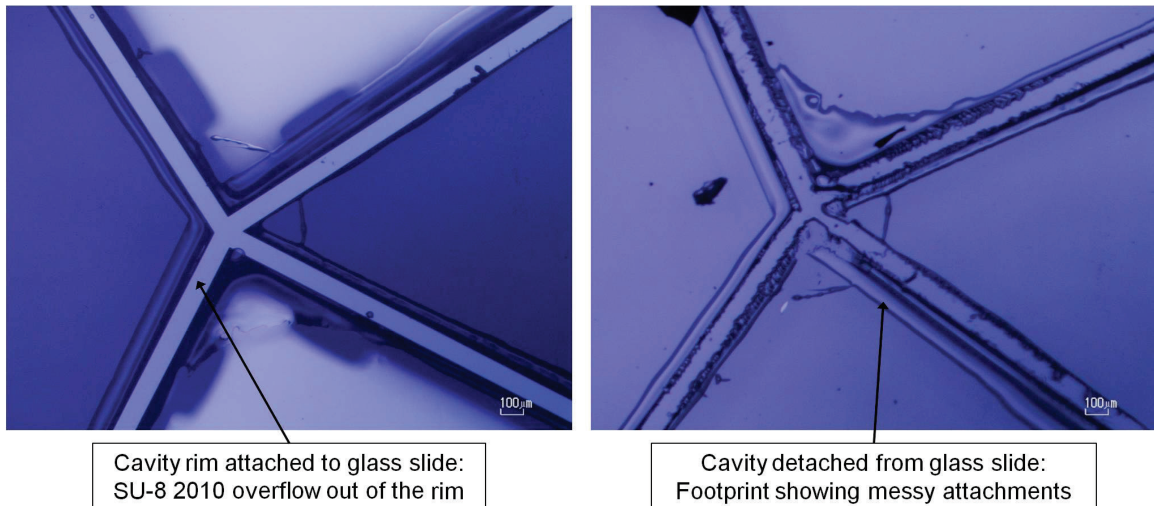

Figure 5-2: The cavity rim of the Helmholtz resonator is attached to the glass slide with SU-8 2010 stamped on the rim. If no curing is performed, overflow of the SU-8 2010 is observed (Left) when the cavity is detached from the glass slide, showing a messy footprint and attachments (Right).

The first curing step is critical for ensuring a clean, easy and strong attachment. For characterization purposes, the SU-8 2010 bonding is performed with a Helmholtz resonator attached on a microscope glass slide instead of the diaphragm actuator such that the bonding quality can be observed under microscope through the glass slide. If the first curing step is skipped or the duration of curing is too short, the wet SU-8 2010 will

overflow and might block the electrode holes on the diaphragm actuator. Figure 5-2 (Left) shows the overflow of SU-8 2010 around the rim of the cavity.

On the other hand, if the first curing step is too long, the SU-8 2010 becomes too dry for a good attachment and incomplete bonding is observed. As seen on Figure 5-3 (Left), the bulging of the SU-8 2010 shows that it did not stick to the glass slide completely since it managed to retain its shape after the SU-8 2010 stamping process. The bonding strength is very weak compared to the part in Figure 5-2. If the curing step properly performed, the SU-8 2010 will bond well with the glass slide with no overflow or bulging observed, as presented in Figure 5-3 (Right).

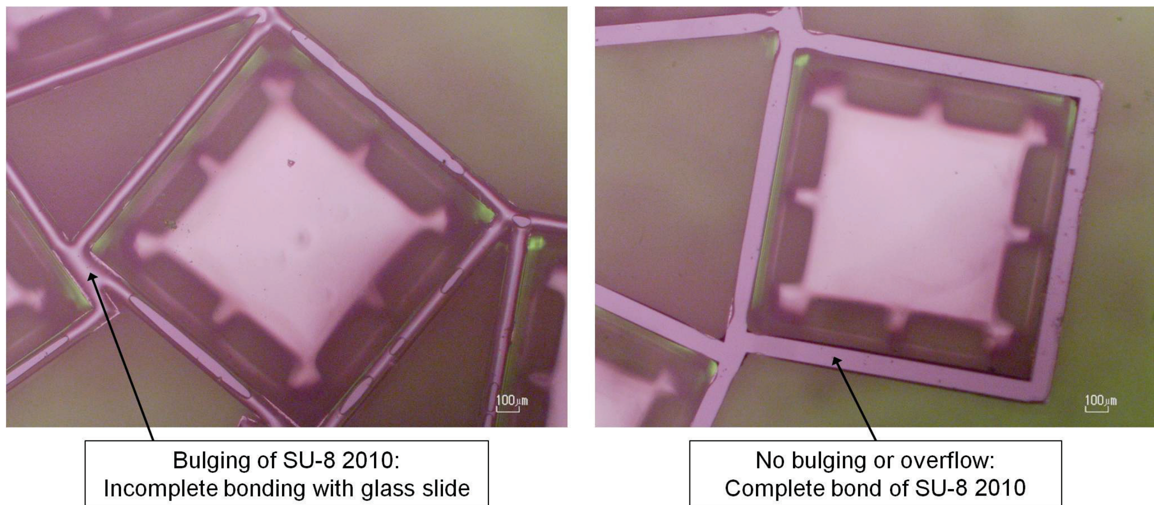

Figure 5-3: (Left) Bulging of SU-8 2010 is observed signifying incomplete bonding with glass slide and (Right) No bulging or overflow of SU-8 2010 showing complete bonding.

Figure 5-4 shows the UJA arrays with three types of design arrangements, checkerboard array, honeycomb array and dream catcher array. The basic requirement for the arrangements is that each jet hole has to be surrounded by three or more U-JETs for flow entrainment purposes. The various designs showed the robustness and versatility of

the fabrication process for UJA. The following results are all for the checkerboard array since the performance can be compared to previous works [41], [42]. Figure 5-5 displays the different components of UJA for checkerboard arrangements on the left and dream catcher arrangements on the right.

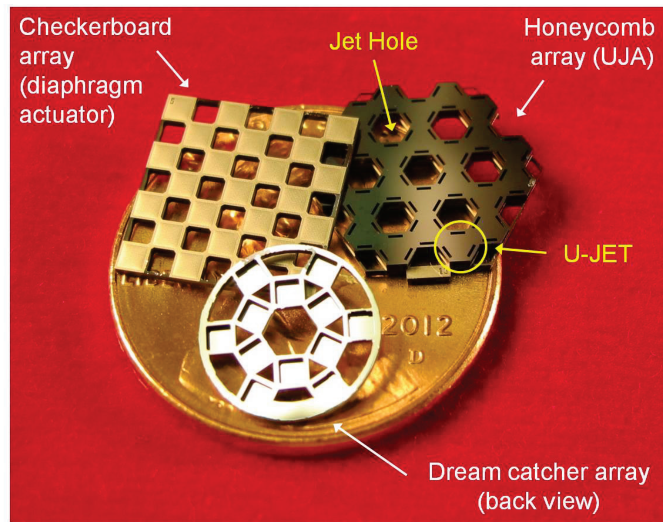

Figure 5-4: UJA arrays with three types of arrangements in Gen. 2 and 3; checkerboard array, honeycomb array and dream catcher array with reference to a US penny.

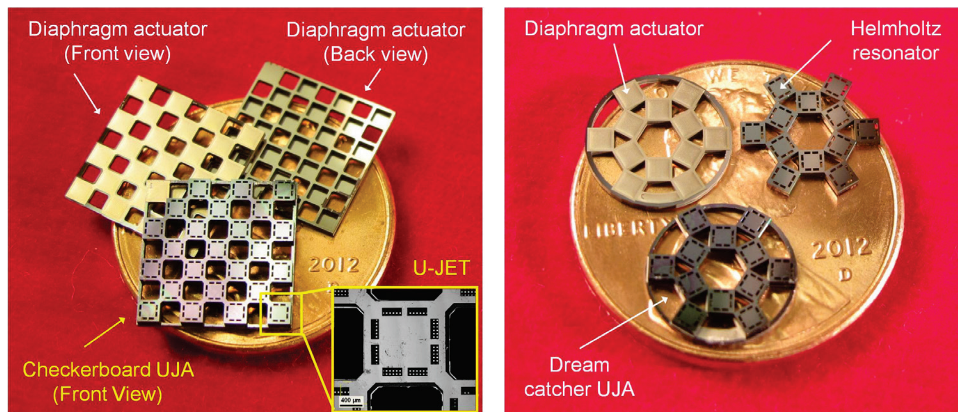

Figure 5-5: (Left) Prototype of a checkerboard UJA showing diaphragm actuator (front and back view) and the assembled UJA, with zoom-in microscope view of a single U-JET. (Right) Prototype of a dream catcher UJA. A diaphragm actuator, a Helmholtz resonator and the assembled UJA with respect to a US penny is displayed.

As seen in Figure 5-4 and Figure 5-5, the UJA design seeks to realize a compact and elegant UJA while achieving the maximum thrust-to-weight ratio. This architecture produces a 5 times lighter weight device compared to [41], [42] without sacrificing mechanical robustness. Additionally, the compact design with reduced area lowers the total parasitic capacitance and therefore the power consumption of the device. Figure 5-6 shows an SEM image of the cross section and microscope image of the top view of the device. Electrode perforations can be seen through the throat holes, showing clean perforations without any particles blocking the air path that might reduce the performance of the device. As may be known to many, the key to a high performance UJA is a device that is clean and particle-free. Therefore, throughout the whole fabrication process of the diaphragm actuator and the assembly of UJA, extensive cleaning steps are included to ensure the cleanliness of the UJA, especially in the gap between the diaphragm and the rigid electrode.

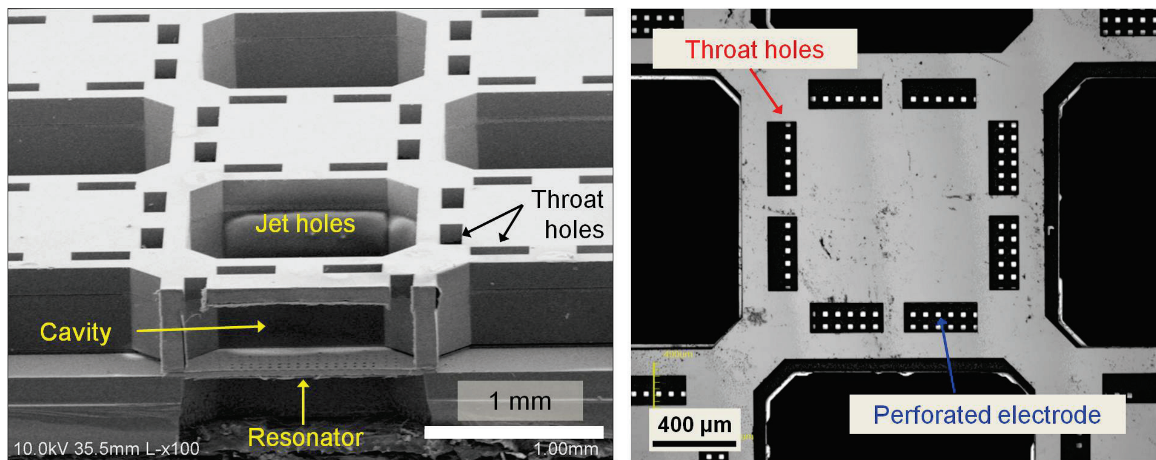

Figure 5-6: (Left) SEM of the cross section, (Right) Image using laser confocal microscope (top view). The perforations on the electrode can be seen through the throat holes.

5.1.1 Design of Contact Pads and Wire Connections

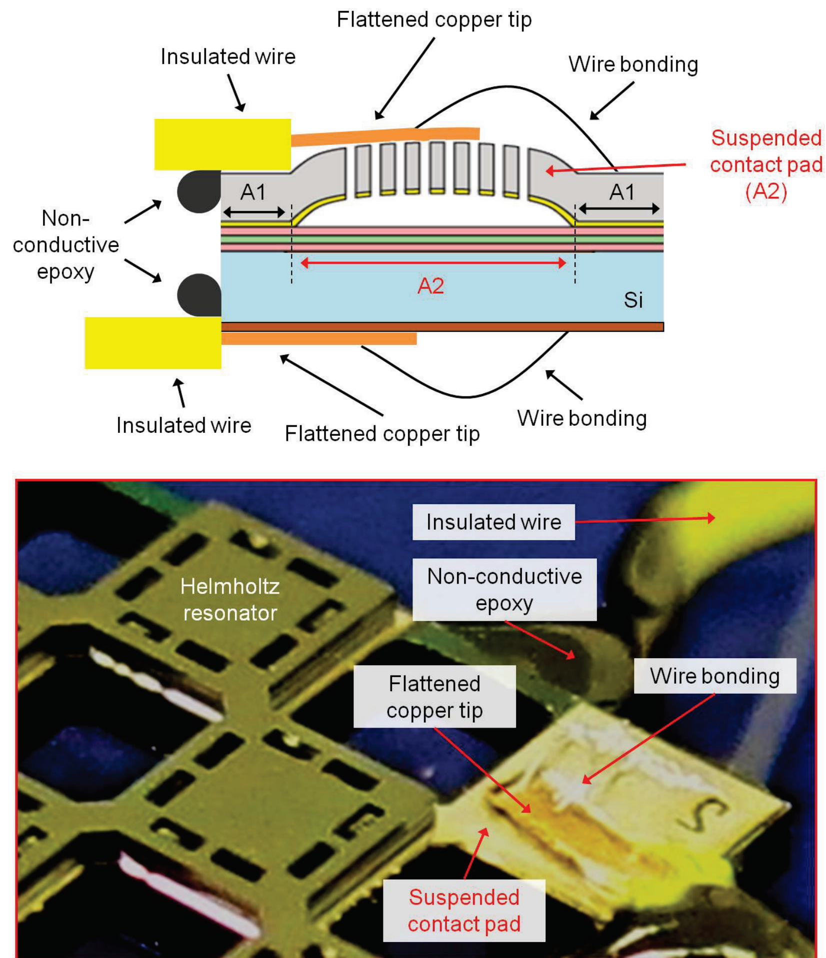

Figure 5-7: (Top) Illustrations of the cross-section of the contact pad with wire connections, and (Bottom) Photograph of the contact pad showing wire connections.

The design of the contact pads and wire connections can greatly influence the performance of the device, especially the parasitic capacitance and resistance. The area of the contact pad (A1 + A2 in Figure 5-7) accounts for most of the total parasitic capacitance. In order to lower the parasitic capacitance, this area has to be reduced. One way to reduce the parasitic capacitance is to suspend the contact pad such that a big portion of the contact pad (A2) has lower capacitance due to the introduction of an

additional air gap as dielectrics. The capacitance can be lowered by at least 50 pF while maintaining large surface area for wire connections. The fabrication process for the diaphragm actuator makes it easy to realize the suspended contact pad structure with no additional mask. For the Gen. 2 and 3 devices, the contact pad for each UJA is designed such that it utilizes the same fabrication process flow as the diaphragm actuator but without the DRIE backside release step, as shown in Figure 5-7.

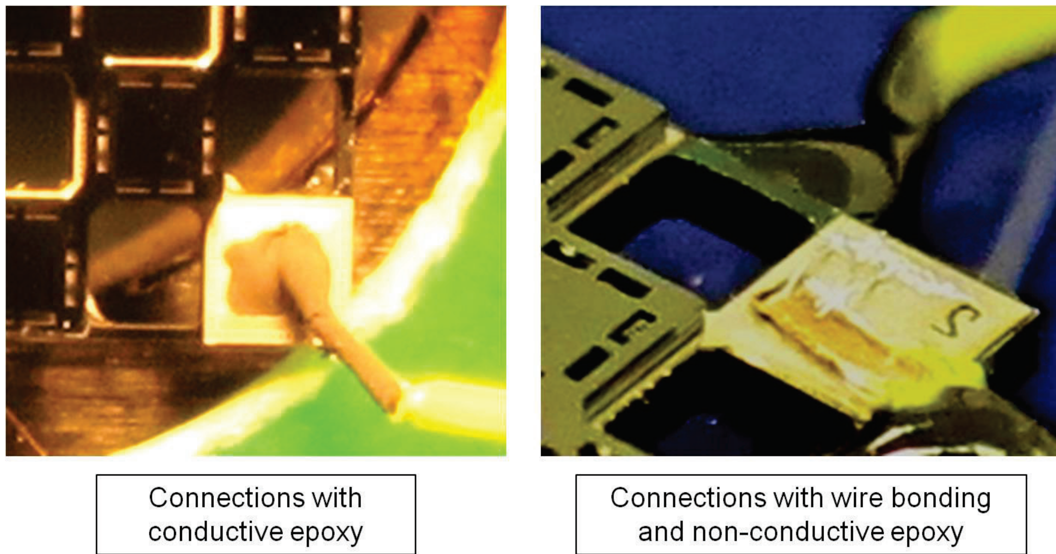

Figure 5-8: (Left) Wire connections made to the contact pad with nickel conductive epoxy and (Right) Connections made with wire bonding and non-conductive epoxy.

Making the wire connections can be very tricky as electrical shorting between the diaphragm and the rigid electrode can occur if bad connections are made. If the resistance path between the diaphragm and the rigid electrode is low, significant resistive heating can occur at high operating voltage and result in high power consumption. Initially, wire connections were made using nickel conductive epoxy and short insulated copper wire (Figure 5-8 (Left)). Soldering is not possible for making wire connections due to the

temperature-sensitive nickel rigid electrode, and only low temperature curing epoxy can be used. Nickel conductive epoxy (EPO-TEK® N20E) is recommended by the company because it can be cured at 80 ºC for 3 hours or at room temperature for a longer period of time. Nickel epoxy is also recommended instead of the common silver epoxy because the silver epoxy will create galvanic corrosion when connected with the aluminum metal layer (metal contact on the diaphragm) [78]. Unfortunately, the conductive epoxy is not the best solution for making wire connections. The epoxy can overflow and create shorts between the nickel rigid electrode and the silicon structure which also connects to the diaphragm. Significant heating is measured with an infrared camera (FLIR SC7000 series) at the conductive epoxy junction, as shown in Figure 5-9.

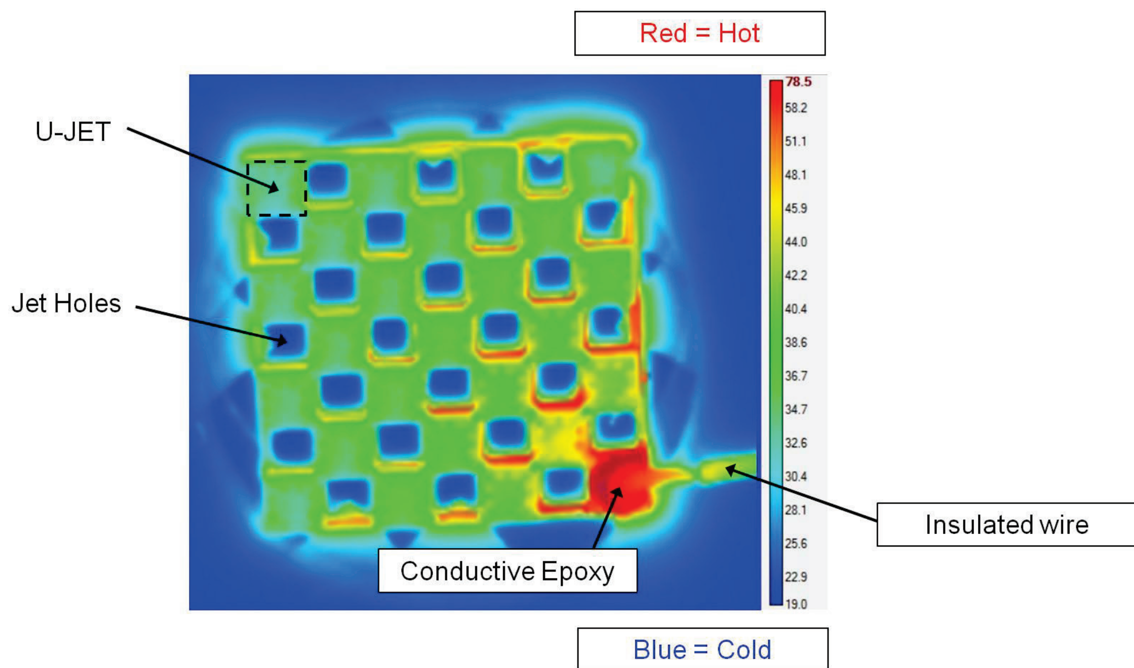

Figure 5-9: An infrared image obtained using FLIR SC7000 series infrared camera, showing relative temperature difference across the UJA. Significant heating is measured at the conductive epoxy junction.

A better way to make wire connections is as presented above in Figure 5-7 and in Figure 5-8 (Right). The short insulated copper wire is first flattened with tweezers and held in place on top of the contact pad with a flat-tip alligator clip. Next, the non-conductive epoxy is used to fix the position of the copper wire. Finally, wire bonding is performed to connect the copper wire to the contact pad. This connection method is less messy than the conductive epoxy and no heating is observed at the junction between the copper wire and the contact pad; however, unexpectedly, the non-conductive epoxy is showing slight heating. The heating of the non-conductive epoxy did not affect much of the performance of the device but further work on electrical connections is warranted.

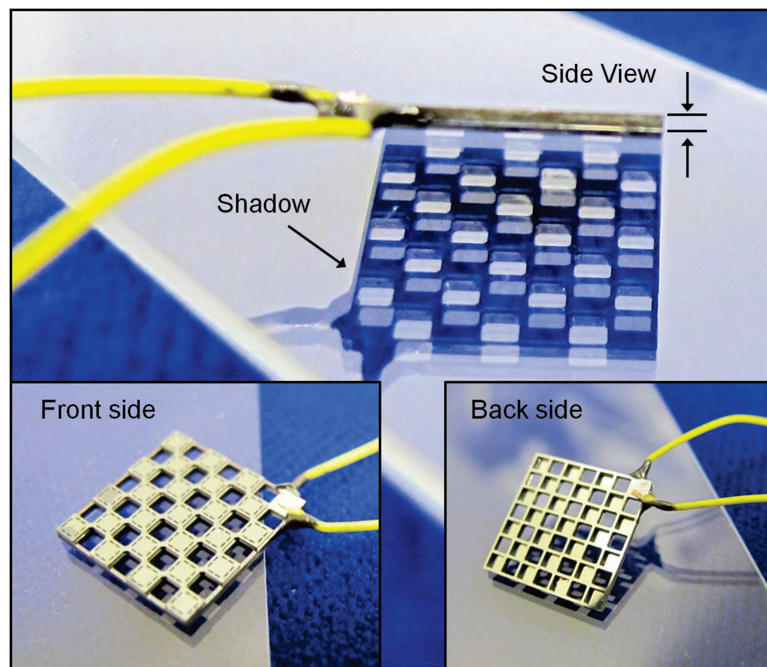

Figure 5-10: Photographs of the final UJA with wire connections, taking from the side view, front view and back view.

Figure 5-10 shows the final product of the UJA with wire connections. The product is designed for its light weight in both the device structure and also wire

connections. The short copper wire provides a means to connect to thinner and lighter wires (enameled copper wire of 50 μm diameter) through soldering. The total weight of the UJA without wires is 600 μN while the total weight with wires is 882 μN. This value is at least 5 times lighter than 5600 μN (reported by Kim *et al*. [42]).

5.2 Characterization of the UJA using Calibrated Microphone

With the completed device, the performance of the UJA can now be explored. A calibrated microphone is a good tool for a quick assessment of the qualitative performance of the UJA. The output voltage of the calibrated microphone is monitored and recorded with an oscilloscope. Although the microphone's output is only calibrated up to 80 kHz, it can be used as a tool to determine the relative performance of the device at frequencies beyond 80 kHz. For example, we will be able to know if a certain voltage waveform will produce higher acoustic output than another waveform but we might not know the absolute sound pressure produced by the UJA.

The setup of the characterization test is shown in Figure 5-11. The UJA is attached to a micro-manipulator fixture and the calibrated microphone is placed at a distance of ~ 3.5 cm away from the UJA. The properties of the UJA used in this characterization test are compiled in Table 5-1. The purpose of this test is to investigate the frequency response of the UJA with respect to four types of voltage waveforms (Figure 5-12 (Left)): (a) Pulse train with 20 % duty cycle and 30 % DC offset, (b) Sine wave with no offset, (c) Biphasic pulse train with 20 % duty cycle, and (d) Biphasic trapezoidal pulse (TRAPZ) with 20 % duty cycle but with a longer fall time.

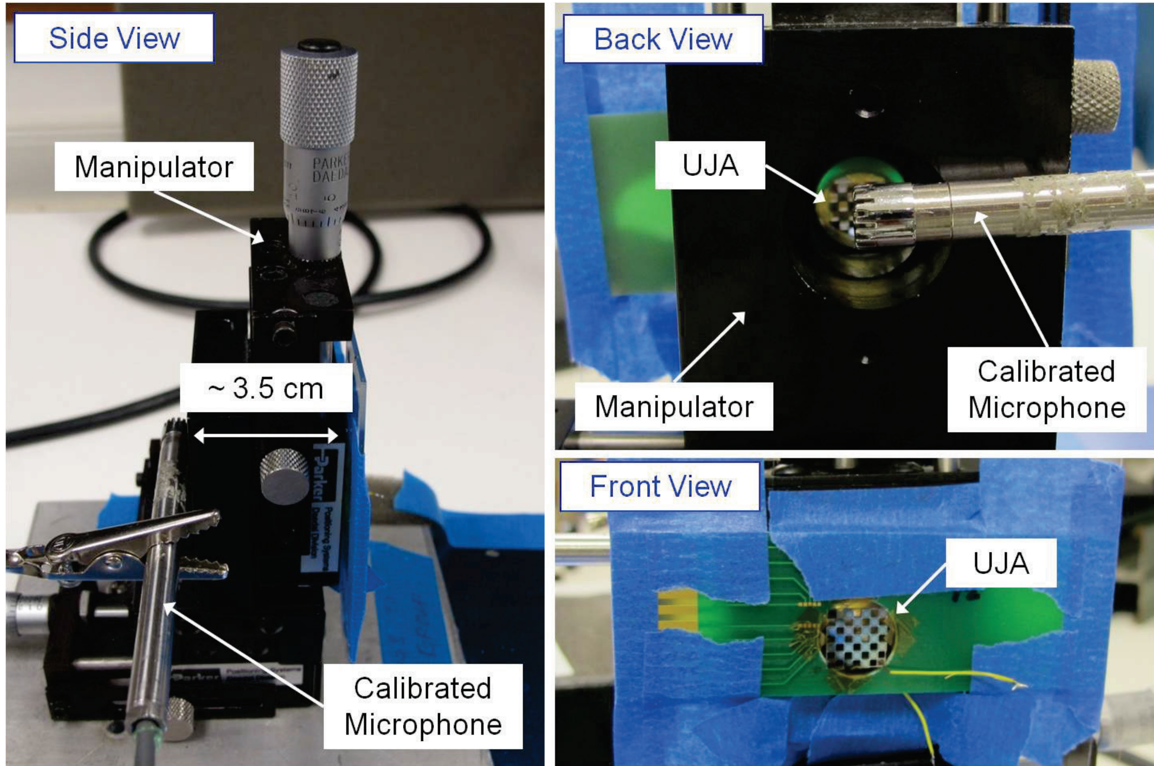

Figure 5-11: Setup of the calibrated microphone test to obtain a frequency response measurement of the UJA. The UJA is attached to the micro-manipulator fixture and the calibrated microphone is placed ~ 3.5 cm away from the UJA. Different views of the setup are included: (Left) side view, (Top Right) back view and (Bottom Right) front view.

Table 5-1: Properties of the UJA used in this characterization test.

Design Paramaters	Device A: P1-B (5-2)
Array Size	0.9 mm x 0.9 mm x 0.07 mm
Weight (without wires) (measured)	600 µN
Diaphragm Resonance (calculated)	103 kHz
Electrostatic Gap (measured average)	9.43 µm
Diaphragm Size	1.2 mm x 1.2 mm
Cavity Dimensions	1.2 mm x 1.2 mm x 400 µm
Throat Holes (measured)	350 µm x 100 µm
Throat Length (measured)	150 µm
Cavity Resonance (calculated)	52 kHz

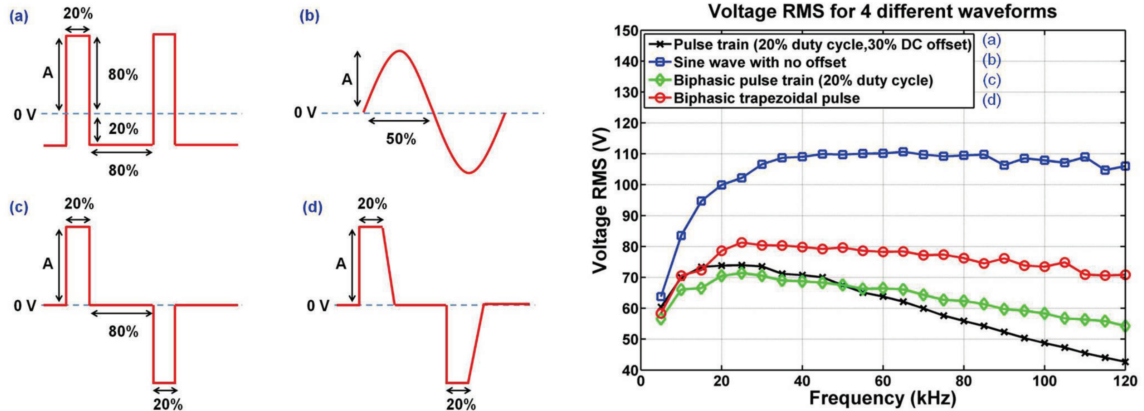

Figure 5-12: (Left) Four different waveforms used in test with amplitude A = 200V. (a) Pulse train with 20% duty cycle and 30% DC offset, (b) Sine wave with no offset, (c) Biphasic pulse train with 20% duty cycle, and (d) Biphasic trapezoidal pulse (TRAPZ) (20% duty cycle but with a larger fall time). (Right) Voltage RMS across the device. Frequency is plotted based on the frequency of the diaphragm's motion.

All four waveforms are generated using a function generator (Agilent 33250A) and amplified by a power amplifier (Trek Model PZD700A-L-CE M/S). For comparison, all waveforms have the same positive amplitude, A, of 200 V. The goal of trying the four different waveforms is to determine the best waveform for maximum pumping where the diaphragm is kept moving constantly; by reducing the amount of time when the diaphragm is in contact with the electrode (due to charging issues) and maximizing the motion of the diaphragm with the least RMS (root-mean-square) voltage. Figure 5-12 (Right) shows the actual RMS voltage across the device for the four different waveforms. Depending on the waveform applied, the diaphragm moves at the same frequency or twice the frequency of the applied voltage. The frequencies plotted in Figure 5-12 (Right), and Figure 5-13 to Figure 5-15 refer to the frequency of the diaphragm motion instead of the frequency of the applied waveform. Due to the lower negative amplitude for the pulse

waveform (waveform (a)), the diaphragm moves at the same frequency as the applied pulse waveform (waveform (a)) while it moves at twice the frequency of the other three applied waveforms (waveform (b), (c) and (d)).

The sine waveform has greater RMS value by at least 30 % than other waveforms. In addition, there seems to be a roll-off of the RMS values for 20 % duty cycle waveforms (pulse train, biphasic pulse train and biphasic TRAPZ). This can be due to the slew rate (> 380 V/µs) and bandwidth (DC to > 150 kHz (-3 dB)) limitation of the power amplifier (Trek PZD700A) causing distortion to the applied voltage.

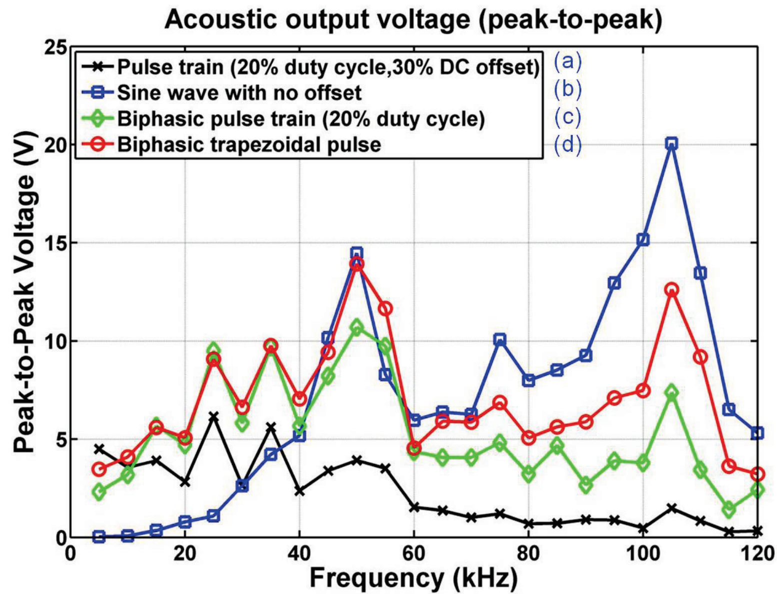

Figure 5-13: Calibrated microphone: Acoustic output voltage (peak-to-peak) (right after voltage is turned on). Frequency is plotted based on the frequency of the diaphragm's motion. Corresponding applied voltage RMS is as plotted in Figure 5-12 (Right).

Figure 5-13 presents the frequency response for the four waveforms (right after voltage is turned on). Since the sine waveform has the highest RMS value among these waveforms, the microphone detected the highest acoustic response from the sine

waveform. Sine waveform is desired for understanding the frequency response of the UJA because only a single frequency is applied at a time. The frequency response for the sine waveform shows two distinct peaks, at 50 kHz and 105 kHz respectively. These frequencies are expected as they correspond to the simulated values of the resonant frequency of the cavity (52 kHz) and the diaphragm (103 kHz) respectively (Table 5-1).

On the other hand, the two biphasic waveforms (pulse 20 % and TRAPZ) are combinations of multiple frequencies. These frequencies induce different modes of vibration of the diaphragm which corresponds to the smaller frequency peaks other than the two distinct peaks (50 kHz and 105 kHz). Although the RMS values for the biphasic waveforms are at least 30 % lower than the sine waveform, the frequency responses for both biphasic waveforms are almost comparable at the resonant peak of 50 kHz. This shows that with lower RMS and more efficient voltage waveform, similar output performance can be expected. The lower RMS value is advantageous because that will reduce charging effects. The trapezoidal biphasic waveform produces higher response than the biphasic pulse train waveform because the input RMS is slightly higher, but in general, both waveforms are pretty similar to each other and are good waveforms to use for testing.

Figure 5-14 presents the acoustic output after some time (~ 30 seconds) where the output settles to a static value. The discrepancy in the output readings between Figure 5-13 and Figure 5-14 might be attributed to the initial charging of the actuator. The sine wave has the highest RMS voltage among the waveforms; however, it also has the highest charging effects or discrepancy of the output readings (Figure 5-15).

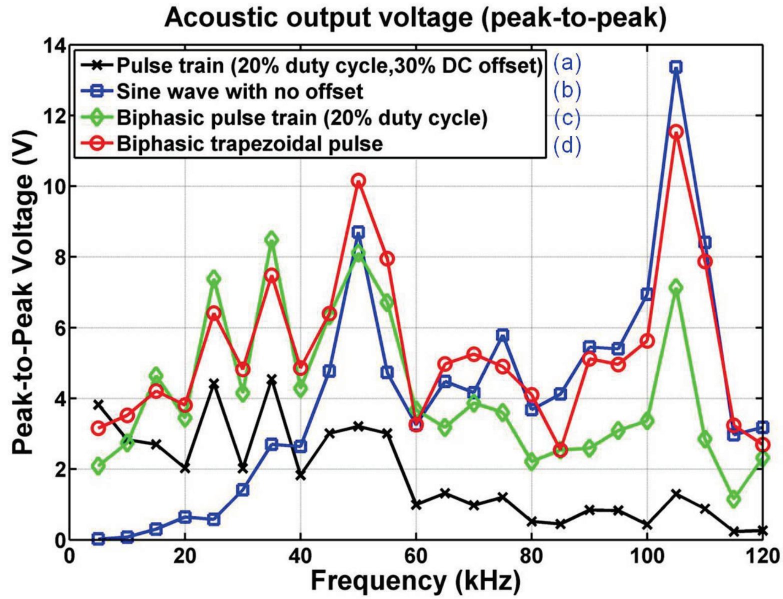

Figure 5-14: Calibrated microphone: Acoustic output voltage (peak-to-peak) (after ~30 seconds). Frequency is plotted based on the frequency of the diaphragm's motion.

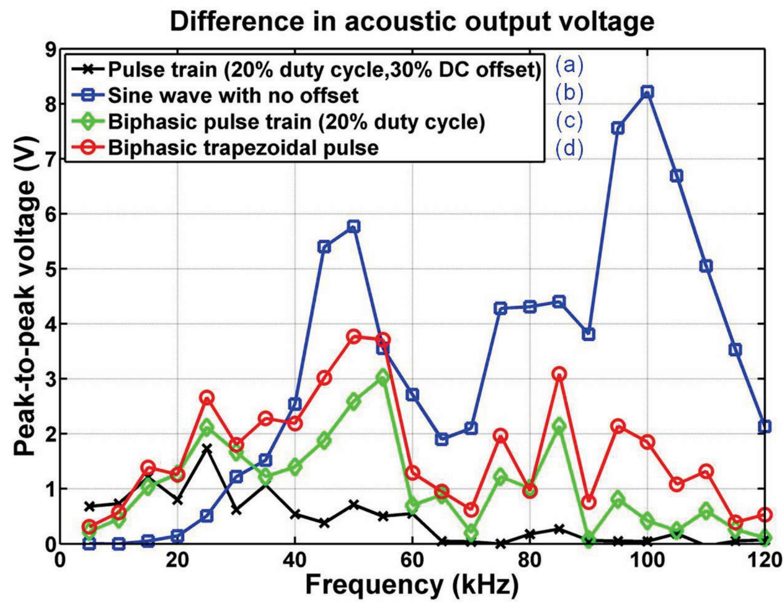

Figure 5-15: Difference in acoustic output voltage from calibrated microphone (discrepancy between Figure 5-13 and Figure 5-14). Frequency is plotted based on the frequency of the diaphragm's motion.

As seen in Figure 5-14, the output for the biphasic TRAPZ waveform can be comparable to the sine waveform because in Figure 5-15, the difference in the biphasic TRAPZ waveform output voltage is at least half that of the sine waveform. Therefore, biphasic TRAPZ is considered the most efficient waveform because it produces the highest acoustic output with the least variation. The pulse waveform has the least discrepancy in the acoustic output but it also has the lowest acoustic output.

5.3 Estimation of Air Micro-Jet Velocity

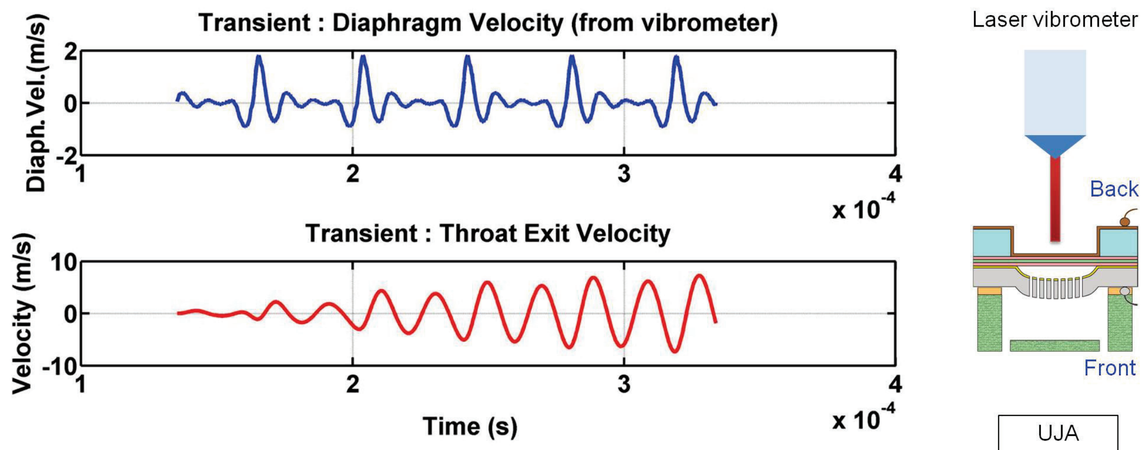

Figure 5-16: Jet velocity of 14 m/s peak to peak is calculated (lower trace) from the velocity of the diaphragm measured using a laser vibrometer system (upper trace).

A preliminary estimation of the air micro-jet velocity through the throat holes has been carried out using the diaphragm velocity data measured with a Polytec laser vibrometer system. Using the modeling equations in Chapter 2 and the diaphragm's motion as measured using the vibrometer system, the volume displacement in the cavity can be calculated (Equation 2.6). From the calculated volume displacement, the air micro-jet velocity can be predicted using Equation 2.2 and 2.3. As shown in Figure 5-16,

a peak air micro-jet speed of 7 m/s through the individual throat holes is estimated. This value is computed based upon the cavity dimensions that is attached during the vibrometer test (h_C = 400 μm, L_C = 1.6 mm, L_T = 125 μm, h_T = 350 μm, w_T = 140 μm) and actuation of pulse train waveform (20 % duty cycle and 30 % DC offset) at 26 kHz and peak-to-peak voltage of 300 V.

The purpose of this preliminary investigation of the air micro-jet velocity is to provide a rough understanding of the relationship between the diaphragm's velocity and the air micro-jet ejected through the throat holes. Of course, the predicted velocity value cannot be treated as the actual velocity because various damping and non-ideal effects are not included in this model. Higher air micro-jet velocity can be expected in the future because the cavity dimensions and the voltage waveform used in this velocity estimation are not optimized due to fabrication challenges. Following work in next sub-section will include cavity parameters fabricated closer to the optimized values with improvements in the developed fabrication technology.

5.4 Pendulum Test for Direct Thrust Measurements

A pendulum test is set up to perform direct thrust measurements, as shown in (Figure 5-17). This test is a standard test used in aerospace engineering to measure generated thrust. The thrust is calculated from the pendulum displacement, *d*, the length of the wire, *L*, and the weight of the device, *mg*, as shown in Equation 5.1.

$$Thrust = mg\sin\theta = mg\left(\frac{d}{L}\right) \tag{5.1}$$

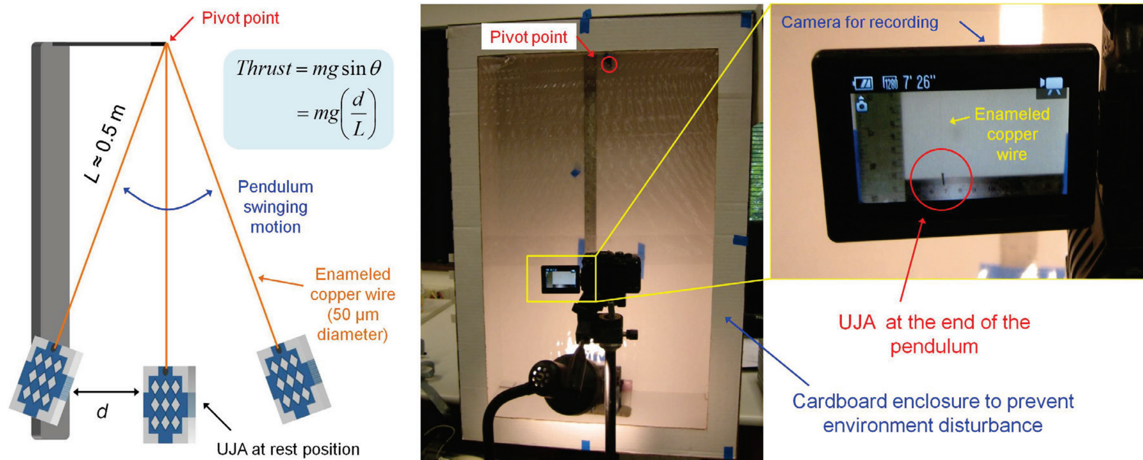

Figure 5-17: (Left) Illustrations of the pendulum test setup where a weight (UJA) is suspended on a pivot point with a string or thin wire. (Right) The pendulum test is enclosed with a cardboard enclosure to prevent environment disturbance and a camera is used to record the motion when the device is actuated.

An enameled copper wire is used to both support the device under test and provide the electrical connection to the drive circuitry. The connection is made by soldering the short insulated wire that was connected to the UJA using wire bonding and non-conductive epoxy (Figure 5-10) to an enameled copper wire of 50 µm diameter. The enameled copper wire is then used as the string to suspend the UJA at the end of the pendulum with an effective length of ~ 50 cm. In Figure 5-17 (Right), the pendulum test setup is enclosed with a cardboard screen to reduce environmental disturbances while collecting data. A ruler is placed at the background to measure total displacement and a digital camera is used to record the pendulum movements which are then converted to thrust.

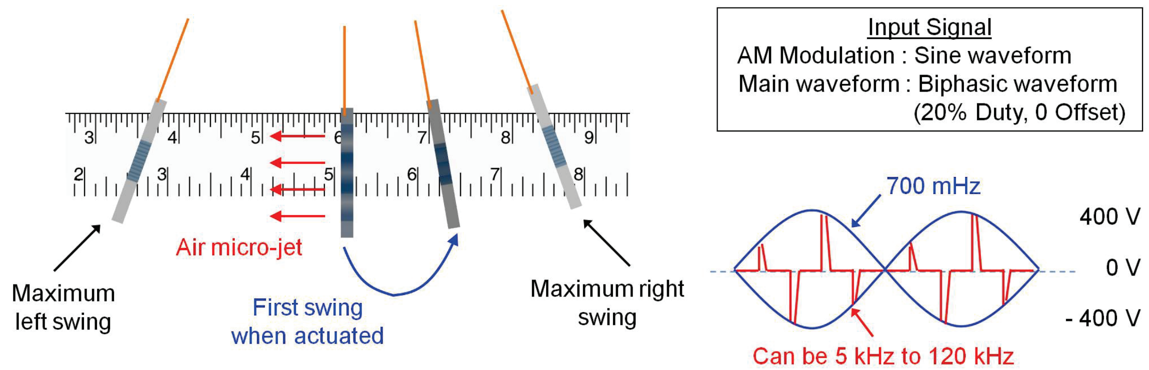

Figure 5-18: (Left) Illustration of the pendulum movement where the first swing of the UJA is to the opposite direction as the ejected air micro-jet, and it later reaches maximum left and right swing when modulated at the resonant frequency of the pendulum, (Right) Applied input signal: Amplitude modulation (AM) with sine wave envelope and biphasic waveform with 20% duty cycle and 0 offset at various frequencies from 5kHz to 120 kHz.

Thrust was measured by applying waveforms at both a fixed frequency and by sweeping over a range of frequencies. At a fixed frequency, the UJA will cause the pendulum to swing to a static displacement, *d*, and the thrust can be calculated. To optimize the waveform, both the frequency and amplitude of the applied waveform can be swept to find the highest thrust output. Care must be taken though to avoid damaging the UJA during a sweep because some waveforms exert more charging effects or stress on the UJA and eventually breaks the UJA before the perfect waveform can be found. Therefore, a good way to do a quick check if the UJA is operational and if the waveform can produce high thrust with the pendulum test is to perform an amplitude modulation test. In the amplitude modulation test, the amplitude of the main waveform is modulated such that the amplitude changes sinusoidally (Figure 5-18 (Right)) using a function generator and a power amplifier.

The amplitude modulation test builds up the displacement over a series of short thrust which can be timed for maximum amplitude. The UJA starts from its rest position at the center below the pivot point. When an impulse of thrust is generated by the air micro-jet, the UJA will have the first kick to the opposite direction of the air micro-jet, in agreement with the Newton's third law. At the end of the first kick where the UJA has the maximum potential energy but minimum kinetic energy, an impulse of thrust is again generated to increase the swing of the pendulum. This action is repeated at the resonant frequency of the pendulum, 700 mHz in this setup, to achieve maximum left and right swing. The achieved peak-to-peak swings generally are proportional to the thrust generated at first kick. The higher response obtained from the peak-to-peak swing allows us to better visualize the frequency response of the UJA.

From here onwards, there will be two types of pendulum tests: (1) "with AM modulation" which refers to when a sine envelope amplitude modulation is applied to the main waveform, and (2) "without AM modulation" which refers to applying a fixed frequency and amplitude. The tests "with AM modulation" are used to observe the relative thrust generation over a frequency spectrum to determine the best waveform for highest thrust performance while the tests "without AM modulation" are used to calculate the total thrust generated by the UJA. As a rough estimation, the static displacement of the pendulum in the test "without AM modulation" corresponds to the first swing in the test "with AM modulation". Although sometimes, the static displacement obtained is lower than the first swing due to the damping of the pendulum system (air friction) [79].

The following pendulum tests include three prototypes of UJA (device A, device B, and device C) with different cavity dimensions. Their parameters are listed in Table 5-2. The design for device A is based upon the optimized parameters using trapezoidal waveform (Table 2-2) except the cavity height, h_C. For initial test, a standard 525 ± 25 µm thick wafer is utilized for ease in handling and fabrication. Therefore, device A has a cavity height of 400 µm and throat length of 150 µm. Later, the fabrication process is improved using thinner wafers and cavity parameters as listed in Table 2-2 are realized (device B). To further improve the design for higher thrust, device C with cavity parameters as optimized using sinusoidal waveform (Figure 2-16) is fabricated. In the following sub-sections, the characterization of the thrust performance of the three prototypes with the pendulum test will be discussed individually. Device A is the same device that was used for the characterization with a calibrated microphone (sub-section 5.2).

Table 5-2: Properties of the three prototypes (A, B, and C) used in the pendulum tests.

Design Paramaters	Device A	Device B	Device C
Batch number (Sample number)	P1-B (5-2)	P1-B (2-4)	P4-A (2-2)
Weight (without wires) (measured)	600 µN	500 µN	1080 µN
Weight (with wires) (measured)	882 µN	862 µN	1505 µN
Diaphragm Resonance (calculated)	103 kHz	103 kHz	103 kHz
Electrostatic Gap (measured average)	9.43 µm	10.03 µm	10.63 µm
Diaphragm Size and Cavity Width	1.2 mm x 1.2 mm	1.2 mm x 1.2 mm	1.2 mm x 1.2 mm
Cavity Heights (measured)	400 µm	125 µm	200 µm
Throat Holes (measured)	350 µm x 100 µm	360 µm x 150 µm	50 µm x 200 µm
Throat Length (measured)	150 µm	100 µm	115 µm
Cavity Resonance (calculated)	52 kHz	73 kHz	45 kHz

5.4.1 Thrust measurements for Device A

As characterized by the calibrated microphone, device A has the highest performance at 105 kHz. Figure 5-19 shows the thrust performance when the device A is actuated at 105 kHz with varying voltages. For the test "with AM modulation", there are two data points: (1) First kick is the displacement from the first burst of thrust after the actuation begins and (2) maximum swing where the pendulum swings to its maximum peak-to-peak displacement after steady-state is reached. For the test "without AM modulation", there is only one data point which is the static displacement.

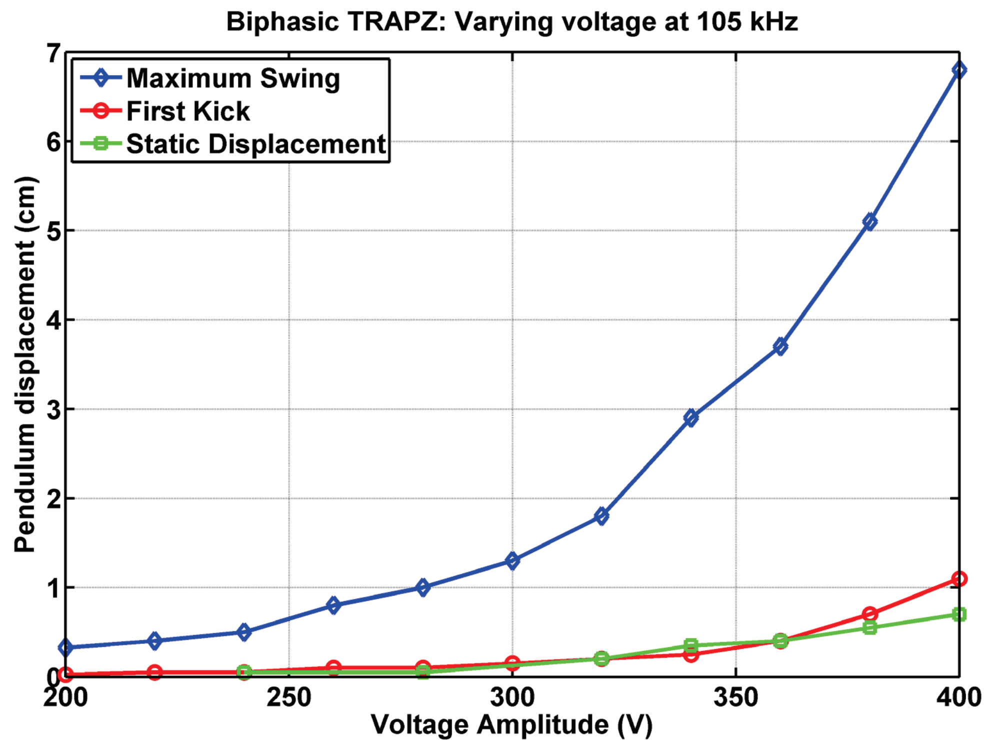

Figure 5-19: Comparisons of the thrust performance taken under two types of pendulum tests. The maximum swing and first kick data are collected under the "with AM modulation" test and the static displacement data is collected under the "without AM modulation" test. As can be seen on the plot, the first kick can be a rough estimate of the static displacement.

The voltages plotted in Figure 5-19 and other following plots are based on the applied voltage as set on the power amplifier. The actual voltage across the device will be lower since some voltage (approximately 15-17.5 %) will be dropped across the series capacitance, C_s, of 0.78 nF. The series capacitance value is lower than previously used for testing of Gen. 1 because the parasitic capacitance for Gen. 2 and Gen. 3 has been reduced. As can be seen in Figure 5-19, the first kick can be a rough estimate of the static displacement but for large drive voltage amplitude, the static displacement is lower. The first kick is used to estimate the response of the device to the waveform with less risk of damage than static displacement tests. The maximum swing also provides a good indication on which electrical parameters to apply for higher thrust generation without applying extensive electrical stress on the device, but it is necessary to account for the air damping in the pendulum system. It was noted during these experiments that the first kick and the static displacement recorded in these tests are in the same direction as the air micro-jets (to the left of the initial position, as shown in Figure 5-23). This behavior is further analyzed and explained towards the end of this sub-section.

The frequency dependency of the thrust performance for device A was obtained between 20 kHz to 120 kHz when actuated with a biphasic TRAPZ waveform of amplitude, A = 320 V. Subsequently, frequency sweeps at higher voltages are conducted around any distinct peaks obtained. Figure 5-20 shows the frequency sweep for A = 320 V with AM modulation and Figure 5-21 shows the comparisons of higher voltages with A = 340 V, 360 V, 380 V and 400 V. In Figure 5-21, the maximum peak-to-peak swings and the first kicks are plotted in two separate graphs. As expected, the

pendulum response increases with increasing applied voltage and peaks at the same resonant frequency. The tests were not extended to a lower frequency ranges because the applied electrical signal exerts high electrical stress on the device and often fractures the diaphragm. Higher voltage than 400 V was not applied because air breakdown might occur and breaks the device.

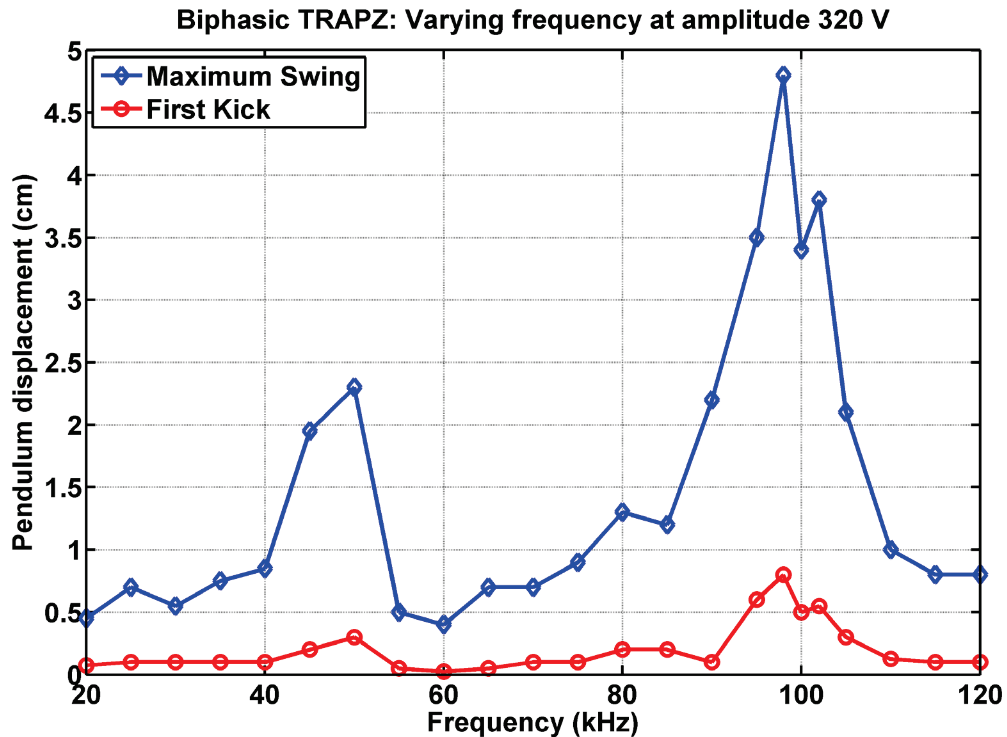

Figure 5-20: Pendulum test data obtained when actuated at voltage amplitude of 320 V and with AM modulation. The frequency response of the first kick and the maximum swing matches, giving us insights to determine the best signal for maximum thrust performance. Pendulum displacement is to the left of the initial position, as shown in Figure 5-23.

The frequency dependency of the static displacement is obtained when actuated without AM modulation. Figure 5-22(Left) summarizes the static displacements for varying frequencies and the corresponding thrust generation is calculated and plotted in

Figure 5-22(Right). A maximum thrust of ~ 12 μN is obtained when actuated at a frequency of 102 kHz and A = 400 V.

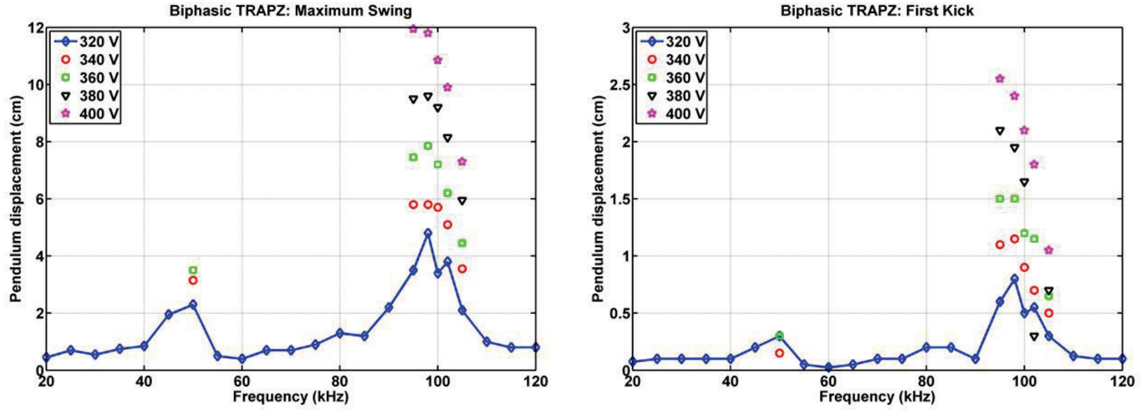

Figure 5-21: (Left) Comparisons of the maximum swing and (Right) comparisons of the first kick for varying applied voltages with AM modulation. Pendulum displacement is to the left of the initial position, as shown in Figure 5-23.

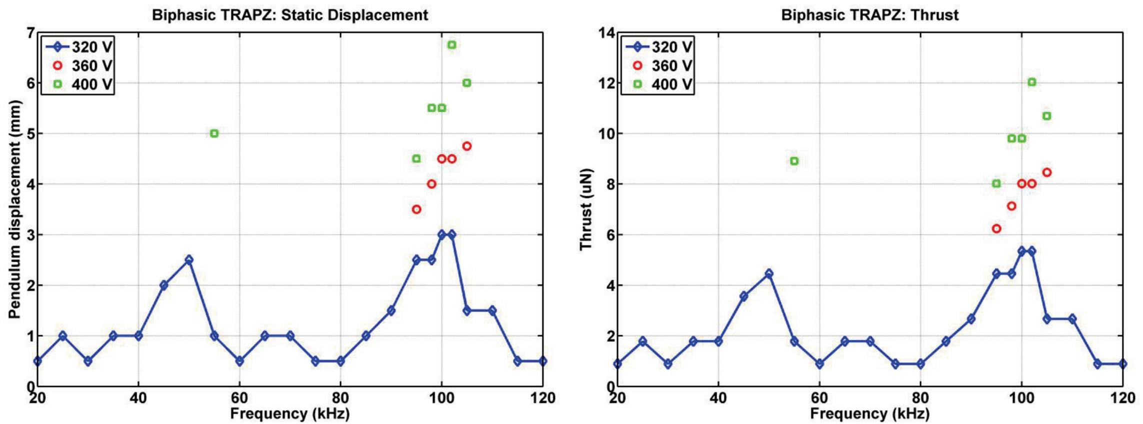

Figure 5-22: (Left) Static displacements versus varying frequencies for A = 320 V, 360 V and 400 V, and (Right) the thrusts calculated from corresponding static displacements. Pendulum displacement is to the left of the initial position, as shown in Figure 5-23.

As aforementioned, the first kick and static displacement of the pendulum is in the same direction as the ejected air micro-jets and this deviates from the expected response. Snapshots of the video clip for the test with AM modulation are merged into one in Figure 5-23 for illustration of the pendulum motion. The device is actuated with a voltage amplitude of A = 400 V at 95 kHz (maximum point in Figure 5-21); however, as noted before, the actual voltage across the device is only ~ A = 300 V due to the series capacitance. As presented in Figure 5-23, the first kick is in the same direction as the air micro-jet which is to the left, with a distance of ~ 2.55 cm and maximum peak-to-peak swing of ~ 11.4 cm.

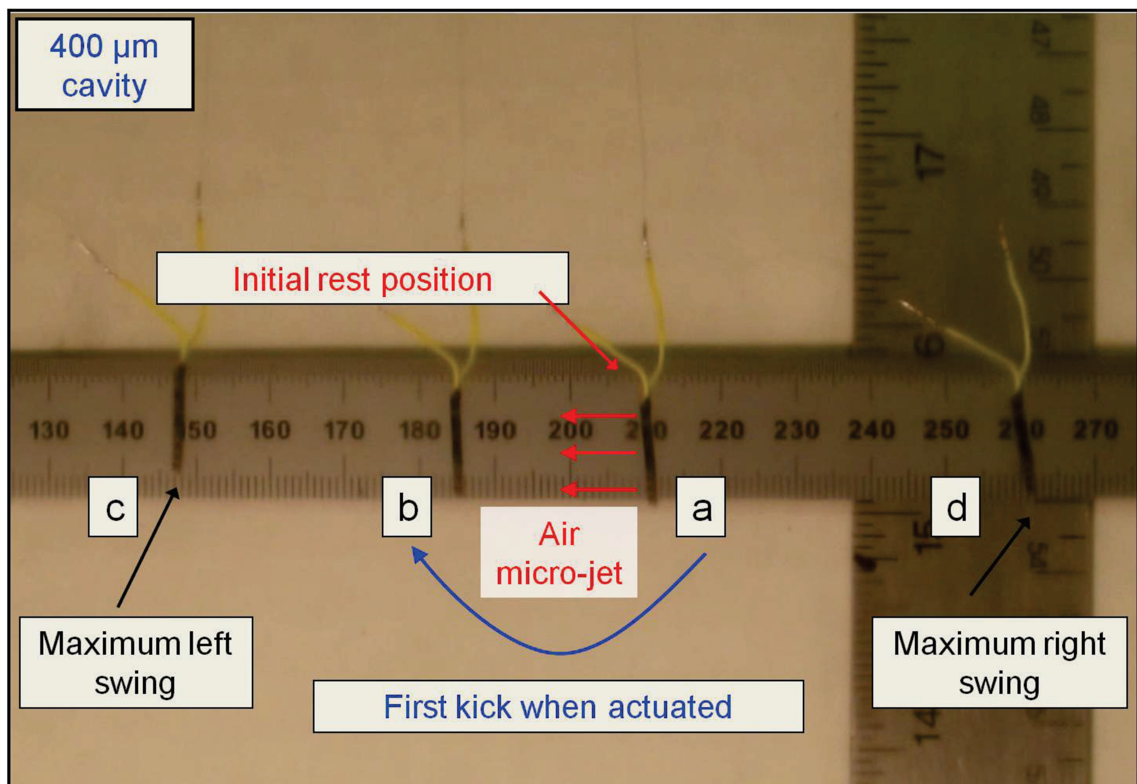

Figure 5-23: Experimental results with device A (snapshots of video clip merged into one): (a) Thruster rest position at time 0 sec, (b) Initial kick-off swing with displacement of ~ 2.55 cm, (c) Maximum swing to the left and (d) Maximum swing to the right when AM modulation is applied.

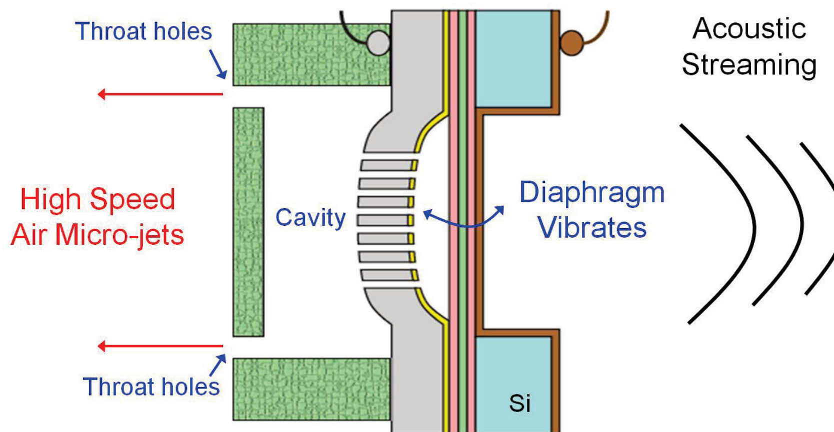

Figure 5-24: The cross-section is drawn to show the operation of a single U-JET. On the left side of the diaphragm, high-speed air micro-jets are expected through the throat holes. On the right side, acoustic streaming effect as explained by Lighthill [56] is observed.

To explain the behavior in Figure 5-23, Figure 5-24 is drawn showing the operation of a single U-JET. As the diaphragm vibrates, it moves the air adjacent to the surfaces of the diaphragm, creating disturbance to the surrounding fluid. On the left, a Helmholtz resonator enhances the air motion and high-speed air micro-jets are expected to eject through the throat holes. On the right, this disturbance is referred to as acoustic streaming by Lighthill [56], which should quickly dissipate through the surrounding medium. According to Lighthill [56], this phenomenon is generally observed at operating frequencies on the order of 1 MHz; however, it is interesting to observe that in this work, significant thrust was observed for the first time at frequencies near 100 kHz. Since the device A moves to the left direction, the thrust produced by acoustic streaming is greater than the air micro-jets. The low thrust from air micro-jets can be due to the non-optimized parameters of the Helmholtz resonator. Instead of enhancing the generated

thrust of the air micro-jets, the Helmholtz resonator acts like a damper and reduces the overall thrust ejected through the throat holes.

Theoretically, acoustic streaming can be estimated using the model developed by Lighthill [56], which is predicted to be orders of magnitude lower than the thrust generated by the air micro-jets. This acoustic streaming can therefore be considered as a parasitic effect. In the future, the performance of the UJA can be further improved to take advantage of the acoustic streaming by re-routing the flow to the same direction as the air micro-jets.

5.4.2 Thrust measurements for Device B

Due to the modular design of a UJA, for a given diaphragm, the design parameters of the Helmholtz resonator can be easily varied to optimize for higher thrust performance. For device B, the main variation from device A is the cavity height, which is reduced from 400 μm to 125 μm (closer to optimized value in Table 2-2). The reduction in the cavity height increases the acoustic resonance of the cavity to 73 kHz, making it closer to the diaphragm's natural resonance of 103 kHz (Table 5-2). Higher thrust is expected if the acoustic resonance is matched with the diaphragm's natural resonant frequency. Similar pendulum tests are performed to obtain thrust measurements with the new dimensions for the cavity for device B.

Figure 5-25 shows the data recorded for the pendulum tests with AM modulation. With the improved design, the pendulum moves in the opposite direction of the air ejected by the micro-jets as expected. The results show that the thrust generated by the air

micro-jets is greater than device B and is able to overcome the acoustic streaming effect on the right hand side.

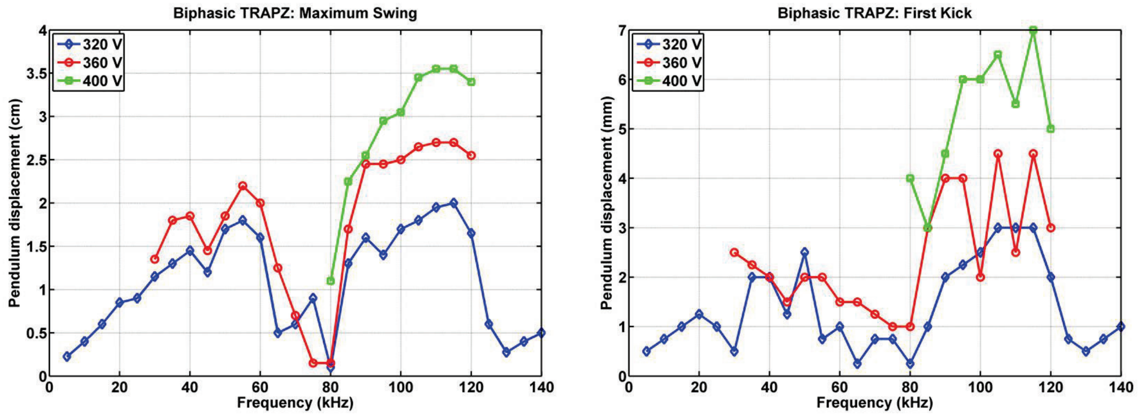

Figure 5-25: (Left) Maximum swing for applied voltage of A = 320 V, 360 V and 400 V with varying frequencies, and (Right) first kick of the pendulum test with AM modulation for device B.

The measured static displacement in Figure 5-26 shows a maximum displacement of 3 mm and this value corresponds to a thrust of near ~ 5 μN; however, this thrust value is the difference between the thrust due to the air micro-jet and the thrust due to the acoustic streaming effect. Therefore, if the thrust obtained by device A is assumed to be generated only by the acoustic streaming effect and similar thrust is assumed for the acoustic streaming effect as device B, then the total thrust produced by the air micro-jets will be ~ 17 μN (5 μN + 12 μN). This assumption of similar acoustic streaming thrust is valid because both devices have the same diaphragm design and are actuated at approximately the same frequencies.

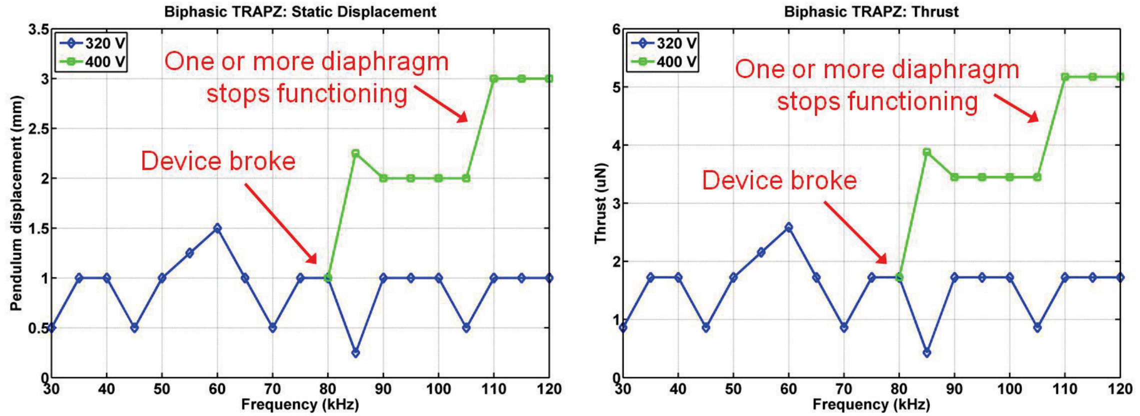

Figure 5-26: Data recorded for pendulum test without AM modulation. (Left) Static displacements versus varying frequencies and (Right) the calculated thrusts based on the measured static displacements. For high voltage operation (A = 400 V), the drop in the measured displacement and thrust can be due to one or more diaphragms breaking and eventually at around 80 kHz, the device stops functioning.

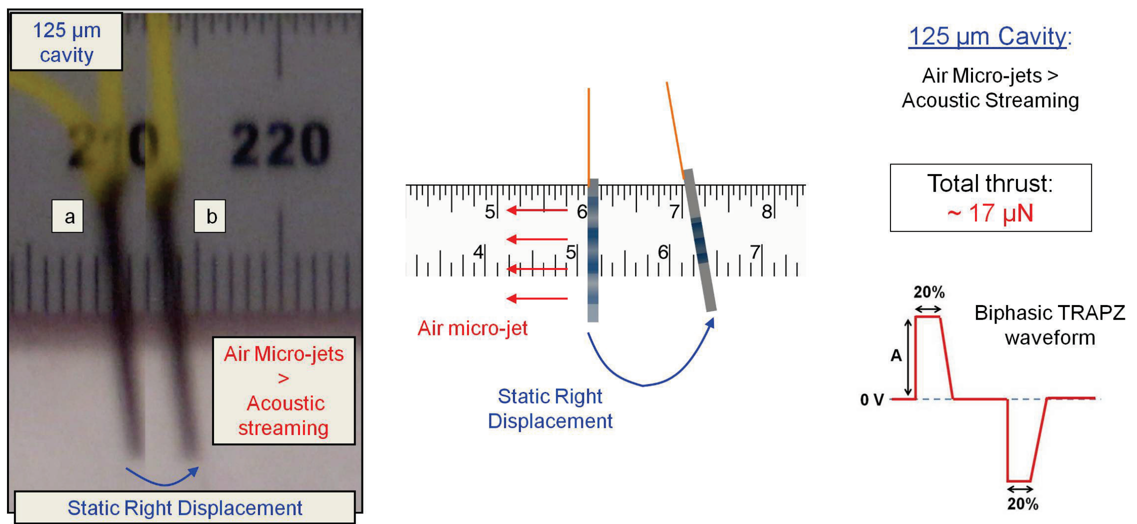

Figure 5-27: Pendulum test without AM modulation with Device B (snapshots of video clip merged into one): (Left) Static displacement to the right showing that thrust by air micro-jets is greater than thrust by acoustic streaming effect. (Middle) Illustration of the direction of the air micro-jet and the static displacement, and (Right) A total thrust ejected by the air micro-jets is predicted to be ~ 17 μN with the biphasic TRAPZ waveform, with the assumption that the air micro-jets needs to overcome the thrust generated by acoustic streaming effect.

Figure 5-27 shows the snapshots of the video clip for pendulum test without AM modulation merged into one. A displacement to the right is observed, signifying that the thrust by the air micro-jets are greater than the acoustic streaming effect. The power consumption for device B is measured to be 2.8 mW per U-JET.

5.4.3 Thrust measurements for Device C

Building on the positive result of optimizing the cavity height of device B, device C is constructed by optimizing other design parameters such as the throat cross-section area (throat height, h_T, and throat width, w_T). Using the simulation results shown in Figure 2-16, the throats dimensions (h_T x w_T) are modified from 150 µm x 360 µm to 50 µm x 200 µm for device C. The cavity height is designed to be 250 µm as this value is simulated to give the highest performance for the throat dimensions of 50 µm x 200 µm; however, due to fabrication variation, the actual cavity height is 200 µm.

Additionally, since the acoustic streaming is like a parasitic effect, the streaming effect is suppressed with both back cavity cap (made from silicon and with the same process as the Helmholtz resonator) and Kapton® tape (if the back cavity cap has throat holes in the design). From all the changes made to device C, the resulting weight of the device is slightly larger than the other two devices. This weight can be reduced in the future by integrating the back cavity cap design.

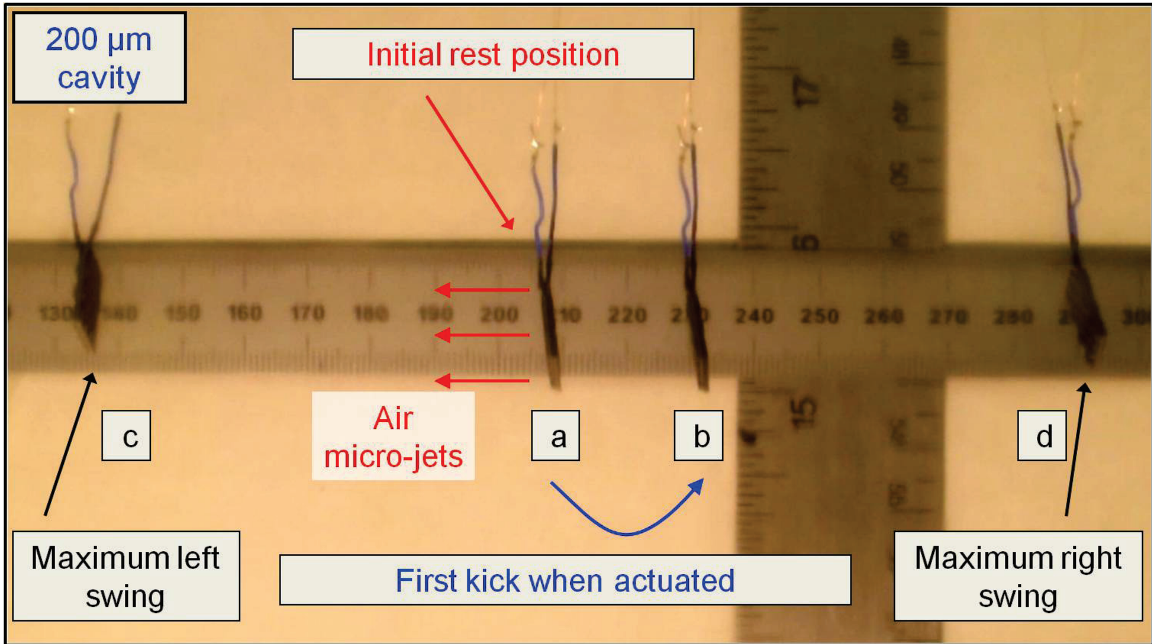

Figure 5-28: AM modulation test with Device C (snapshots of video clip merged into one): (a) Thruster rest position at time 0 sec, (b) Initial kick-off swing with displacement of ~ 2.3 cm, (c) Maximum swing to the left and (d) Maximum swing to the right when AM modulation is applied.

Again, an AM modulation test was conducted to explore the thrust generated by device C. Very large swings of the pendulum were observed and the best result is presented in Figure 5-28. With the suppressed acoustic streaming, the pendulum can kick-start only to the opposite direction of the air micro-jets. The first kick is ~ 2.3 cm and the maximum swing (peak-to-peak) is ~ 15.5 cm. The actual voltage across the device is ~ 330 V and the diaphragm moves at 55 kHz. The optimum frequency is lower than those for devices A and B because the smaller throat area reduces the acoustic resonance to a lower value. Figure 5-29 shows the maximum static displacement measured with device C (~ 1.3 cm). The calculated thrust from this displacement is ~ 46 µN.

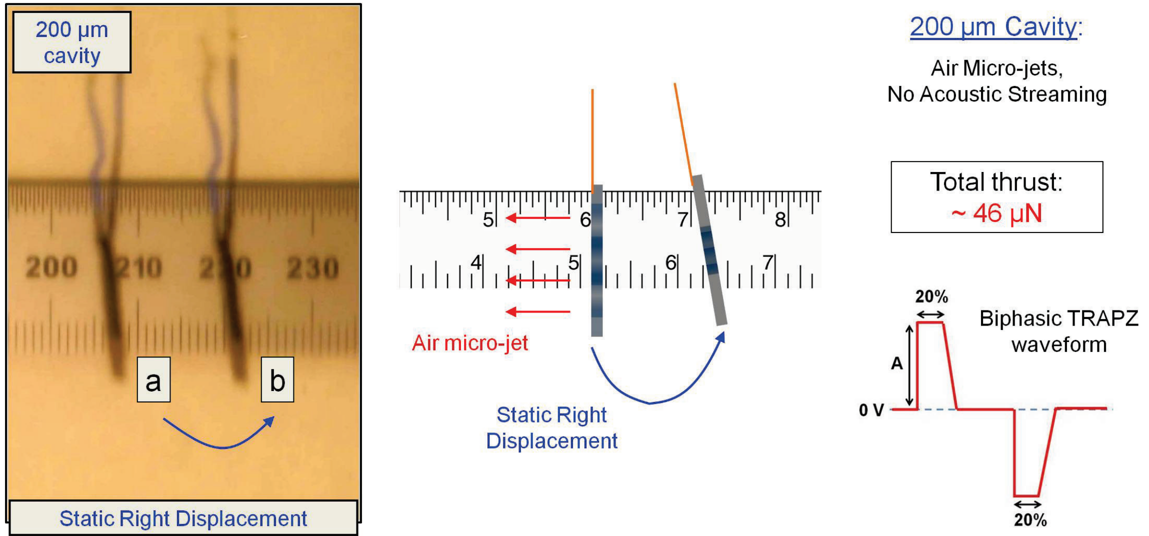

Figure 5-29: Pendulum test without AM modulation with Device C (snapshots of video clip merged into one): (Left) Static displacement to the right showing a large displacement of ~ 1.3 cm. (Middle) Illustration of the direction of the air micro-jet and the static displacement, and (Right) A total thrust ejected by the air micro-jets is calculated as 46 µN with suppressed acoustic streaming.

The results obtained from the experiment with device C are interesting. They show that higher air micro-jet speed can be achieved using the optimization procedure for sinusoidal waveform where h_T and w_T are varied at the same time while keeping the ratio of h_T to w_T constant. The peak thrust is found to be at 55 kHz and this frequency is close to the predicted resonance of the cavity (45 kHz). A power consumption of 10 mW per U-JET is measured with device C, which is much higher than device B. The higher power consumption can be attributed to the slight heating of the non-conductive epoxy which was holding the insulated wires in place. In the future, with further optimization of the device and assembly, lower power consumption with higher thrust performance is expected.

5.5 Summary

Development of UJA is realized by assembling the U-JET with a Helmholtz resonator. The two curing step SU-8 bonding provides a clean way to perform alignment of the parts and achieve sufficient bonding strength. The method used to make wire connections showed good performance and the wires only slightly increased the total weight of the device. In the future, a non-conductive epoxy with higher breakdown voltage should be used to reduce the slight heating of the epoxy during high voltage applications.

Table 5-3: Summary of this work compared to the state of the art.

Design Parameters	Chou *et al*. [41]	Kim *et al*. [42]	This Work	
			Device B	Device C
Cavity height	100 µm	100 µm	125 µm	200 µm
Array Size	1.6 cm x 1.6 cm	1.6 cm x 1.6 cm	0.9 mm x 0.9 mm	
Weight (no wires)	-	5600 µN	500 µN	1080 µN
Weight (with wires)	5684 µN	19600 µN	862 µN	1505 µN
Operation frequency	70 kHz	70 kHz	105 kHz	55 kHz
Voltage (V)	120 V	140 V	300 V	330 V
Electrostatic gap	4 µm	8.8 µm	~ 10 µm	
Jet Velocity	0.8 m/s	1 m/s	7 m/s (estimated peak velocity)	
Thrust per array	27 µN	55.6 µN	17 µN	46 µN
Thrust / Weight	0.0047	0.0099	0.034	0.043
Power Consumption per U-JET	12 mW	3.1 mW	2.8 mW	10 mW

Table 5-3 summarizes the design parameters as well as the performance for device A and B, and C, and compares to the state of the art. The generated air micro-jet is estimated to achieve a peak speed of 7 m/s, which is a 7x improvement over previous work. By optimizing the cavity depth and throat sizes, as well as reduction of acoustic streaming by the use of a back cavity cap, total thrust was increased from 17 µN to 46 µN.

The compact design of the UJA produces a light-weight device with greater than 5x improvements compared to previous work. A maximum thrust of 46 μN is generated by device C resulting in a thrust-to-weight ratio of 0.043. As compared to previous work, this ratio shows an improvement of a factor of 4.3.

The acoustic property of the cavity plays an important role in generating high-speed air jets. The resonant frequency of the cavity needs to be designed such that it is close to the resonant frequency of the resonating diaphragm. Reducing the cavity height, throat length and increasing the throat area will increase the resonant frequency of the cavity; however, damping effects need to be taken into considerations. Therefore, there is an optimum point where high thrust can be produced.

From the experimental investigation with the pendulum test, substantial acoustic streaming from the diaphragm can be observed at 100 kHz frequency range. Future designs of the UJA can take advantage of this parasitic effect by routing the generated thrust to the same side as the air micro-jets. Or even better, a dual cavity design can be used to enhance the acoustic streaming of the diaphragm on both sides to produce higher thrust.

The pendulum test with devices A, B, and C has lead us to better understanding of the influence of each design parameters. In the future, more improvements can be made to the design of the devices such as reducing the cavity height of device C to increase the resonant frequency of the cavity or reducing the throat length, L_T, with improved fabrication without compromising the mechanical integrity and robustness.

CHAPTER 6

CONCLUSIONS AND FUTURE WORKS

6.1 Conclusions

This thesis work presented the design and development of a high-frequency, large-gap diaphragm actuator having high reliability. The diaphragm actuator is fabricated and utilized in the development of the ultrasonic jet array (UJA) for eventual micro propulsion applications.

The main contributions of this research work are summarized as follows:

1. Incorporation of the non-linearity of the large deflection due to increased flexural rigidity into the modeling of a single-sided electrode of a forced Helmholtz resonator. The non-linear diaphragm resonant frequency is fitted from a non-linear computational analysis using COMSOL.
2. From the modeling efforts and experimental investigations, the acoustic resonant frequency of the Helmholtz resonator needs to be designed such that it is close to the mechanical resonant frequency of the diaphragm, with damping effects taken into considerations. The h_T and w_T parameters need to be optimized at the same time while keeping a constant ratio of h_T to w_T to produce designs with more realistic parameters. The modularity of

the fabrication process allows easy optimization of the Helmholtz resonator to further increase the thrust performance.

3. The design parameters for the ultrasonic jets (U-JET) are optimized to achieve the final goal of a thrust-to-weight ratio greater than one. Theoretical results show the possibility of achieving flight with a thrust-to-weight ratio of up to 2.8 with the optimized design parameters and trapezoidal drive waveform.
4. A new, simple, and robust fabrication technology is developed to realize a reliable high-frequency, large-gap electrostatic diaphragm actuator. The versatile nature of the fabrication technology allows different arrangements for the UJA such as the checkerboard, honey comb and dream catcher arrangements.
5. A new type of electrode, the filleted electrode, is designed to improve the reliability of the large-gap diaphragm actuator. Reliable actuation of > 229 billion cycles was demonstrated with the filleted electrode design without any diaphragm breakage.
6. Design and optimization of a compact and lightweight ultrasonic jet array (UJA) for potential applications such as micro propulsion and chip cooling. The UJA consists of 24 actuators and has a volume of 0.9 x 0.9 x 0.1 cm^3. A 5x lighter device is produced with a maximum thrust generation of 46 μN, resulting in a 4.3x improvement in the thrust-to-weight ratio over previous work.

7. The best electrical waveform for driving the diaphragm efficiently is determined using various test methodologies such as an optical microscope, a laser vibrometer system, a calibrated microphone and a pendulum test setup. A biphasic trapezoidal waveform with 20 % duty cycle is best when driving the diaphragm at voltages beyond pull-in. Charging effects can be greatly reduced if the contact time between the diaphragm and the rigid electrode is reduced. Therefore, a biphasic trapezoidal waveform is recommended to minimize charging effects.
8. Significant acoustic streaming from the diaphragm was observed for the first time at frequencies near 100 kHz. This parasitic streaming effect can be taken advantage of in the future design by routing the acoustic streaming to the same direction as the generated air micro-jets, such as the proposed dual-cavity design.

There are several damping effects and non-idealities in the system which are not included in the modeling effort or require better estimations, possibly leading to the performance discrepancy in the simulated versus experimental results. For example, the squeeze-film damping effect in the gap between the diaphragm and the rigid perforated electrode was assumed to be small compared to other damping effects and was neglected in the model. The damping effects as estimated in the inertia and viscous lengths (L_E and L_V) may require a more accurate estimation using newer and more sophisticated modeling tools. In the simulation model, the diaphragm is assumed to deflect only at the first mode of vibration; however, in reality, the modes of vibration can be different especially when

actuated with a trapezoidal waveform. These modes of vibration can greatly affect the total volume displacement and therefore the produced thrust.

Although the thrust-to-weight ratio is far from one, we are one step closer to the goal of flight, as shown in Figure 7-1. Various tasks can be performed in the future to increase the thrust-to-weight ratio and will be discussed in the next sub-section.

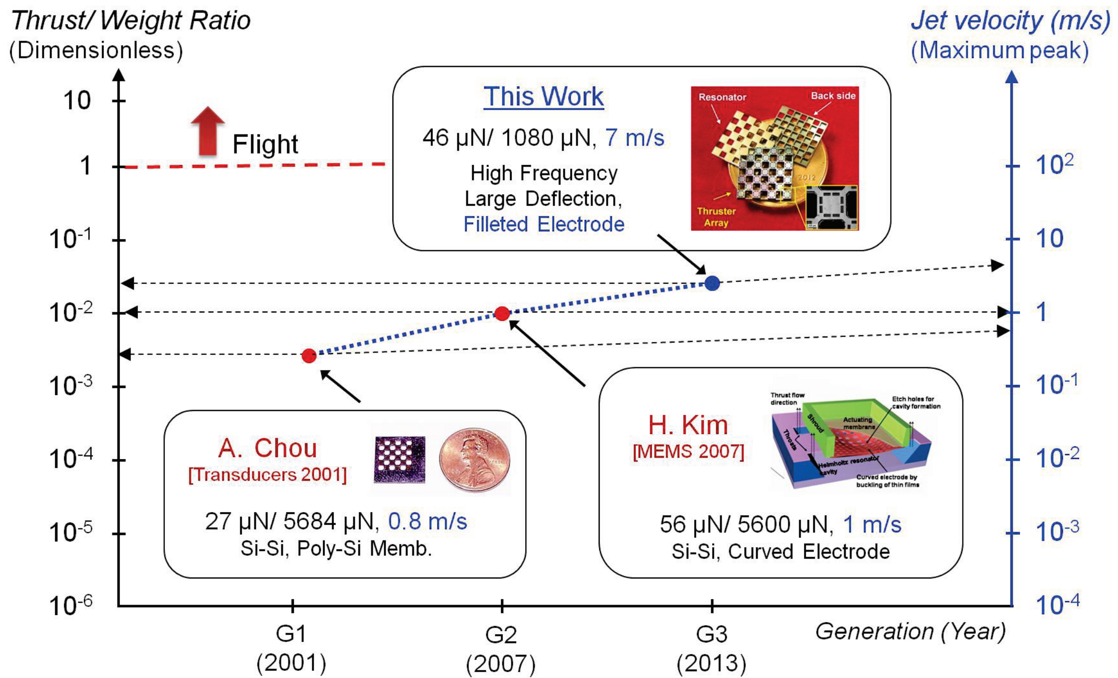

Figure 7-1: Comparisons of the performance achieved in this work with respect to previous work in the group. An improvement of 4.3 times in the thrust-to-weight ratio is achieved with new fabrication technologies and designs as well as more efficient way to drive the diaphragm actuators.

6.2 Future Work

Further research can be conducted to increase the thrust-to-weight ratio, such as the following:

1. Further optimization of the parameters of the Helmholtz resonator where the acoustic resonant frequency is brought closer to the mechanical resonant frequency of the diaphragm and with damping effects taken into considerations.
2. Investigation on the influence of different arrangements of the UJA such as the honey comb and dream catcher design. The area density of the U-JETs in the UJA as well as the shape of the diaphragm actuator can influence the flow entrainment properties.
3. Development of dual-cavity design by taking advantage of the acoustic streaming on both sides of the diaphragm to produce higher thrust. More experiments are required to optimize the dual-cavity design for maximum thrust performance.
4. Exploration on other actuation methods such as piezoelectric actuation, or combinations of piezoelectric or electromagnetic with electrostatic actuation to lower the high operating voltage.
5. Discovery of other materials with compatible fabrication techniques to build stronger and lighter weight UJA.

By incorporating the above suggested work, it will be possible to ultimately achieve the goal of flight. It is believed that this dream of flight will be brought to reality and small flying silicon platforms can be utilized for various micro propulsion applications. Additionally, the developed technologies in this work can be used in various other applications such as chip cooling, gas pumping, and high performance acoustic transducers.

APPENDIX A

MATLAB CODE FOR COUPLED SYSTEM MODELING

A1.1 Example of Parameter Sweep

```
% Filename: new_sweep_11.m

%----------------------------------------------------------------------------

% Start with setting Lt to be 75 um.
% Lc = 1.2 mm
% hc = 100 um
% vary throat areas: ht x wt, at 200V and 400V.
% Area1 ratio is 1:2.5.

%----------------------------------------------------------------------------
% 80x200 for 200V

% ------------------------
% Device Parameter (length modified)
% ------------------------

clear all
format long

h2_thrust=[];
h2_velocity=[];
h2_pressure=[];
h2_disp=[];
h2_frequencyMax=[];
h2_resonancefreq=[];
h2=[];

% --------------
% Parameters (Vary hc2 2)
% --------------

Lm = 1.2*10^(-3);                          % membrane length
ho = 10*10^(-6);                           % membrane diaphragm distance
Nt = 8;                                    % number of throats
ht = 80*10^(-6);                           % throat height (length)
wt = 200*10^(-6);                          % throat width
Lt = 75*10^(-6);                           % Throat length
hc = [50 75 100 125 150 175 200 250 300]*10^(-6);                    % cavity height
Lc = 1.2*10^(-3);                          % cavity length
Vo = 200;                                  % voltage applied
```

```
for kloop = 1:9

    [ue,pc,hDmax, thrust, flow_length, volume_ratio, wd, f1, fo] = RK_new_sweep_2(Lt, ht,
wt, hc(kloop), Lm, Lc, ho, Nt, Vo);

    fd_sweep = wd.*f1./(2*pi);



    fid = fopen(sprintf('2_h2_%gum',hc(kloop)*10^6), 'wt');
    fprintf(fid, 'frequency\tvelocity\tpressure\tdisplacement\tthrust\tflow
length\tvolume ratio\tfo\n');
    for i=1:length(fd_sweep)
        if(i == 1)
            fprintf(fid, '%s\t%s\t%s\t%s\t%s\t%s\t%s\t%s\n', fd_sweep(1), ue(1), pc(1),
hDmax(1), thrust(1), flow_length(1), volume_ratio(1), fo);
        else
            fprintf(fid, '%s\t%s\t%s\t%s\t%s\t%s\t%s\n', fd_sweep(i), ue(i), pc(i),
hDmax(i), thrust(i), flow_length(i), volume_ratio(i));
        end
    end
    [max_value, max_index] = max(thrust);
    fprintf(fid, 'Peak:\n');
    fprintf(fid, '%s\t%s\t%s\t%s\t%s\t%s\t%s\n', fd_sweep(max_index), ue(max_index),
pc(max_index), hDmax(max_index), thrust(max_index), flow_length(max_index),
volume_ratio(max_index));
    fclose(fid);

    % save important parameters
    h2_thrust(kloop)=thrust(max_index);
    h2_velocity(kloop)=ue(max_index);
    h2_pressure(kloop)=pc(max_index);
    h2_disp(kloop)=hDmax(max_index);
    h2_frequencyMax(kloop)=fd_sweep(max_index);
    h2_resonancefreq(kloop)=fo;
    h2(kloop)=hc(kloop);



    ue = [];
    pc = [];
    hDmax = [];
    thrust = [];
    flow_length = [];
    volume_ratio = [];

end

%==========================================================================
```

```
%-------------
% Plot data
%-------------

% Plot thrust
figure(1)
plot(h2*10^6,h2_thrust*10^6,'k','LineWidth',3);
title('Vary hc2: Thrust','fontsize',20,'fontweight','b');
xlabel('hc (um)','fontsize',20,'fontweight','b');
ylabel('Thrust (uN)','fontsize',20,'fontweight','b');

grid on
set(gca,'fontsize',20, 'linewidth', 2, 'fontweight', 'bold');

% save to file
set(gcf,'PaperUnits','centimeters','PaperPosition',[0 0 30 20])
print('-dpng', '2_h2_thrust.jpg', '-r300');
saveas(gcf,'2_h2_thrust.fig');

%-------------------

% Plot velocity
figure(2)
plot(h2*10^6,h2_velocity,'k','LineWidth',3);
title('Vary hc2: Velocity','fontsize',20,'fontweight','b');
xlabel('hc (um)','fontsize',20,'fontweight','b');
ylabel('Velocity (m/s)','fontsize',20,'fontweight','b');

grid on
set(gca,'fontsize',20, 'linewidth', 2, 'fontweight', 'bold');

% save to file
set(gcf,'PaperUnits','centimeters','PaperPosition',[0 0 30 20])
print('-dpng', '2_h2_velocity.jpg', '-r300');
saveas(gcf,'2_h2_velocity.fig');

%------------------

% Plot pressure
figure(3)
plot(h2*10^6,h2_pressure*10^(-3),'k','LineWidth',3);
title('Vary hc2: Pressure','fontsize',20,'fontweight','b');
xlabel('hc (um)','fontsize',20,'fontweight','b');
ylabel('Pressure (kPa)','fontsize',20,'fontweight','b');

grid on
set(gca,'fontsize',20, 'linewidth', 2, 'fontweight', 'bold');

% save to file
set(gcf,'PaperUnits','centimeters','PaperPosition',[0 0 30 20])
print('-dpng', '2_h2_pressure.jpg', '-r300');
saveas(gcf,'2_h2_pressure.fig');

%------------------

% Plot displacement
figure(4)
plot(h2*10^6,h2_disp*10^6,'k','LineWidth',3);
title('Vary hc2: Displacement','fontsize',20,'fontweight','b');
xlabel('hc (um)','fontsize',20,'fontweight','b');
ylabel('Displacement (um)','fontsize',20,'fontweight','b');

grid on
```

```
set(gca,'fontsize',20, 'linewidth', 2, 'fontweight', 'bold');

% save to file
set(gcf,'PaperUnits','centimeters','PaperPosition',[0 0 30 20])
print('-dpng', '2_h2_displacement.jpg', '-r300');
saveas(gcf,'2_h2_displacement.fig');

%------------------

% Plot frequency
figure(5)
plot(h2*10^6,h2_frequencyMax*10^(-3),'k',h2*10^6, h2_resonancefreq*10^(-
3),'r','LineWidth',3);
title('Vary hc2: Frequency','fontsize',20,'fontweight','b');
xlabel('hc (um)','fontsize',20,'fontweight','b');
ylabel('Frequency (kHz)','fontsize',20,'fontweight','b');
legend ('Diaphragm Frequency', 'Cavity Resonance');

grid on
set(gca,'fontsize',20, 'linewidth', 2, 'fontweight', 'bold');

% save to file
set(gcf,'PaperUnits','centimeters','PaperPosition',[0 0 30 20])
print('-dpng', '2_h2_frequency.jpg', '-r300');
saveas(gcf,'2_h2_frequency.fig');



% save data
save ('2_h2', 'h2', 'h2_thrust', 'h2_velocity', 'h2_pressure', 'h2_disp',
'h2_frequencyMax', 'h2_resonancefreq');

%===========================================================================
```

A1.2 Embedded Function 1

```
% Filename: RK_new_sweep_3.m

% (ODE45) Coupled System Model for Optimizing MACE // Seow Yuen Yee //

% -----------------------------------------------------------------------
% Finding exit velocity and cavity pressure and thrust (length modified)
% (modified 2p back to p and LeLv and also limit with event location)
% -----------------------------------------------------------------------

function [ue,pc,hDmax, thrust, flow_length, volume_ratio, wd, f1, fo] = RK_new_sweep_3(Lt,
ht, wt, hc, Lm, Lc, ho, Nt, Vo)

% -------------
% Constants
% -------------

c = 340;                                 % speed of sound (m/s)
p_amb = 101325;                          % ambient pressure (Pa)
n = 1.8*10^(-5);                        % viscosity of air (kg/(ms))
rho_amb = 1.2041;                        % ambient air density (kg/m3)
eps0 = 8.854*10^(-12);                   % air permittivity
% ---------------------
% Resonance frequency
% ---------------------

At = ht*wt;                               % throat cross section area

% % When hc is much larger than ht
% Le = Lt+2*sqrt(pi*At)/4;                    % Effective inertia throat length (thick)
% Lv = Lt;                                    % Effective viscous throat length

% When hc is comparable with ht :
Le = Lt + 0.0004*(ht/hc)+(Lm/pi)*(ht/hc)+2*sqrt(pi*At)/4;              % Effective
inertia throat length
Lv = Lt + 0.0004*(ht/hc)^3 + (Lm/pi)*(ht/hc)^3;                        % Effective
viscous throat length

Ad = Lm*Lm;                               % diaphragm area
Ac = Lc*Lc;
Vd0 = (4/(pi^2))*Ad*ho;                   % initial membrane diaphragm volume
Vc = (Ac*hc+Ad*ho)-Vd0;                   % cavity volume

vr = sqrt(Vc/(At*Le*Nt));                 % resonator volume ratio for high Re value
fo = (c/(2*pi*Le*vr))                     % Helmholtz resonance

% vd = (4/pi^2)*Ad*ho/Vc;                   % non-dimensional diaphragm displacement
volume
% if dimensional, do not divide by Vc


% -------------------------------
% Diaphragm Resonance Frequency
% -------------------------------

h_oxide = 0.66*10^(-6);                           % oxide thickness = 0.3 um
h_oxide2 = 0.66*10^(-6);                          % oxide thickness 2 = 0.3 um
h_nitride = 0.16*10^(-6);                         % nitride thickness = 0.23 um
h_nitride2 = 0.16*10^(-6);
% h_poly = 1.3*10^(-6);
h_metal = 0.3*10^(-6);                           % gold thickness = 0.5 um
```

```
h_tot = h_oxide + h_nitride + h_oxide2 + h_nitride2; % + h_poly;   % total thickness
td = h_metal/100;                                   % diaphragm thickness

rho_nit = 3100;                                     % density of nitride(kg/m3)
rho_ox = 2660;                                      % density of oxide (kg/m3)
rho_poly = 2300;

stress_nit = 1050*10^(6);                            % stress in nitride (3088Ang)
stress_ox = -150*10^(6);                            % stress in oxide (2814Ang)
stress_poly = 50*10^(6);

sigma =
(stress_ox*h_oxide2+stress_nit*h_nitride+stress_ox*h_oxide+stress_nit*h_nitride2)/h_tot;
         % residual diaphragm stress

%+stress_poly*h_poly

% density of diaphragm
rho_d = (rho_ox*h_oxide2 + rho_nit*h_nitride + rho_ox*h_oxide + rho_nit*h_nitride2)/h_tot;
%  + rho_poly*h_poly

wd = pi*(sqrt(2*sigma/(rho_d*Ad)));           % in rad/s
fd = wd/(2*pi)                                % in Hz



% ---------------------------
% Calculate pull-in voltage
% ---------------------------

poisson_ox = 0.27;
poisson_ni = 0.27;
poisson_poly = 0.23;

poisson = (poisson_ox*h_oxide + poisson_ox*h_oxide2 + poisson_ni*h_nitride +
poisson_ni*h_nitride2)/h_tot;

% + poisson_poly*h_poly

E_ox = 70*10^(9);
E_ni = 300*10^(9);
E_poly = 160*10^(9);

E = (E_ox*h_oxide + E_ox*h_oxide2 + E_ni*h_nitride +E_ni*h_nitride2)/h_tot;

% + E_poly*h_poly

% Old design in Allen's thesis
% poisson = 0.23;               % 0.23
% E = 140*10^(9);               % ~ 140 GPa

R = 0.44;                     % R = 44%
C1 = (pi^4)/32;               % 3.0440 (Allen)
C2 = ((pi^6)/(32*(1-poisson^2)))*(5/64-((5-6*poisson)/(2*(81*pi^2+64+poisson*(64-
9*pi^2)))));
% 2.4113 (Allen)
p1 = 0;

w = 0:ho/1000:ho;
% % Nw = length(w);
% % for i=1:Nw
% if assuming no residual stress, w = 0.0151*p*a^4*(1-poisson^2)/(E*td^3);
p1 = C1.*sigma.*h_tot.*w./(Lm/2)^2 + C2.*E.*h_tot.*w.^3./(Lm/2)^4;
```

```
% d = ho
Ve1 = sqrt((2.*(ho-w).^2.*p1)./(eps0*(1-R)));

Ve_max = max(Ve1)

% --------------
% Simulation
% --------------

thrust = 0;
flow_length = 0;
volume_ratio = 0;
ue = 0;
pc = 0;
hDmax = 0;


% Frequency response evaluated at nondimensional frequencies, f1

f1 = [0.1:0.01:2.1];
N = length(f1);
Kd = ((pi^2)/4)*(1/(rho_d*h_tot));        % Coupling effect constant

yi = [0, 0, rho_amb, 0, 0, Vc];

% Vo = 100;

for i = 1:N
%     [upp,pcpp,hDpp, yo] = diff_1_sweep2(f1(i), wd, Le, Lv, Ad, At, ht, Kd, ho, Vo, Nt,
100, yi, td);
%     [upp,pcpp,hDpp, yo] = diff_1_sweep2(f1(i), wd, Le, Lv, Ad, At, ht, Kd, ho, Vo, Nt,
3, yo, td);        % steady state
    [upp,pcpp,hDpp, thpp, flowpp, volpp, yo] = diff_2_sweep_length2_mf2(f1(i), wd, Le, Lv,
Ad, At, ht, Kd, ho, Vo, Nt, 200, yi, td, Vc);
    [upp,pcpp,hDpp, thpp, flowpp, volpp, yo] = diff_2_sweep_length2_mf2(f1(i), wd, Le, Lv,
Ad, At, ht, Kd, ho, Vo, Nt, 10, yo, td, Vc);        % steady state
    ue(i) = upp;
    pc(i) = pcpp;
    hDmax(i) = hDpp;
    thrust(i) = thpp;
    flow_length(i) = flowpp;
    volume_ratio(i) = volpp;
end


% --------
% Plots (Vary hc2)
% --------

% Plot thrust
figure(1)
plot((f1*wd)/(2*pi)*10^(-3),thrust*10^6,'b','LineWidth',3);
title('Throat Exit Thrust','fontsize',20,'fontweight','b');
xlabel('Frequency (kHz)','fontsize',20,'fontweight','b');
ylabel('Thrust (uN)','fontsize',20,'fontweight','b');

grid on
set(gca,'fontsize',20, 'linewidth', 2, 'fontweight', 'bold');
```

```
% save to file
set(gcf,'PaperUnits','centimeters','PaperPosition',[0 0 30 20])
print('-dpng', sprintf('3_h2_%gum_thrustF.jpg',hc*10^6), '-r300');
saveas(gcf, sprintf('3_h2_%gum_thrustF.fig',hc*10^6));

%-------------------

% Plot velocity
figure(2)
plot((f1*wd)/(2*pi)*10^(-3), ue,'b','LineWidth',3);
title('Throat Exit Velocity','fontsize',20,'fontweight','b');
xlabel('Frequency (kHz)','fontsize',20,'fontweight','b');
ylabel('Velocity (m/s)','fontsize',20,'fontweight','b');

grid on
set(gca,'fontsize',20, 'linewidth', 2, 'fontweight', 'bold');

% save to file
set(gcf,'PaperUnits','centimeters','PaperPosition',[0 0 30 20])
print('-dpng', sprintf('3_h2_%gum_velocityF.jpg',hc*10^6), '-r300');
saveas(gcf, sprintf('3_h2_%gum_velocityF.fig',hc*10^6));

%------------------

% Plot pressure
figure(3)
plot((f1*wd)/(2*pi)*10^(-3),pc/1000,'b','LineWidth',3);
title('Cavity Differential Pressure','fontsize',20,'fontweight','b');
xlabel('Frequency (kHz)','fontsize',20,'fontweight','b');
ylabel('Differential Pressure (kPa)','fontsize',20,'fontweight','b');

grid on
set(gca,'fontsize',20, 'linewidth', 2, 'fontweight', 'bold');

% save to file
set(gcf,'PaperUnits','centimeters','PaperPosition',[0 0 30 20])
print('-dpng', sprintf('3_h2_%gum_pressureF.jpg',hc*10^6), '-r300');
saveas(gcf, sprintf('3_h2_%gum_pressureF.fig',hc*10^6));

%------------------

% Plot displacement
figure(4)
plot((f1*wd)/(2*pi)*10^(-3),hDmax*(10^6),'b','LineWidth',3);
title('Diaphragm Displacement Amplitude','fontsize',20,'fontweight','b');
xlabel('Frequency (kHz)','fontsize',20,'fontweight','b');
ylabel('Displacement (um)','fontsize',20,'fontweight','b');

grid on
set(gca,'fontsize',20, 'linewidth', 2, 'fontweight', 'bold');

% save to file
set(gcf,'PaperUnits','centimeters','PaperPosition',[0 0 30 20])
print('-dpng', sprintf('3_h2_%gum_displacementF.jpg',hc*10^6), '-r300');
saveas(gcf, sprintf('3_h2_%gum_displacementF.fig',hc*10^6));

%------------------
```

```
% Plot flow length
figure(5)
plot((f1*wd)/(2*pi)*10^(-3),flow_length,'b','LineWidth',3);
title('Flow Length','fontsize',20,'fontweight','b');
xlabel('Frequency (kHz)','fontsize',20,'fontweight','b');
ylabel('Flow Length','fontsize',20,'fontweight','b');

grid on
set(gca,'fontsize',20, 'linewidth', 2, 'fontweight', 'bold');

% save to file
set(gcf,'PaperUnits','centimeters','PaperPosition',[0 0 30 20])
print('-dpng', sprintf('3_h2_%gum_flowlengthF.jpg',hc*10^6), '-r300');
saveas(gcf, sprintf('3_h2_%gum_flowlengthF.fig',hc*10^6));
```

A1.3 Embedded Function 2

```
% Filename: diff_2_sweep_length2_mf2.m

function [upp,pcpp,hDpp, thpp, flowpp, volpp, yo] = diff_2_sweep_length2_mf2(f, wd, Le,
Lv, Ad, At, ht, Kd, ho, Vo, Nt, Nc, yi, td, Vc)

% yo = final state of the system

tspan = [0:(2*pi/(1000*f*wd)):(2*Nc*pi/(f*wd))];
[t,y] = ode45('MACE_differential_new_sweep_length2_mf2',tspan, yi, [], f, wd, Le, Lv, Ad,
At, ht, Kd, ho, Vo, Nt, td);

u = y(:,1);
pc = y(:,2);
den = y(:,3);
hD = y(:,4);
d_hD = y(:,5);
V = y(:,6);

N1 = length(u);

upp = (max(u)-min(u))/2;
pcpp = (max(pc)-min(pc))/2;
denpp = (max(den)-min(den))/2;
hDpp = (max(hD)-min(hD))/2;


% -----------------------
% Thrust and Flow Length
% -----------------------

thrust2 = 0;
flow2 = 0;
vol2 = 0;

delta_t = t(2)-t(1);

for z = 1:(N1)
    if u(z) > 0
        thrust2 = thrust2 + delta_t*(f*wd)/(2*pi)*Nt*At.*den(z).*(u(z).^2);
        flow2 = flow2 + delta_t.*u(z)./ht;
        vol2 = vol2 + delta_t*(Nt*At/Vc).*u(z);
    end
end

thpp = thrust2/Nc;
flowpp = flow2/Nc;
volpp = vol2/Nc;

yo = [y(N1,1:6)];
```

```
% Only turn on when investigating transient response

% ---------------------
% Plots for transients
% ---------------------

% wd*f/(2*pi)
%
% figure(1)
% subplot(3,1,1)
% plot(t,u,'k','LineWidth',3);
% title('Transient : Throat Exit Velocity','fontsize',20,'fontweight','b');
% xlabel('Time (s)','fontsize',20,'fontweight','b');
% ylabel('Velocity (m/s)','fontsize',20,'fontweight','b');
% set(gca,'fontsize',20, 'linewidth', 2, 'fontweight', 'bold');
%
% % figure
% subplot(3,1,2)
% plot(t,pc/1000,'r','LineWidth',3);
% title('Transient : Cavity Differential Pressure','fontsize',20,'fontweight','b');
% xlabel('Time (s)','fontsize',20,'fontweight','b');
% ylabel('Pressure (kPa)','fontsize',20,'fontweight','b');
% set(gca,'fontsize',20, 'linewidth', 2, 'fontweight', 'bold');
%
% % figure
% subplot(3,1,3)
% plot(t,hD*10^6,'b','LineWidth',3);
% title('Transient : Membrane Displacement','fontsize',20,'fontweight','b');
% xlabel('Time (s)','fontsize',20,'fontweight','b');
% ylabel('Displacement (um)','fontsize',20,'fontweight','b');
%
% grid on
%
% set(gca,'fontsize',20, 'linewidth', 2, 'fontweight', 'bold');

% % save to file
% set(gcf,'PaperUnits','centimeters','PaperPosition',[0 0 30 20])
% print('-dpng', 'Transient_20.jpg', '-r300');
% saveas(gcf,'Transient_20.fig');
```

A1.4 Embedded Function 3

```
% Filename: diff_2_sweep_length2_mf2.m

function dy = MACE_differential_new_sweep_length2_mf2(t, y, OPTIONS, f, wd, Le, Lv, Ad,
At, ht, ...
              Kd, ho, Vo, Nt, td)


ue = y(1);
p = y(2);
rho = y(3);
hD  = y(4);
d_hD = y(5);
V = y(6);

% -------------
% Constants
% -------------
c = 340;                                 % speed of sound (m/s)
p_amb = 101325;                          % ambient pressure (Pa)
n = 1.8*10^(-5);                        % viscosity of air (kg/(ms))
rho_amb = 1.2041;                        % ambient air density (kg/m3)
eps0 = 8.854*10^(-12);                   % air permittivity
% --------------
% Computation
% --------------

tmp =sin(f*wd*t/2);

% % -------- Trapezoid wave ---------
% timeR = rem(t,2*pi/(f*wd));
%
% if tmp > 0
%     if  timeR >= 0 && timeR < (pi/(10*f*wd))
%         Ve = Vo/(pi/(10*f*wd))*timeR;
%     else if timeR >= pi/(10*f*wd) && timeR < (9*pi/(10*f*wd))
%             Ve = Vo;
%         else if timeR >= 9*pi/(10*f*wd)  && timeR < (pi/(f*wd))
%                 Ve = -Vo/(pi/(10*f*wd))*timeR + Vo*10;
%             end
%         end
%     end
% else
%     Ve = 0;
% end



% % -------- Square wave ---------
%
% if tmp > 0
%     Ve = Vo;
% else
%     Ve = 0;
% end

% % --------- Sine Wave --------

% if tmp > 0             % half sine wave. (rectified sine wave)
%     Ve = Vo*tmp;
% else
%     Ve = 0;
% end
```

```
% % --------- Sine Wave --------

Ve = Vo*tmp;


if hD>(ho-td)
    hD = ho-td;
end

g = 1/((1.000001-hD/ho)^0.846);                    % assuming that -ho < hD < +ho

if (imag(g))                                       % check for error
    error('WRONG!')
end

pe = g*(eps0/2)*(Ve/ho)^2;

if hD >= (ho-td) && d_hD >0
    d_hD = 0;
end

d_V = -(4*Ad/pi^2)*d_hD;

% wd_vary = sqrt((2.131*10^(13)*(hD^2)+5.6402*10^(7)*hD+3.5494*10^(3))/(6.75955*10^(-9)));
wd_vary = 3*10^15*(hD^2) + 2*10^10*hD + 723184;

d_dhD = -Kd*(p-pe)-(wd_vary)^2*hD;
                                                     % need to add perforation damping term
for more accurate results

if hD >= (ho-td) && d_hD >= 0 && d_dhD > 0
    d_dhD = 0;
end

if (ue < 0)
    d_ue = (1/Le)*(p/rho_amb)+(ue^2/(2*Le))-8*(n/rho_amb)*(ue/ht^2)*(Lv/Le);
    d_rho = -rho_amb*(ue*Nt*At/V)-rho*(d_V/V);
    d_p = c^2*d_rho;
else
    d_ue = (1/Le)*(p/rho)-(ue^2/(2*Le))-8*(n/rho)*(ue/ht^2)*(Lv/Le);
    d_rho = -rho*(ue*Nt*At/V)-rho*(d_V/V);
    d_p = c^2*d_rho;
end

dy = [d_ue; d_p; d_rho; d_hD; d_dhD; d_V];
```

APPENDIX B

DETAILED FABRICATION RECIPE FOR UJA

MACE4 Process Date: 11-05-2012

Materials:

(1) Single Sided Silicon Wafer (P-type)
    Resistivity: 10-20 ohm-m
    Thickness: 525 um +/- 25 um
(2) Double Sided Silicon Wafer (P-type)
    Resistivity: 10-40 ohm-m
    Thickness: 525 um +/- 25 um
(3) Mask
    Total: 6 (1-3, 6 for resonator; 4-5 for cavity)
    Company: Photo-Sciences
    Type: 5" Chrome (Soda Lime)
    Critical Dimensions Tolerance: 3 um ± 0.5 um
    Clear Mask: 1, 6
    Dark Mask: 2, 3, 4, 5
(4) Conductive epoxy (N20E) for electrical connections (used this for Al contact pads to avoid galvanization)

Process Steps: Resonator wafer

(1) Piranha clean on all wafers

(a) Hydrogen Peroxide (H_2O_2) : Sulfuric Acid (H_2SO_4) = 1:1

(b) Time: 10-15 mins

(2) ***(Flexus-2320-S)*** Measure initial bow of wafers for thin film stress measurements

2 um oxide wafers	– (3)	– ONO	(P1-A, P1-B, P1-C), (P4-A, P4-B)
	– (3)	– NONO	(P2-A, P2-B, P2-C)
Blank double sided	– (10)	– ONO	(P3-A,B,C,D,E,F,G,H,I,J)
	– (2)	– ONO	(T-ONO, T-ONO2)

Monitor wafer	– (1)	– NONO	(M-NONO)
	– (1)	– ONO	(M-ONO)
	– (1)	– N	(M-N)
	– (1)	– O	(M-O)
	– (1)	– 2nd NO	(M-NO)

* P1-A and P1-C broke during LAM frontside etch. P1 is without any oxide on backside. P4 is with oxide patterned on both sides.

(3) Spin PR on front side to protect for P1 wafers

Type: PR 1827
RPM: 4k rpm
Thickness: 3 um
Bake: 90 sec at 115 ^oC (hotplate)

(4) ***(Mask 6)*** (Only for P4) Pattern thermal oxide on back side for P4 wafers

(a) Spin PR on front to protect wafer surface

Type: PR 1827
RPM: 4k rpm
Thickness: 3 um
Bake: 90 sec at 115 ^oC (hotplate)

(b) Spin PR on back for lithography

Type: PR 1827
RPM: 4k rpm
Thickness: 3 um
Bake: 90 sec at 115 ^oC (hotplate)

(c) ***(MA6)*** Expose PR

Time: 13 sec

(d) Develop PR

Developer: MF319
Time: 1 min 6 sec

(e) Rinse with DI water

Time: 2 min

(5) ***(LAM 9400)*** Strip all oxide on backside for P1 wafers or pattern oxide on P4 wafers

Recipe: **mnf_oxide1_sy**
(a) Time: 15 mins (on data, etch rate is 1400Ang/min)

(6) Strip PR on all wafers

(7) ***(Flexus-2320-S)*** Measure bow of wafers for with 2 um oxide on front only

2 um oxide wafers – (3) – ONO (P1-A, P1-B, P1-C), (P4-A, P4-B)

(8) ***(Mask 6)*** Pattern thermal oxide on front side for P1 and P4 wafers

(f) Spin PR on back to protect wafer surface

Type: PR 1827
RPM: 4k rpm
Thickness: 3 um
Bake: 90 sec at 115 ^{o}C (hotplate)

(g) Spin PR on front for lithography

Type: PR 1827
RPM: 4k rpm
Thickness: 3 um
Bake: 90 sec at 115 ^{o}C (hotplate)

(h) ***(MA6)*** Expose PR

Time: 13 sec

(i) Develop PR

Developer: MF319
Time: 1 min 6 sec

(j) Rinse with DI water

Time: 2 min

(9) ***(LAM 9400)*** Etch and pattern oxide on front side for P1 and P4 wafers

Recipe: **mnf_oxide1_sy**
(a) Time: 15 mins

(10) Strip PR on all wafers

(11) ***(Flexus-2320-S)*** Measure bow of wafers for wafers with 2 um oxide on front only

2 um oxide wafers – (3) – ONO (P1-B), (P4-A, P4-B)

(12) ***(PFC + Furnace S2/T3)*** LPCVD Nitride/ Oxide (HTO) / Nitride / Oxide (HTO)

(a) Pre-Furnace Clean

Time: 2 hours

(b) Dielectric on membrane: Monitor wafer at slot #10 (from door, or left to right)

Nitride1		Actual (Average)
Deposition Time:	59 mins	
Target Thickness:	0.31 um	3098.88 Ang
Target Stress:	+1050 MPa	+ 1047 MPa to +1042 MPa
Oxide1		
Deposition Time:	2 hours 10 mins	
Target Thickness:	0.62 um	6332.12 Ang
Target Stress:	-150 MPa	- 142 MPa to -147 MPa
Nitride2		
Deposition Time:	59 mins	
Target Thickness:	0.31 um	3115.00 Ang
Target Stress:	+1050 MPa	
Oxide2		
Deposition Time:	2 hours 10 mins	
Target Thickness:	0.62 um	6339.80 Ang
Target Stress:	-150 MPa	

*Nitride1 : Slot 10 – M-N   Oxide1: M-O   Nitride2: M-NO

Slot 11 – M-NONO
Slot 12 – P2-A
Slot 13 – P2-B
Slot 14 – P2-C
Slot 15 – M-ONO
Slot 16 – T-ONO
Slot 17 – T-ONO2
Slot 18 – P1-B
Slot 19 – P4-A
Slot 20 – P4-B
Slot 21:30 – P3-A:J

* To measure stress on Nitride1 and Oxide1, spin PR on front side. Etch backside with LAM 9400. Strip PR. Measure with Flexus-2320-S.

*Etched nitride using mnf_nitride1_sy for 360+120 = 480 sec. Seems like 360 sec is already overetch, but still not sure of the etch rate. Expected on data was 600 Ang/min.

*Etched oxide using mnf_oxide1_sy for 300 sec.

(13) ***(Mask 3)*** Alignment mark on backside of wafer

(a) Spin PR on front to protect wafer surface

Type:	PR 1827
RPM:	4k rpm
Thickness:	3 um
Bake:	90 sec at 115 ^{o}C (hotplate)

(b) Spin PR on back for lithography

Type:	PR 1827
RPM:	4k rpm
Thickness:	3 um
Bake:	90 sec at 115 ^{o}C (hotplate)

(c) ***(MA6)*** Expose PR

Time:	13 sec

(d) Develop PR

Developer:	MF319
Time:	1 min 6 sec

(e) Rinse with DI water

Time:	2 min

(f) ***(LAM 9400)*** Etch Oxide1/Nitride/Oxide2

Recipe: **mnf_oxynit2_sy**

<u>Oxide1</u>

Target thickness:	6200 Ang
Time:	240 sec (1600Ang/min = 4 min)

<u>Nitride</u>

Target thickness:	3400 Ang
Time:	120 sec (1600 Ang/min = 2 min)

<u>Oxide2</u>

Target thickness:	6200 Ang
Time:	240 sec (1600Ang/min = 4 min)
Total time:	**600 sec (10 min)**

(g) Remove PR in PRS2000 (Optional: + Piranha clean)

Time:	30 min

(14) ***(Mask1)*** Sacrificial PR

(a) Spin PR on back to protect wafer surface

Type:	PR 1827
RPM:	4k rpm
Thickness:	3 um
Bake:	90 sec at 115 ^{o}C (hotplate)

(b) (flat electrode) Spin PR

Type:	PR 9260
RPM:	2k rpm
Thickness:	10 um
Bake:	Soft-90°C, 40 min (oven)

(curved electrode) Spin PR

Type: PR 9260
RPM: 3k rpm
Thickness: 7-8 um
Bake: Soft-90°C, 40 min (oven) / 4 min 30 sec at 115 ^{o}C (hotplate)

(c) ***(MA6)*** Expose PR

Time: 67 sec (flat), 47 sec (curve)

(d) Develop PR

Developer: AZ400K (1:3) DI water
Time: 1 min 30 sec to 2 min 30 sec depending on freshness of developer

(e) Rinse with DI water

Time: 2 min

(f) Hard bake PR

Time: 10-20 min at 135 ^{o}C (oven)

(g) (curved electrode) PR reflow

Type: Heat up Acetone to 75°C on hotplate for 5-10 mins, flip wafer upside down on beaker, cover partially for maximum solvent vapor
Time: 10 mins (rotate for uniform reflow)

(h) (curved electrode) Hard bake PR again

Time: 30 min – 135 ^{o}C (oven)

(15) ***(Lab18-2)*** Sputter Nickel seed layer

Cr/Au
Target Thickness: 300Ang/4000Ang (67sec/190sec+190sec)
Stress in Film: Cr : ~300MPa, Au : (2X) ~-20MPa
Deposition rate: Cr: 4.5 Ang/sec, Au: 10.7 Ang/sec

(16) ***(Mask2)*** PR mold for Nickel Electroplating

(a) Spin PR 1

Type: PR9260
RPM: 2k rpm – 3 sec (no spread)
Thickness: 21-25 um
Bake: Soft-90°C, 1 hour 20 min (oven)

(b) ***(MA6)*** Expose PR

Time: 200 sec

(c) Develop PR

Developer: AZ400K (1:3) DI water
Time: 8-10 min with fresh developer

(17) ***(Chem-acid bench)*** Nickel electroplating

Temperature:	50 ^{o}C (700 rpm)
Current density:	10 mA/cm^2
Current:	0.25 A (actual 0.22 A) (Area = 22.34 cm^2)
Voltage:	1.88-2.09 V
Time:	150 min
Target stress:	< 5MPa
Target thickness:	18 um
Plating rate:	0.12 um/min

* Pulse Timing: Fwd On – 90 ms, Fwd Off – 0 ms, Fwd duration – 90 ms
Rev On – 10 ms, Rev Off – 0 ms, Rev duration – 10 ms
* With filter pump connected and on

(18) Remove PR mold

Solvent: Acetone + IPA + DI water (do not dry)
Time: 3 hours

(19) Etch seed metal layer

Au

Etchant:	GE-8148
Time:	2 min and 30 sec (over-etch)
Target thickness:	4000 Ang

Cr

Etchant:	CR-14 (Chrome Mask Etchant)
Time:	30 sec (over-etch)
Target thickness:	300 Ang

(20) ***(Plasmatherm)*** Ash PR (if backside PR not removed)

Recipe: **sy_ash2**
Time: > 10 mins
(can be as long as 2 hours if previous hard bake step is long)

(21) Spin PR to protect backside

Type:	PR 1827
RPM:	4k rpm
Thickness:	3 um
Bake:	90 sec at 115 ^{o}C (hotplate)

(22) ***(LAM)*** Etch Oxide1/Nitride/Oxide2

Recipe: **mnf_oxynit2_sy**

<u>Oxide1</u>	
Target thickness:	6200 Ang
Time:	240 sec (1600Ang/min = 4 min)
<u>Nitride</u>	
Target thickness:	3400 Ang
Time:	120 sec (1600 Ang/min = 2 min)
<u>Oxide2</u>	
Target thickness:	6200 Ang
Time:	240 sec (1600Ang/min = 4 min)
Total time:	**600 sec (10 min)**

(23) Remove sacrificial PR

Solvent:	PRS2000 + Acetone + IPA (add Plasmatherm ashing if PR not removed)
Time:	> 1 day

(24) ***(Mask3)*** PR mold for DRIE etching

(a) Spin PR 1

Type:	PR9260
RPM:	1k rpm
Thickness:	15 um
Bake:	8 min at 115 ^{o}C (hotplate)

(b) ***(MA6)*** Expose PR

Time:	110 sec

(c) Develop PR

Developer:	AZ400K (1:3) DI water
Time:	5 min and 30 sec with fresh developer

(25) Mount wafer on carrier wafer for backside etching with crystal bond

Weight: 0.6 - 1.0 gram
Temperature: 80 ^{o}C
Time in vacuum: 10 mins (spread) + 10 mins (spread) + 10 mins (spread) + 10 mins (attach)

*Weight and drop crystal on process wafer in center, spread with sharp swab, put in vacuum jar for 10 mins and repeat. After making sure it is fully covered with crystal bond, drop carrier wafer on top of process wafer, and put in vacuum jar for 10 mins. Then, wipe the overflow of crystal bond on the edges.

(26) ***(Pegasus 4)*** DRIE backside silicon etching

Recipe:	LNF Recipe 3 Red Power Weibin
Time:	~ 2 hours and 30 mins (Etch rate is ~ 3.5 um/min)
Target thickness:	525 um

*Power is reduced from Recipe 3 to 800W and 600W, similar to old STS power.

(27) ***(Plasmatherm)*** Remove PR mask

Recipe:	**sy_ash2**
Time:	> 2 hours (with 30 mins intervals)

(28) ***(Lab18-2)*** Sputter metal on membrane

Cr/Al

Target Thickness:	500Ang/3000Ang (111 sec/1071 sec)	(Cr/Al : -42.86 MPa)
	or 300Ang/1000Ang (67 sec/360 sec)	(Cr/Al: -7.7MPa)
	new samples used 300Ang/2000Ang (160 sec/870 sec)	
Stress in Film:	Cr: ~300MPa, Ti: ~125MPa, Al: ~-100MPa	
Dep Rate:	Cr: 4.5 Ang/sec, Al: 2.8 Ang/sec	

(29) Remove crystal bond

Performed rinsing in the following order:
(1) Acetone: ~ 1 day
(2) DI water: ~ 1 day
(3) Acetone: < 8 hours
(4) IPA: < 8 hours
(5) Methanol: < 8 hours

* For drying: (1.2 mm x 1.2 mm diaphragms) 1-2 mins at 70 ^{o}C (Hotplate)
(larger size diaphragms) Use critical point dryer (set to 3.5 for purge timer and slowly turn on the fill knob)

MACE4 Process Date: 11-05-2012

Process Steps: Resonator wafer

(1) ***(Mask 4)*** Mask for throat holes

(a) Spin PR for lithography

Type:	PR 9260
RPM:	2k rpm
Thickness:	10 um
Bake:	4 min 20sec at 115 ^{o}C (hotplate)

(b) ***(MA6)*** Expose PR

Time: 67 sec

(c) Develop PR

Developer:	AZ400K(1:3)DI
Time:	3 min

(d) Rinse with DI water

Time: 2 min

(2) ***(Pegasus 4)*** DRIE throat holes

Recipe:	LNF Recipe 1
Time:	~30 mins (Etch rate is ~ 5.6 um/min)
Target thickness:	150 um (always target 50um extra than throat length needed)

(3) ***(Mask 5)*** Mask for cavity

(e) Spin PR for lithography

Type:	PR 9260
RPM:	2k rpm
Thickness:	10 um
Bake:	4 min 20sec at 115 ^{o}C (hotplate)

(f) ***(MA6)*** Expose PR

Time: 67 sec

(g) Develop PR

Developer:	AZ400K(1:3)DI
Time:	3 min

(h) Rinse with DI water

Time: 2 min

(4) Mount wafer on carrier wafer for backside etching with crystal bond

Weight: 0.5 gram per 50um throat length (for 100 um throat length, use 1.5g since etch 50um extra during first step)
Temperature: 80 ^oC
Time in vacuum: 10 mins (spread) + 10 mins (spread) + 10 mins (spread) + 10 mins (attach)

*Weight and drop crystal on process wafer in center, spread with sharp swab, put in vacuum jar for 10 mins and repeat. After making sure it is fully covered with crystal bond, drop carrier wafer on top of process wafer, and put in vacuum jar for 10 mins. Then, wipe the overflow of crystal bond on the edges.

(5) ***(Pegasus 4)*** DRIE backside silicon etching

Recipe:	LNF Recipe 1 or LNF Recipe 3 Red Power Weibin
Time:	~72 mins (Etch rate is ~ 5.6 um/min)
Target thickness:	400 um (for 500um thick wafer, and 100um throat length)

* Remove crystal bond in Water or Acetone for > 1 days (no heating)
* Then, do piranha clean for ~10-15 mins on the pieces.
* Then, put in IPA for ~5 mins, then Methanol for ~5 mins, and then dry on hotplate (115°C).

Process Steps: Assembly with SU-8 2010 (2 curing steps)

(1) First curing step

(a) Spin SU-8 2010

Type:	SU-8 2010
RPM:	4k rpm
Thickness:	10 um

*Drop the cavity pieces on the wet SU-8 such that the foot of the cavity will have SU-8. Lightly tap on the pieces to ensure uniform SU-8 on the foot of the cavity, and then quickly pick up with tweezers.

(b) Bake : 1 min at 95 ^oC (hotplate)

* Cavity pieces are bake upside down.

(2) Align actuator with cavity parts:

* Align the parts under microscope with yellow light, and then clamped together with flat tip copper alligator clips.

(3) Second curing step

(a) Bake : 10 min at 150 ^{o}C (hotplate)

* With the clips still attached.

(b) Bake : 1min at 150 ^{o}C (hotplate)

* Without the clips, just to ensure better curing.

REFERENCES

[1] S. Hauert, J.-C. Zufferey, and D. Floreano, “Evolved swarming without positioning information: an application in aerial communication relay,” *Autonomous Robots*, vol. 26, no. 1, pp. 21–32, 2009.

[2] RIA Novosti, “Chilean Miners Rescue Plan,” *Infographics*, 2010. [Online]. Available: http://en.rian.ru/infographics/20101013/160941495.html.

[3] Shawcity Limited, “Gasclam Borehole Monitor,” *Electronics Arena*. [Online]. Available: http://www.electronicsarena.co.uk/companies/shawcity-limited/products/gasclam-borehole-monitor. [Accessed: 04-May-2012].

[4] DaVinci Institute, “Grace Hopper,” *The Vault Artwork*. [Online]. Available: http://davincivault.com/the-vault-artwork/grace-hopper-2/.

[5] S. Cangeloso, “CES 2010 - HP Desktops and Workstations,” *geek.com*, 06-Jan-2010. [Online]. Available: http://www.geek.com/articles/chips/ces-2010-hp-desktops-and-workstations-2010016/.

[6] J. C. Benedict, “MacBook white,” *Wikipedia The Free Encyclopedia*, 17-Jan-2008. [Online]. Available: http://en.wikipedia.org/wiki/File:MacBook_white.png.

[7] M. Sharma, “Cheap Android Mobile Phones Below 10000 Rs,” *Buzz Paras*, 16-Dec-2011. [Online]. Available: http://www.buzzparas.com/2011/12/cheap-android-mobile-phones-below-10000-rs-3242.

[8] R. C. Michelson, “Novel Approaches to Miniature Flight Platforms,” *Proceedings of the Institution of Mechanical Engineers, Part G: Journal of Aerospace Engineering*, vol. 218, no. 6, pp. 363–373, Jun. 2004.

[9] T. Mueller, “On the Birth of Micro Air Vehicles,” *International Journal of Micro Air Vehicles*, vol. 1, no. 1, pp. 1–12, Mar. 2009.

[10] T. van Dijk, “Detective dragonfly,” *Delft Outlook*, pp. 12–16, 2003.

[11] Prox Dynamics, “Micro helicopters and ornithopters.” [Online]. Available: http://www.proxdynamics.com/r_d/micro_helicopters_and_ornithopters.

[12] T. N. Pornsin-sirirak, Y. C. Tai, H. Nassef, and C. M. Ho, “Titanium-alloy MEMS wing technology for a micro aerial vehicle application,” *Sensors and Actuators A: Physical*, vol. 89, no. 1–2, pp. 95–103, Mar. 2001.

[13] L. Petricca, P. Ohlckers, and C. Grinde, “Micro- and Nano-Air Vehicles: State of the Art,” *International Journal of Aerospace Engineering*, vol. 2011, pp. 1–17, 2011.

[14] AeroVironment, “AeroVironment Develops World’s First Fully Operational Life-Size Hummingbird-Like Unmanned Aircraft for DARPA,” Washington, at AAAS Conference, 17-Feb-2011.

[15] A. M. Flynn, “Flapping Nano Air Vehicles,” MicroPropulsion Technical Report 100, Jan. 2010.

[16] R. Wood, “Fly, Robot, Fly,” *Spectrum, IEEE*, vol. 45, no. 3, pp. 25 –29, Mar. 2008.

[17] K. Y. Ma, P. Chirarattananon, S. B. Fuller, and R. J. Wood, “Controlled Flight of a Biologically Inspired, Insect-Scale Robot,” *Science*, vol. 340, no. 6132, pp. 603–607, May 2013.
[18] J. M. McMichael and M. S. Francis, “Micro Air Vehicle - Toward a New Dimension in Flight,” 1997. [Online]. Available: http://www.fas.org/irp/program/collect/docs/mav_auvsi.htm. [Accessed: 12-Apr-2012].
[19] D. Darling, “Aeolipile,” *The Encyclopedia of Science*. [Online]. Available: http://www.daviddarling.info/encyclopedia/A/aeolipile.html.
[20] D. H. Lewis, S. W. Janson, R. B. Cohen, and E. K. Antonsson, “Digital micropropulsion,” *Sensors and Actuators A: Physical*, vol. 80, no. 2, pp. 143–154, 2000.
[21] K. L. Zhang, S. K. Chou, S. S. Ang, and X. S. Tang, “A MEMS-based solid propellant microthruster with Au/Ti igniter,” *Sensors and Actuators A: Physical*, vol. 122, no. 1, pp. 113–123, Jul. 2005.
[22] S. Tanaka, R. Hosokawa, S. Tokudome, K. Hori, H. Saito, M. Watanabe, and M. Esashi, “MEMS-Based Solid Propellant Rocket Array Thruster,” *TRANSACTIONS OF THE JAPAN SOCIETY FOR AERONAUTICAL AND SPACE SCIENCES*, vol. 46, no. 151, pp. 47–51, 2003.
[23] E. . Mukerjee, A. . Wallace, K. . Yan, D. . Howard, R. . Smith, and S. . Collins, “Vaporizing liquid microthruster,” *Sensors and Actuators A: Physical*, vol. 83, no. 1–3, pp. 231–236, May 2000.
[24] J. Xiong, Z. Zhou, X. Ye, X. Wang, Y. Feng, and Y. Li, “A colloid micro-thruster system,” *Microelectronic Engineering*, vol. 61–62, no. 0, pp. 1031–1037, Jul. 2002.
[25] J. Xiong, Z. Zhou, D. Sun, and X. Ye, “Development of a MEMS based colloid thruster with sandwich structure,” *Sensors and Actuators A: Physical*, vol. 117, no. 1, pp. 168–172, Jan. 2005.
[26] C. Warsop, M. Hucker, A. J. Press, and P. Dawson, “Pulsed Air-jet Actuators for Flow Separation Control,” *Flow Turbulence Combust*, vol. 78, no. 3–4, pp. 255–281, Jun. 2007.
[27] O. Ducloux, R. Viard, A. Talbi, L. Gimeno, Y. Deblock, P. Pernod, V. Preobrazhensky, and A. Merlen, “A magnetically actuated, high momentum rate MEMS pulsed microjet for active flow control,” *Journal of Micromechanics and Microengineering*, vol. 19, no. 11, p. 115031, 2009.
[28] J. C. Zito, R. J. Durscher, J. Soni, S. Roy, and D. P. Arnold, “Flow and force inducement using micron size dielectric barrier discharge actuators,” *Applied Physics Letters*, vol. 100, no. 19, pp. 193502–193502, 2012.
[29] N. Bénard, J. Jolibois, E. Moreau, R. Sosa, G. Artana, and G. Touchard, “Aerodynamic plasma actuators: A directional micro-jet device,” *Thin Solid Films*, vol. 516, no. 19, pp. 6660–6667, Aug. 2008.
[30] D. J. Coe, M. G. Allen, B. L. Smith, and A. Glezer, “Addressable Micromachined Jet Arrays,” in *Solid-State Sensors and Actuators, 1995 and Eurosensors IX.. Transducers ’95. The 8th International Conference on*, 1995, vol. 2, pp. 329 –332.

[31] Z.-B. Luo, Z.-X. Xia, and B. Liu, “New generation of synthetic jet actuators,” *AIAA journal*, vol. 44, no. 10, pp. 2418–2420, 2006.
[32] Z. Luo, Z. Xia, and B. Liu, “An adjustable synthetic jet by a novel PZT-driven actuator with a slide block,” in *Journal of Physics: Conference Series*, 2006, vol. 34, p. 487.
[33] L. Gimeno, A. Talbi, R. Viard, A. Merlen, P. Pernod, and V. Preobrazhensky, “Synthetic jets based on micro magneto mechanical systems for aerodynamic flow control,” *Journal of Micromechanics and Microengineering*, vol. 20, no. 7, p. 075004, 2010.
[34] J. S. Agashe, M. Sheplak, D. P. Arnold, and L. Cattafesta, “MEMS-Based Electrodynamic Synthetic Jet Actuators for Flow Control Applications,” in *IUTAM Symposium on Flow Control and MEMS*, vol. 7, J. F. Morrison, D. M. Birch, and P. Lavoie, Eds. Springer Netherlands, 2008, pp. 25–32.
[35] J. Deng, W. Yuan, J. Luo, D. Shen, and B. Ma, “Design and fabrication of a Piezoelectric Micro Synthetic Jet Actuator,” in *2011 IEEE International Conference on Nano/Micro Engineered and Molecular Systems (NEMS)*, 2011, pp. 301–304.
[36] Y. Liang, Y. Kuga, and M. Taya, “Design of membrane actuator based on ferromagnetic shape memory alloy composite for synthetic jet applications,” *Sensors and Actuators A: Physical*, vol. 125, no. 2, pp. 512–518, Jan. 2006.
[37] O. J. Aldraihem, T. S. Al-Saud, W. Aki, and A. Baz, “Piezoelectric micro-thruster,” *World Forum on Smart Materials and Smart Structures Technology (SMSST 2007)*. 22-May-2007.
[38] “Lumped Element Modeling of Piezoelectric-Driven Synthetic Jet Actuators (AIAA).” [Online]. Available: http://arc.aiaa.org.proxy.lib.umich.edu/doi/abs/10.2514/2.1936. [Accessed: 24-May-2013].
[39] Z. Trávníček, A. I. Fedorchenko, and A.-B. Wang, “Enhancement of synthetic jets by means of an integrated valve-less pump: Part I. Design of the actuator,” *Sensors and Actuators A: Physical*, vol. 120, no. 1, pp. 232–240, Apr. 2005.
[40] B. Parviz, K. Najafi, M. Muller, L. Bernal, and P. Washabaugh, “Electrostatically driven synthetic microjet arrays as a propulsion method for micro flight,” *Microsystem Technologies*, vol. 11, no. 12, pp. 1292–1300, 2005.
[41] T.-K. A.Chou, K. Najafi, M. O. Muller, L. P. Bernal, and P. D. Washabaugh, “Characterization of micromachined acoustic ejector and its applications,” in *The Fifteenth IEEE International Conference on Micro Electro Mechanical Systems, 2002*, 2002, pp. 264–267.
[42] H. Kim, A. H. Jauregui, C. Morrison, K. Najafi, L. P. Bernal, and P. D. Washabaugh, “Low-power electrostatic microthruster for propulsion based on helmholtz-resonance,” in *Micro Electro Mechanical Systems, 2007. MEMS. IEEE 20th International Conference on*, 2007, pp. 127 –130.
[43] K. Azar, “The history of power dissipation,” *Electronics Cooling*, vol. 6, no. 1, pp. 42–50, 2000.

[44] “The end of Moore’s ‘law’?,” *thenextwave*. [Online]. Available: http://thenextwavefutures.wordpress.com/2009/08/02/the-end-of-moores-law/. [Accessed: 17-Jul-2013].

[45] “Researches on Improving Energy-Efficiency in Processors.” [Online]. Available: http://arch.naist.jp/Files/2011/energy_efficiency_arch.en.html. [Accessed: 17-Jul-2013].

[46] D. S. Kercher, J.-B. Lee, O. Brand, M. G. Allen, and A. Glezer, “Microjet cooling devices for thermal management of electronics,” *Components and Packaging Technologies, IEEE Transactions on*, vol. 26, no. 2, pp. 359 – 366, Jun. 2003.

[47] H. P. J. De Bock, J. L. Jackson, B. P. Whalen, and P. Chamarthy, “Experimental Flow Performance Evaluation of novel miniaturized Advanced Piezoelectric Dual Cooling Jet,” in *Journal of Physics: Conference Series*, 2012, vol. 395, pp. 12035–12045.

[48] J. Campbell, S.J., W. Z. Black, A. Glezer, and J. G. Hartley, “Thermal management of a laptop computer with synthetic air microjets,” in *Thermal and Thermomechanical Phenomena in Electronic Systems, 1998. ITHERM ’98. The Sixth Intersociety Conference on*, 1998, pp. 43 –50.

[49] A. Tsung-Kuan, Chou, K. Najafi, M. O. Muller, L. P. Bernal, P. D. Washabaugh, and B. A. Parviz, “Micromachined e-jet for IC chip cooling,” in *Solid-State Circuits Conference, 2002. Digest of Technical Papers. ISSCC. 2002 IEEE International*, 2002, vol. 1, pp. 356 –357 vol.1.

[50] H. Kim, “An integrated electrostatic peristaltic gas micropump with active microvalves,” Ph.D. dissertation, University of Michigan., MI, 2006.

[51] P. S. Krueger, A. A. Moslemi, J. T. Nichols, I. K. Bartol, and W. J. Stewart, “Vortex Rings in Bio-Inspired and Biological Jet Propulsion,” *Advances in Science and Technology*, vol. 58, pp. 237–246, 2008.

[52] T.-K. A. Chou, “All-silicon micromachined acoustic ejector arrays for micro propulsion and flow control,” Ph.D. dissertation, University of Michigan., MI, 2001.

[53] J. W. Strutt, B. Rayleigh, and R. B. Lindsay, *The theory of sound*, vol. 1. Dover New York, 1945.

[54] W. L. Nyborg, “Acoustic Streaming due to Attenuated Plane Waves,” *The Journal of the Acoustical Society of America*, vol. 25, no. 1, pp. 68–75, 1953.

[55] P. J. Westervelt, “The Theory of Steady Rotational Flow Generated by a Sound Field,” *The Journal of the Acoustical Society of America*, vol. 25, no. 1, pp. 60–67, 1953.

[56] J. Lighthill, “Acoustic streaming,” *Journal of Sound Vibration*, vol. 61, pp. 391–418, Dec. 1978.

[57] H. Yu and E.-S. Kim, “Micropropulsion of air and liquid jet by acoustic streaming,” in *IEEE The Sixteenth Annual International Conference on Micro Electro Mechanical Systems, 2003. MEMS-03 Kyoto*, 2003, pp. 76–79.

[58] H. von Helmholtz, “On the sensations of tone (1863),” *English translation by AJ Ellis*, 1885.

[59] A. S. Hersh and B. Walker, “Fluid mechanical model of the Helmholtz resonator,” *Final Report Hersh Acoustical Engineering, Chatsworth, CA.*, vol. 1, 1977.

[60] A. Parviz, K. Najafi, O. Muller, P. Bernal, and D. Washabaugh, “Electrostatically driven synthetic microjet arrays as a propulsion method for micro flight: Part II: microfabrication and initial characterization,” *Microsyst. Technol.*, vol. 11, no. 12, pp. 1292–1300, Nov. 2005.
[61] M. O. Muller, “Flow structure, performance and scaling of acoustic jets,” *ProQuest Dissertations And Theses; Thesis (Ph.D.)--University of Michigan, 2002.; Publication Number: AAI3058024; ISBN: 9780493736198; Source: Dissertation Abstracts International, Volume: 63-07, Section: B, page: 3366.; 218 p.*, 2002.
[62] B. Amirparviz, “Development of ultrasonic electrostatic microjets for distributed propulsion and microflight,” Ph.D. dissertation, University of Michigan., MI, 2001.
[63] O. C. Jeong, S. W. Park, S. S. Yang, and J. J. Pak, “Fabrication of a peristaltic PDMS micropump,” *Sensors and Actuators A: Physical*, vol. 123–124, pp. 453–458, Sep. 2005.
[64] E. E. Aktakka, H. Kim, and K. Najafi, “Wafer level fabrication of high performance MEMS using bonded and thinned bulk piezoelectric substrates,” in *Solid-State Sensors, Actuators and Microsystems Conference, 2009. TRANSDUCERS 2009. International*, June, pp. 849–852.
[65] E. H. Yang, S. S. Yang, and O. C. Jeong, “Fabrication and electrostatic actuation of thin diaphragms,” *KSME International Journal*, vol. 12, no. 2, pp. 161–169, Mar. 1998.
[66] H. Kim, A. B. Ucok, and K. Najafi, “Large-Deflection Stacked Multi-Electrode Electrostatic Actuator,” presented at the Solid-State Sensor, Actuator and Microsystems Workshop, Hilton Head Island, South Carolina, 2004.
[67] W. van der Wijngaart, H. Ask, P. Enoksson, and G. Stemme, “A high-stroke, high-pressure electrostatic actuator for valve applications,” *Sensors and Actuators A: Physical*, vol. 100, no. 2–3, pp. 264–271, Sep. 2002.
[68] J. Branebjerg and P. Gravesen, “A new electrostatic actuator providing improved stroke length and force,” in *IEEE Micro Electro Mechanical Systems, 1992, MEMS ’92, Proceedings. An Investigation of Micro Structures, Sensors, Actuators, Machines and Robot*, 1992, pp. 6–11.
[69] C. Liu and Y. W. Yi, “Micromachined magnetic actuators using electroplated Permalloy,” *IEEE Transactions on Magnetics*, vol. 35, no. 3, pp. 1976 –1985, May 1999.
[70] A. B. Yu, A. Q. Liu, J. Oberhammer, Q. X. Zhang, and H. M. Hosseini, “Characterization and optimization of dry releasing for the fabrication of RF MEMS capacitive switches,” *Journal of Micromechanics and Microengineering*, vol. 17, no. 10, pp. 2024–2030, Oct. 2007.
[71] J.-B. Yoon, C.-H. Han, E. Yoon, and C.-K. Kim, “Novel two-step baking process for high-aspect-ratio photolithography with conventional positive thick photoresist,” in *Micromachining and Microfabrication*, 1998, pp. 316–325.
[72] J. I. Seeger and S. B. Crary, “Stabilization of electrostatically actuated mechanical devices,” in *, 1997 International Conference on Solid State Sensors and Actuators, 1997. TRANSDUCERS ’97 Chicago*, 1997, vol. 2, pp. 1133–1136 vol.2.

[73] T. Kuphaldt, “Lessons in Electric Circuits Volume II - AC.” [Online]. Available: http://www.barnesandnoble.com/w/lessons-in-electric-circuits-volume-ii-ac-tony-kuphaldt/1105349495. [Accessed: 13-Jul-2013].
[74] International Rectifier Power MOSFET, “Transformer-Isolated Gate Driver Provides very large duty cycle ratios.” .
[75] “STW11NM80 STMicroelectronics | Mouser,” *Mouser Electronics*. [Online]. Available: http://www.mouser.com/Search/ProductDetail.aspx?R=STW11NM80virtualkey51120000virtualkey511-STW11NM80. [Accessed: 13-Jul-2013].
[76] N. Tavassolian, M. Koutsoureli, E. Papandreou, G. Papaioannou, B. Lacroix, Z. Liu, and J. Papapolymerou, “The effect of silicon nitride stoichiometry on charging mechanisms in RF-MEMS capacitive switches,” *IEEE Transactions on Microwave Theory and Techniques*, vol. 57, no. 12, pp. 3518–24, Dec. 2009.
[77] Zhen Peng, Xiaobin Yuan, J. C. M. Hwang, D. Forehand, and C. L. Goldsmith, “Top vs. bottom charging of the dielectric in RF MEMS capacitive switches,” in *2006 Asia Pacific Microwave Conference, 12-15 Dec. 2006*, Piscataway, NJ, USA, 2006, pp. 117–20.
[78] Epoxy Technology, “Tech Tip 12 - Compatible Metallization with Electrically Conductive Silver Epoxies.” [Online]. Available: http://www.epotek.com/SSCDocs/techtips/Tech%20Tip%2012%20-%20Compatible%20Metallization.pdf.
[79] G. G. Stokes, “On the Effect of the Internal Friction of Fluids on the Motion of Pendulums,” in *Mathematical and Physical Papers*, vol. 3, Cambridge University Press, 2009.